WAKE BEHIND A DISCONTINUOUS CYLINDER: UNVEILING THE ROLE OF THE LARGE SCALES IN WAKE GROWTH AND ENTRAINMENT

Venkata Subba Rao Mandava

UNIVERSITAT ROVIRA i VIRGILI

Wake Behind a Discontinuous Cylinder: Unveiling the Role of the Large Scales in Wake Growth and Entrainment

VENKATA SUBBA RAO MANDAVA

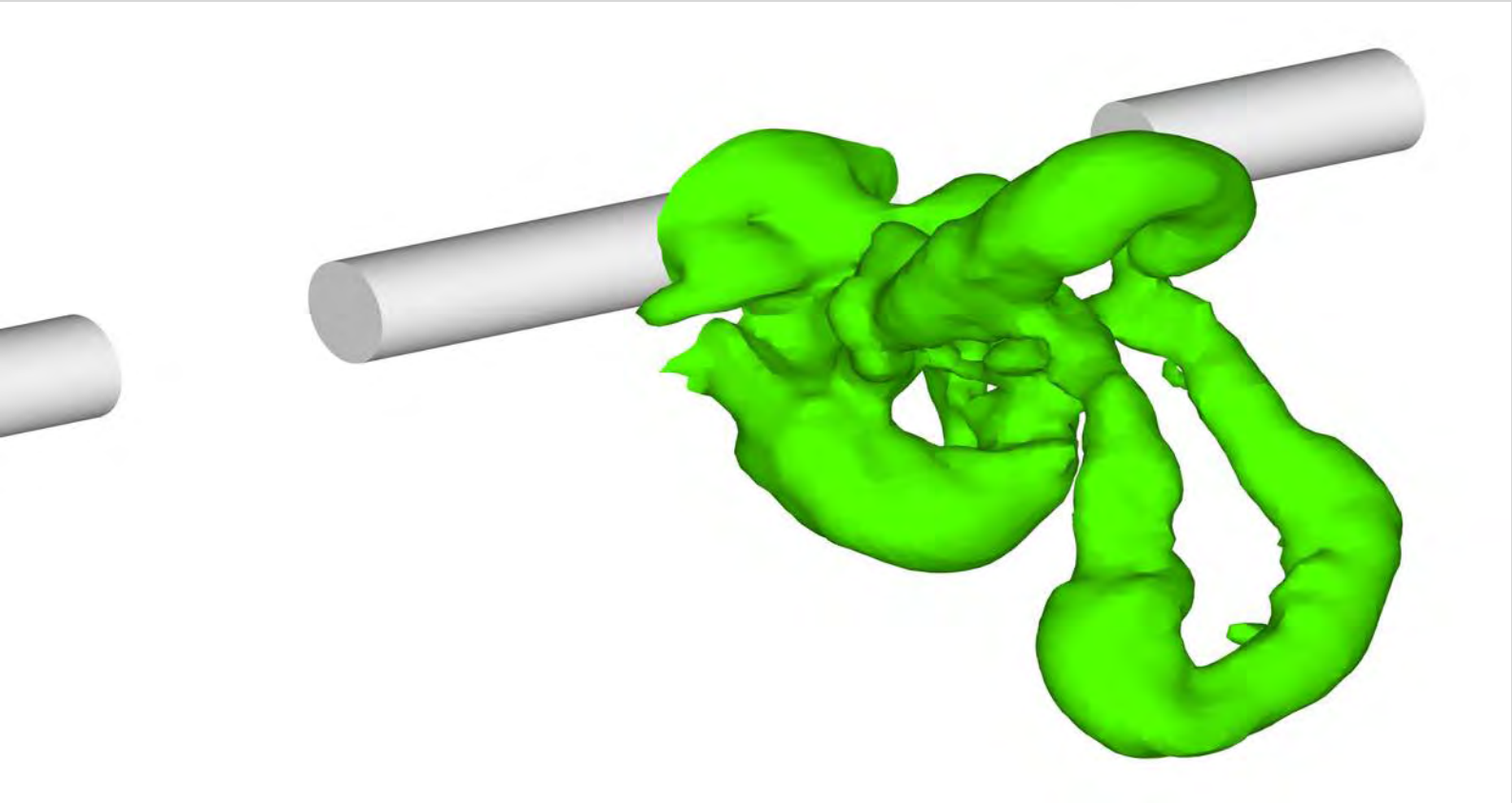

DOCTORAL THESIS
2022

Wake Behind a Discontinuous Cylinder: Unveiling the Role of the Large Scales in Wake Growth and Entrainment

Doctoral Thesis

Student
Venkata Subba Rao Mandava

Supervised by
Dr. Francesc Giralt Prat
Dr. Juan Herrero Sabartés

UNIVERSITAT ROVIRA i VIRGILI

Departament d´Enginyeria Química
Universitat Rovira i Virgili
Tarragona 43007

2022

UNIVERSITAT ROVIRA i VIRGILI

We STATE that the present study, entitled "**Wake behind a discontinuous cylinder: Unveiling the role of the large scales in wake growth and entrainment**", presented by **Venkata Subba Rao Mandava** for the award of **Doctoral degree**, has been carried out under our supervision at the **Department of Chemical Engineering** of this university.

Tarragona, 31-01-2022

Doctoral Thesis Supervisor/s

GIRALT PRAT FRANCESC D'ASSIS - 37250132E

Digitally signed by GIRALT PRAT FRANCESC D'ASSIS - 37250132E
Date: 2022.02.01 10:56:14 +01'00'

[Dr. Francesc Giralt Prat]

[Dr. Juan Herrero Sabartés]

Acknowledgements

The most pleasant task in writing thesis is the acknowledgement of help, without such help it would have been scarcely possible. It is my great privilege to thank my supervisors *Prof. Francesc Giralt Prat* and *Prof. Juan Herrero Sabartés, Department of Chemical Engineering, Universitat Rovira i Virgili, Tarragona, Spain,* who amidst all their busy schedule could find time for guiding me to make this work successful. Their unfailing patience when I delayed to deliver and their undying spirit of enthusiasm can never be portrayed in a single word. I am thankful to P*rof. Gregory A. Kopp, Department of Civil and Environmental Engineering, University of Western Ontario (UWO), London, Ontario, Canada,* for accommodating me in his research group and for allowing me to use the wind tunnel facilities at *Boundary Layer Wind Tunnel Laboratory (BLWTL)* at *UWO*, when I visited his group on research short stay, for conducting early part of the measurements in the thesis work, and also for guiding me with his highly valuable suggestions through out the thesis work.

I am grateful to Catalan Government for providing me the financial support to carry out this work. At the outset, I would like to express my sense of gratitude to director of the department for providing us the best possible learning ambiance in our university campus. I would like to thank all professors and students in the department for their help during the entire work.

Venkata Subba Rao Mandava

Abstract

The turbulent flow in the wake of a discontinuous cylinder (DC) was investigated both experimentally and numerically to ascertain the role of large-scale flow patterns, such as horseshoe or double roller structures, in the entrainment process originating close to the wake interface. The DC geometry consisted of cylinder segments $5D$ long (with D being the diameter of the cylinder) separated by gaps of width $2.5D$. This DC cylinder configuration was selected after analyzing the numerical calculations carried out at low Reynolds number to ensure that the interaction of the discontinuous wake with the flow between two cylinder segments, alternating side by side, triggered the shedding of horseshoe vortices (HSV) behind each segment. Particle Image Velocimetry (PIV) and Hot-Wire Anemometry (HWA) measurements were used to analyze the flow at two Reynolds numbers, $Re = 4,000$ and 10,000, for $x/D \leq 180$. Large eddy simulations (LES) for both the DC and the infinite continuous cylinder (CC) wakes were also carried out at Re = 10,000. A three-dimensional near wake with HSV's was formed as a result of the interaction between the high momentum flow between segments and the alternating Kármán-like vortices formed behind each segment. The difference between the CC and the DC wakes is that in the former two-dimensional Kármán vortices, straddled with hairpin–vortices, are shed. The HSV or double roller (DR) vortices generated in the very near wake region of the DC wake can help unveiling the role that these three–dimensional HSVs, which were previously identified in the CC far wake, play in the entrainment process in turbulent wakes. The DC wake was found to grow and spread in the direction transverse to the cylinder axis with a much faster rate than for the CC wake, up until about $x/D \approx 50$, but with a small spanwise spread into the jet regions. The enhanced growth rate of the DC wake was due to the progressive stretching and vertical displacement (kinking) of HSV's. The shape of mean HSV's was found to be consistent with the cross-stream mean flow entrainment from the jet region into the wake region. The reported increase in the wake spreading and entrainment rates observed in the DC wake, measured in terms of wake width, was about 3 times that of the CC wake, while the maximum mean velocity defect was about half at the wake downstream loaction $x/D \approx 50$. This enhanced entrainment rate was caused and regulated by the presence of highly stretched DRs, indicating the predominant role that they play in the engulfment contribution of the entrainment process, which is coupled with a nibbling process taking place at smaller scales.

Contents

Nomenclature

List of Symbols, Constants and Variables

Δt Time step in LES simulations

Δ Grid filter width in LES simulations

δ Cronecker delta

$\hat{p}$ Instantaneous dynamic (modified LES filtered) pressure

λ Thickness of a thin steel plate

ν Fluid kinematic viscosity

ν_t Eddy viscosity

$\omega_x^f, \omega_y^f, \omega_z^f$ Numerical instantaneous streamwise, transverse and spanwise vorticity fluctuation components, respectively

ω_{RMS} r. m. s. vorticity fluctuations

ω_{str} Vortex stretching component

$\overline{\hat{p}}$ Mean dynamic (modified LES filtered) pressure

$\overline{\omega}_z$ Experimental mean (time averaged) spanwise vorticity component

$\overline{\tilde{\omega}}$ Numerical mean (time averaged) vorticity

$\overline{\tilde{\omega}}_x, \overline{\tilde{\omega}}_y, \overline{\tilde{\omega}}_z$ Numerical mean (time averaged) streamwise, transverse and spanwise vorticity components, respectively

$\overline{\tilde{u}}, \overline{\tilde{v}}, \overline{\tilde{w}}$ Numerical mean (time averaged) streamwise, transverse and spanwise velocity components, respectively

$\overline{I}$ Intermittency factor

$\overline{I}_{max}$ Maximum intermittency factor

$\overline{PD}_{shr}$ Mean shear production

$\overline{u'v'}$ Experimental Reynolds shear stress

$\overline{u^f v^f}$ Numerical Reynolds shear stress

$\overline{u}, \overline{v}, \overline{w}$ Experimental mean (time averaged) streamwise, transverse and spanwise velocity components, respectively

$\overline{u}_d$ Mean streamwise velocity defect

ρ Fluid density

τ_{ij}^r Anisotropic residual stress tensor

τ_{ij} Residual stress tensor

τ_w Wall shear stress at the cylinder surface

$\tilde{\omega}_x, \tilde{\omega}_y, \tilde{\omega}_z$ Numerical instantaneous streamwise, transverse and spanwise vorticity components, respectively

$\tilde{p}$ Instantaneous LES filtered pressure

$\tilde{u}, \tilde{v}, \tilde{w}$ Numerical instantaneous streamwise, transverse and spanwise velocity components, respectively

A, B & n Constants obtained by calibration in hot-wire anemometry

C Threshold level for the turbulence detector function (F)

C_d Drag coefficient

C_s Smagorinsky LES model coefficient

D Diameter of the cylinder

E Bridge voltage in hot-wire anemometry

F Turbulence detector function

F_d Mean drag force on the cylinder surface per unit cylinder length

H Height of the simulation domain

I Turbulence indicator function

K Length of the simulation domain

k_r Residual kinetic energy

L Length of the solid cylinder segment

L_R Recirculation bubble length or wake-closure length

L_u Length scale of streamwise r. m. s. velocity component

N Number of grid nodes on the outer surface of a cylinder cross-section

p^f Instantaneous dynamic (modified LES filtered) pressure fluctuations

p_{atm} Atmospheric pressure

PD_{shr} Instantaneous shear production

R_w & R_g Operating and cold wire resistances, respectively, in hot-wire anemometry

Re Reynolds number

S Gap between the solid cylinder segments

S_t Strouhal number

S_{ij} Filtered or resolved strain tensor

T Mean time period of a shedding cycle

u, v, w Experimental instantaneous streamwise, transverse and spanwise velocity components, respectively

u^f, v^f, w^f Numerical instantaneous streamwise, transverse and spanwise velocity fluctuation components, respectively

u^+ Non-dimensional velocity at the cylinder surface

u', v', w' Experimental instantaneous streamwise, transverse and spanwise velocity fluctuation components, respectively

U_0 Free-stream velocity

u_t Tangential velocity at the cylinder surface

U_{ef} Effective cooling velocity in hot-wire anemometry

u_{RMS} streamwise r. m. s. velocity

W Width of the simulation domain

x, y, z Streamwise, transverse and spanwise coordinates

y^+ Non-dimensional normal distance between the cylinder surface and the adjacent calculation node

$y_{1/2}$ Wake half width

List of Acronyms

$BLWTL$ Boundary Layer Wind Tunnel Laboratory

CC Infinite Continuous Cylinder

CCD Charge-Coupled Device

CS Coherent Structures

DC Discontinous Cylinder

DNS Direct Numerical Simulations

DR Double Roller Vortices

HSV Horseshoe Vortices

HWA Hot-Wire Anemometry

LES Large Eddy Simulations

ODE Ordinary Differential Equation

PIV Particle Image Velocimetry

$TNTI$ Turbulent and Non-Turbulent Interface

URV Universitat Rovira i Virgili

VKV Von Kármán Vortices

List of Tables

List of Figures

Chapter 1

Introduction

The wake behind a circular cylinder is an ideal flow system to study the genesis of large-scale structures and their dynamical evolution with respect to initial flow conditions in turbulent free flows. Numerous numerical and experimental studies have been carried out in the past to characterize the large-scale structures in the near-, mid- and far-wake regions of turbulent wakes. Early classical works investigated the vortex street [1] and the variation of drag of cylinders with aspect ratio [2]. Flow instability and transitions in the near wake have been studied by many researchers e.g.,[3], [4], [5], [6], [7]. Cantwell et al. 1983 [8] used flying hot–wire devices together with phase averaging techniques to obtain conditional averages of normal and shear stresses, intermittency, vorticity, and velocities in the near wake of a circular cylinder at a Reynolds number of $Re = 1.4 \times 10^5$. These authors observed that the maximum value of random shear stress, which is not related to the von Kármán vortices shed close to the cylinder, occurs near the saddle point between the Kármán vortices, thus, suggesting the presence of other three-dimensional structures in the near wake, which were also later observed by Hayakawa et al.1989 [9].

Hayakawa et al.1989 [9] observed the presence of three-dimensional organized structures in the von Kármán vortex street in the near and mid-far wake, ($10 \leq x/D \leq 40$; here x is the streamwise coordinate and D is diameter of the cylinder) at a Reynolds number of $Re = 13,000$. These authors employed a methodology based on the detection of vorticity peaks in the hot wire time records. They reported that the von Kármán vortices (VKV's) could be interconnected with secondary vortices having streamwise vorticity. Ferré et al. 1989a [10], using a pattern recognition approach, analyzed the evolution of large-scale organized motions in the mid wake ($10 \leq x/D \leq 40$) at $Re = 9,000$. They found that the periodic activity of the Kármán vortices persists up to 60 diameters downstream. Yamane et al. 1988 [11] analyzed

the wake behind a circular cylinder at $Re = 2,100$ and $4,200$, using a flow visualization technique and simultaneous hot wire measurements. They reported the predominance of Kármán vortices at $x/D = 10$, the presence of a complex flow field near $x/D = 60$, where transition from Kármán vortices to some new coherent structures (CS) takes place, and far-wake large-scale structures that are formed at $x/D = 90$. More recently, the direct numerical simulations carried out by McClure et al. 2019 [12] showed that Kelvin-Helmholtz instabilities led to the formation of hairpin structures in the near wake for $Re \geq 800$ when streamwise vortex pairs pinch off vorticity from Kármán vortices and reorient to form the legs of hairpins. They reported that this regime is characterized by a significant increase in vortex deformation and a wake flow with many hairpin formations.

The existence of large-scale coherent flow structures in the turbulent far wake of the cylinder has also been known for quite long. More generally, the importance of three-dimensional structures in turbulent wakes was well established by the pioneering works of Theodorsen 1952 [13], Townsend 1956 [14] and Grant 1958 [15]. Theodorsen 1952 [13] proposed that the predominant structure in a developed wake should be a horseshoe–like vortex. Grant 1958 [15] postulated, based on a comprehensive set of correlation measurements in the far wake of a cylinder at $x/D = 533$, the existence of shear-aligned double roller eddies and mixing jets as ejections of turbulent flow from the center of the wake towards the non–turbulent external flow region. Payne et al. 1967 [16] reexamined the correlation data of Grant 1958 [15] using the orthogonal decomposition technique [17] to refine some details regarding the double roller structure. The results of their analysis, however, were not fully consistent with the hypothesis of Grant 1958 [15] as the large eddies depicted by Payne et al. 1967 [16] were normal to the center plane instead of along the shear axis, as originally suggested by Grant 1958 [15].

Notwithstanding, the results obtained by Keffer 1965 [18] and Keffer 1967 [19] in a cylinder wake strained through a constant-area distorting duct gave support to Grant's hypothesis. LaRue et al. 1974 [20] performed the auto– and cross–spectral analysis of temperature signals measured at $x/D = 400$ and found that the interface bulges were related to the large-scale structures of the bulk flow, a fact that was consistent with the large–eddy scenario proposed by Grant 1958 [15]. Ferré et al. 1989a [10] refined the pattern recognition technique, previously developed by Mumford 1983 [21], to analyze large-scale motion at $x/D = 140$. They found that the large-scale flow organization consisted of double roller eddies. Similar double roller–like structures in the far wake were identified later by several researchers e.g.,[9], [22], [23], [24]. In particular, Giralt et al. 1993 [25] determined that the double roller structure, i.e., a pair of counter rotating vortices, is simply a

horizontal slice through a horseshoe vortex near the wake half-width. Vernet et al. 1997 [26] gave further evidence, based on their simultaneous temperature and velocity measurements, that Townsend's and Grant's double roller and mixing jet structures might be different views of a single flow structure, likely a horseshoe–shaped vortex. Vernet et al. 1999a [27] identified the complete three-dimensional topology of the large-scale structures by using conditional sampling. They confirmed that the structure shape was like a horseshoe vortex. Philip et al. 2012 [28] proposed a simplified axisymmetric wake model, based on randomly inclined vortical structures, which was able to reproduce the experimental mean velocity and normal and shear stress profiles. The genesis of these large-scale structures present in the far wake should be the secondary hairpin vortices characterized by McClure et al. 2019 [12] in the near wake. A precise definition of the large-scale structures and their organized motion was given more recently in Marusic et al. 2013 [29].

Another approach to study the spreading turbulent wake flows is to examine the turbulent/non–turbulent interface (TNTI hereinafter) that separates the turbulent wake flow from the external non-turbulent flow. The TNTI is usually sharp, with a thickness of about one to two orders of magnitude smaller than the integral flow scale [30], [31], [32]. The rate of momentum entrainment of non–turbulent flow into the turbulent wake would be largely determined by the characteristics of the TNTI itself and by the vertical motions present in the turbulent region near the TNTI. Entrainment at the TNTI is a time dependent and multistage process, which due to its importance in many engineering and geophysical flows has been thoroughly investigated, e.g., [22], [27], [28], [33], [34], [35], [36], [37], [38], [39], [40], [41]. Two important hypothesis were postulated by Corrsin et al. 1955 [33]: (i) that there is a step–like change in velocity across the TNTI, and (ii) that the spreading process of turbulence into the non–turbulent flow region was like turbulent diffusion, a process of phenomena that has been commonly referred to as nibbling. Note that the latter hypothesis suggests that large–scale flow structures play a minor role in the entrainment process. Townsend 1976 [34] disagreed with Corrsin et al.1955 [33] second hypothesis and claimed that the bulk motion is sufficient to determine the wake spreading and entrainment rates in free shear flows.

Engulfment is the name given to the quasi-inviscid process where large eddies draw an amount of fluid from the non–turbulent region into the wake region where subsequently mixing occurs by viscous diffusion [34], [42]. Brown and Roshko 1974 [42] successful models for entrainment in plane mixing layers, with overall rates being determined by the engulfing action of large eddies. Dahm et al. 1987 [43] used visualizations and measurements of a scalar

concentration field in the near region of a jet to show that the entrainment process was dominated by the engulfment of large-scale structures. They also showed that local large scales of the flow can be used to characterize the rate of the entrainment process. Ferré et al. 1989b [22] analyzed the organized motions of the temperature field in the wake of a heated cylinder at $x/D = 140$ and they concluded from the distribution of colder and warmer spots in vertical and horizontal planes of the wake that the double roller vortices are in fact associated with the large–scale entraining motions. Ferré et al. 1990 [23] and Giralt et al. 1993 [25] argued that horseshoe vortices should play an important role in the momentum transfer as they maintain the correlation between the streamwise and vertical velocity fluctuations (i.e., Reynolds shear stress). According to this scenario, the external fluid is first ingested by the highly stretched DRs, with z-vorticity at their top, and then twisted and mixed by the action of the counterrotating DR legs to produce small-scale velocity fluctuations [35].

Some more recent studies [36], [37], [38], [44], [45] suggested that nibbling was the main mechanism of entrainment in turbulent jet flow, in agreement with the second hypothesis of Corrsin et al. 1955 [33]. Westerweel et al. 2009 [39] showed that large–scale engulfment would account for less than 10 percent of the total fluid mass entrained and suggested that the entrainment process is mainly dominated by small scale nibbling. More recently, Philip et al. 2012 [28] showed that the mean velocities and second order statistics in jet and wake flows could be obtained by the large-scale eddy model that they proposed and concluded that the primary cause of entrainment could be the large–scale engulfment combined with small scale nibbling.

To summarize, there have been several important observations in the literature. First, coherent structures within turbulent shear flows play an important role in setting the details of the TNTI and the rate of entrainment. Second, coherent structures develop and evolve depending on the initial and boundary conditions of the flow. These two observations imply that the relative importance of the nibbling and engulfment mechanisms depend on the flow conditions and the details of the CS. Thus, by controlling the development of the CS, like the near wake instabilities leading to the formation of hairpins do in a CC turbulent wake, one should control the extent to which each of the mechanisms contribute to the overall entrainment rate. The key question, then, is how to do that? How to generate dominant hairpin-like structures in the near wake with high vorticity under turbulent conditions?

We developed what we call a discontinuous cylinder wake, which consists of cylinder segments $5D$ long (with D being the diameter of the cylinder) separated by gaps of width $2.5D$. Hereinafter, we will refer to this geometry as a discontinuous cylinder (DC) configuration. Our first working hypothesis is

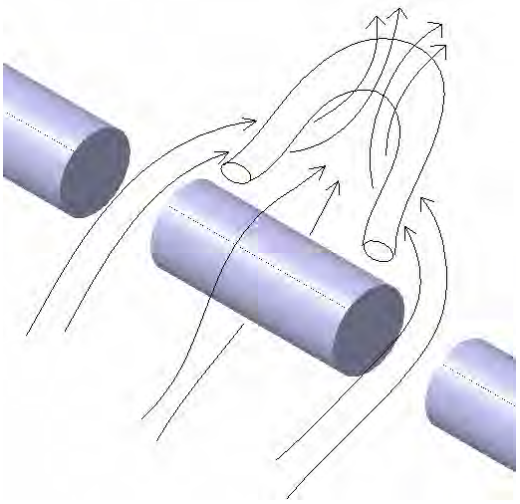

Figure 1.1: Sketch of the flow in the proximity of the discontinuous cylinders (DC).

that it is possible to generate a three-dimensional (3-D) wake behind a cylindrical shape by substituting the solid cylinder (hereafter, continuous cylinder; CC) with regularly alternating discontinuous cylinder segments, each shedding horseshoe–like vortices that resemble the HSV or DR flow patterns, which are aligned with the mean shear in far wake flows. Flow between two adjacent cylindrical pieces would split towards the two low pressure regions located behind them causing an extra input of momentum that would enhance both the kinking and the rotational energy of the shed horseshoe–like vortices, as sketched in figure 1.1. The shear alignment of the horseshoe vortices is critical because it accounts for the engulfing mechanism that has to be maintained for a significant duration due to vortex stretching. Note that a lack of shear alignment would led them to decay, like VKVs do. This implies that far-wake CC structures, such as the shear-aligned HSV vortices, should be associated with relatively higher entrainment and growth rates than typical near wake structures, such as VKVs, which are not shear-aligned, as reported by Vernet et al. 1999a [27] and Kopp et al. 2002 [35].

The second hypothesis is that, in the mid and far wake regions, these horseshoe vortices, shed behind each cylindrical segment, enhance the transfer of momentum from the mean flow, both laterally and vertically and, thus, result in a faster recovery of wake velocity with respect to the external free flow. Also, if their role is equivalent to that of the double rollers (DR) identified in a CC far wake, the smaller mean velocity–defect of the DC wake should decrease with $(x/D)^{-0.5}$ and its larger half–width wake size increase

with $(x/D)^{0.5}$. The third and final hypothesis is that the DR that would evolve from the 3-D horseshoe vortices shed by the DC, as they are further stretched and randomized while convected downstream into the mid and far wake regions, would contribute more to the turbulent kinetic energy than those observed in the CC wake. This should be so given their higher vorticity and size, since they already originate from 3-D horseshoe vortices with higher $z-$vorticity at their top than that of VKV shed by a CC. This could, in turn, entail the generation of larger turbulent bulges protruding into the free stream by the stretching action of the legs of the DR, and cause an associated net lateral fluid entrainment and enhanced turbulent diffusion in the spanwise direction of the non-turbulent fluid surrounding these protrusions. These large-scale DR structures maintain their entrainment role by being continuously stretched as they are convected downstream. As a result, the DC wake should grow vertically with the square root of distance from the origin, as does the CC wake in the far region, but with a greater thickness.

We carried out Particle Image Velocimetry (PIV) and Hot-Wire Anemometry (HWA) measurements as well as Large Eddy Simulations (LES) to analyze/characterize the wake growth and entrainment rates in the near and far wake of the DC. In order to establish the proper comparisons and to test the current setup, measurements and calculations were also performed for the continuous cylinder wake, at $Re = 1.0 \times 10^4$. PIV and HWA measurements data were used to obtain length scales of wake half-width as well as the distribution of velocity–defect. Numerical (LES) data was used to characterize the instantaneous shape of large-scale structures in the near wake of the DC. The momentum transfer into the wake region from the free stream flow region and from the free stream flow in the gap region between cylinder segments was also analyzed with the numerical data.

The rest of this thesis is organized as follows. In Chapter 2 we describe the experimental and numerical methods that were used in the present research, and the validation of those methods. The results are presented in Chapters 3 to 7. In particular, the mean flow statistics in the near wake ($x/D \leq 10$), obtained with both the CC and DC arrangements, are compared in Chapter 3. Chapter 4 is devoted to a comparative analysis of the growth rates of the CC and DC wakes in terms of the most used characteristic length scales. The details of wake interface identification is presented in Chapter 5. Evidence of the presence of large-scale flow structures (horseshoe–like vortices) in the near wake of the DC is presented in Chapter 6. The mean activity of the large-scale structures and the entrainment process in the DC wake are presented in Chapter 7. Final remarks are provided in Chapter 8.

The current thesis is the result of work carried out discontinuously over the past 18 years due to unfortunate and unpredictable personal health and

family circumstances, both early in the thesis and afterwards. This explains and justifies that the first results of the work were published as conference papers in 2009 and 2010 in Appendices D and E, respectively, and that a final archival publication will appear in the Journal of Fluid Mechanics in 2022 (Appendix F).

Chapter 2

Methods

2.1 Approach

To investigate our hypotheses, we examined the wake of a segmented circular cylinder, which we referred to as a Discontinuous Cylinder (DC). As depicted in figure 2.1, the DC is defined with two non-dimensional parameters: the ratio of the solid segment length to cylinder diameter, L/D, and the gap between the solid segments, S/D. The idea here is to choose values of L/D and S/D such that there is early formation of horseshoe vortices (HSV), as depicted in figure 1.1, but with a far wake that is two-dimensional in the mean. By forcing the early occurrence of HSV, rather than allowing the normal development of three-dimensional structures in the CC wake, we can examine differences in the overall rates of entrainment. By maintaining a two-dimensional far wake, the self-preserving states between the DC and CC wakes can be compared. Analysis of the self-preserving state provides a framework for the comparison. If the growth rate of the self-preserving states of the two far wakes are the same, then the difference in wake thickness should ascertain the difference in entrainment due to the near DC wake structure.

Several studies have examined the effects of finite cylinder length on the vortex structure in the near wake e.g.,[6], [46], [47], [48], [49]. These studies have found a complex dependence of the near wake vortices on the aspect ratio, L/D. Of importance for the current study, Inoue et al. 2008 [49] found periodic shedding of HSV for $L/D = 5$ at $Re = 300$ using Direct Numerical Simulations (DNS). This size compares favourably with the spanwise extent of HSV in the far wake, which Vernet et al. 1999a [27] found to be about $5D$. This suggests that L/D should be similar and, hence, a value of $L/D = 5$ was chosen.

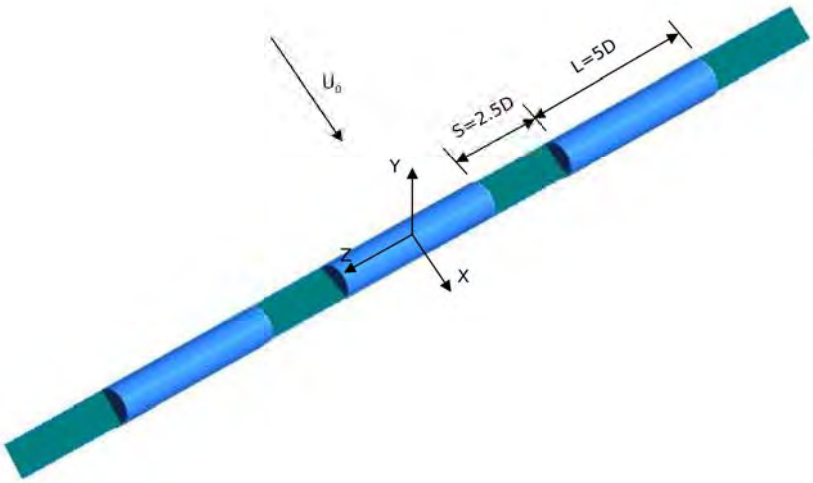

Figure 2.1: Sketch of the discontinuous cylinder model M_1 used in BLWTL and the co-ordinate system defined. Five and seven cylinder segments were respectively used in the URV models M_2 and M_3; see table 2.1.

To obtain a far wake behind the DC that is two-dimensional in the mean, the gap between the solid cylinder segments, S, should not be too large. However, if S is too small, the gap may be ineffective in allowing the HSV to form in the near wake. We carried out several DNS simulations at low Reynold's number, $Re = 300$, when designing our experimental setup. This led to the conclusion that $S/D = 2.5$ and $L/D = 5$ were optimal to shed HSVs behind each segment of the DC configuration in a synchronized manner, as shown in figure 2.2. This shedding was confirmed experimentally to also form in the near wake of the DC for $Re = 10,000$, as reported by Mandava et al. 2009 [50]. When these rows of HSVs alternating with jet-like flows in the spanwise direction get randomized, as they are advected downstream, these spanwise variations are smeared away by turbulence and the far wake becomes 2D on average, as is also the case in the CC far wake. It should also be noted that, given the intricately variable wake structures that occur for finite cylinders, the additional parameter, S/D, for the DC could also lead to a rich set of vortical structures. This remains to be explored in future work. We carried out Particle Image Velocimetry (PIV) and Hot-Wire Anemometry (HWA) measurements as well as Large Eddy Simulations (LES) to analyze/characterize the wake growth and entrainment rates in the near and far wake of the DC and the analogous CC at the same Re.

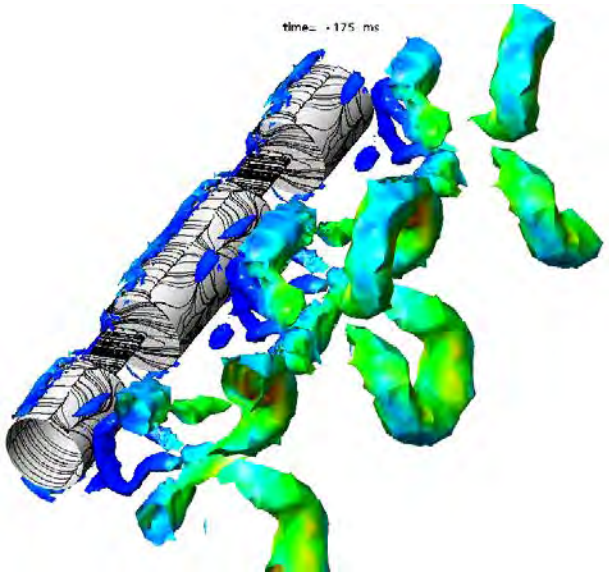

Figure 2.2: Preliminary simulation results, to design the experimental setup, at low Reynold's number, $Re = 300$, to find the optimal S and L parameters to shed horseshoe vortices in the DC near wake. Isosurfaces of pressure in the DC near wake.

2.2 Experimental set-up

Experiments were carried out in an open-return wind tunnel at the Boundary Layer Wind Tunnel Laboratory (BLWTL), University of Western Ontario, Canada, and in the open-return wind tunnel at the Universitat Rovira i Virgili (URV) in Tarragona, Spain. Figure 2.3 shows the wind tunnel at BLWTL, at University of Western Ontario, Canada. It is a suction type wind tunnel with a cross-section of 0.45 m $\times$ 0.45 m and with a length of 1.5 m. The intake flow was straightened through a honeycomb and fine screen prior to entering a 7.4:1 contraction. This tunnel was used earlier for wide range of inflow velocities from 1.25 m/s to 17.8 m/s (see [51], [52], [53], [54]). A free stream velocity of $U_0 = 9.2$ m/s was chosen in the current experiments. At this velocity, the free stream turbulence intensity was 1%. Figure 2.4 shows the wind tunnel at URV in Tarragona, Spain. It is also a suction type with a cross-section of 0.6 m $\times$ 0.6 m and a length of 3 m. A set of flow straighteners and filters and a contraction zone of ratio 9:1 produced a low turbulence (less than 0.2%) for the $U_0 = 9.2$ m/s free-stream velocity of the current experiments. For the interested reader, previous measurements carried out in this tunnel were published by Vernet et al. 1999a [27] and Kopp et al.

Figure 2.3: Wind tunnel at the Boundary Layer Wind Tunnel Laboratory (BLWTL), University of Western Ontario, Canada.

2002 [35]. The value of the Reynolds number, $Re = 1.0 \times 10^4$, was chosen for the current experiments because at that Reynolds number the boundary layer on the cylinder surface is laminar while the flow in the wake is fully turbulent [55].

Three DC models were used in the current study, as defined in table 2.1. Two of the DC models, M_1 and M_2, were used to carry out the measurements in the near and intermediate wake regions (up to $x/D = 56$) in the BLWTL at UWO and wind tunnel at URV, respectively. The different cross-sections of both tunnels required 3 cylindrical segments in the former and 5 in the latter. The diameter of the cylinder segments in these two models was $D = 0.0163$ m, a value chosen to provide the desired Reynolds number of $Re = 1.0 \times 10^4$. In both the M_1 and M_2 models the relative length of each cylinder segment was $L = 5D$ and the relative gap between cylinder segments was equal to $2.5D$ (see figure 2.1 and table 2.1). A thin steel plate having a thickness of $\lambda = 0.815 \times 10^{-3}$ m and a width equal to D held the cylinder segments together without interfering significantly with the flow between the gaps. To carry out the measurements in the far wake region, $70 \leq x/D \leq 180$, we used a third DC model (M_3) with seven cylinder segments having a smaller diameter ($D = 0.0065$ m) in order to bring the far wake into the optimal

Figure 2.4: Wind tunnel at the Universitat Rovira i Virgili (URV) in Tarragona, Spain.

measurement region of the wind tunnel. The thickness of the steel plate in the M_3 model was reduced to $\lambda = 0.30 \times 10^{-3}$ m to keep a value of the D/λ ratio similar to that of M_1 and M_2 (see table 2.1). As we maintained the $U_0 = 9.2$ m/s free-stream velocity level in the M_3 model experiments the Reynolds number in the far wake measurements was lower, namely $Re = 4.0 \times 10^3$. The geometrical details of the three models, tunnel specifications and experimental conditions are summarized in table 2.1.

We carried out Particle Image Velocimetry (PIV) measurements in the two wind tunnels. In both tunnels atomized olive oil was used for seeding particles of an average size of $1\mu m$, which were illuminated by Nd:YAG lasers yielding 120 mJ/pulse at a wavelength of 532 nm. Charge-coupled device (CCD) cameras were used to capture the images with a resolution of 1200 pixels $\times$ 1600 pixels, at a rate of 15 double frames per second in both cases. Two-component PIV was used in the BLWTL measurements whereas both two-component and stereo-PIV were used in the measurements conducted at URV. The locations of the measurement windows in the different sets of PIV measurements carried out in both tunnels are shown in tables 2.2, 2.3 and 2.4.

A first set of measurements carried out with the M_1 model were conducted

Model name	M_1	M_2	M_3
Wind tunnel label	BLWTL	URV	URV
Cylinder diameter, D (m)	0.0163	0.0163	0.0065
Length of cylinder segment, L	5D	5D	5D
Gap between cylinder segments, S	2.5D	2.5D	2.5D
Number of cylinder segments	3	5	7
Plate thickness, λ (mm)	0.815	0.815	0.30
D/λ	20	20	21.67
Tunnel cross-section (m×m)	0.45×0.45	0.60×0.60	0.60×0.60
Tunnel length (m)	1.5	3.0	3.0
Free-stream velocity, U_0 (m/s)	9.2	9.2	9.2
Reynolds number, Re	1.0×10^4	1.0×10^4	4.0×10^3
Free-stream flow turbulence intensity (%)	1.0	0.2	0.2
Measurements in wake region	$0 \leq x/D \leq 9$ At several z stations	$0 \leq x/D \leq 56$ At $z = 0$	$70 \leq x/D \leq 180$ At $z = 0$
Type of measurement plane and PIV system used	$x - y$ planes 2D PIV	$x - y$ planes Stereo PIV $x - z$ planes 2D PIV	$x - y$ planes Stereo PIV $x - z$ planes 2D PIV

Table 2.1: Geometrical details of the three discontinuous cylinder configurations, wind tunnel specifications and experimental conditions.

$(x/D_{start}, y/D_{start})-(x/D_{end}, y/D_{end})$ window	(0, –2D) — (9D, 2D)
z/D	0 0.5 1 1.5 2 2.5 3 3.75

Table 2.2: Two-component PIV window sizes and $x - y$ measurement planes in the near wake region ($0 \leq x/D \leq 9$), carried out with model M_1.

$(x/D_{start}, y/D_{start})-(x/D_{end}, y/D_{end})$ plane window at $z = 0$	DC Model
(0, -2) − (9, 2)	M_2
(9, -2) − (16, 2)	M_2
(26, -2) − (36, 6)	M_2
(43, -2) − (56, 8)	M_2
(70, -2) − (90, 8)	M_3
(110, -2) − (130, 8)	M_3
(170, -2) − (180, 10)	M_3

Table 2.3: Stereo–PIV window sizes and $x - y$ measurement planes in the near and far wake regions. Model M_2 was used for $0 \leq x/D \leq 56$ and model M_3 was used for $70 \leq x/D \leq 180$.

$(x/D_{start}, z/D_{start})$ − $(x/D_{end}, z/D_{end})$ plane window	y/D	DC Model
(10, -4) − (20, 4)	2.0	M_2
(26, -4) − (36, 4)	3.3	M_2
(43, -4) − (56, 4)	3.7	M_2
(72, -4) − (86, 4)	5.0	M_3
(119, -4)− (32, 4)	6.0	M_3

Table 2.4: Two-component PIV window sizes and $x - z$ measurement planes in the intermediate and far wake regions. Model M_2 was used for $10 \leq x/D \leq 56$ and model M_3 was used for $70 \leq x/D \leq 132$, in the wind tunnel at URV.

in the near wake region at $x/D \leq 9$ and several transverse $x-y$ planes along the cylinder axis (see table 2.2). Also, a few measurements were also carried out on the same $x-y$ window at selected axial locations with $z < 0$ to check flow symmetry. An additional set of consistency-check measurements on the same $x-y$ window at $z = 0$ were later performed in the URV tunnel with model M_2, i. e., with five cylinder segments instead of three. The data obtained in the URV tunnel were in good agreement with the earlier experimental data obtained in the BLWTL. Measurements in the URV tunnel extended further downstream in the wake with DC models M_2 and M_3. The corresponding experiments with the continuous cylinder (CC) models were also carried out in the URV tunnel using stereo-PIV. In these CC experiments the measurement windows were chosen to be the same as those used in the DC measurements listed in table 2.3. The diameters and experimental conditions of the two CC models were identical to those of the DC models M_2 and M_3 except, of course, for the absence of gaps and splitter plates. Measurements at several horizontal $(x-z)$ planes using two-component PIV were also conducted in the URV tunnel in the mid $(10 \leq x/D \leq 56)$ and far $(72 \leq x/D \leq 132)$ wake with models M_2 and M_3, respectively, as summarized in table 2.4.

A total of 4,500 instantaneous image pairs were collected and saved to disk in each experimental run in BLWTL and URV. The TSI Insight 3G software was used, in all cases, for a frame-to-frame correlation to generate instantaneous velocity fields with an interrogation window of size 32×32 pixels with 50% overlap.

Hot-wire anemometry (HWA) experiments were also carried out in the wake region of a discontinuous cylinder. Measurements were carried out in the wind tunnel at URV with the DC model M_3, at $Re = 4.0 \times 10^3$. Three normal-wire constant temperature anemometers (DISA 55M01/55M10 bridges and 55P11 probes) were used to sample the turbulent stream-wise velocities in the wake. The normal wires were operated at an overheat ratio of 1.8, and calibrated assuming a Kings law relation [56],

$$\frac{E^2}{R_w - R_g} = A + BU_{ef}^n \tag{2.1}$$

where E is the bridge voltage, R_w and R_g are the operating and cold wire resistances, respectively, U_{ef} is the effective cooling velocity, and A, B and n are constants obtained by calibration.

Measurements were carried out at several downstream stations ($x/D =$ 12, 16, 26, 52, 76, 120 and 170), in the near and far wake regions of the DC wake. A horizontal rake, which is movable on the transverse axis, was placed parallel to the spanwise axis. The rake consists of three normal wire probes,

Downstream station (x/D)	Spatial resolution (Spacing/D)
12	0.11
16	0.11
26	0.15
52	0.23
76	0.31
120	0.38
170	0.46

Table 2.5: Spatial resolutions of hot–wire anemometry (HWA) measurements on the transverse ($y-$)axis at different downstream stations in the DC wake region. Model M_3 was used in the wind tunnel at URV.

positioned at the center of the middle cylinder piece ($z = 0$), at the end of the middle cylinder piece ($z/D = 2.5$) and at the center of the gap region ($z/D = 3.75$), respectively, as shown in figure 2.5. It was used to measure the streamwise velocity (u) data at three spanwise locations simultaneously. At every downstream station, the rake was moved on the transverse axis and collected data from middle of the wake ($y = 0$) to the outer edge of the wake. The spatial resolutions on the transverse axis were different from the near wake to the far wake, as shown in table 2.5. At all points, the data were acquired for 120 seconds at a sampling rate of 5 kHz, low pass filtered at 2 kHz and stored on a computer for subsequent processing. These data are used to show the evolution of mean and rms (root mean square) values of the fluctuations of the stream-wise velocity. These data were also used to verify the consistency of the PIV results.

2.3 Numerical simulations

2.3.1 Mathematical model

Calculations were performed for both the CC and DC flow configurations for a geometry and flow conditions similar to that of models M_1 and M_2 in table 2.1, except that, as shown in figure 2.1, only two cylinder segments were considered and these segments were not attached to a plate (i.e., the cylinder segments were suspended in the air in the computational domain). More precisely, in the model the cylinder diameter was $D = 0.0163$ m, the length of the cylinder segments was $L = 5D$ and the gap between segments was $S = 2.5D$. The free-stream velocity was set to $U_0 = 9.2$ m/s to yield

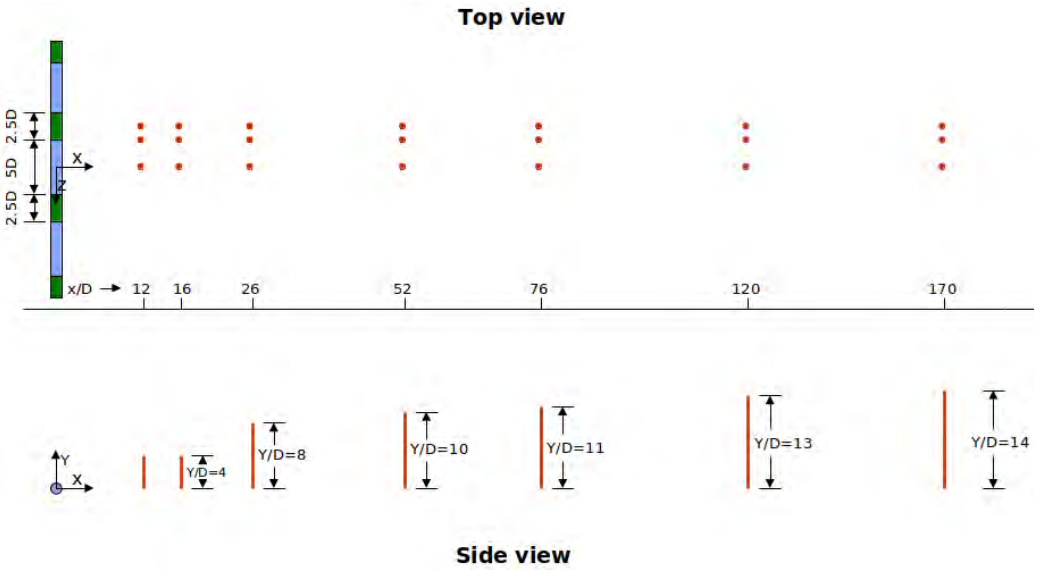

Figure 2.5: Sketch of the normal wire positions in the HWA measurements in the URV tunnel at Tarragona, Spain.

a Reynolds number of $Re = 1.0 \times 10^4$. The length, height and width of the computational domain were $K/D = 65, H/D = 30$ and $W/D = 15$, respectively, and the cylinder axis, and thus the $x = 0$ origin (see figure 2.1), was placed 15 diameters downstream from the inlet plane.

We assumed an incompressible flow of a Newtonian fluid. The flow is, therefore, governed by the Navier-Stokes equations, which for the Cartesian coordinate system may be written as,

$$\frac{\partial u_i}{\partial t} + \frac{\partial u_i u_j}{\partial x_j} = -\frac{1}{\rho}\frac{\partial p}{\partial x_i} + \frac{\partial}{\partial x_j}\left(\nu \frac{\partial u_i}{\partial x_j}\right) \tag{2.2}$$

where u_i (with the i =1, 2 and 3 indexes standing for the x, y and z axes, respectively) are the components of the instantaneous velocity field, p is the modified pressure, which incorporates the hydrostatic head induced by gravity, ρ is the fluid density and ν is its kinematic viscosity. The mass conservation (continuity) equation may be written as:

$$\frac{\partial u_i}{\partial x_i} = 0 \tag{2.3}$$

Because of the huge computational cost that would be involved in a direct numerical solution (DNS) of equations (2.2 and 2.3) at $Re = 1.0 \times 10^4$ we adopted the large-eddy simulation (LES) approach instead. In LES, the

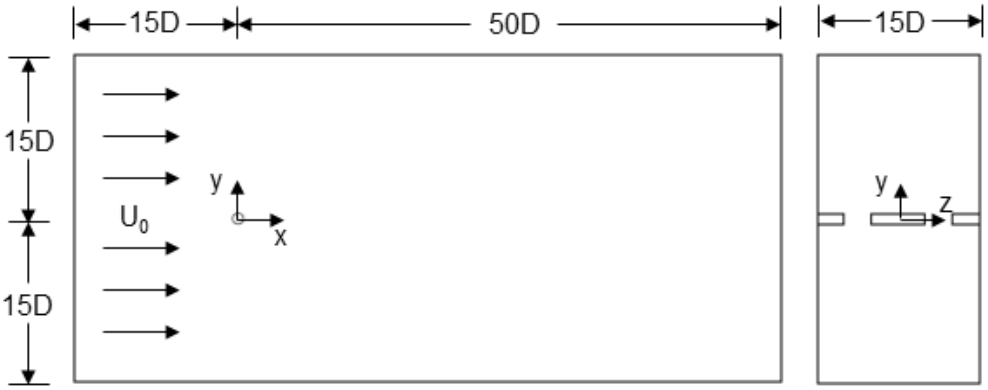

(a)

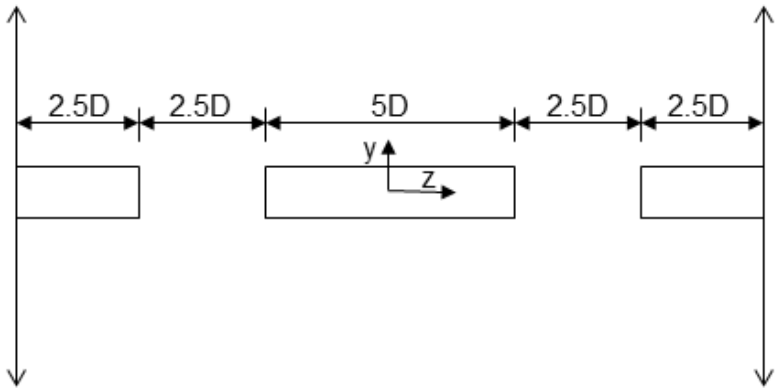

(b)

Figure 2.6: Computational domain used for the LES simulations of a DC wake at Reynolds number, $Re = 1.0 \times 10^4$ (a) vertical $x - y$ plane at $z = 0$ and (b) part (zoomed view) of vertical $y - z$ plane at $x = 0$.

large three-dimensional unsteady motions are directly represented, whereas the effects of the small-scale motions are modelled. The instantaneous velocity and pressure fields are decomposed as the sum of a filtered (resolved) component and a residual (or subgrid-scale, SGS) component,

$$u_i(x,t) = \tilde{u}_i(x,t) + u_i'(x,t); \quad p(x,t) = \tilde{p}(x,t) + p'(x,t) \qquad (2.4a, b)$$

When the decomposition (2.4) is introduced into the Navier-Stokes and continuity equations (2.2, 2.3) the conservation equations that govern the dynamics of large-scale motion are obtained:

$$\frac{\partial \tilde{u}_i}{\partial t} + \frac{\partial \tilde{u}_i \tilde{u}_j}{\partial x_j} = -\frac{1}{\rho}\frac{\partial \tilde{p}}{\partial x_i} + \frac{\partial}{\partial x_j}\left(\nu \frac{\partial \tilde{u}_i}{\partial x_j} - \tau_{ij}\right) \qquad (2.5)$$

$$\frac{\partial \tilde{u}_i}{\partial x_i} = 0 \qquad (2.6)$$

The term τ_{ij} in equation (2.5), is the residual stress tensor, which is defined as,

$$\tau_{ij} = \widetilde{u_i u_j} - \tilde{u}_i \tilde{u}_j \qquad (2.7)$$

and the residual kinetic energy is given by

$$k_r = \frac{1}{2}\tau_{ii} \qquad (2.8)$$

As a result, then the anisotropic residual stress tensor may be defined as

$$\tau_{ij}^r = \tau_{ij} - \frac{2}{3}k_r \delta_{ij} \qquad (2.9)$$

The isotropic residual stress is included to the filtered pressure and the modified filtered pressure is

$$\hat{p} = \tilde{p} + \frac{2}{3}\rho k_r \qquad (2.10)$$

With the above definitions, the filtered momentum conservation equation (2.5) may be rewritten as:

$$\frac{\partial \tilde{u}_i}{\partial t} + \frac{\partial \tilde{u}_i \tilde{u}_j}{\partial x_j} = -\frac{1}{\rho}\frac{\partial \hat{p}}{\partial x_i} + \frac{\partial}{\partial x_j}\left(\nu \frac{\partial \tilde{u}_i}{\partial x_j} - \tau_{ij}^r\right) \qquad (2.11)$$

The filtered continuity and momentum equations (2.6) and (2.11) are not closed as the anisotropic residual stress tensor (τ_{ij}^r), which incorporates

the effects of small-scale flow eddies into the large-scale motion, needs to be modelled. Under the basic assumption that the small scales have a universal character, i.e., their dynamics being independent of the particular flow geometry, the anisotropic residual stress tensor was modelled [57] as:

$$\tau_{ij}^{r} = -2\ \nu_t\ \tilde{S}_{ij} \tag{2.12}$$

where $\tilde{S}_{ij}$ is the filtered/resolved strain tensor

$$\tilde{S}_{ij} = \frac{1}{2}\left(\frac{\partial \tilde{u}_i}{\partial x_j} + \frac{\partial \tilde{u}_j}{\partial x_i}\right) \tag{2.13}$$

and ν_t is the eddy viscosity, which in turn is modeled as:

$$\nu_t = (C_s\Delta)^2\ \tilde{S} = (C_s\Delta)^2\ (2\tilde{S}_{ij}\tilde{S}_{ij})^{1/2} \tag{2.14}$$

In equation (2.14), C_s is the Smagorinsky coefficient and Δ is the filter width. A shortcoming in the original Smagorinsky SGS model is that the value of C_s is not universal but it depends on the particular flow regime. For example, it is known that a value of $C_s = 0.15$ works well for high-Reynolds number free turbulent flows whereas a smaller value should be used near a wall; C_s should decay to zero as the laminar flow regime is approached. We have therefore adopted the dynamic SGS model [58, 59] where the filter width Δ is locally defined as a function of the computational mesh spacing and C_s is not a constant but is instead calculated as a function of the local values of the filtered strain tensor $\tilde{S}_{ij}$.

A well-known limitation of LES is that SGS models may become inoperative in the vicinity of a solid surface because of its inability to properly represent the flow driving mechanisms within the turbulent boundary layer region [60]. To overcome such a limitation, it is possible to prescribe a sufficiently fine computational grid within the turbulent boundary layer. That is, the near wall dynamics are resolved as they would be in DNS at the expense of a large computational grid (the required number of computational nodes would roughly grow as Re^2). We opted instead for the use of wall laws, a much less costly approach relying on the assumption of a certain velocity profile within the region between the wall and the adjacent calculation node. As a result of such an assumption, the values of velocity and/or its gradients at the solid surface are provided by the wall model. We implemented the Werner et al. 1993 [61] model that is based on the following velocity profile,

$$u^+ = \left\{ \begin{array}{ll} y^+ & if\ y^+ \leq 11.81 \\ 8.3\ (y^+)^{1/7} & otherwise \end{array} \right\} \tag{2.15}$$

where the tangential velocity, u_t, and the normal distance from the wall, y, are scaled with the norm of the wall shear stress at the surface (τ_w), i.e., $u^+ = u_t/u^*$ and $y^+ = yu^*/\nu$ with $u^* = (\tau_w/\rho)^{1/2}$. Integration of the profile (2.15) provides an estimate for the components of the instantaneous wall shear stress as a function of the tangential components of instantaneous velocity at the adjacent calculation node. Note that Werner et al. 1993 [61] wall model is, therefore, suitable for turbulent boundary layer flows having separation points.

2.3.2 Numerical methods

Equations (2.6) and (2.11) were discretized in space according to a second order-accurate finite-volume methodology like the one reported by Mahesh et al. 2004 [62]. These authors used a predictor-corrector scheme that emphasizes the local energy conservation for the convection and pressure gradient terms in mesh elements of arbitrary shapes. A collocated variable arrangement is used, like the one in Rhie et al. 1983 [63] method although the details of the discretization are different. In the present calculations, all volume elements were of the hexahedral type and the computational mesh was carefully crafted in order to guarantee an accurate representation of the flow dynamics in the near-wake region ($x/D \leq 10$). Figures 2.7a and 2.7b respectively show a portion of a vertical and a horizontal cross-plane of the computational mesh.

The three-dimensional (3-D) computational mesh was generated as follows. First, a two-dimensional (2-D) quadrilateral mesh with 29,940 cells was generated on the vertical $(x-y)$ plane for $z = 0$ (that is, for a spanwise location containing a cross-section of the cylinder). As can be seen in figure 2.7a, the grid nodes were clustered in the boundary layer region around the cylinder and in the wake region. The grid nodes adjacent to the cylinder surface were placed at a radial distance equal to $0.001D$ from the wall (this represents, on average, a dimensionless normal distance of about $y+ = 1.0$). The size of the cells increases gradually from the near wake to the far wake region to the point that the $x-$spacing at the outflow boundary, $x/D = 50$, was set equal to one diameter. In those $z-$locations where there is no cylinder, i.e., in the $2.5 < |z/D| < 5$ gap (see figure 2.7b), 4,480 additional quadrilateral cells were added to fill the region of the $x - y$ plane that would be occupied by the cylinder had not it been discontinued, i.e., a circle of radius $D/2$. As is illustrated in figure 2.8, this circle was divided into two regions: an inner circle of radius $0.4D$ (region 2B) and the annular region (2A) with inner and outer radius equal to $0.4D$ and $0.5D$, respectively. To match the section of the computational mesh around the cylinder circle in the $(x - y)$ plane

(see figure 2.7a), a similarly structured grid was generated in region 2A (see figure 2.8a), with a 6% growth rate of the radial spacing. A new algorithm was developed to generate a suitable distribution of quasi-quadrilateral cells in the 2B region (see figure 2.8b), and more details about the algorithm are given in Appendix A. Figure 2.9 shows the result when the 2A and 2B parts of the computational mesh are added and the ensemble is connected to the outer mesh. The 2-D meshes in the $x-y$ plane were subsequently extruded along the spanwise (z) direction to generate the 3-D computational mesh. In the DC model simulation, a total number of 175 $x-y$ planes, with a non-uniform $z-$spacing, were generated. The $x-y$ planes were clustered at the edges of the cylinder segments with the $z-$spacing varying from $0.05D$ at the edge of a segment to $0.1D$ at its center (see figure 2.7b); the total number of hexahedral cells in the 3-D mesh was 5,487,320. In the CC model simulation, a uniform $z-$mesh with one hundred and one $x-y$ planes was deployed instead so that the total number of hexahedral cells in the 3-D mesh was $29,940 \times 100 = 2,994,000$.

The left and right $z-$boundaries of the calculation domain were truncated at the middle of a cylinder segment (see figure 2.7b) and periodic boundary conditions were applied. A turbulence-free, uniform flow was prescribed at the inflow boundary ($x/D = 15$) whereas at the right $x-$boundary ($x/D = 50$) we applied a typical outlet condition consisting of a zero velocity gradient together with a constant level (p_{atm}) of the surfaced-averaged pressure. Finally, a symmetry boundary condition was applied to the top and bottom $y-$boundaries ($y/D = \pm 15$). It is obvious that the choice of such boundary conditions along the $y-$ and $z-$directions, motivated by the rational of avoiding unnecessary degrees of freedom in the calculations, precludes an accurate simulation of the real flow near the walls of the wind tunnel. Notwithstanding, we checked that the main goal of the simulations, that is, the accurate characterization of the flow dynamics in the near wake was in no way hindered by the use of such approximate boundary conditions.

The ordinary differential equation (ODE) system resulting from the spatial discretization of equations (2.6) and (2.11) was advanced in time using the implicit second order backward-differencing (BDF2) scheme, which has the property of being A-stable [64]. Since we implemented a fully implicit time-marching approach, we had to adapt the original approach for the velocity-pressure coupling in Mahesh et al. 2004 [62] method, which was based on an explicit time-integration scheme. At each time-step, several internal pseudo-time steps were performed. Within each internal time-step, the new velocity values on each computational cell were first calculated iteratively and afterwards corrected, following Mahesh et al. 2004 [62] scheme, using the newly calculated pressure values. Internal pseudo-time steps were carried out until

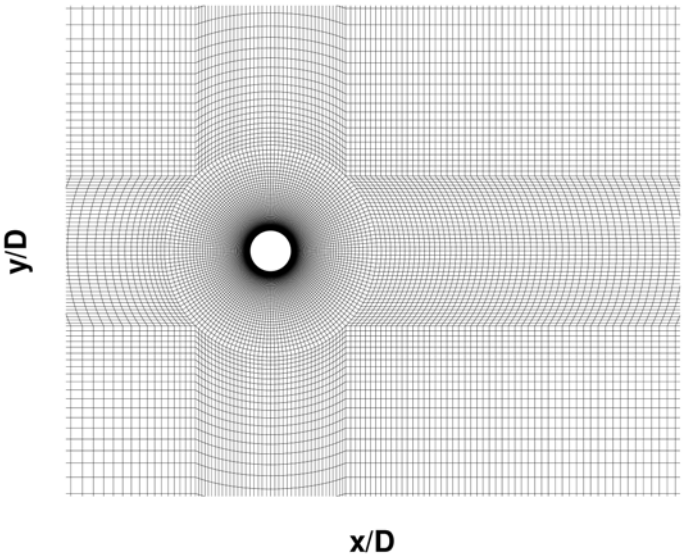

(a)

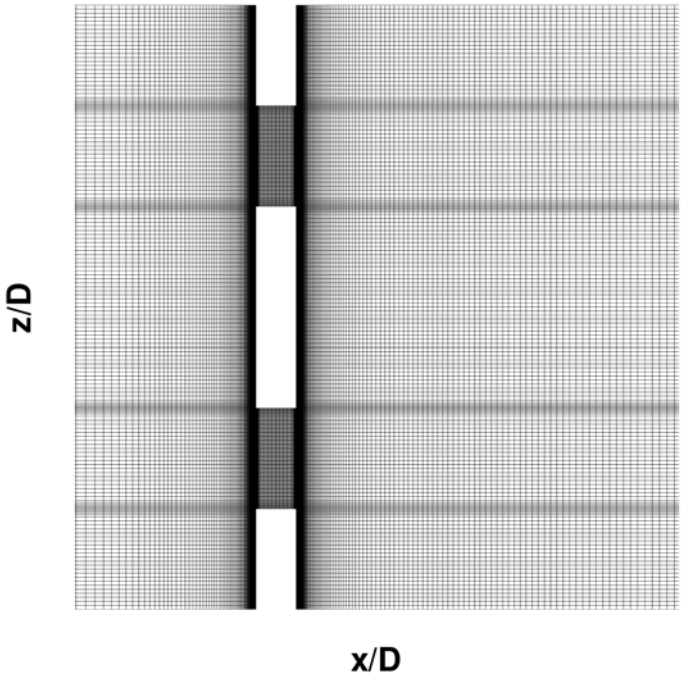

(b)

Figure 2.7: Cross–section of the computational mesh used in the LES calculation of the DC flow (a) $x-y$ plane with $z = 0$, and (b) $x-z$ plane with $y = 0$. In both cases the extent of the $x-$domain is limited to $-5 \leq x/D \leq 10$.

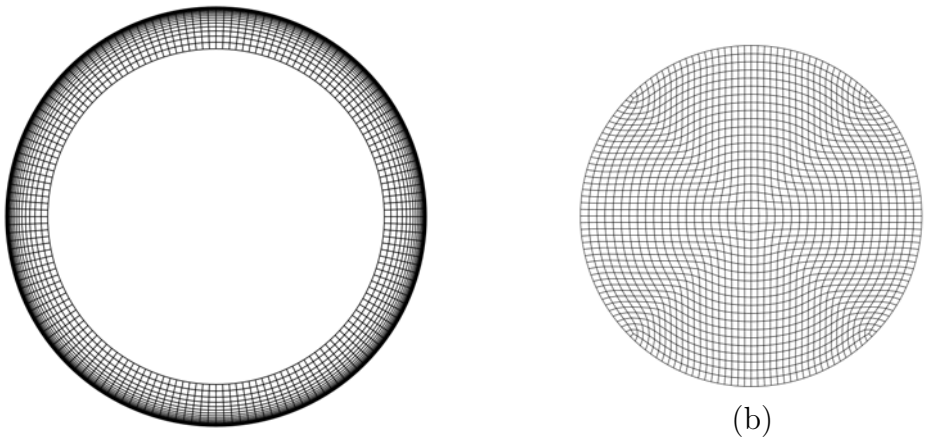

(a) (b)

Figure 2.8: Detail of the cross section of the computational mesh on the vertical $x - y$ plane with $z/D = 3.75$ in the region surrounding the cylinder axis. (a) Region 2A ; (b) region 2B.

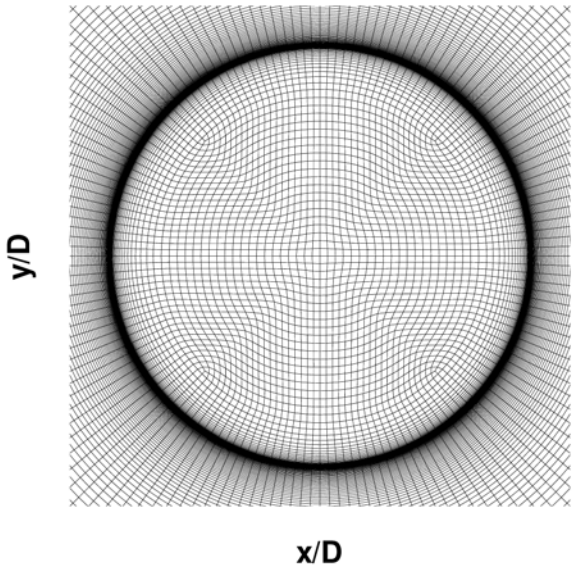

Figure 2.9: Detail of the cross section of the computational mesh on the vertical $x - y$ plane at $z/D = 3.75$ in the region around the cylinder axis, $-0.6 \leq x/D \leq 0.6$ and $-0.6 \leq y/D \leq 0.6$.

the prescribed accuracy for global convergence of both momentum and mass conservation equations was achieved. The number of internal pseudo-time steps per real time step was always modest, only three were required, at most.

All time–integrations were performed using a constant time–step of $\Delta t = 3 \times 10^{-5} s = 0.017(D/U_0)$. Assuming a Strouhal number of $S_t = D/(TU_0) = 0.14$ (where T denotes the mean period of a shedding cycle) for the main flow oscillation in the DC model, it follows that the average number of time–steps per shedding cycle was $T/\Delta t \approx 422$. After an initial transient equivalent to about 21 shedding cycles, time–marching in the DC simulation was carried for a further period of about 53 shedding cycles (equivalent to $376\, D/U_0$). Instantaneous velocity and pressure values were recorded every one out of ten time steps, that is, about 42 times per shedding cycle. In the CC model simulation, a Strouhal number of $S_t = 0.202$ by Norberg 2003 [7] was assumed and the integration period after the initial transient was equivalent to about 51 shedding cycles ($248\, D/U_0$). Note that the integration period used to calculate the mean field in the present study was larger than the value of ($150\, D/U_0$) adopted previously by Mahesh et al. 2004 [62] and also larger than the $40 - 50$ shedding cycles of Dong et al. 2006 [65] in their respective numerical simulations.

2.4 Validation of experimental and numerical methods

The current experimental setup and numerical methods were validated using previously published data on the continuous cylinder wake flow. The drag coefficient, C_d, is defined as,

$$C_d = \frac{2F_d}{\rho D U_0^2} \tag{2.16}$$

where F_d denotes the mean drag force on the cylinder surface per unit cylinder length. For the present PIV measurements, F_d was indirectly calculated based on the mean streamwise velocity profile in the wake [66],

$$F_d = (\frac{\rho U_0}{D}) \int_{-\infty}^{\infty} \overline{u}_d \; dy \tag{2.17}$$

where $\overline{u}_d = U_0 - \overline{u}$ denotes the mean streamwise velocity defect. Hereinafter we will use the u, v and w symbols to respectively denote the x, y and z velocity components. An overline on a quantity will denote its mean (time-averaged) value. Equation (2.17) was used with the measured $\overline{u}_d$ values at the

Author	Reynolds number (Re)	S_t	C_d	Recirculation length (L_R/D)
Current LES	1.0×10^4	0.202	1.125	1.550
Current PIV	1.0×10^4	-	1.080	1.510
Dong et al. 2006 [65]	1.0×10^4	0.203	1.143	-
Norgerg 1998 [67]	1.0×10^4	-	-	1.520
Afgan et al. 2011 [68]	3.9×10^3	0.207	1.020	1.490
Mahesh et al. 2004 [62]	3.9×10^3	0.218	1.000	1.350

Table 2.6: Comparison of the current PIV and current LES results of the continuous cylinder wake with the published data in the literature.

PIV station with $x/D = 1.5$ and $z = 0$. The C_d values for the present LES results were calculated by direct numerical integration of pressure and viscous shear forces on the cylinder surface. Table 2.6 shows a comparison of current measured and predicted C_d values with data from other sources previously reported in the literature. The drag coefficient and shedding frequency of the large-scale vortices in the CC wake calculated by the current LES simulations agree with the corresponding data published in the literature, as shown in table 2.6. The recirculation bubble length, or wake-closure length, L_R, is one of the mean near wake characteristics that is sensitive to the Reynolds number. It is defined as the mean (time averaged) closure point (i.e., the saddle point on the wake centerline, $y = 0$). Some literature data for the CC wake at a lower Reynolds number, $Re = 3.9 \times 10^3$, are also included in table 2.6 for the sake of comparison. Current predictions are also in agreement with these data.

In the wind tunnel measurements with the DC wake generator models (M_1, M_2 and M_3) a thin plate had to be used to hold the cylinder segments. It was therefore imperative to assess the level of intrusiveness of the plate on the flow in the DC wake. The width of the plate was equal to the diameter of the cylinder segments (see figure 2.1) and the ratio of the cylinder diameter to plate thickness was 20 in the models M_1 and M_2, and 21.67 in the model M_3 (see table 2.1). Figure 2.10 shows the vertical profiles of $\overline{u}/U_0$ and $\overline{\omega}_z D/U_0$ at the downstream station $x/D = 1$ and several spanwise locations in the range ($0 \leq z/D \leq 3.75$). The wake defect and the strength of the vorticity levels in the wake at the gap region ($z/D = 3.75$) are much smaller than those in the wake directly behind the cylindrical segment ($0 \leq z/D \leq 2.5$). The profiles in the gap region at $z/D = 3.75$ therefore show that the thin

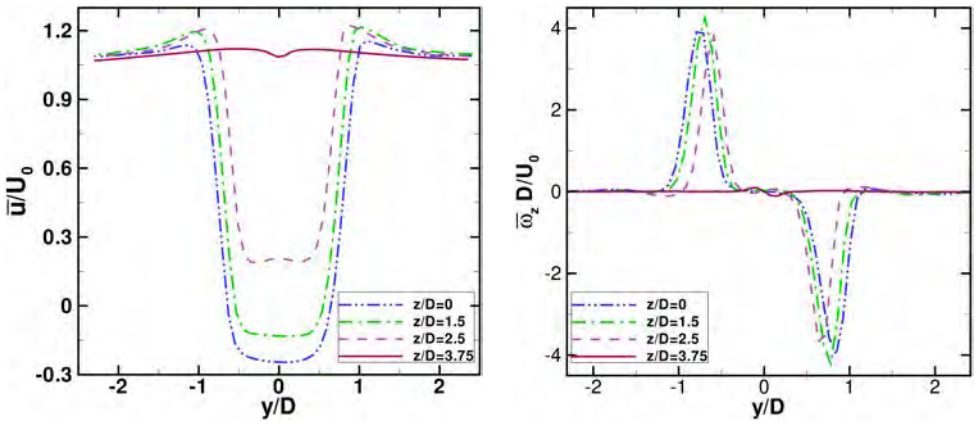

(a) (b)

Figure 2.10: Mean profiles of DC wake at downstream station $x/D = 1$ (a) mean streamwise velocity $(\overline{u}/U_0)$ (b) mean spanwise vorticity $(\overline{\omega}_z D/U_0)$. PIV results at Reynolds number, $Re = 1.0 \times 10^4$.

plate that was used to connect the cylinder segments does not significantly alter the flow behind it.

As a preliminary step before carrying out the DC flow measurements and calculations the consistency between current PIV measurements and LES simulation for the CC geometry was tested. As an example, figure 2.11 shows the mean profiles of streamwise velocity $(\overline{u}/U_0)$ and spanwise vorticity $(\overline{\omega}_z D/U_0)$ at downstream stations x/D=2 and 8 in the wake of the CC at Reynolds number $Re = 1.0 \times 10^4$. Here and in subsequent plots where both measured and calculated mean values are compared an overline is used to indistinctly denote a time averaged quantity (e.g., in figure 2.11a the quantity plotted for the LES results should be labelled, strictly speaking, as $\overline{\widetilde{u}}$).

To further assess the accuracy of the current PIV experimental setup, comparisons were established with measurements obtained by means of the very well established hot-wire anemometry (HWA) technique. In all current HWA measurements the DC model M_3 was used, i. e., the same tunnel free-stream velocity, $U_0 = 9.2$ m/s, was kept so that the free-stream flow Reynolds number was $Re = 4.0 \times 10^3$ (see table 2.1). The DC model M_3 was primarily used to bring the far wake $(70 \leq x/D \leq 180)$ into the optimal measurement region of the wind tunnel.

Figure 2.12 compares HWA and PIV measurements in the far wake to assess the current PIV experimental setup and it shows the mean streamwise velocity $(\overline{u}/U_0)$ at several down-stream stations in the vertical plane at $z = 0$

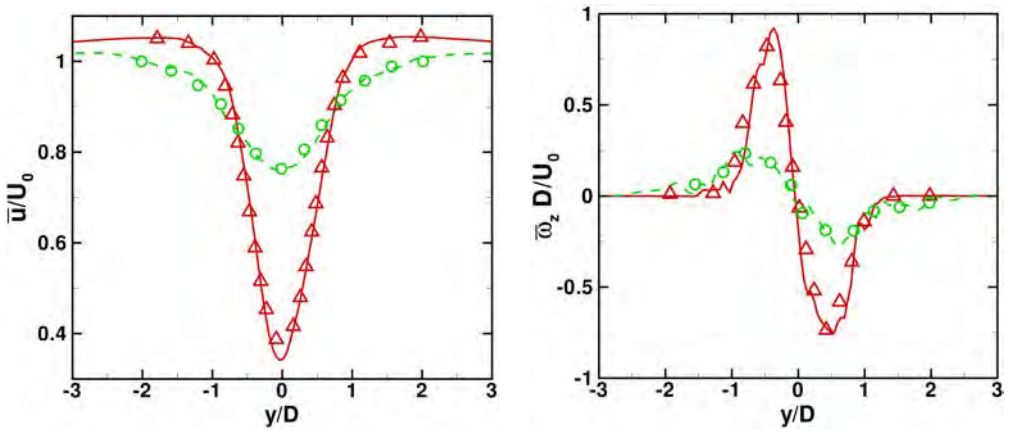

(a) (b)

Figure 2.11: Comparison of present PIV and LES results of the CC wake flow at a Reynolds number of $Re = 1.0 \times 10^4$. Vertical profiles in the plane with $z = 0$ are shown for different x/D stations. (a) Mean streamwise velocity $(\overline{u}/U_0)$. (b) Mean span-wise vorticity $(\overline{\omega}_z D/U_0)$. Lines show the LES results: $x/D = 2$ (continuous line) and $x/D = 8$ (dashed line); symbols show the PIV results: $x/D = 2(\triangle)$ and $x/D = 8(o)$.

of the DC wake flow. The PIV measurements shown in figure 2.12a were carried out with the model M_2 and the free-stream Reynolds number was therefore $Re = 1.0 \times 10^4$. The comparison in figure 2.12a thus shows that the DC wake flow behaves similarly despite the difference in the Reynolds number. In the further downstream wake at locations $x/D = 76$ (figure 2.12b) and $x/D = 170$ (figure 2.12c) both HWA and PIV results were obtained at the same Reynolds number, $Re = 4.0 \times 10^3$. As it can be seen in these two plots, the agreement between the measured HWA and PIV profiles is reasonably good.

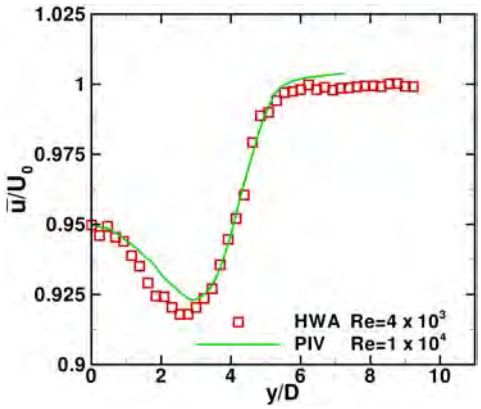

(a)

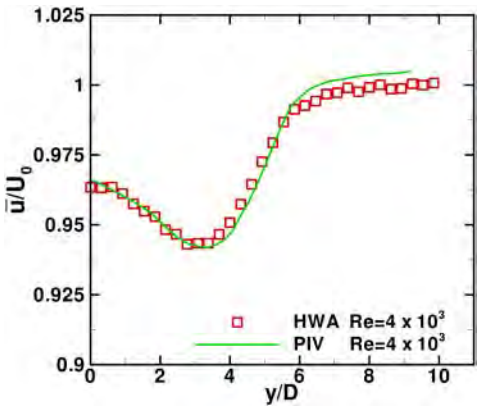

(b)

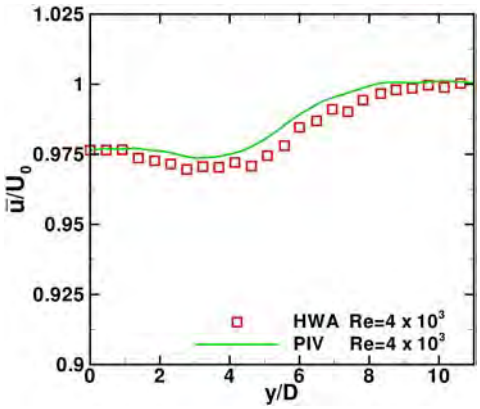

(c)

Figure 2.12: Comparison of HWA and PIV results of mean stream-wise velocity ($\overline{u}/U_0$) at several downstream stations in the plane $z = 0$ of the DC wake: (a) $x/D = 52$, (b) $x/D = 76$ and (c) $x/D = 170$.

Chapter 3

Comparison of the continuous and discontinuous cylinder near wakes

The flow in the wake of the discontinuous cylinder (DC) can be envisaged as a modified three-dimensional version of the flow behind a continuous cylinder (CC). In this subsection we compare the CC near wake ($x/D \leq 10$) with the DC near wake at the mid-segment ($z = 0$) $x - y$ plane by using both PIV measurements and LES results for a free-stream Reynolds number of $Re = 1.0 \times 10^4$. The instantaneous PIV data were ensemble-averaged to determine the mean streamwise and transverse velocities, Reynolds shear stress and mean vorticity patterns on the measurement planes.

Figure 3.1 shows the streamwise profiles of the mean streamwise velocity component ($\overline{u}$) on the flow centerline ($y = 0$, $z = 0$). Both simulations and measurements show that the recirculation length, i.e., the wake-closure length (L_R), which is defined as the mean (time–averaged) closure point (i.e., the saddle point on the wake centerline, $y = 0$), is much larger in the DC wake ($L_R/D = 3.63$ from PIV measurements) than it is for the CC wake ($L_R/D = 1.51$). Accordingly, the minimum value in the DC profile of figure 3.1 is much lower (more negative) than it is for the CC profile. It is observed that the CC profile recovers quite soon ($x/D \approx 3$) to a value as high as $\overline{u}/U_0 \approx 0.70$, but there is a rapid slope change at $x/D \approx 3$ with much slower changes as the flow evolves downstream. In contrast, the momentum recovery is initially slower in the DC profile, but the rate of change (i.e., the slope of the curve) is much higher for the DC wake for $x/D > 3$. At $x/D = 10$ both profiles have attained an almost identical level of $\overline{u}/U_0 \approx 0.75$ at the $y = 0$ centerline, although the slope remains higher for the DC wake at this point.

Figure 3.2 shows the contours and selected vertical profiles of ($\overline{u}/U_0$) in the CC and DC wakes. Comparison of the contours in figures 3.2a and 3.2b confirm the differences in the length and intensity of the respective

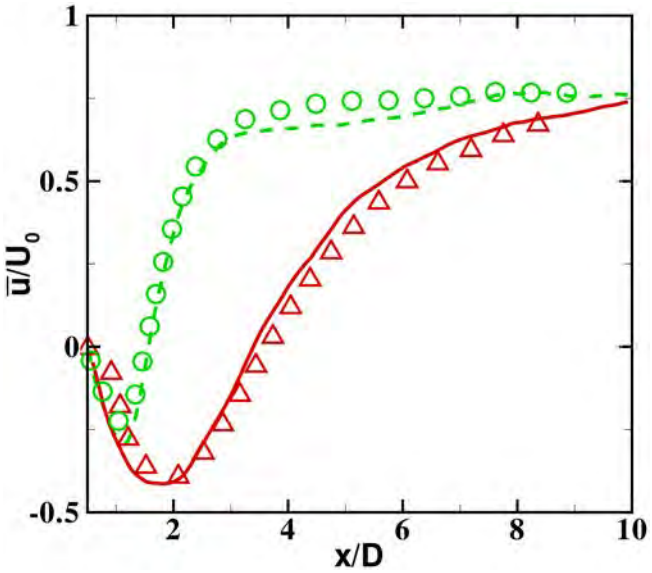

Figure 3.1: Comparison of mean streamwise velocity ($\overline{u}/U_0$) on wake centerline ($y = 0$) and mid–plane ($z = 0$) for the DC and CC wakes. Lines show the LES results: DC wake DC (solid line) and CC (dashed line). Symbols show the PIV results: DC wake ($\triangle$), CC wake (o).

recirculation bubbles that were already inferred by figure 3.1. In addition, the contour plot for the DC wake in figure 3.2b reveals the comparatively high momentum deficit for the DC wake in the region behind the recirculation bubble. Inspection of the vertical $\overline{u}/U_0$ profiles in figure 3.2c,d,e, together with the contour plots in figures 3.2a,b, provides an indication of the different rates of flow development for these two wakes. At the streamwise station, $x/D = 2$, it is probably too early for the concept of wake width to make sense since the formation of the wake vortices is incomplete. However, the corresponding DC and CC profiles at $x/D = 4$ (figure 3.2d) suggest that the widths of both wakes are similar since the limiting $\overline{u} = U_0$ values are reached at $y/D \approx \pm 1.5$. Further downstream, by $x/D = 8$ (figure 3.2e), the DC wake has become significantly wider. Note that the same effect can be observed in the contour plots of figures 3.2a,b when examining the isoline for $\overline{u}/U_0 = 1$.

Figures 3.3a and 3.3b show the contours of the mean vertical component of velocity ($\overline{v}/U_0$) in the CC and DC wakes, respectively. The vertical $\overline{v}/U_0$ profiles at selected streamwise locations in figures 3.3c,d,e show again the good agreement between the current PIV-measurements and LES calculations. Figure 3.3a shows the presence of strongly negative $\overline{v}$ values in the near wake ($x/D \leq 2$) of the CC wake, with a local minimum of $\overline{v}/U_0 = -0.29$

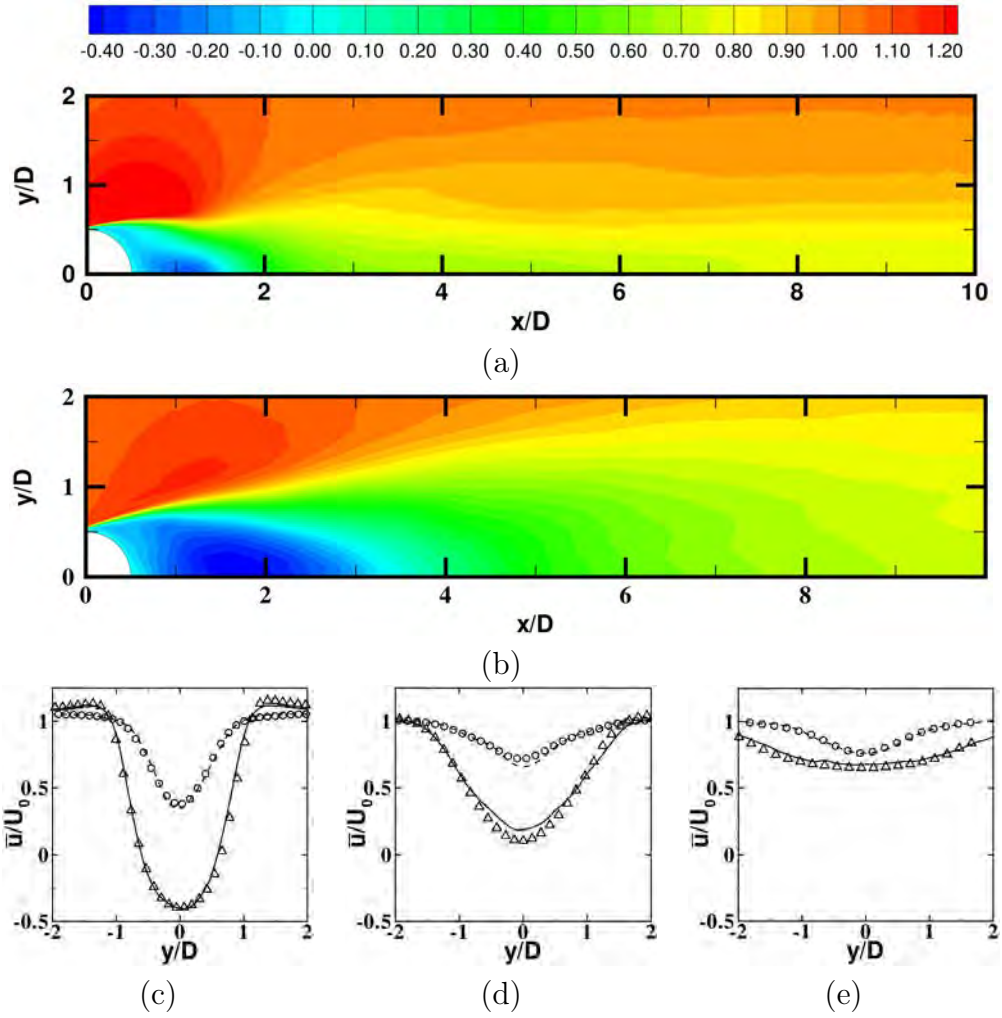

Figure 3.2: Vertical distribution of mean streamwise velocity ($\overline{u}/U_0$) in the CC and DC wakes at $z = 0$. Contours show LES results for (a) the CC wake and (b) the DC wake. Vertical profiles from the LES calculations for the DC (solid line) and CC (dashed line) wakes, along with the measured ones for the DC ($\triangle$) and CC (o) wakes at three downstream locations: (c) $x/D = 2$, (d) $x/D = 4$ and (e) $x/D = 8$.

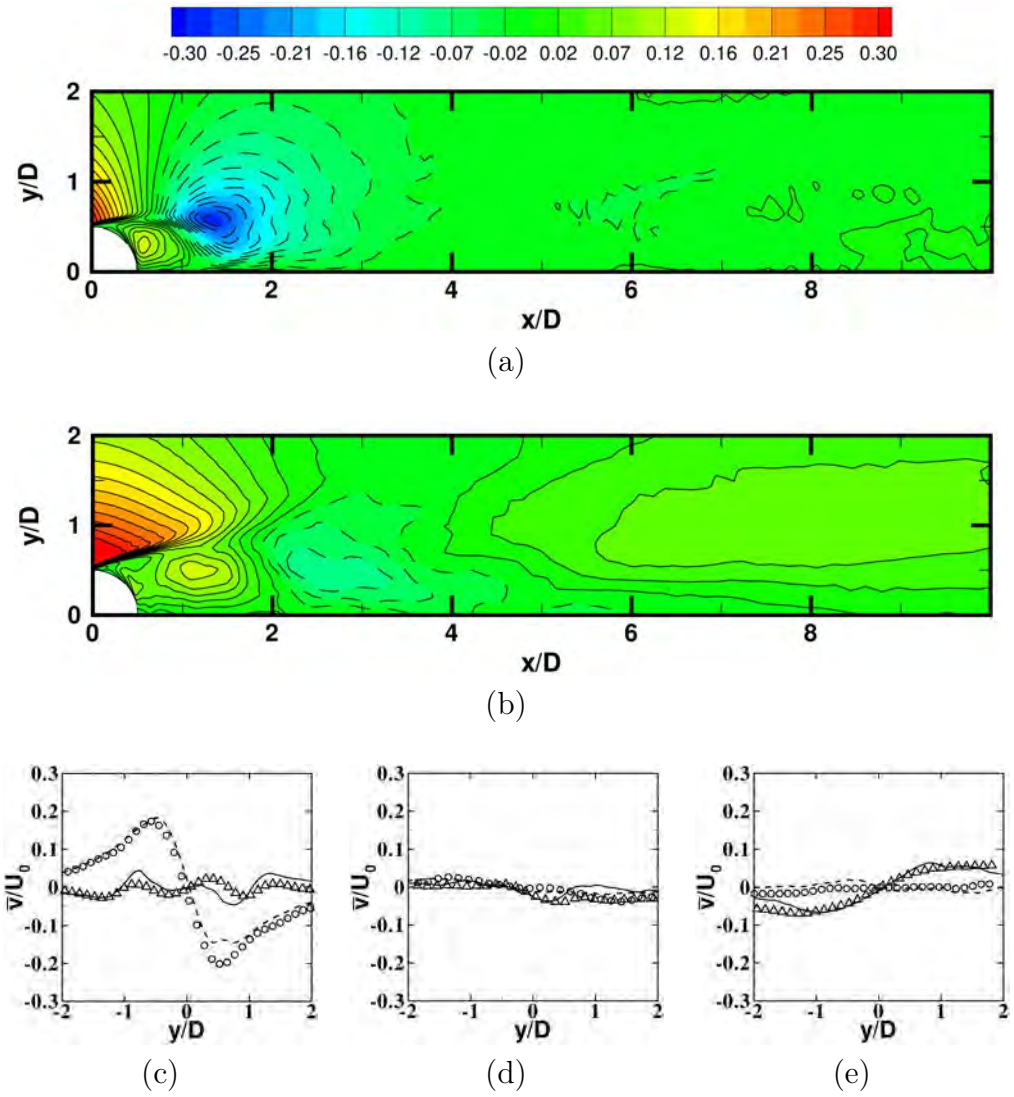

Figure 3.3: Vertical distribution of mean vertical velocity ($\overline{v}/U_0$) in the CC and DC wakes at $z = 0$. Contours show LES results for (a) the CC wake and (b) the DC wake. Vertical profiles from the LES calculations for the DC (solid line) and CC (dashed line) wakes, along with the measured ones for the DC ($\triangle$) and CC (o) wakes at three downstream locations: (c) $x/D = 2$, (d) $x/D = 4$ and (e) $x/D = 8$.

at $(x/D, y/D) \approx (1.34, 0.58)$. The presence of such foci of highly negative (or positive, in the $y < 0$ half-plane) $\overline{v}$ means that, on the average, fluid with higher momentum is driven inwards toward the midplane ($y = 0$) region, a mechanism that explains the fast momentum recovery of the CC near wake in figures 3.1 and 3.2a, following the formation of the VKV, as discussed by Cantwell et al. 1983[8], Ong et al. 1996[69], and Ma et al. 2000[70]. In the corresponding $\overline{v}$ contours of the DC wake, figure 3.3b, we see that the downwards (upwards for $y < 0$) flow pattern associated with the entrainment mechanism is considerably weaker and it occurs further downstream, $2 \leq x/D \leq 4$. Figure 3.3b also shows that this flow pattern in the DC wake is stronger closer to the cylinder, $x/D \leq 2$. Another significant difference between the CC and DC contours of figures 3.3a and 3.3b is that, in the latter, there is a small but consistent flow pattern with fluid moving upwards in the upper half wake in the $4 \leq x/D \leq 10$ streamwise region, a fact that is also reflected in the DC vertical profile of figure 3.3e (to be discussed later in Chapter 7).

Figure 3.4 shows the corresponding contours and profiles of the correlation of the fluctuations of $x-$ and $y-$velocity components (u and v). For PIV measurements, the quantities plotted are precisely the ($\overline{u'v'}$) component of the Reynolds shear stress. In the LES results, the velocity fluctuations are calculated on the basis of the following decomposition:

$$u_i^f(t, x, y, z) = \tilde{u}_i(t, x, y, z) - \overline{\tilde{u}}_i(x, y, z) \tag{3.1}$$

Note that for the sake of simplicity, when referring to LES calculations the time-averaged filtered quantities, such as $\overline{\tilde{u}}_i$, will be denoted using a single overline, i.e., $\overline{u}_i$. According to the decomposition in equation (3.1), the LES counterpart of the PIV Reynolds stress components will be calculated using the discrete form of the time integral:

$$\overline{u_i^f u_j^f}\ (x, y, z) = \frac{1}{T} \int_0^T u_i^f u_j^f\ dt, \qquad i, j = 1, 2, 3 \tag{3.2}$$

In theory, the contours of $\overline{u^f v^f}$ plotted in figures 3.4a and 3.4b would be comparable to the corresponding PIV contours of $\overline{u'v'}$ provided that the threshold for the LES filtering in equation 2.4 is properly defined. That is, the $u'(x, t)$ and $v'(x, t)$ fluctuations that are filtered out in equation (2.4) should be completely random and, therefore, uncorrelated. The vertical profiles in figure 3.4c suggest that the agreement between PIV ($\overline{u'v'}$) and LES ($\overline{u^f v^f}$) results for the averaged fluctuating shear stress is not as good as it was for the mean velocities ($\overline{u}, \overline{v}$). To clarify this issue, we have plotted in figure 3.5 the corresponding $\overline{u'v'}$ contours obtained from PIV measurements. Comparison

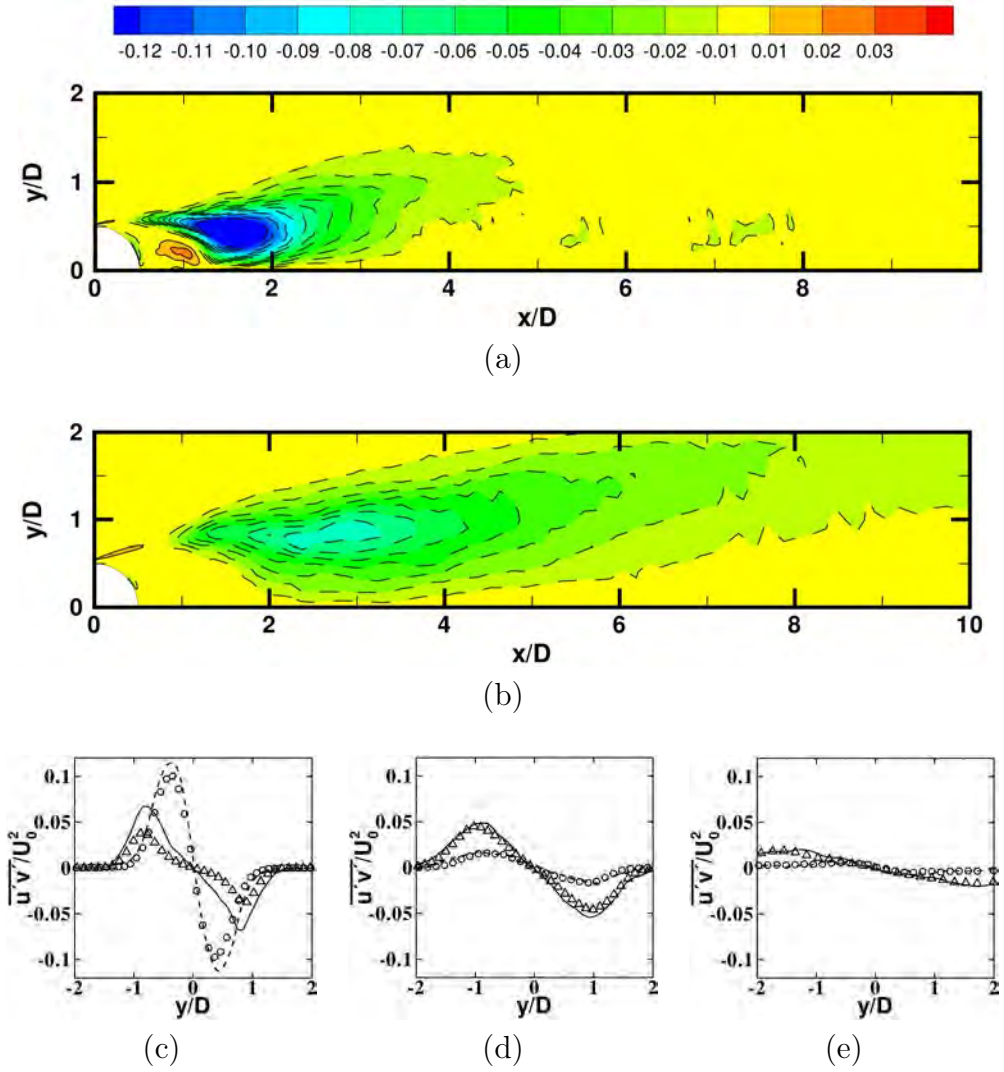

Figure 3.4: Vertical distribution of the $\overline{u^f v^f}$ component of the fluctuation stress, as defined in equations (3.1) and (3.2), in the CC and DC wakes at $z = 0$. Contours show LES results for (a) the CC wake and (b) the DC wake. Vertical profiles from the LES calculations for the DC (solid line) and CC (dashed line) wakes, along with the measured ones (u'v' values) for the DC ($\triangle$) and CC (o) wakes at three downstream locations: (c) $x/D = 2$, (d) $x/D = 4$ and (e) $x/D = 8$.

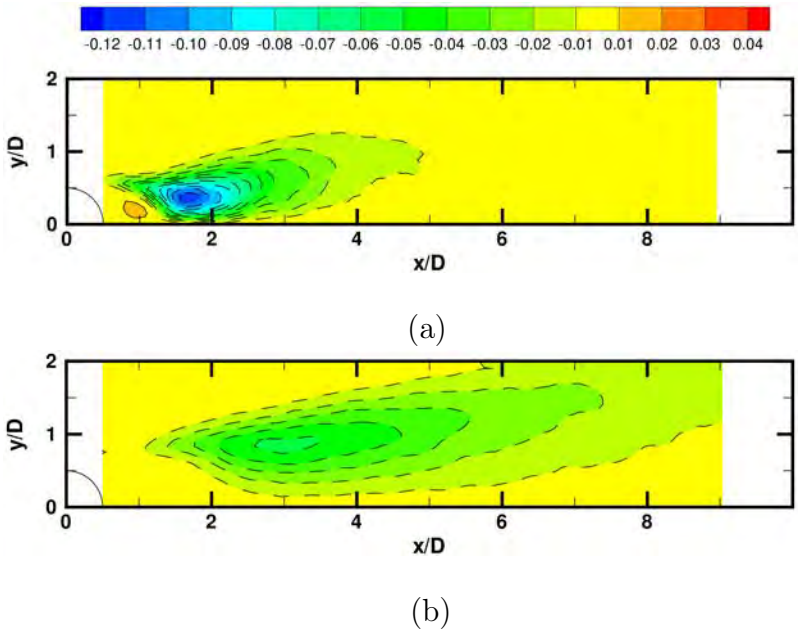

(a)

(b)

Figure 3.5: Vertical distribution of the $x - y$ component of the Reynolds shear stress, $\overline{u'v'}/U_0^2$, in the CC and DC wakes at $z = 0$. Contours measured by PIV in: (a) the CC wake and (b) the DC wake.

of figure 3.5a with figure 3.4a and of figure 3.5b with figure 3.4b shows a reasonably good agreement between PIV and LES results with the main difference being that LES overestimate, both in the CC and DC wakes, the maximum of the $u' - v'$ correlation, i.e., the intensity of the local minima in the contours of figures 3.4a and 3.4b.

Despite such a difference in the predicted $\overline{u'v'}$ minimum levels, both the LES and PIV results show in figures 3.3a and 3.3b that the strongest (negative) correlation between the u and v velocity components is located, in both cases, nearby the region with the highest mean vertical motion. Previous knowledge of the main features of the CC wake flow suggests that such a spatial coincidence of spots with strong mean vertical motion and strong (negative) $\overline{u'v'}$ denotes the periodic passage of von Kármán vortices (VKV) in that region. In the CC wake flow, the VKV's are generated at a short streamwise distance past the cylinder and in the near wake region ($x/D \leq 2$) they are very active.

The contours of the mean spanwise vorticity component, $\overline{\omega}_z$, for the CC wake flow, shown in figure 3.6a, confirm a strong average vortical activity in the CC near wake region closest to the cylinder ($x/D \leq 2$). Moreover, this plot also shows a horizontal strip with relatively low spanwise vorticity ($\overline{\omega}_z \leq$

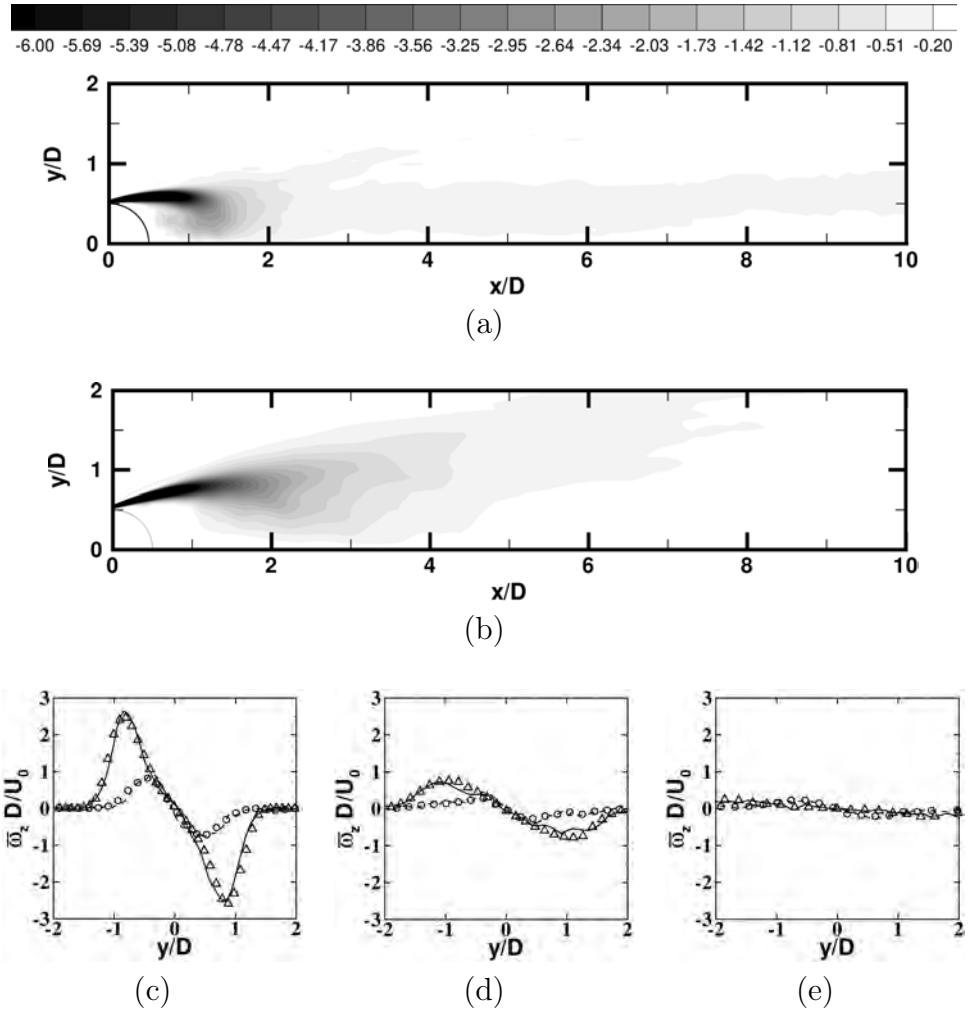

Figure 3.6: Vertical distribution of mean spanwise vorticity ($\overline{\omega}_z\ D/U_0$) in the CC and DC wakes at $z = 0$. Contours show LES results for (a) the CC wake and (b) the DC wake. Vertical profiles from the LES calculations for the DC (solid line) and CC (dashed line) wakes, along with the measured ones for the DC ($\triangle$) and CC (o) wakes at three downstream locations: (c) $x/D = 2$, (d) $x/D = 4$ and (e) $x/D = 8$.

-0.2), which is basically circumscribed within the midplane region, $|y/D| \leq 1$. By comparison, the DC wake contours depicted in figure 3.6b show that large-scale vortices are similarly being generated behind the cylinder but instead of travelling close to the wake centerline they also move away from the horizontal midplane (see also figure 3.3b). Not surprisingly, figure 3.6b also shows highly negative $\overline{\omega}_z$ values in the $2 \leq x/D \leq 4$ streamwise region of the DC wake, that is, the region where strong downwards motion (figure 3.3b) and strong correlation between u and v fluctuations (figures 3.4b and 3.5b) were also observed. Note also in figure 3.6b that the region with significant spanwise vorticity levels ($\overline{\omega}_z \leq -0.2$) reaches the $y/D = 2$ edge of the plot at a streamwise location slightly below $x/D = 8$. This means that in the DC wake the large-scale vortices move away from the $y = 0$ midplane as they travel downstream. This is distinct to what is observed for the CC wake in figure 3.6a. This evidence of fluid with significant vorticity and comparatively low momentum moving away from the midplane, hints again at the possibility of an enhanced growth rate of the DC wake (compared to the CC wake), a notion that will be analyzed in detail below.

Chapter 4

Wake growth characteristics

In this chapter the comparative analysis of the CC and DC wake flows, restricted so far to the near wake region ($x/D \leq 10$), is extended to the mid and far wake region with the help of both PIV and HWA measurements as well as of previous data for the CC wake, which were obtained in the same wind tunnel at URV.

In the near wake, the high vorticity and size of the vortices cause recirculation and backflow at wake centreline ($y = 0; z = 0$), as illustrated in figure 4.1a. This figure shows that in the near wake region ($x/D \leq 10$) the value of the centerline ($y = 0$) streamwise velocity ($\overline{u}$) is considerably lower (higher $(\overline{u}_d)_{max}$, where $(\overline{u}_d)_{max} = (U_0 - \overline{u})_{max}$) in the DC wake than it is in the CC wake, but it recovers quickly to the point that at around $x/D = 10$ the $(\overline{u}_d)_{max}$ values in the DC and CC wake are similar. This was also illustrated in figure 3.1 of chapter 3. Figure 4.1b shows that the enhanced mean momentum recovery in the DC wake persists in the mid wake region $10 \leq x/D \leq 20$. For example, at $x/D = 16$ (i.e., $(x/D)^{-0.5} = 0.25$), $(\overline{u}_d)_{max} = 0.19U_0$ for the DC wake, which is clearly smaller than the corresponding value of $(\overline{u}_d)_{max} = 0.23U_0$ for the CC wake. Further downstream, we can see that the momentum recovery rates are similar in the two wakes, as indicated by the same slopes. However, the DC wake has a much smaller maximum momentum deficit at the same physical locations. As a result, the maximum velocity-defect in the DC wake at $x/D = 50$ is $(\overline{u}_d)_{max} \approx 0.089U_0$, which can be found at about $x/D = 127$ in the CC wake; at just ten diameters further downstream in the DC wake ($x/D = 60$) the equivalent streamwise location in the CC wake would be $x/D \approx 172$. Thus, even though the DC wake has a higher momentum deficit initially, it recovers much faster than the CC wake so that the maximum defect is significantly lower in the self-preserving far wake region.

A second quantity often used to characterize the growth rate of the CC

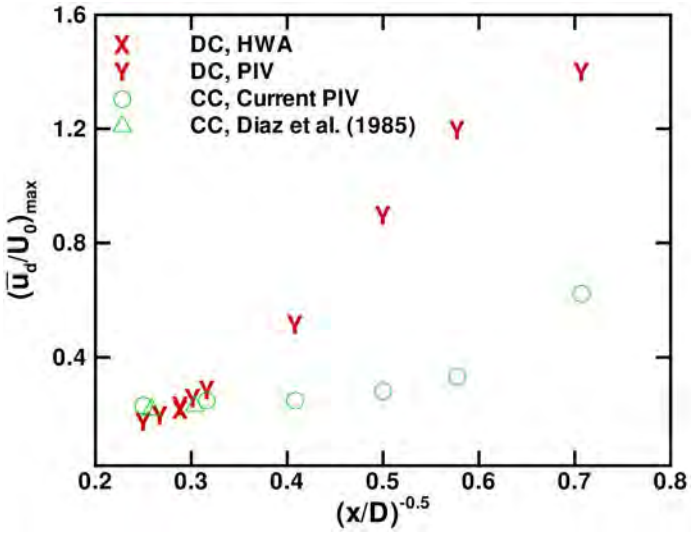

(a)

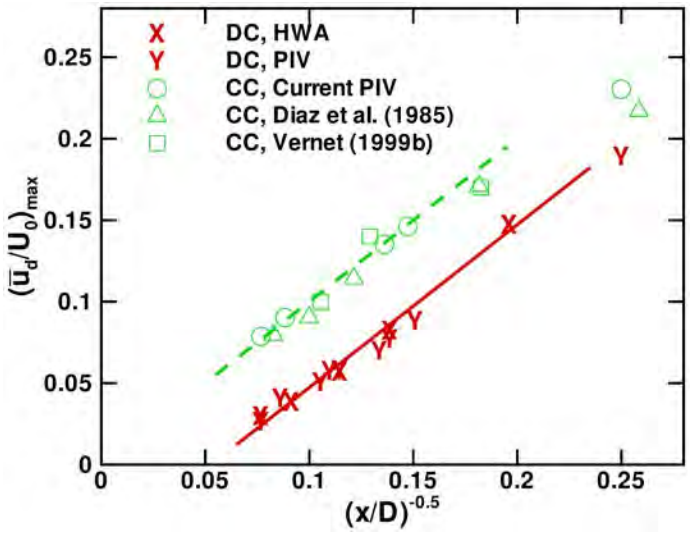

(b)

Figure 4.1: Streamwise variation of the maximum mean velocity–defect $(\overline{u}_d/U_0)_{max}$ in the $x-y$ vertical plane at $z=0$ in the CC and DC mid–far wake: (a) $2 \leq x/D \leq 25$; (b) $16 \leq x/D \leq 180$. All of the HWA and PIV measurements in the $70 \leq x/D \leq 180$ range were obtained with model M_3 at a Reynolds number of $Re = 4.0 \times 10^3$ (see tables 2.3 and 2.5). PIV measurements in the $10 \leq x/D \leq 56$ range were obtained at $Re = 1.0 \times 10^4$. Diaz et al. 1985 [71] and Vernet 1999b [72] results were obtained at $Re = 9.0 \times 10^3$ and 7.0×10^3, respectively. The dashed and solid lines for the CC and DC data, respectively, indicate the $1/(x/D)^{0.5}$ variation associated with the self–preserving solution.

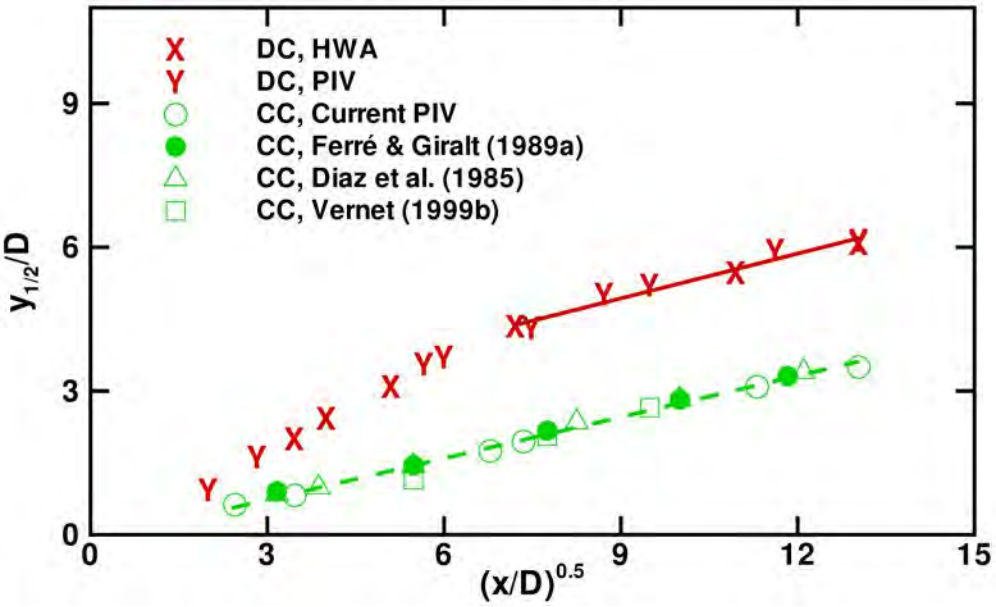

Figure 4.2: Variation of $y_{1/2}/D$ with streamwise location in the CC and DC wake. All of the current HWA and PIV measurements in the $70 \leq x/D \leq 180$ range were obtained with model M_3 at a Reynolds number of $Re = 4.0 \times 10^3$. Current PIV results in the $0 \leq x/D \leq 56$ range (both CC and DC) were obtained at $Re = 1.0 \times 10^4$. Diaz et al. 1985 [71] and Ferré et al. 1989a [10] data were obtained at $Re = 9.0 \times 10^3$ whereas Vernet 1999b [72] data were obtained at $Re = 7.0 \times 10^3$. The fitted equations of the self–preserving solutions for the CC wake (dashed line) and the DC wake (solid line) are $y_{1/2}/D = 0.28((x/D) - 3.05)^{0.5}$ and $y_{1/2}/D = 0.40((x/D) + 67.63)^{0.5}$, respectively.

wake is $y_{1/2}$, defined as the vertical location where the mean velocity is half of the maximum of $\overline{u}_d$. Figure 4.2 shows the streamwise variation of $y_{1/2}/D$ obtained from current HWA and PIV data in the DC wake and from current PIV measurements for the CC wake. Data previously reported for the CC wake by Diaz et al. 1985 [71], Ferré et al. 1989a [10] and Vernet 1999b [72] in the same URV wind tunnel have been added for the sake of comparison. Figure 4.2 shows that in the near to mid wake of the DC, up to $x/D \approx 40$, $y_{1/2}$ rises much faster with downstream location than for the CC wake. Further downstream, the larger vertical size of the DC wake grows at the same rate with streamwise distance, i.e., with $(x/D)^{0.5}$, as does the size of the CC wake (figure 4.2). For example, at $x/D = 50$ we have $y_{1/2} \approx 4.33D$ in the DC wake whereas the equivalent streamwise location in the CC wake would be $x/D \approx 235$. Furthermore, a value of $y_{1/2} \approx 4.54D$ for the DC wake at $x/D = 60$ would be found at $x/D \approx 258$ in the CC wake. The growth rate of the wake in the streamwise direction can also be characterized by the length scales of the Reynolds stress components. Figure 4.3 shows the values of the L_u length scale, defined as the vertical location of the half centerline value of the r.m.s. streamwise velocity ($u_{RMS} = (\overline{u'u'})^{1/2}$), obtained from the current HWA and PIV measurements at several streamwise locations in the DC and CC wakes. The comparison of the streamwise evolutions of L_u in the DC and in the CC wakes suggests once again that the DC wake grows considerably faster than the CC wake.

It might be argued that quantities such as centerline $\overline{u}_d$ and $y_{1/2}$, which were originally devised to characterize the growth rate of the CC wake, may not work well when applied to the analysis of the DC wake. In fact, the $\overline{u}_d$ vertical profiles for the DC wake in figure 4.4a show an unexpected feature with a local maximum at an intermediate vertical location, which is not present in the corresponding CC wake profiles. Note that the local maximum in the $\overline{u}_d$ profile of figure 4.4a first appears at $x/D = 16$. Similarly, an unexpected feature is also apparent in the u_{RMS} vertical profiles shown in figure 4.4b. In particular, the u_{RMS} profiles early in the DC wake ($x/D \leq 26$) feature a local minimum in the vertical region with $0 \leq y/D \leq 2$, with two peaks, one on the centerline and the other off the centreline. As the wake grows, the u_{RMS} peak values gradually decrease and at downstream station $x/D = 170$, the profile is flatter, with low fluctuation levels, with maxima close to $y_{1/2}$. Figure 4.5 shows the streamwise evolution of the measured maximum values and locations in the vertical profiles of mean streamwise velocity deficit and r.m.s. streamwise velocity depicted in figure 4.4. For the sake of completeness, we have also added in these plots data values obtained from PIV measurements.

To elucidate what is causing the $\overline{u}_d$ and u_{RMS} peaks in figure 4.4 and,

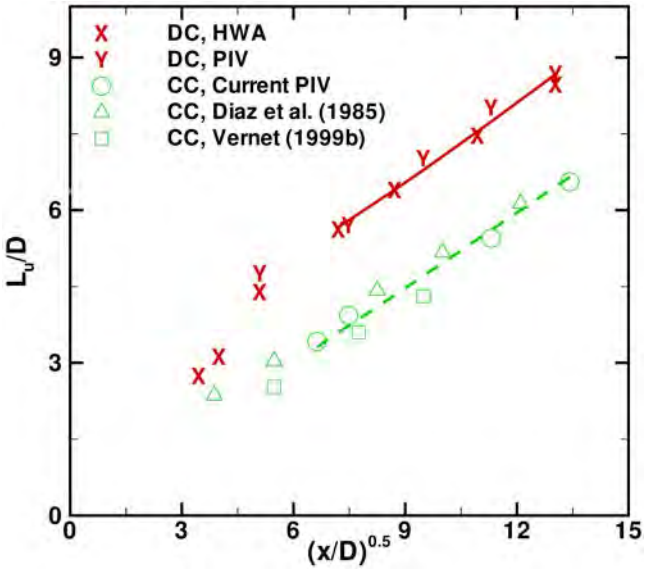

Figure 4.3: Values of the L_u length scale (defined in the main text) in the vertical $x-y$ plane with $z=0$ in the CC and DC wakes. All of the current HWA results as well PIV measurements in the far wake ($70 \leq x/D \leq 180$) were obtained with model M_3 at a Reynolds number of $Re = 4.0 \times 10^3$ (see tables 2.1 and 2.5). Current PIV measurements in the mid-far wake ($0 \leq x/D \leq 56$) were obtained at $Re = 1.0 \times 10^4$. Diaz et al. 1985 [71] and Vernet 1999b [72] results were respectively obtained at $Re = 9.0 \times 10^3$ and $Re = 7.0 \times 10^3$. The equations of the tendency lines plotted for the CC data (dashed line) and the DC data (solid line) are $L_u/D = 0.49(x/D)^{0.5} + 0.04$ and $L_u/D = 0.51(x/D)^{0.5} + 1.91$, respectively.

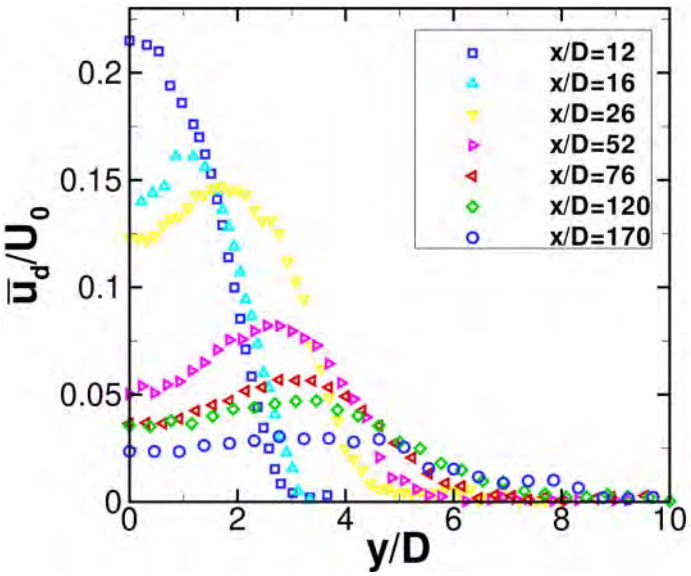

(a)

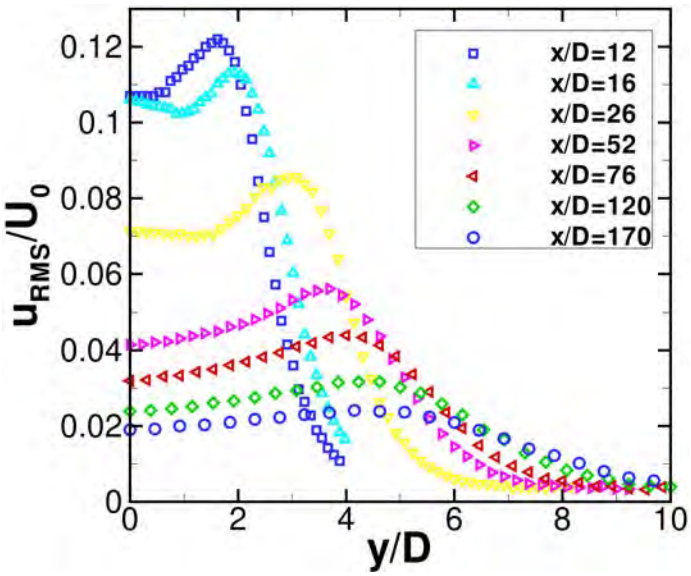

(b)

Figure 4.4: Vertical profiles of (a) the mean streamwise velocity–defect $\overline{u}_d/U_0$ and (b) the r.m.s. streamwise velocity, u_{RMS}/U_0, at several streamwise stations in the $x-y$ plane at $z=0$ in the DC wake for HWA measurements with the DC model, M_3, at a Reynolds number of $Re = 4.0 \times 10^3$.

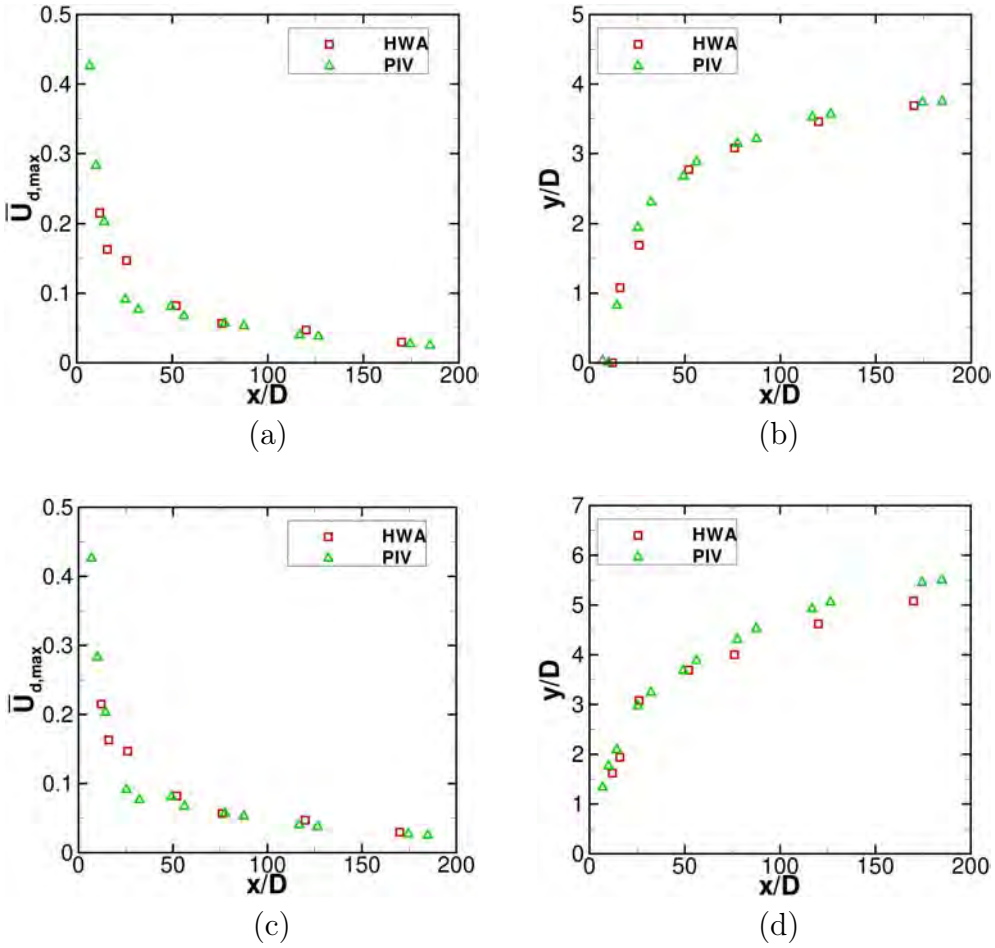

Figure 4.5: Value and location of the maximums in the vertical profiles of figures 4.4a and 4.4b as a function of the streamwise location, x/D. (a) and (b) respectively show the $\overline{u}_d$ maximum value and its vertical location, whereas (c) and (d) respectively shown the u_{RMS} maximum value and its vertical location. All of the current HWA and PIV measurements in the $70 \leq x/D \leq 180$ range were obtained with model M_3 at a Reynolds number of $Re = 4.0 \times 10^3$. Current PIV results in the $0 \leq x/D \leq 56$ range were obtained at $Re = 1.0 \times 10^4$.

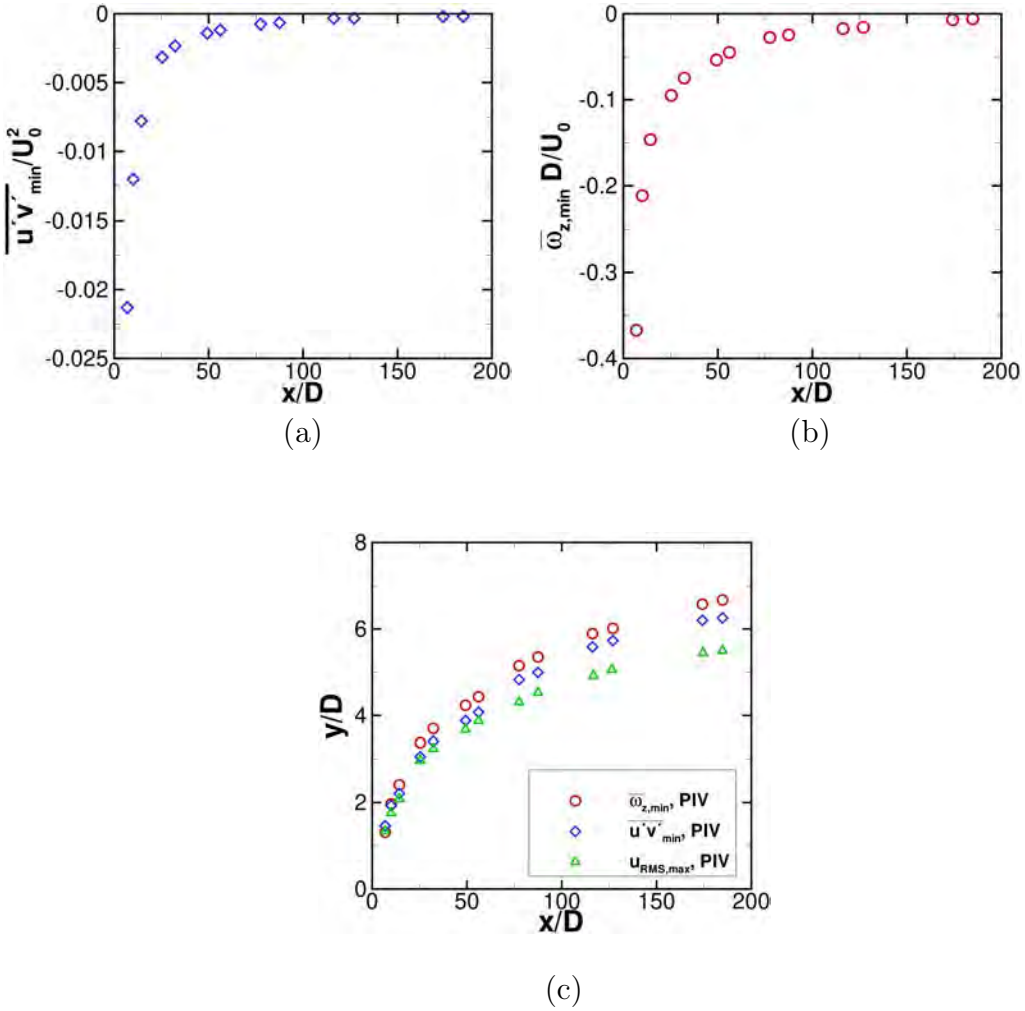

Figure 4.6: Variation with x of the maximum values in the vertical profiles of (a) $\overline{u'v'}$ and (b) $\overline{\omega}_z$ at the vertical plane with $z = 0$. The corresponding vertical locations of the $\overline{u'v'}$, $\overline{\omega}_z$ and u_{RMS} $y-$profile maximums are plotted together in part (c). All of the data shown in this figure were obtained from PIV measurements. In particular, measurements for $x/D \leq 56$ were obtained with the DC model M_2 at a Reynolds number of $Re = 1.0 \times 10^4$ whereas for $x/D \geq 70$ measurements were obtained with the DC model M_3 at $Re = 4.0 \times 10^3$.

more particularly, whether these peaks in the mean field profiles may be related to the periodic passage of large scale vortical structures, we have plotted in figure 4.6 the corresponding values and vertical locations of $\overline{u'v'}$ and $\overline{\omega}_z$ at several streamwise locations. Figure 4.6c shows that there is a good correlation between the vertical locations of the u_{RMS}, $\overline{u'v'}$ and $\overline{\omega}_z$ peaks thus suggesting that the peak locations in the mean field are indeed indicative or the periodic passage of coherent vortical structures. While it seems plausible to assume that such vortical structures in the DC wake are the counterpart of the Kármán vortices in the CC wake it is noteworthy that they depart quite quickly from the $y = 0$ centerline as they travel downstream. For example, we see in figure 4.6c that as early as $x/D = 20$ these vortices have already attained, on the average, the $y/D \approx \pm 2.5$ location while the $y/D = \pm 4$ vertical location is already reached at $x/D \approx 55$.

The corresponding plots for PIV measurements on the CC wake are shown in figure 4.7. As expected, these plots confirm the well-known fact that in the CC wake the Kármán vortices (VKV) are moving away from the vertical midplane ($y = 0$) as they travel downstream. Comparison of figure 4.7c with figure 4.6c shows that such a progressive vertical displacement is much slower than the corresponding displacement of the vortical structures in the DC wake (figure 4.6). For example, the VKV are located in figure (4.7), on the average, at about $y/D = \pm 1.6 - 1.7$ at x/D = 55, which is smaller that the $y/D = \pm 4$ observed for the DC wake in figure 4.6. This vertical location is never reached in the CC wake for $x/D \leq 180$. It is also interesting to compare the respective $\overline{u'v'}$ and $\overline{\omega}_z$ peak values for the DC (figures 4.6a and 4.6b) and CC (figures 4.7a and 4.7b) wakes. The near wake peak values are larger for the DC wake (especially in the $\overline{u'v'}$ profile). However, further downstream their rate of decay is, at a qualitative level, comparable in both cases. In fact, comparison of figure 4.6a and 4.7a suggests that at $x/D \approx 90$ the $\overline{u'v'}$ maximum (absolute) value for the DC wake is smaller than for the CC wake. In summary, these results indicate that the main difference between the DC and CC vortical structures, or to be more precise on the differences in footprints that they leave at the $z = 0$ vertical plane, is not in their respective strength but in the fact that the vertical motion of the former HSV vortices away from the $y = 0$ midplane is strikingly fast. We have also seen that momentum recovery (figure 4.1), vertical spreading (figure 4.2) and upraising of vortical structures (figure 4.6) takes place much sooner in the DC wake than it does in the CC wake. Thus, it can be said that the downstream position where wake is considerably reduced (i.e., $\overline{u}_d$ approaches 0) occurs much earlier because of the segmentation of the cylinder, at which point the wake is much thicker.

Self–preservation analysis applied to the far wake of the continuous cylin-

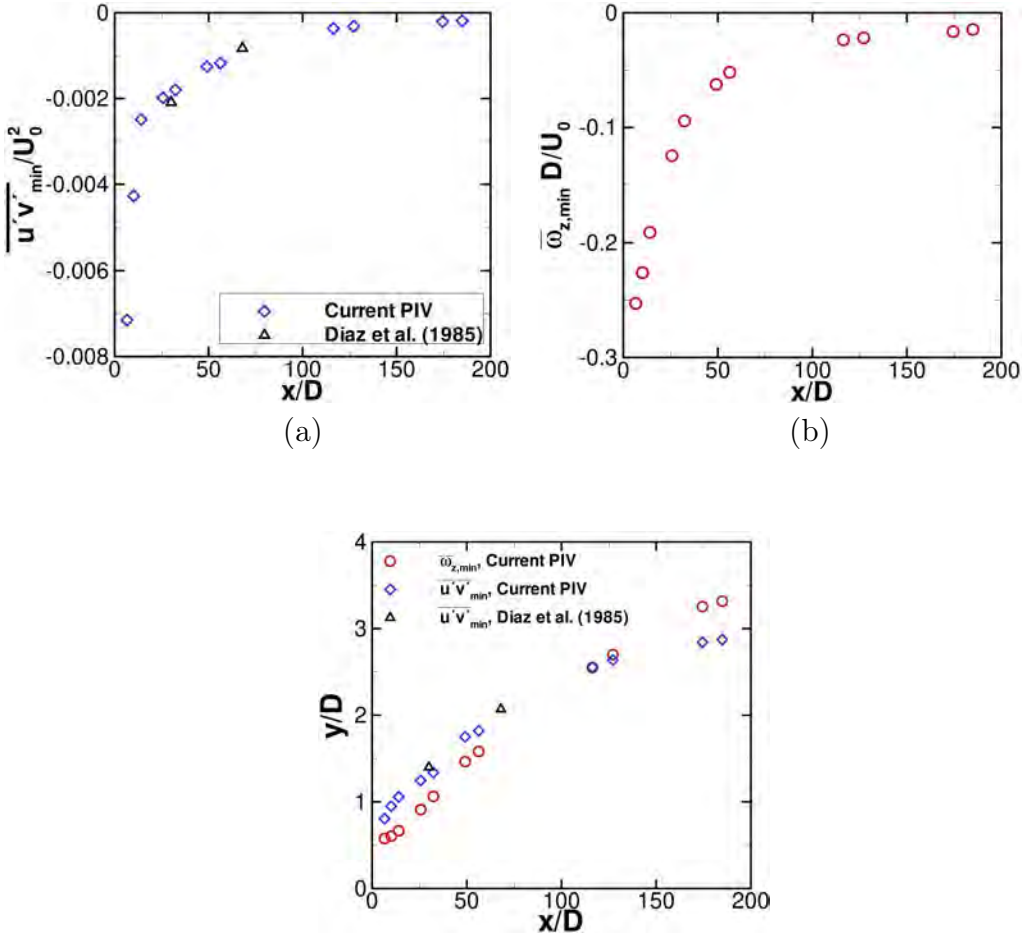

Figure 4.7: Maximum values of (a) $\overline{u'v'}$ and (b) $\overline{\omega}_z$ at several x/D locations in the vertical plane with $z = 0$. The maximum values were extracted from the vertical profiles obtained from PIV measurements with the CC version of models M_2 and M_3. In part (a), the experimental values previously reported by Diaz et al. 1985 [71] have also been added for the sake of comparison. In part (c), we plot the corresponding vertical locations at which these maximum values were located.

der (Townsend 1956 [14]; Tang et al. 2016 [73]) provides the following scaling laws for the centerline $\overline{u}_d/U_0$ and $y_{1/2}/D$ quantities:

$$\frac{\overline{u}_d}{U_0} = C_1 \left[\frac{x - x_0}{D}\right]^{-0.5} \tag{4.1}$$

$$\frac{y_{1/2}}{D} = C_2 \left[\frac{x - x_0}{D}\right]^{0.5} \tag{4.2}$$

Considering that, as will be discussed further below, the vertical growth of the wake is closely related to the vertical displacement of vortical structures, it makes sense to use equation (4.2) to compare both wakes. For the CC far wake, values of $C_2 \approx 0.20$ and $-x_0/D$ in the $25 - 125$ range have been reported in the literature (see Tang et al. 2016 [73], and references therein). For the DC data in figure 4.2, we have $C_2 = 0.63$ and $x_0 = 1.9\,D$ in the region with $4 \leq x/D \leq 36$ and $C_2 = 0.40$ and $x_0 = -67\,D$ for $52 \leq x/D \leq 170$.

Chapter 5

Wake interface identification

It is customary to decompose the flow behind a continuous cylinder into two separate flow regions, namely a wake region and a free-stream flow region. The flow in the wake region is rotational and turbulent whereas the flow in the free-stream region, which is the source of momentum and energy supporting wake growth, is neither. The growth of the wake behind the cylinder is a complex phenomenon involving both the spatial spreading of vorticity (turbulent) fluctuations and momentum thickening, i.e., a decrease in mean momentum deficit within the wake as fluid is convected downstream. Momentum thickening was analyzed in chapters 3 and 4 for both the CC and the DC wake. The focus here is on how the velocity and vorticity fluctuation fields, extracted from the LES calculations, spread vertically in the near-mid DC wake.

Several methods for the identification of a turbulent/non-turbulent flow interfaces have been proposed, e.g., [74], [75]. The general idea is to select an indicator quantity (such as a component of velocity or vorticity) and then plot profiles of this quantity in the direction normal to the interface. In the present study we first adopted a well-established methodology, previously used by numerous researchers [35], [76], [77], [78], to identify the interface between the CC wake and the free flow region. This methodology is based on the so-called turbulence indicator function:

$$I(x,y,z,t) = \left\{ \begin{array}{ll} 1 & if\ F \geq C\ \ (turbulent flow) \\ 0 & if\ F < C\ \ (non-turbulent flow) \end{array} \right\} \tag{5.1}$$

Here, F is a turbulence detector function and C is a threshold level. We used the detector function of Tabatabai et al. 1989 [78],

$$F = \left[(\tilde{u} - U_0) \frac{\partial \tilde{u}}{\partial t} \right]^2 \tag{5.2}$$

where $\tilde{u} = \tilde{u}(x, y, z, t)$ denotes the $x-$component of velocity. Equation (5.1) was used with $C = 1.0 \times 10^4\ m^4 s^{-6}$, a threshold value which was found to work well in the DC near wake ($x/D \leq 10$). The intermittency factor, $\overline{I}(x, y, z)$, which is the time average of $I(x, y, z, t)$, was calculated on every node of the computational domain.

As pointed out by Kopp et al. 2002 [35], the method for the identification of a turbulent/non-turbulent interface based on equations (5.1) and (5.2) makes full sense in experiments where a normal wire, yielding only the streamwise component of velocity, is used. Since turbulence is characterized by random vorticity fluctuations, we also implemented an alternative interface detection method as follows. The mean of squared vorticity can be decomposed, in an analogous way to what is customarily done with the velocity field, as

$$\overline{\omega^2} = \overline{\omega}^2 + \left(\overline{\omega'_x \omega'_x} + \overline{\omega'_y \omega'_y} + \overline{\omega'_z \omega'_z}\right) = \overline{\omega}^2 + \omega^2_{RMS} \tag{5.3}$$

Since high/low ω_{RMS} values are to be found respectively in the wake/free stream flow regions, it seems reasonable to assume that this quantity might also be an effective indicator to identify or locate the DC wake interface.

Let us consider first the vertical growth of the DC wake at the mid cylinder segment ($z = 0$) location. The $\overline{I}$ profiles in figure 5.1a portray a rather ample buffer region where the (absolute) slope is not very high so that one cannot tell for sure where a hypothetical point denoting the wake interface ought to be drawn. Looking at figure 5.1a we can say, for example, that there is a very high probability that at $x/D = 10$ the vertical location of the wake interface would be around $|y/D| = 5$, and at $x/D = 5$ the vertical location would be close to $|y/D| = 4.3$. A limitation of the wake identification method based on equations (5.1) and (5.2) arises from the fact that the highest $\overline{I}$ levels characterizing the wake proper region, $\overline{I}_{max}$, decay with increasing downstream location. In figure 5.1a we see $\overline{I}_{max} \geq 0.95$ at $x/D = 5$ but the maximum $\overline{I}$ level has already decayed a little ($\overline{I}_{max} \geq 0.90$) at $x/D = 10$. The vertical profiles of ω_{RMS} in figure 5.1b suggest that the interface of the wake region might be identified at the vertical locations where a sudden decrease in the profile slope occurs. They also show that the probable vertical location of the interface at two downstream stations is like what was observed with the intermittency factor.

We have so far considered only the vertical spread of the wake along the mid-segment ($z = 0$) $x - y$ plane. The DC wake is clearly more challenging than the CC wake because in the former the rate of vertical growth is $z-$dependent since it also spreads laterally from the edge of the cylinder segment ($z/D = \pm 2.5$) and further downstream thereafter (see figure 2.1).

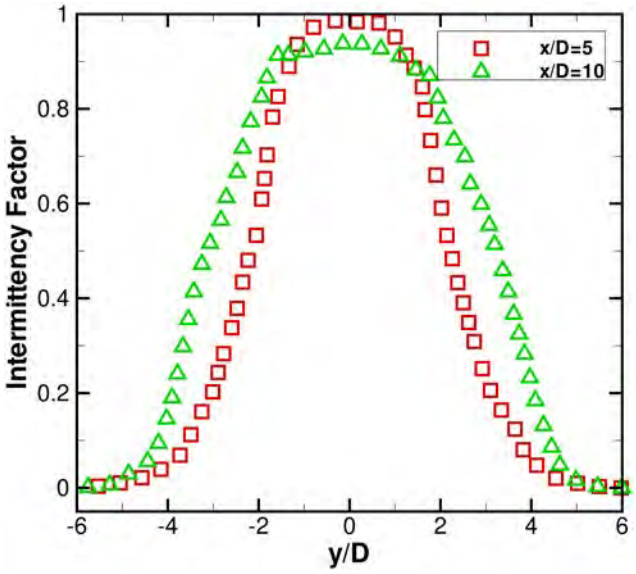

(a)

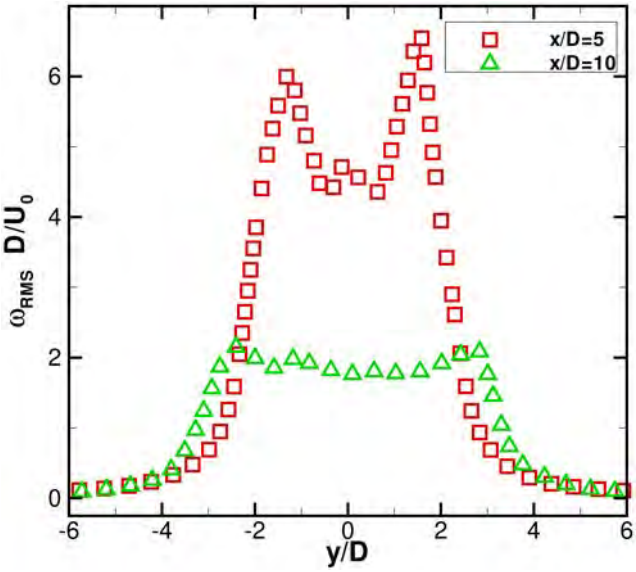

(b)

Figure 5.1: The vertical profiles of (a) $\overline{I}$ and (b) $\omega_{RMS}D/U_0$, at two different stream-wise locations, namely $x/D = 5(\square)$ and $x/D = 10(\triangle)$, in the vertical plane at $z = 0$.

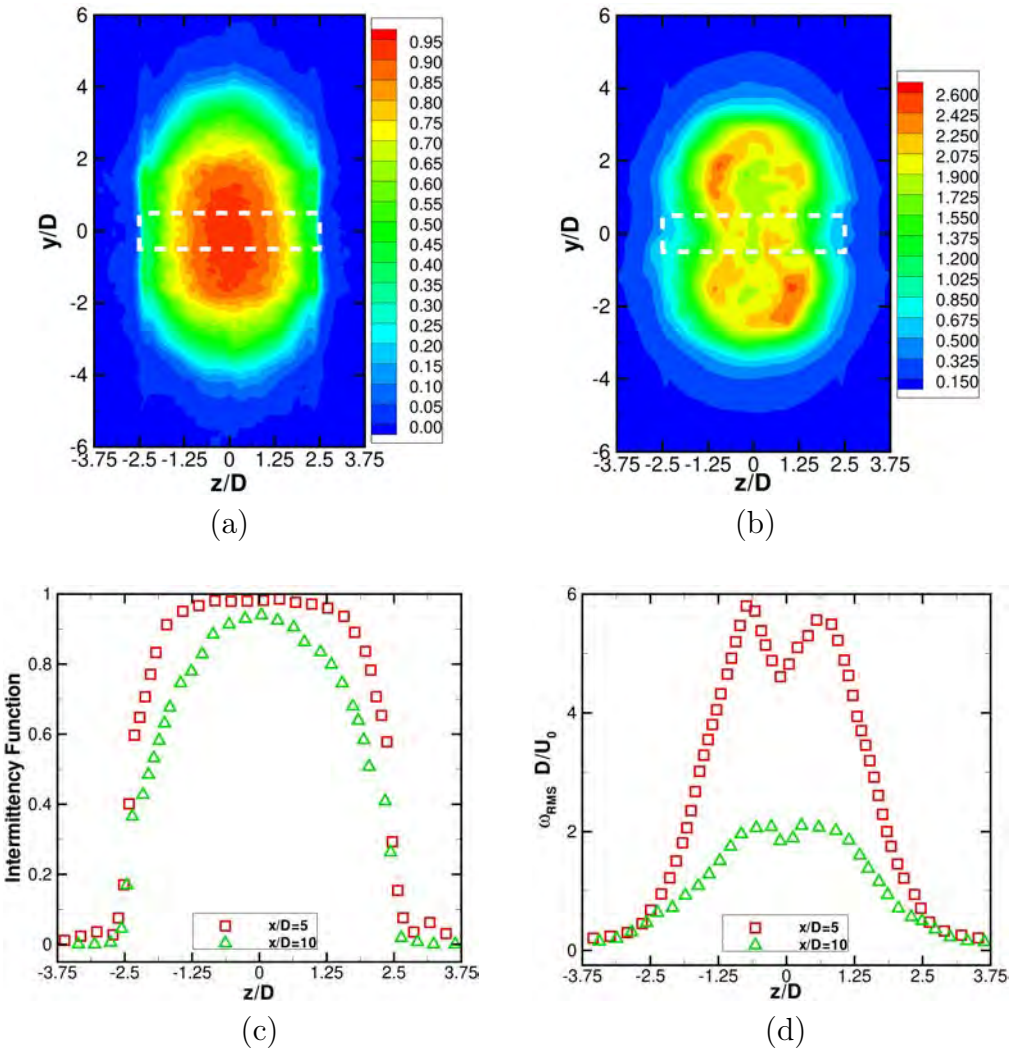

Figure 5.2: Contours of (a) the intermittency factor $(\overline{I})$ and (b) mean vorticity fluctuation $(\omega_{RMS}\ D/U_0)$ at the vertical $y-z$ plane with $x/D=10$. Spanwise profiles on wake midplane $(y=0)$ at two streamwise locations are plotted in parts (c) and (d) for $\overline{I}$ and $(\omega_{RMS}\ D/U_0)$, respectively.

Figure 5.2 shows the results of the two wake identification methods, $\overline{I}$- and ω_{RMS}-based, applied at vertical $y-z$ planes within the DC near-wake, at $x/D = 10$. At a given stream-wise location, the width of the DC wake is maximum at mid-segment axial location ($z = 0$) and it progressively decays with increasing lateral $z-$distance from the mid-segment, as illustrated by the distribution of intermittency and mean vorticity fluctuations in the vertical $y-z$ plane (figure 5.2a-b). The $\overline{I}$ contours in figure 5.2a show spikes at the segment edges ($|z/D| = 2.5$), a fact related to the binary character of equation (5.1). The vorticity fluctuation contours in figures 5.2b look comparatively smoother; the particular shape of the contours with the highest ω_{RMS} levels in the plot will be a subject of discussion in the next chapter. The negative counterpart of the apparent smoothness of the ω_{RMS} contours in figure 5.2b is observed in the corresponding spanwise profiles of figure 5.2d. The transition between the wake region and the free-stream flow in the gap region between cylinder segments as we move along the z direction is too gradual, not a sharp one at all. On the other hand, the $\overline{I}$ $z-$profiles in figure 5.2c suggest that the locations where an abrupt increase in slope occurs might be thought of as the projection of the wake lateral interface. Note that in figures 5.2a,b the levels of both $\overline{I}$ and ω_{RMS} in the gap region ($|z/D| > 2.5$) are small but nonetheless above the corresponding free-stream background levels ($\overline{I} = 0$ and $\omega_{RMS}\ D/U_0 = 0.15$).

The DC-wake spreads vertically as well as laterally. But, why the lateral spread is small compared to vertical? And why is the vertical spread faster in the mid-segment location ($z = 0$) than it is near the cylinder segment edges as illustrated in figures 5.2a,b? One would expect that as the flow within the gap region between cylinder segments has relatively high mean momentum, the level of mean momentum recovery within the DC wake ought to be, at a given x location, larger near the segment edges than it is in the mid-segment ($z = 0$) location. We used the current HWA measurements of the mean velocity component ($\overline{u}$) to confirm such an assumption. Figure 5.3 shows measured vertical profiles for the mean u-velocity deficit, ($\overline{u}_d/U_0$), at three spanwise locations. What is most relevant in these plots for the current discussion is the comparison between the profiles at $z = 0$ (cylinder mid-segment) and $z/D = 2.5$ (edge of the cylinder segment). As expected, the mean momentum recovery rate at the segment edge is much faster than it is at the mid-segment location. This fact suggests that, on the average, a good amount of momentum might be transferred into the DC wake through its lateral interface.

We can give a common answer to the two questions we posed above, e.g., why is the DC wake lateral spread is small compared to vertical, and why its vertical spread is considerably faster around the mid-segment location

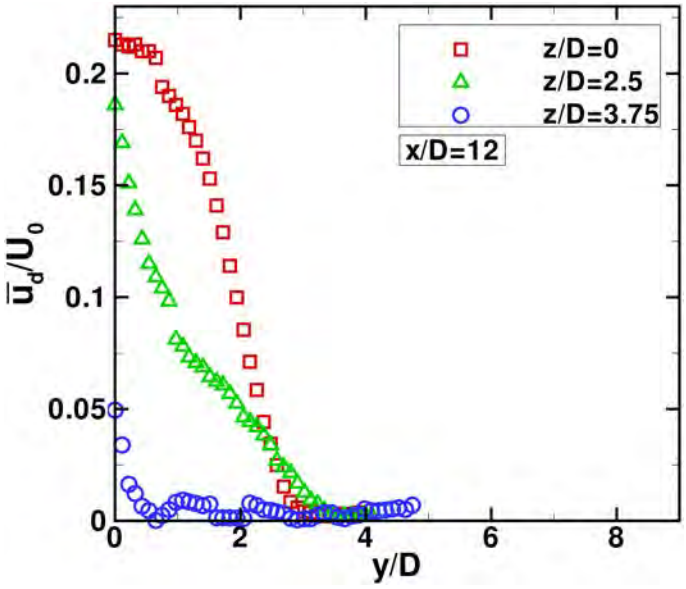

(a)

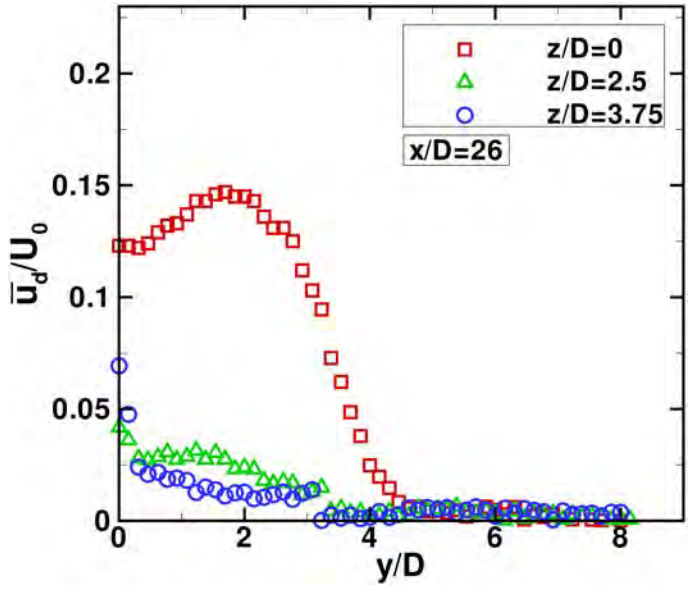

(b)

Figure 5.3: Comparison of the vertical profiles of mean velocity deficit ($\overline{u}_d/U_0$) at three spanwise locations, namely $z/D = 0$, 2.5 and 3.75, at the streamwise locations with (a) $x/D = 12$ and (b) $x/D = 26$ in the DC wake. All of the results included in these plots correspond to HWA measurements with the DC model M_3 at a Reynolds number of $Re = 4.0 \times 10^3$.

($z = 0$)? What we propose implies a change of paradigm in regard of the transfer mechanisms through the lateral interface of the DC-wake: it is not the wake that spreads outwards into the free-stream flow in the gap region between cylinder segments, but it is precisely the other way round. It is the flow in the gap region between cylinder segments that spreads into the wake. Support and an ample discussion for our alternative point of view is provided in the next chapters.

Chapter 6

Identification of large-scale flow structures

The present discontinuous cylinder (DC) geometry was devised to replicate already in the near wake region the self-preserving structures of the far CC wake reported previously. These three-dimensional CC wake flow structures are commonly referred to as horseshoe or double roller vortices [22], [26]; for the sake of conciseness, we will refer to them as HSV's or DR's hereinafter. Figure 6.1 shows vector plots of velocity fluctuations in the $x-y$ plane with $z=0$ for an instantaneous field obtained from PIV measurements in the DC wake. In the near wake ($x/D<10$), the rolls portrayed in figure 6.1a remind one of the typical patterns that are generated by the von Kármán vortices in the CC wake, indicating that wake periodicity is maintained. Figure 6.1b shows that further downstream ($x/D>30$) the intensity of the fluctuation rolls in the vertical plane is still high and that their centers have been considerably displaced away from the $y=0$ centerline (note the change in vertical scale). Such a vertical displacement is consistent with the results for the DC wake field previously discussed in chapter 4 (e.g., figure 4.6c). The first difference between the Von-Kármán vortices in the CC wake and the HSV's in the DC wake is that the latter maintain higher intensity levels in the mid wake and at the vertical midplane with $z=0$. Also, they move much more quickly away from the $y=0$ centerline while convected downstream.

The second and not less relevant difference between the Von-Kármán vortices and the HSV's is in the fully three-dimensional (3-D) character of the latter. The plots in figure 6.2, showing instantaneous vectors of velocity fluctuations in horizontal $x-z$ windows at two different vertical levels (obtained also from PIV measurements in the DC wake), illustrate why the HSV's were also named double-rollers. As we move along the spanwise direction, away

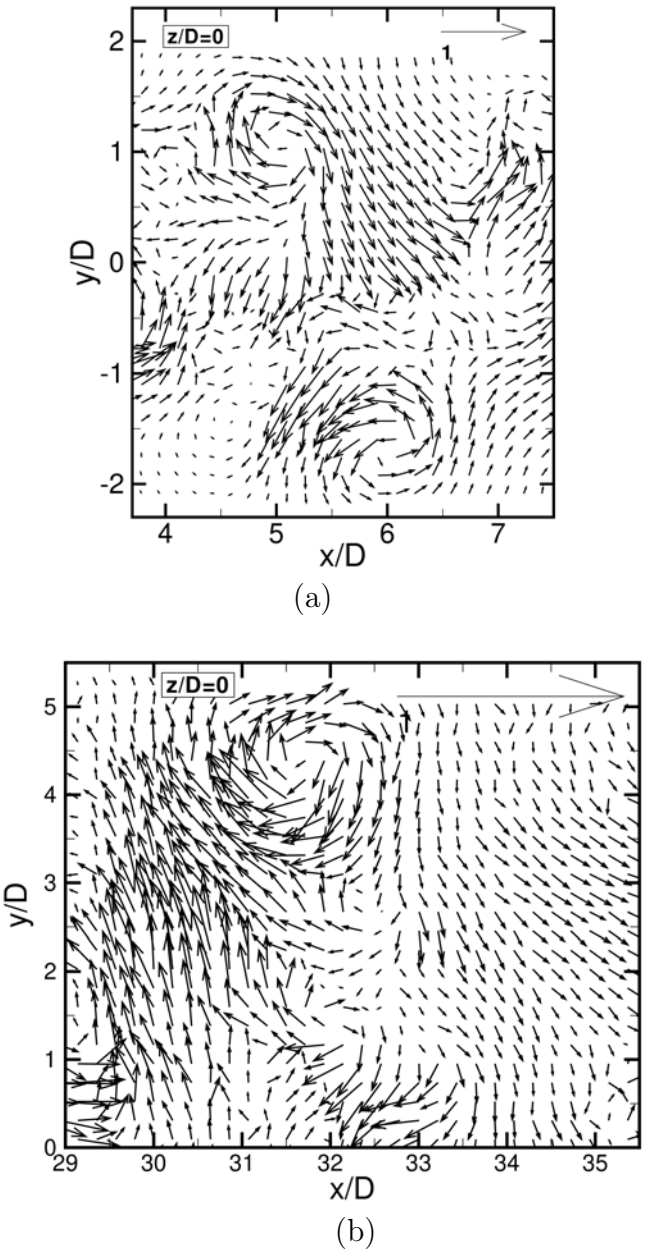

Figure 6.1: Vector plots of the instantaneous velocity fluctuations (u', v') in the vertical $(x - y)$ plane at $z = 0$ (a) in the near wake and (b) middle–far wake behind the discontinuous cylinder. The vector scale used in (b) is 2.4 times larger than in (a). In each case, the arrow near the top of the figure frame denotes what would be the vector length for the reference velocity U_0. The results in these plots correspond to PIV measurements with model M_2 at a Reynolds number of $Re = 1.0 \times 10^4$.

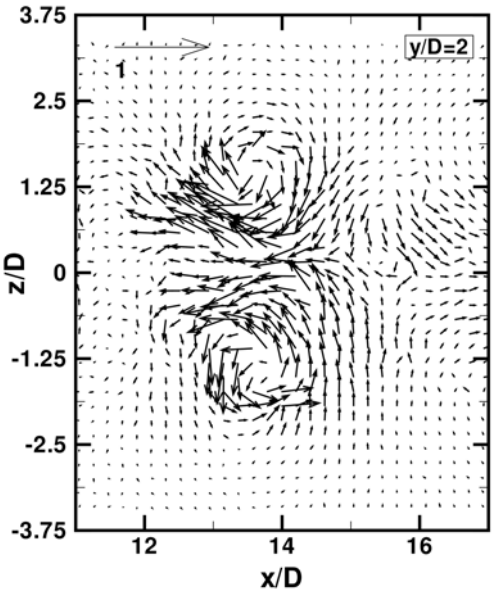

(a)

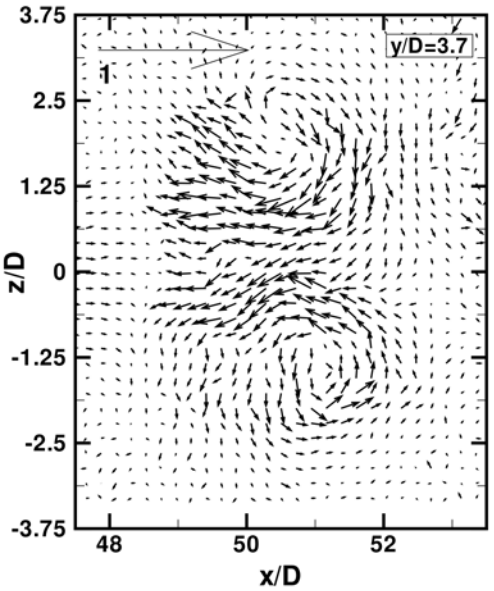

(b)

Figure 6.2: Vector plots of the instantaneous velocity fluctuations (u', w') in the horizontal $(x-z)$ planes at $y/D = 2$ (a) and 3.7 (b) in the middle (a) and medium–far (b) wake of the discontinuous cylinder. The arrow near the top of the figure frame denotes what would be the vector length for the reference velocity U_0. The results in these plots correspond to PIV measurements with model M_2 at a Reynolds number of $Re = 1.0 \times 10^4$. Note that the length of the cylinder segment is $5D$ ($-2.5 \leq z/D \leq 2.5$; see Figure 2.1).

from the mid-segment ($z = 0$) location, the projection of the (so-called) legs of the HSV becomes apparent. It is again remarkable that the presence of relatively high strength of the circulation around the HSV legs remains at a streamwise location as far downstream as $x/D = 50$, as shown in figure 6.2b. The cut views of the HSV on vertical ($x - y$) and horizontal ($x - z$) planes in the further downstream wake are shown in figure 6.3.

A well-established method to portray the shape of large 3-D flow structures is to plot iso-surfaces with a certain level of pressure. Figure 6.4 shows that numerically calculated iso-surfaces with a properly chosen pressure value can be used to track reasonably well the HSV envelopes in the DC near wake. Figure 6.5 shows iso-surfaces with $(\hat{p}-p_{atm})/(\rho U_0^2) = -0.1346$, obtained from an instantaneous field in the LES calculation of the DC wake. These two plots show the shape of the three-dimensional HSV's and how they grow as they move downstream. The genesis of HSV's occurs very early in the DC wake with their presence clearly observed already at $x/D \approx 3$ to 4. This is distinct from the CC wake for which the three–dimensional rib structures take some time to develop (Hayakawa et al. 1989 [9]).

We have hitherto pictured HSV's as instantaneous, large-scale flow structures. It is now time to pose a relevant question: if, as suggested by the vector plots in figures 6.1-6.4, HSV's feature (at given times and spatial locations) strong circulation/vorticity levels, do these vortices indeed leave an imprint on the time-averaged fields? Or, in other words, are the mean fields somehow reflecting the periodic passage of instantaneous HSV's? The combined plots of mean velocity vectors $(\overline{\widetilde{v}}, \overline{\widetilde{w}})$ and modulus of mean vorticity ($|\overline{\omega}\ D/U_0|$) contours in the vertical $y - z$ planes at several downstream stations in the near wake of DC, shown in figure 6.6, confirm that this is indeed the case. Around the mid–segment ($z = 0$) location, away from the cylinder segment edges, HSV's keep, on average, the $z-$alignment of their axes. Notwithstanding, near the segment edges ($|z/D| = 2.5$) HSV's move laterally inwards while being kinked due to the lateral pressure ($z-$) gradients between the region behind the cylinder segment and the relatively high pressure gap region ($|z|\ /D > 2.5$). This pressure gradient causes the HSV's upwards/downwards kinking, what in more colloquial terms we could refer to as the generation of the HSV legs (figure 6.6). As these legs are being generated, the ($z-$aligned) HSV head is being rapidly moved upwards/downwards. Moreover, as the HSV head moves away from the $y = 0$ centerline it is being convected by a higher velocity streamwise ($x-$) motion. As a result, the HSV is being slanted forward (see the sketch in figure 1.1). Thus, while we should expect the $z-$component of vorticity to be (on the average) the dominant one within the HSV heads, its legs should instead present relatively high levels of both the $x-$ and $y-$vorticity components. More details about the realign-

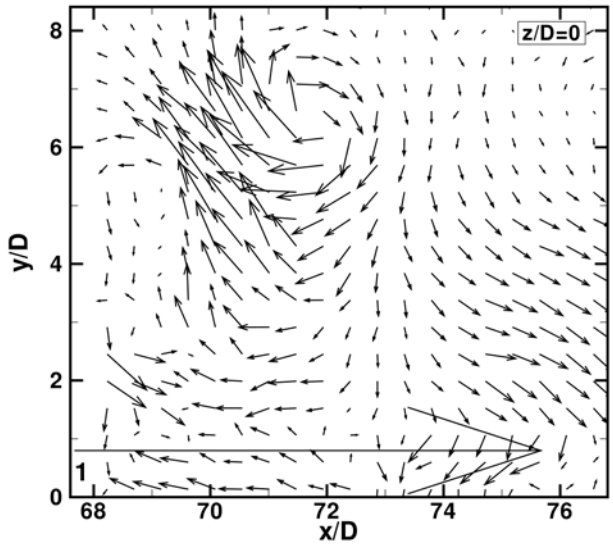

(a)

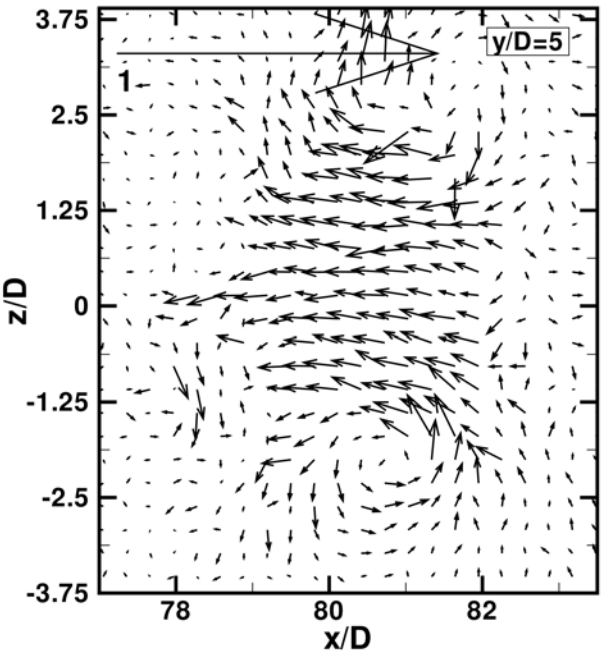

(b)

Figure 6.3: Vector plots of the instantaneous velocity fluctuations (a) (u', v') in the vertical plane at $z = 0$ and (b) (u', w') in the horizontal plane at $y/D = 5$ in the wake of the discontinuous cylinder. The arrow in the figure frame denotes what would be the vector length for the reference velocity U_0. The results in these plots correspond to PIV measurements with model M_3 at a Reynolds number of $Re = 4.0 \times 10^3$. Note that the length of the cylinder segment is $5D$ ($-2.5 \leq z/D \leq 2.5$; see Figure 2.1).

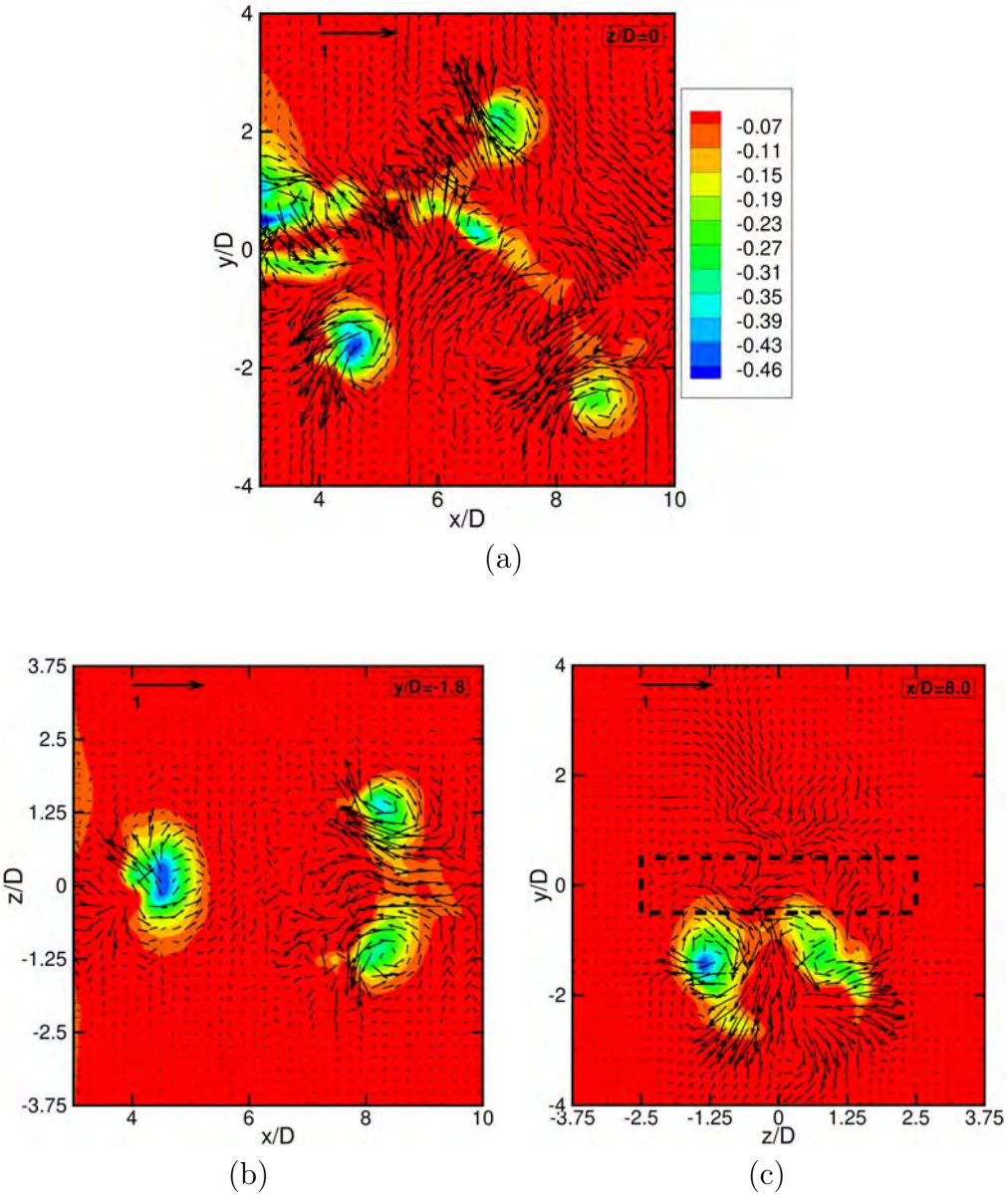

Figure 6.4: Contours of instantaneous dynamic pressure, $(\hat{p} - p_{atm})/(\rho U_0^2)$, together with vector plots of velocity fluctuations. Results are correspond to one time instant, same as in figure 6.5, of an LES at $Re = 1.0 \times 10^4$ (a) (u^f, v^f) vector plots in the vertical plane at $z = 0$; (b) (u^f, w^f) vector plots in the horizontal plane at $y/D = -1.8$; and (c) (v^f, w^f) vector plots in the vertical $y - z$ plane at $x/D = 8$.

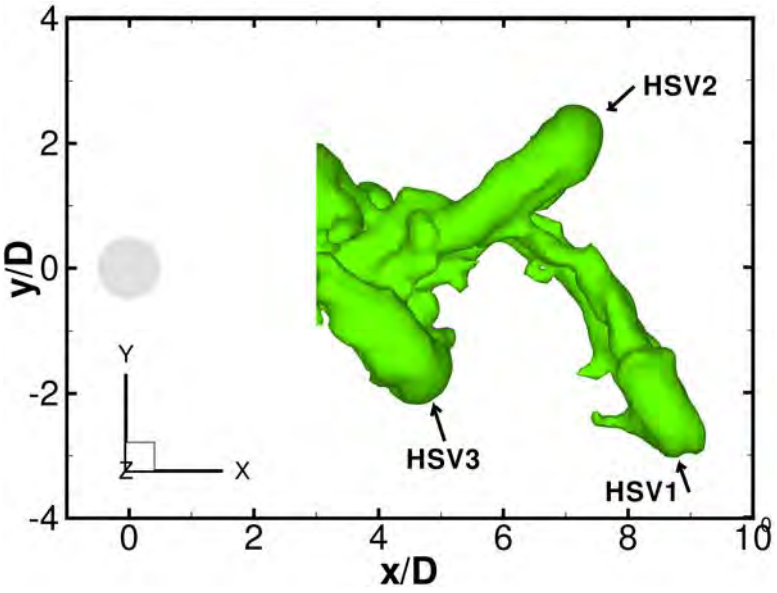

(a)

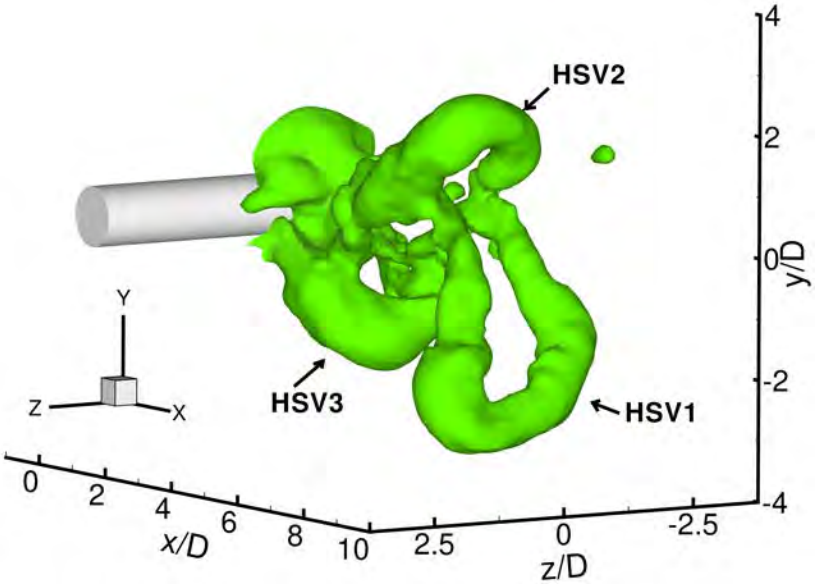

(b)

Figure 6.5: Iso–surfaces of $(\hat{p} - p_{atm})/(\rho U_0^2) = -0.1346$ in the DC near wake at one instant of time from the LES simulation at $Re = 1.0 \times 10^4$: (a) Side view of $x - y$ plane and (b) three-dimensional view of three different instantaneous vortices, labeled as HSV1, HSV2, and HSV3.

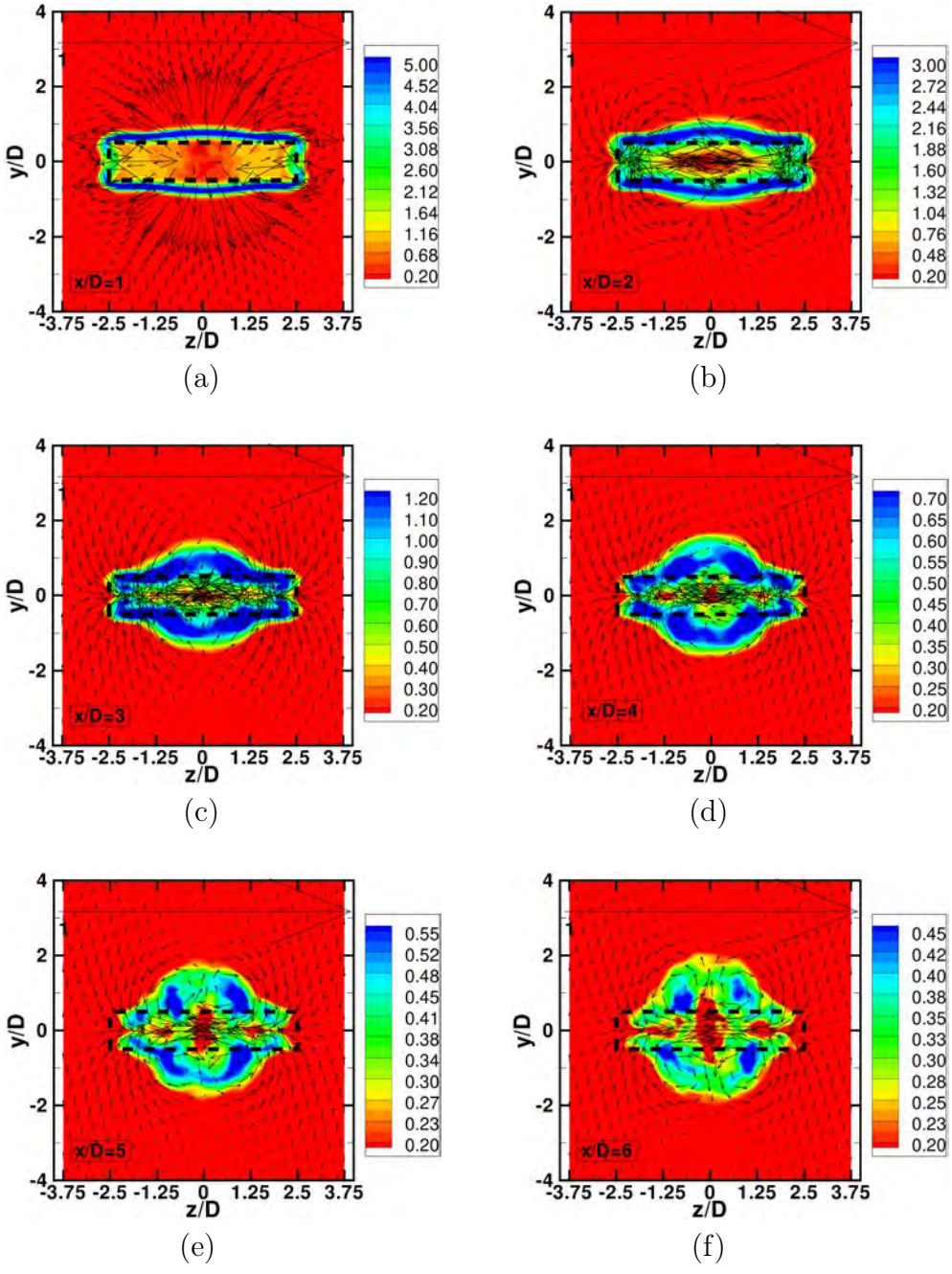

Figure 6.6: Mean velocity vector plots $(\overline{\tilde{v}}, \overline{\tilde{w}})$ and modulus of mean vorticity $(|\overline{\tilde{\omega}}\ D/U_0|)$ contours in the vertical planes at (a) $x/D = 1$ (b) $x/D = 2$ (c) $x/D = 3$ (d) $x/D = 4$ (e) $x/D = 5$ and (f) $x/D = 6$, obtained from the DC LES simulation. In all of the plots the velocity vectors are scaled so that an arrow length equal to the horizontal span of the plot would denote the reference velocity level, U_0. Note that the vorticity contour levels are different for each plot as shown in legend.

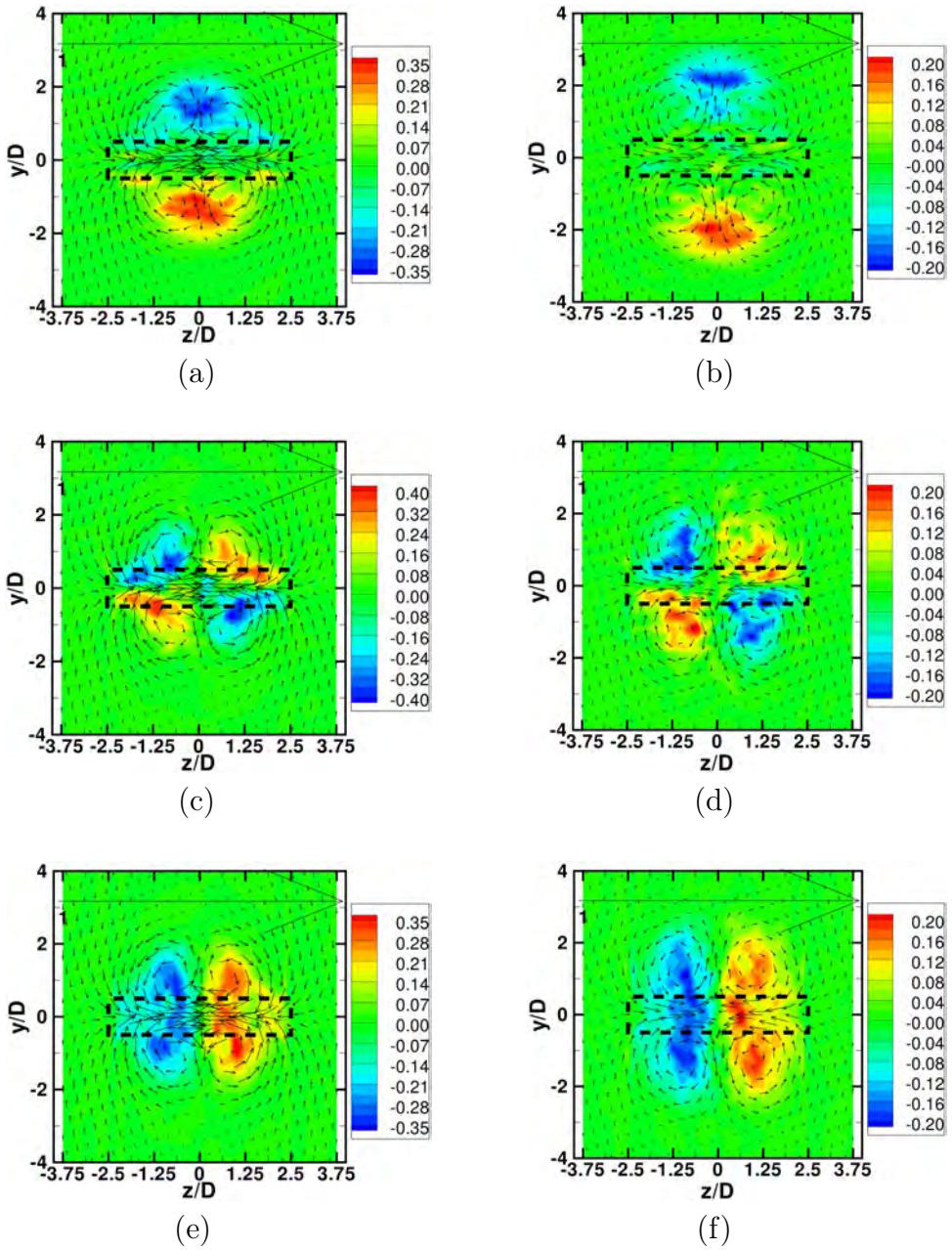

Figure 6.7: Mean velocity vector plots $(\overline{\tilde{v}}, \overline{\tilde{w}})$ and mean vorticity contours in the vertical planes with $x/D = 6$ (a, c, e) and 10 (b, d, f), obtained from the DC LES simulation. (a, b) Spanwise (z) vorticity component, $\overline{\tilde{\omega}}_z\ D/U_0$. ($c$, d) Streamwise (x) vorticity component, $\overline{\tilde{\omega}}_x\ D/U_0$. ($e$, f) Vertical (y) vorticity component, $\overline{\tilde{\omega}}_y\ D/U_0$. In all of the plots the velocity vectors are scaled so that an arrow length equal to the horizontal span of the plot would denote the reference velocity level, U_0. Note that the vorticity contour levels are different for each plot, as indicated by the accompanying color box on the right side.

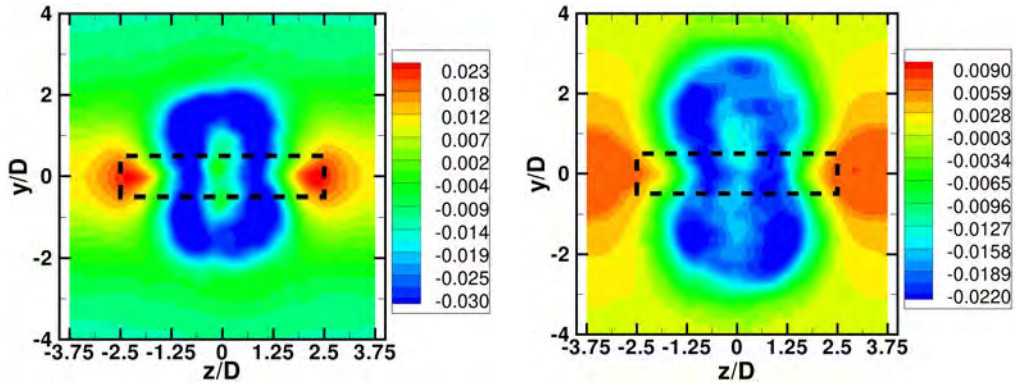

(a) (b)

Figure 6.8: Contours of mean dynamic pressure $\left((\overline{\hat{p}} - p_{atm})/(\rho U_0^2)\right)$ on the vertical planes with $x/D = 6$ (a) and 10 (b), obtained from the DC LES simulation. Note that the contour levels are different at each streamwise station, as indicated in the respective color boxes.

ment of the vortex i. e., the transformation of the $z-$aligned vortices (figure 6.6a) to the horseshoe shaped vortices (figure 6.6f) are given in Appendix B.

Figure 6.7a-f shows the combined plots of mean velocity vectors and mean vorticity contours in the vertical $y-z$ planes calculated with LES at two different x locations in the DC wake. The $\overline{\widetilde{\omega}}_z$ contours plotted in figures 6.7a and 6.7b show that, on the average, the spanwise range of the HSV's heads is approximately $-1 \leq z/D \leq 1$ and vertically they are centered at about $y/D = \pm 1.5$ at $x/D = 6$ (figure 6.7a) and at about $y/D = \pm 2.2$ at $x/D = 10$ (figure 6.7b). The foci with high/low $\overline{\widetilde{\omega}}_x$ levels in figures 6.7c ($x/D = 6$) and 6.7d ($x/D = 10$) are consistent with the cross-stream ($y - z$) projections of the rolls that are hinted at by the mean velocity vectors. The corresponding $\overline{\widetilde{\omega}}_y$ plots in figures 6.7e and 6.7f confirm the notion that the HSV legs are slanted forwards (along the streamwise direction), i.e., they are neither aligned vertically nor horizontally forwards but at some intermediate angle. Comparison of figures 6.7b,d,f with figure 5.2b suggests that the envelop of the HSV is also well characterized by the regions having high ω_{RMS} levels. It is no surprise that those flow regions with high vorticity fluctuation levels are also featuring relatively high mean vorticity. Note however that the maximum ω_{RMS} levels in figure 5.2b are almost one order of magnitude higher than are the mean vorticity levels in figures 6.7b,d,f. That is, contrary to what happens in the analogous decomposition of the velocity field, the fluctuation part is the dominating term in the r.h.s. of equation (5.3).

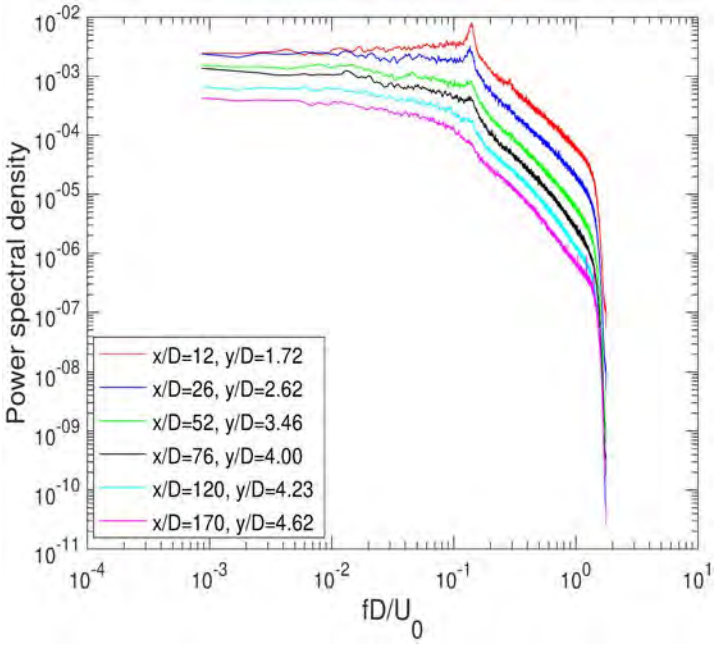

Figure 6.9: Spectra of the streamwise velocity fluctuations at different downstream stations in the plane $z/D = 0$ of the DC wake. The data obtained for these plots correspond to HWA measurements with model M_3 at $Re = 4.0 \times 10^3$.

Since the passage of instantaneous HSV leaves an imprint on the time-averaged velocity and vorticity fields it is no surprise that it does so also into the mean pressure field, as it is shown in the pressure contours of figure 6.8. In these plots the HSV's imprint, shaping as a ring-like, double horseshoe because of the central vertical symmetry, is clearly observable at $x/D = 6$ (figure 6.8a) and somewhat blurred at $x/D = 10$ (figure 6.8b). We note again a certain similarity in the shape of the contours with the lowest mean pressure in figure 6.8b and the contours with highest ω_{RMS} in figure 5.2b. The spanwise $(z-)$ pressure gradients near the edges of the cylinder segment $(z/D = \pm 2.5)$ around the $y = 0$ centerline in figure 6.8 are consistent with the lateral momentum transfer of fluid that is observed in the vector plots of figure 6.7.

Figure 6.9 shows the spectra of the streamwise velocity fluctuations on vertical $(x - y)$ plane at $z/D = 0$ at several downstream stations in the DC wake. The spectra indicate that the non-dimensional shedding frequency, i.e., the Strouhal number, of the large structures in the DC wake is $S_t = 0.137$, which is considerably lower than the corresponding values for the CC wake

($St = 0.202$ from current LES at $Re = 10^4$, in good agreement with the $St = 0.202$ and 0.203 values respectively reported by Norberg 2003 [7] and Dong et al. 2006 [65] at similar Re). Spectra also show that the dominant structures in the DC wake have higher energy levels up to the downstream station $x/D = 120$, and in the further downstream wake large structures are comparable with the energy levels of the surrounding turbulent flow.

Chapter 7

Role of HSV in fluid entrainment

The DC wake grows (thickens) much faster than the CC wake does (chapter 4). What controls the difference between the CC and the DC wakes in terms of wake growth rate? Does the presence of HSV's early in the DC wake somehow contribute to its enhanced growth rate? Figure 7.1 sketches a rather simplistic view of the cylinder wake growth from the customary lateral viewpoint. This lateral view is also relevant because, as an overall mean momentum budget would suggest, most of the momentum being transferred from the free stream region enters the CC/DC wake through its upper (and lower) interface. We have seen that the difference between the DC and the CC wake is not at the conceptual level: in both cases, the notion of the wake being a region with low mean velocity and high vorticity fluctuation levels holds. The difference between the two wakes is neither in their turbulence intensity: the velocity and vorticity fluctuation levels (at the $z = 0$ plane) in the DC and the CC wakes are comparable. The reason for the different wake growth rates between both wakes is due to the significant changes in the large-scale vortices induced in the near wake by the discontinuity in the cylinder geometry. In the DC near wake, the flow is three–dimensional ($\overline{\widetilde{w}}/U_0 \neq 0$) and dominated by the shed HSV and the strong shear–aligned vorticity in their legs. In the CC, the mean flow is initially almost two–dimensional ($\overline{\widetilde{w}}/U_0 = 0$) and controlled by the spanwise vorticity of the shed Kármán vortices with also the weaker vorticity associated to the ribs or legs of incipient hairpin vortices. A complete analogy between both wakes, on an average flow basis, would only hold when $z-$velocities are close to zero in the DC wake ($\overline{\widetilde{w}}(x, y, z)/U_0 \approx 0$), a situation only possible for large downstream distances. Notwithstanding, it should be noted that the dynamics of HSV in the DC wake will help to understand their role in wake growth and entrainment in both wake flows.

The mean velocity vectors and the mean vorticity components on vertical

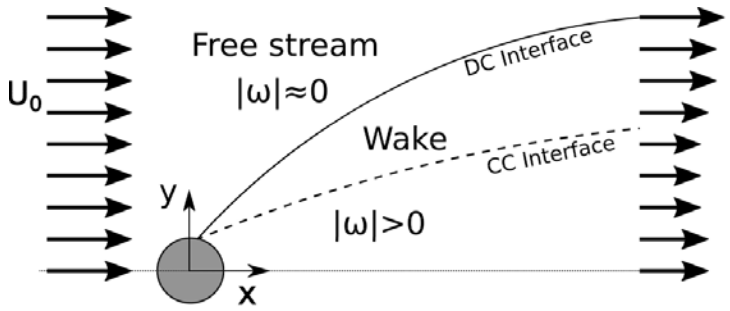

Figure 7.1: Sketch with a qualitative comparison of the growth rates in the DC and CC wakes.

$(y - z)$ plane at different downstream stations (figure 6.7) show the alignment of the legs of the HSV with the mean velocity field in the near wake $(x/D \leq 10)$. They also show that there is lateral momentum exchange from free-stream flow in the gap region between cylinder segments to the wake region, connected to the vertical momentum exchange by the head of the HSV ($z-$vorticity), as seen in figure 6.1a. Figures 7.2a and 7.2b respectively show the wake centerline profiles of the mean $w-$ and $u-$velocity components at several streamwise locations in the near wake $(x/D \leq 10)$. As is illustrated by the $\overline{\tilde{u}}$ contours in the $y - z$ plane at $x/D = 10$, shown in figure 7.2c, the entrained fluid being brought either from the free-stream flow or free-stream flow in the gap region between cylinder segments, possesses comparatively high momentum levels. The velocity vector plots in figures 6.7 and 7.2c also suggest that (on the average) near the mid-segment location $(z = 0)$ a portion of such high momentum entrained fluid is moving upwards/downwards. That is, the time-averaged field suggests that the cross-stream, lateral momentum transfer mechanism is contributing to the enhanced vertical spreading of the DC wake when compared to the CC wake. Or, in other words, the velocity vector plots, contours plots and centerline velocity profiles in figures 6.7 and 7.2 strongly suggest that the (mean) lateral momentum transfer of fluid contributes to the fast momentum recovery in the DC near wake. Moreover, the (mean) lateral fluid momentum transfer is probably also the cause that the peak in the $\overline{u}_d$ vertical profiles, shown in figure 4.4a, has moved away from the $y = 0$ centerline, i.e., the $\overline{u}_d$ vertical profiles are not Gaussian, for $x/D \geq 16$.

The kinking and subsequent (forward) slanting of the horseshoe vortices in the near DC wake $(x/D \leq 10)$ should be related, according to figure 6.7, to the lateral in-flow of fluid from the flow passing through the gap region $(|z|/D \geq 2.5)$. Further downstream $(x/D > 10)$, the lateral momentum ex-

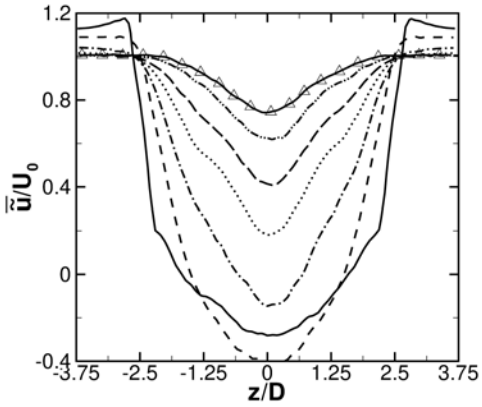

(a)

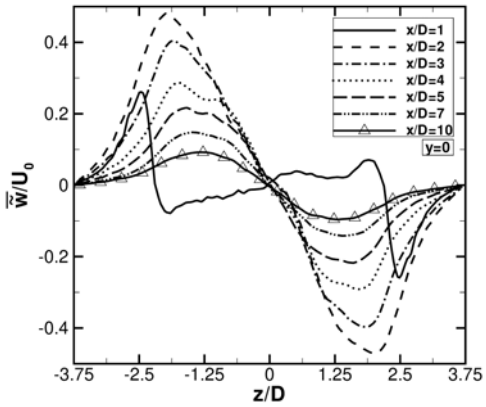

(b)

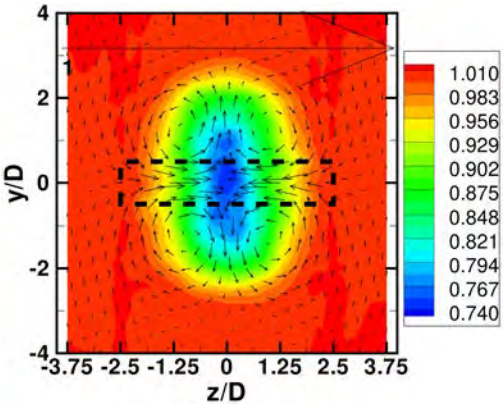

(c)

Figure 7.2: Selected $z-$profiles of (a) mean $w-$velocity and (b) mean $u-$velocity components at the DC near wake centerline ($y = 0$) and several streamwise locations, as indicated in the respective plot legends. In part (c), mean cross-stream velocity vectors $(\overline{\tilde{v}}, \overline{\tilde{w}})$ and mean $u-$velocity $(\overline{\tilde{u}})$ contours are plotted in the vertical plane with $x/D = 10$. All of the results in these plots were extracted from the LES calculation.

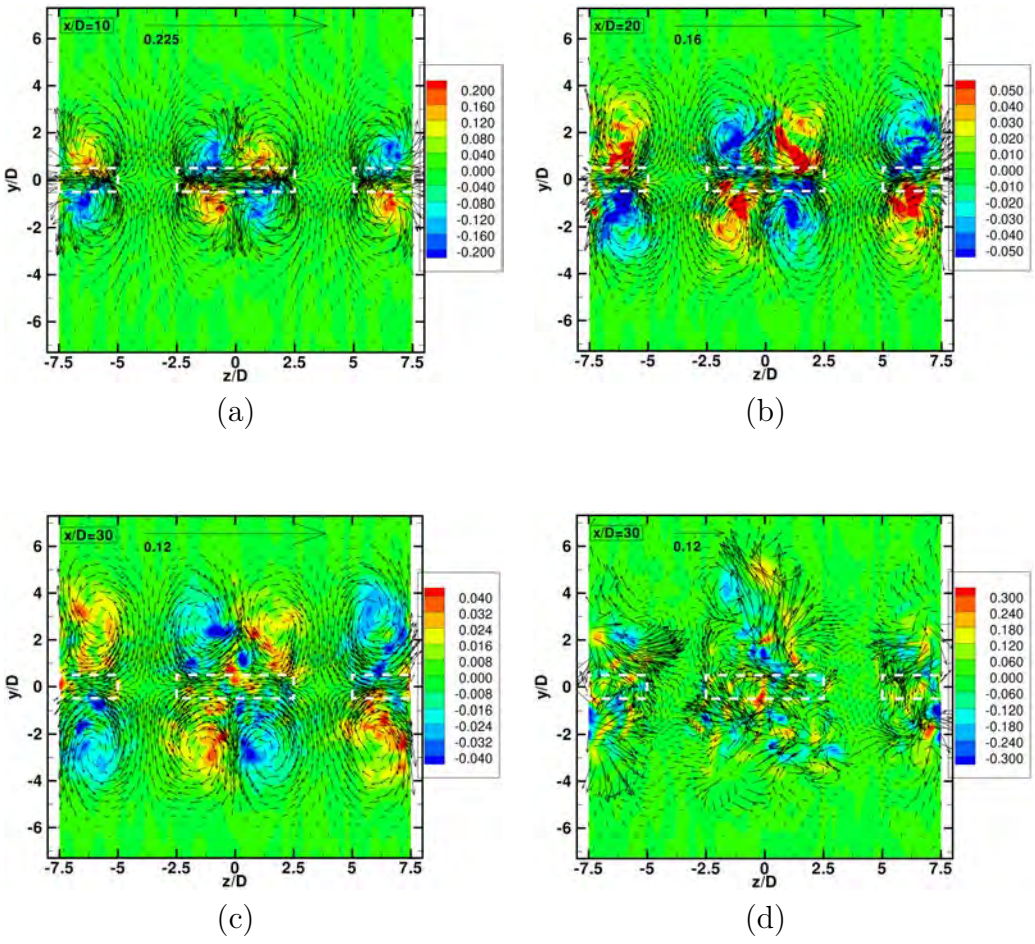

Figure 7.3: Distribution of mean velocity vector plots $(\overline{v}, \overline{w})$ and mean $x-$vorticity contours in the vertical $y-z$ planes at (a) $x/D = 10$, (b) $x/D = 20$, and (c) $x/D = 30$. Plot (d) shows the corresponding plots at $x/D = 30$ using an instantaneous field instead. The arrow and the accompanying number on the top of each plot show the fraction of the reference velocity, U_0, represented by the length of the arrow. The levels of the mean $x-$vorticity contours are different for each plot, as indicated in the respective boxes on the right side of the plot. All of the results were extracted from the LES of the DC wake.

change mechanism is still at work, as shown in figure 7.3a-c, where mean $x-$vorticity contours are plotted together with velocity vectors in the $y-z$ planes for $x/D = 10$, 20 and 30. An instantaneous field is also plotted for the latter $y-z$ plane in figure 7.3d for comparison purposes. As expected, the projection of an instantaneous flow field in figure 7.3d looks fully chaotic. Note that the maximum (absolute) instantaneous $x-$vorticity levels and velocity vector lengths are about 7-8 times larger than the corresponding values in the mean field plot (figure 7.3c). As the imprint left by HSV's on the mean velocity field is, however, a quite regular one (figures 7.3 a-c), we can say that HSV's behave as large-scale coherent flow structures in regard of their stamp in the mean and fluctuation flow statistics.

The vector plots in figure 7.3 also suggest that there is, on the average, some return of fluid (and thus momentum transfer) between the wake region (behind the cylinder segment, $|z/D| \leq 2.5$) and the (originally) free-stream flow through the gap region ($2.5 < |z/D| < 5$). We have seen in chapter 5 that there is basically less lateral spreading in the DC near wake ($x/D \leq 10$, see figures 5.2a-b). However, the plots in figure 7.3 strongly suggest that further downstream ($x/D > 10$), the gap region will be, to some extent, affected by relatively high turbulence intensity levels. Figure 7.4, where vertical profiles of u_{RMS}/U_0, obtained from HWA measurements, are plotted for several streamwise locations, supports such an assumption. In all these plots we can see that in the $z/D = 3.75$ profile the centerline ($y = 0$) values are clearly above the corresponding free-stream levels ($u_{RMS}/U_0 \approx 0.01$, as observed in the rightmost part of each profile). Moreover, as we move downstream the ratio between the centerline values of u_{RMS}/U_0 measured at $z = 0$ and at $z/D = 3.75$ clearly tends to one, to the point that in the far wake ($x/D = 170$, figure 7.4f) the u_{RMS} levels have already become roughly independent of the spanwise location. This is because the DRs or HSV forced in the near DC wake diffuse in the spanwise direction as they are advected downstream.

The results shown in figures 7.3 and 7.4 support the notion that in the DC mid–wake region ($x/D > 10$) the lateral fluid momentum exchange mechanism keeps contributing to the progressive stretching of HSV's and thus to the vertical growth of the DC wake as well.

Let us consider a simple scaling analysis to illustrate the effects on the three–dimensional mean flow associated with the shedding of HSV in the DC wake. The (mean) mass conservation requirement on a small control volume around the mid–span centerline, $(x, 0, 0)$ is

$$\frac{\partial \overline{\tilde{u}}}{\partial x}(x,0,0) = -\frac{\partial \overline{\tilde{w}}}{\partial z}(x,0,0) - \frac{\partial \overline{\tilde{v}}}{\partial y}(x,0,0) \qquad (7.1)$$

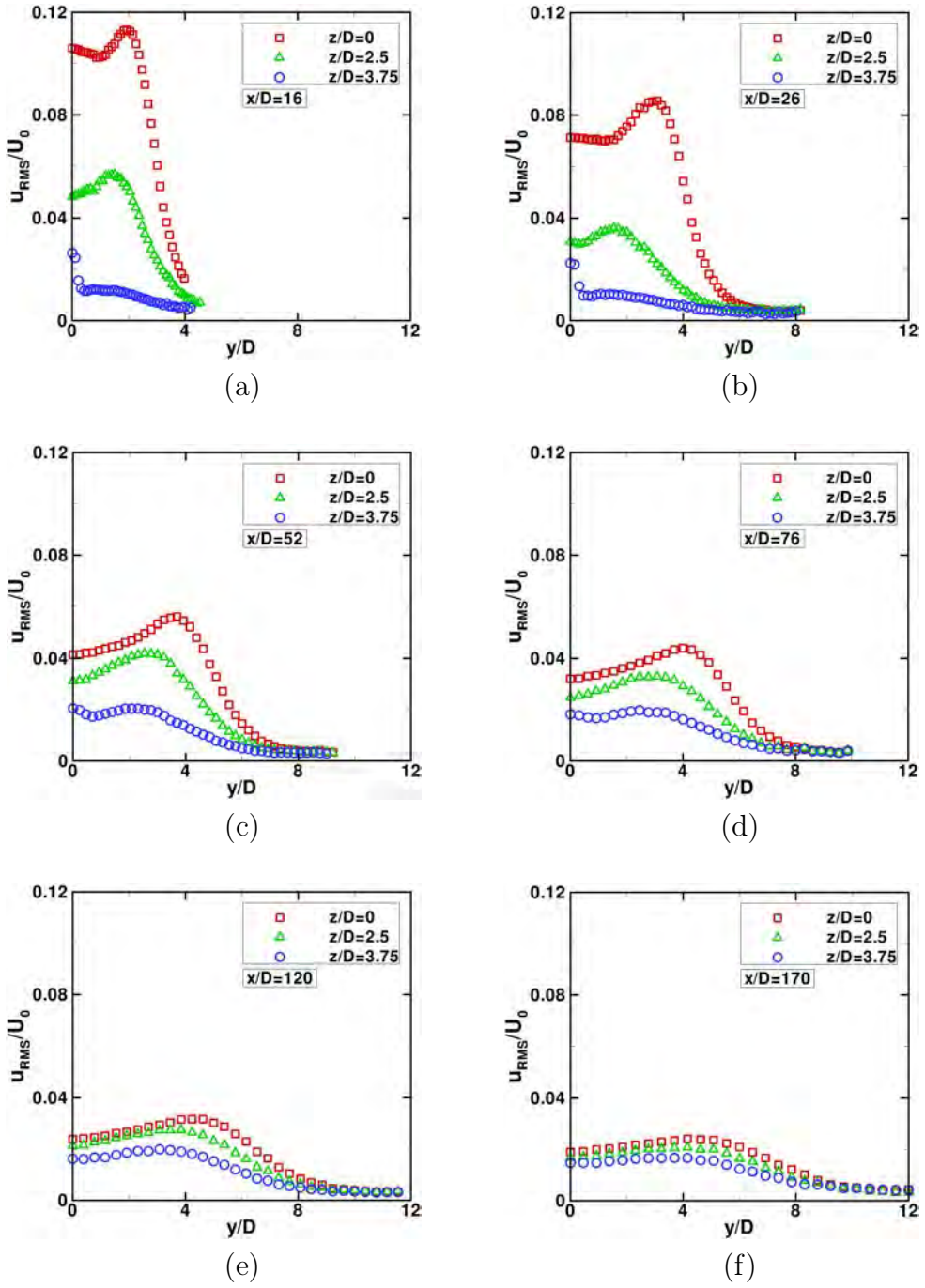

Figure 7.4: Comparison of vertical profiles of u-velocity fluctuations (u_{RMS}/U_0) at the spanwise locations z/D = 0, 2.5 and 3.75 and several downstream stations of the DC wake (the respective x/D values are indicated in the plot legend). All of the results in these plots were obtained from HWA measurements with model M_3 at a Reynolds number of $Re = 4.0 \times 10^3$.

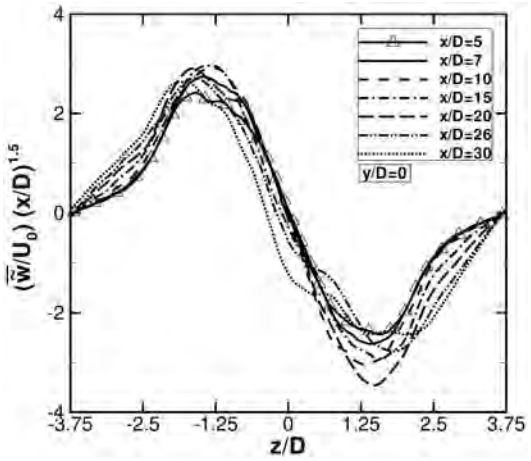

Figure 7.5: Selected spanwise profiles of normalized mean $z-$velocity, $(\overline{\tilde{w}}/U_0)(x/D)^{1.5}$, at the centerline ($y = 0$) and several streamwise locations in the DC wake, as indicated in the plot legend, from LES simulations.

If we consider that $\partial\overline{\tilde{w}}/\partial z \approx \Delta w/L$, Δw can be estimated as the total drop (from peak to peak) measured in a centerline $z-$profile (see figure 7.2a), and assume that the scaling $(\overline{u}_d/U_0) \approx (x/D)^{-0.5}$ (see subsection 4 and figure 4.1a) is approximately valid in the near DC wake, then (7.1) becomes

$$\frac{\partial\overline{\tilde{u}}}{\partial x}(x,0,0) = -\frac{\partial\overline{\tilde{u}}_d}{\partial x}(x,0,0) \approx \frac{1}{2}\left(\frac{U_0}{D}\right)\left(\frac{x}{D}\right)^{-1.5} \approx \frac{\Delta w(x)}{L} - \frac{\partial\overline{\tilde{v}}}{\partial y}(x,0,0) \tag{7.2}$$

If we assume that the inflow in the $y-$direction and toward the midplane $(x,0,0)$ that is induced at the front of each HSV by its top rotation, is approximately balanced by the outflow in the opposite $y-$direction and toward the external flow that occurs at the back of each HSV, then $\partial\overline{\tilde{v}}/\partial y \approx 0$ or smaller than $\partial\overline{\tilde{w}}/\partial z$ in absolute terms. If this is the case, $\partial\overline{\tilde{u}}/\partial x \approx -\partial\overline{\tilde{w}}/\partial z$, and all $\overline{\tilde{w}}$ profiles should scale as $(\overline{\tilde{w}}/U_0)(x/D)^{1.5}$.

Figure 7.5 depicts the centerline ($y = 0$) $z-$profiles of the dimensionless spanwise velocity $(\overline{\tilde{w}}/U_0)(x/D)^{1.5}$ at several streamwise locations. The profiles in this figure show that the proposed scaling for $\overline{\tilde{w}}$ holds in the DC wake for $x/D \leq 30$ in the spanwise direction. These results also show that the lateral fluid exchange mechanism and momentum transfer in the spanwise direction associated with the HSV, contribute significantly to the asymptotic increase with x/D of the average centerline velocity $\overline{\tilde{u}}(x,0,z)$ toward U_0. It should be noted that, as HSV are advected downstream and their spanwise and vertical locations are progressively randomized by turbulence, and as

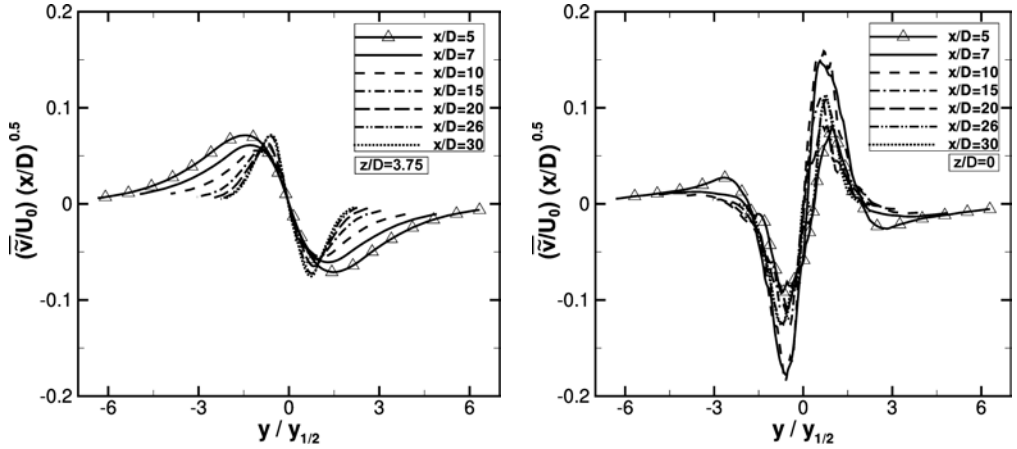

(a) (b)

Figure 7.6: Selected vertical profiles of the normalized mean $y-$velocity, $(\overline{\tilde{v}}/U_0)(x/D)^{0.5}$, at several streamwise locations in the DC wake at (a) the mid–gap spanwise location $(z/D = 3.75)$ and (b) the mid–segment spanwise location $(z = 0)$, from the LES simulations.

the mean spanwise velocity tends to zero, $\overline{\tilde{w}} \approx 0$, the role of $\partial\overline{\tilde{v}}/\partial y$ in DC wake growth and entrainment progressively becomes predominant. Simultaneously, the dominant contribution of the HSV to the total kinetic energy of the DC wake flow should also progressively diminish. The power spectral density of the streamwise velocity fluctuations (figure 6.9) indicates that this occurs for $x/D \geq 120$.

The implications of the above scaling analysis (figure 7.5) in the early DC wake development and growth by the large scale motions that are linked to the progressive stretching of HSV, can only be fully understood when analyzing the streamwise evolution of $\overline{\tilde{v}}$ profiles in the transverse direction at $z/D = 3.75$ and 0. Figure 7.6a shows that the transverse $\overline{\tilde{v}}$ profiles at the middle of the gap between cylinder segments $(z/D = 3.75)$ tend towards self-similarity as x/D increases, when scaled as $(\overline{\tilde{v}}/U_0)(x/D)^{0.5}$. According to (7.2), this can only be the case if $\overline{\tilde{w}} = 0$ and $\partial\overline{\tilde{w}}/\partial z = 0$, as is the case in figure 7.5, and the streamwise variations of $\overline{\tilde{u}}$ and $\overline{\tilde{v}}$ are solely caused by a net vertical inflow of fluid from the external, at both sides of the wake, towards the center plane. Since this is also the case for a fully developed CC wake, it justifies the current adoption of the scaling arising from the self-preservation analysis of the CC far wake (Tang et al. 2016 [73]), where $(\overline{\tilde{v}}/U_0) \propto (x/D)^{-0.5}$, with distances normalized with $y_{1/2}$. Results in figure 7.6a are consistent with the mean vertical motions portrayed in figure 7.3.

The vertical $\overline{\tilde{v}}$ profiles at the mid-segment ($z = 0$) spanwise locations shown in figure 7.6b also scale well with $(\overline{\tilde{v}}/U_0)(x/D)^{0.5}$ for $x/D \leq 30$. At this spanwise location the vertical fluid motion at the center of the HSV ($z/D = 0$) has to be outward, with $\partial\overline{\tilde{v}}(x,0,0)/\partial y > 0$, and opposite to that in figure 7.6a for $z/D = 3.75$, because HSV protrude vertically into the external flow to drive wake growth while stretched by the strain field, as reported by Kopp et al. 2002 [35] for a fully–developed CC turbulent wake. In this CC case, HSV were located inside turbulent bulges that protruded into the external flow and defined the intermittent turbulent/non turbulent wake interface.

Let us assume that such a scale for the mean vertical motion in the DC wake, say V_ω, is also proportional to the rate of vertical growth of the wake. Then if $\delta(x_0)$ is the thickness of the DC wake at a reference streamwise location x_0, we can infer the following scaling for the wake rate of growth,

$$\delta(x) - \delta(x_0) \;\approx\; V_\omega \,\triangle t \;\propto\; U_0 \left(\frac{x}{D}\right)^{-0.5} \left(\frac{x - x_0}{U_0}\right) \;\propto\; \left(x^{0.5} D^{-0.5}\right) \quad (7.3)$$

or, equivalently, a wake vertical growth according to $\triangle\delta(x)/D \propto (x/D)^{0.5}$. Note the consistency of this result with the $y_{1/2}/D \propto (x/D)^{0.5}$ behaviour observed in subsection 4 for the DC near-to-mid wake (see figure 4.2). The outward vertical motion of the HSV shown in figure 7.6b, together with the increase in the centerline streamwise velocity as x/D increases, must fulfil continuity and be matched by the vertical inward fluid motion of figure 7.6b, coupled with the spanwise motion towards the center of the HSV ($\partial\overline{\tilde{w}}/\partial z \ll 0$), as illustrated in figure 7.5 and discussed in detail below.

Figures 7.6a and 7.6b show, on a comparable ordinate scale, the evolution of the initial growth of the DC wake in terms of the transverse velocity at the spanwise side and at the center of the HSV, respectively. These streamwise evolutions of dimensionless vertical velocities, which are clearly related to momentum transfer into the wake from the external flow and to wake growth by HSV stretching, respectively, are dominated by the shedding of HSVs. These two figures show that both inward and outward transverse profiles progressively evolve towards self–similar profiles at both spanwise locations as x/D increases. Figure 7.6a shows that at $z/D = 3.75$ the recirculation associated to the shed HSV causes a reverse flow inward at the sides of each HSV, which is linked to the upward flow observed at their center ($z/D = 0$) in figure 7.6b. This recirculation pattern, which also involves the spanwise velocity component of figure 7.5, is initially dominated by the kinking of the shed HSVs caused by the flow from the gap between cylinder segments toward the back of each cylinder center. As a result, the highest vertical

velocities occur at the center of the HSV for $x/D < 10$, as observed in figure 7.6b. Further downstream, as x/D increases, vertical velocities and the wake growth shown in figures 4.1 and 4.2, become more and more controlled by the stretching of the HSV. This alignment and stretching by the strain field, makes the HSV to protrude toward the external flow, with vertical velocities progressively showing a self-similar behaviour for $x/D \geq 26$ in figure 7.6b. Thus, all vertical motions clearly associated with the HSV in the DC wake show self-similarity in figures 7.6a and 7.6b when scaled according to CC wake velocity and length reference parameters. This is also the case for the gradients of the vertical profiles at the center of the HSV in figure 7.6b, where $\partial\overline{\tilde{v}}/\partial y\ (x,0,0) \propto (U_0/D)(x)^{-1.6}$ for $x/D \leq 30$, which is very close to the -1.5 power variation that holds for fully developed turbulent CC wakes. Thus, the average fluid motions that are related wake growth and entrainment by the HSV in the DC near wake scale as in the CC wake, where large-scale structures like the current HSV have been identified and claimed to play a dominant role in wake growth and entrainment.

The smooth and self-equilibrating evolution towards self-similarity and self-preservation in the DC wake flow shown in figure 7.6, which is controlled by shed HSV, from genesis to self-preservation, is consistent with the streamwise variations of the maximum mean velocity-defect and of $y_{1/2}/D$ shown in figures 4.1 and 4.2, respectively, for the DC wake. The same behaviour towards self-similarly and wake growth mechanism associated with donut-like vortices or double rollers was also reported by Vernet et al. 1999a [27] and Kopp et al. 2002 [35], respectively, in CC turbulent wakes, but for much larger streamwise distances. In the CC case, the large-scale coherent motions that develop from the hairpin vortices arising from instabilities in the VKV street (Cao et al. 2014 [79], McClure et al. 2019 [12]), require much larger advection times or streamwise distances to develop and become shear aligned, i.e., $\partial\overline{\tilde{v}}/\partial y\ (x,0,0) \propto (U_0/D)(x)^{-1.5}$. The vertical profiles at the mid-gap ($z/D = 3.75$) and mid-segment ($z = 0$) spanwise locations, shown in figure 7.6, together with the scaling of (7.3), confirm that the DC geometry brings into the near wake, not only the HSV, but also another characteristic feature of the far CC wake, i.e., the self-preservation of the mean velocity profiles.

The incorporation of high momentum free-stream fluid by the linked lateral-vertical entrainment process, depicted in figures 6.1b, and 6.3a, and 7.3, which is governed by HSV, implies the extraction of energy from the mean flow and the persistence of turbulence in the wake. Mean shear production contours calculated from PIV data measured in the DC indicate that the highest production rates occur at $y_{1/2}$ and at the center of the HSV for $x/D \geq 5$, as shown in figure C.4 in Appendix C. This is consistent with

the momentum transfer associated with the donut-like structures reported by Vernet et al. 1999a [27] in a CC wake at $x/D = 150$, and with the role in the entrainment process that has been claimed for the DR identified in the far wake of a CC by Kopp et al. 2002 [35]. When this entrainment process is completely established in the wake of the DC at approximately $x/D = 50$, i.e., when the wake grows with $(x/D)^{0.5}$, as shown in figure 4.2, and $\partial\overline{\tilde{v}}/\partial y\ (x, 0, 0) \propto (U_0/D)(x)^{-1.5}$, HSV should be shear aligned, optimally stretched, and scalable according to (7.2) and figure 7.6. The CC wake also grows with $(x/D)^{0.5}$, as shown in figure 4.2. Note that turbulent bulges and the corresponding large-scale motions or DR in both the DC and CC wakes (Kopp et al. 2002 [35]) are in a region where high momentum free stream fluid can be entrained, as shown for the DC in figures 6.1, 6.2, 6.3, 6.7 and 7.3. Current findings also confirm that the entrainment process is the result of linked lateral rotating motions and vertical outward jet-like motions and the rear of the DR. The overall process is strongly dominated by the stretching of the shear aligned vortex legs, i.e., by lateral entraining motions and inward motions at the front of the HSV, that in turn generate the outward jet-like motions responsible for wake growth. Turbulent diffusion seems to play a secondary role in the entrainment process but necessary one in the energy cascade and dissipative nature of the turbulent wake flow.

Chapter 8

Final remarks

A study of the existing literature indicates that there is a lack of agreement regarding the mechanism of entrainment in TNTI in free flows, with various studies finding differences in the relative importance of the nibbling and engulfment mechanisms. This suggests a significant flow dependence and that by controlling the development of large-scale structures, one can control the extent to which each of these mechanisms contribute to the overall entrainment rate. The hypothesis motivating this study is that enhancing vortices that are aligned with the mean shear will increase the rate of entrainment based on observations of flow structure and entrainment in the self-preserving regions of far wakes. We test this hypothesis by modifying the formation of the vortices in the near wake of a circular cylinder such that shear-aligned horseshoe vortices are formed early in the wake. We contrast this with growth and spread of the circular cylinder wake, which is controlled by the von Kármán vortex street in the near wake. To achieve this, we develop and examine what we call a discontinuous cylinder wake.

The turbulent flow in the wake of the DC was investigated both experimentally and numerically to ascertain the nature of large-scale flow patterns and how these alter the overall growth and spread of the wake. We ensemble-averaged the instantaneous PIV data to determine the wake characteristics such as mean streamwise velocity, mean transverse velocity, mean Reynolds shear stress, and mean spanwise vorticity patterns on the measurement planes of the DC and CC wakes. The mean streamwise velocity of the DC wake was compared with the corresponding result of the CC wake and found that the wake bubble behind the cylinder segments of the DC is significantly longer than that for the CC, i. e., the wake formation length is longer. This delay in shedding may be related to the converging streamlines in the wake from the ends of the cylinder segment due to the inflow of high momentum fluid through the gaps. It also showed that the velocity-defect is larger in the near

wake of the DC, but it recovers very quickly; at $x/D = 10$, the velocity-defect in the DC wake was almost the same as that in the CC wake. The mean streamwise velocity field also hints that the DC wake width is much wider than that of the CC wake. The instantaneous vector plots on $x - z$ plane depict the presence of DRs in the DC wake while the instantaneous iso-surfaces of pressure confirmed the generation of DRs or HSV's early in the near wake ($x/D \leq 10$) of the DC. The dominant flow structures in the DC wake are shown to be quasi-periodic, three-dimensional horseshoe vortices, which are fully formed by about $x/D \approx 3$. This structure contrasts with the periodic quasi-two-dimensional von Kármán vortices in the near wake of the CC. Following the vortex formation region of both wakes, the DC wake grows at faster rate than the CC wake, although the rate of initial development of the quasi-two-dimensional Kármán vortices is significantly higher within $x/D <\approx 3$. However, the Kármán vortices decay quickly because of the lack of shear alignment whereas the HSV then develop a high rate over a significantly longer spanwise distance. So, while the wakes have approximately the same thickness at $x/D = 4$, the DC wake is substantially wider by $x/D \approx 8$ and maintains a higher growth rate until about $x/D \approx 50$. Further downstream, beyond $x/D \approx 50$, the wakes grow at the same rates, consistent with the two-dimensional self-preserving solution. However, the DC wake is significantly wider, such that, at $x/D = 50$, the mean velocity half width is almost 3 times larger than that for the CC at the same physical location. At this same point, the maximum velocity defect for the DC is about half that for the CC even though the maximum velocity defect is significantly greater in the cylinder base region. The velocity-defect at $x/D = 50$ in the DC wake was similar to the velocity-defect in the CC wake at around $x/D = 127$. These results indicate a much greater entrainment rate for the discontinuous cylinder with fully formed horseshoe vortices in the near wake region, where flow already approaches self-preservation, but with a rate that is higher than in the fully developed far wake region. A simple scaling analysis indicates that the lateral entraining motions and the vertical stretching of the HSV can explain the growth rate of the DC wake. The spectra of the velocity data, which were measured using hot-wire anemometry, showed that the non-dimensional shedding frequency (Strouhal number) of the DR or HSV's in the DC wake was 0.137.

Since the kinetic energy associated with the fluctuations of the near-wake, which are originated by the DRs or HSV structures, is high, the flow system was suitable to clarify the role of these velocity patterns in the entrainment process of wake flows. The rotation associated with the $z-$vorticity at the top of the HSV entrains fluid towards the horizontal centerline plane ($y = 0$). The mean velocity vectors together with the mean streamwise vorticity

component showed that the shape of mean HSV was consistent with the mean flow pattern on $y-z$ plane in the DC wake. The counterrotating motion of the two legs of the HSV entrain fluid laterally from the free stream flow in the gap region between the cylinder segments and, together with the inflow at front of the HSV, forms a jet-like upstream motion at their back and towards the top/bottom edge of the wake. The high energy upstream jet motion in turn contributes to the vortex stretching and eventually to the vertical growth of the wake. The mean and instantaneous velocity and vorticity results showed that the entrainment process is the result of linked lateral rotating motions and vertical outward jet-like motions and the rear of the DR. The overall process, the increase in the wake spreading and momentum transfer rates observed in the DC wake, was caused, and dominated by the presence of highly stretched DR or HSV's, which originated early in the near wake with high energy levels. When the entrainment cycle is completely established in the wake of the DC at approximately $x/D = 50$, i.e., when HSV progressively become randomized, shear aligned and optimally stretched, the wake grows with $(x/D)^{0.5}$, which is consistent with the role in the entrainment process that has been claimed for the DR identified in the far wake of a CC. The DC wake is far from being uniform in the spanwise direction close to the origin, but becomes fully 2-D in the mean at $x/D = 170$, i.e., no variation of mean values in the spanwise direction, when the passage of HSVs becomes completely randomized by turbulence, a process that is already noticiable at $x/D = 50$.

Current results, together with the evidence reported by Ferré et al. 1989a [10] that more than 50% of velocity signals recorded in a fully developed turbulent CC wake showed the random occurrence of shear aligned large scale vortical structures, i.e., shear aligned and stretched HSV or double rollers, lead to the conclusion that entrainment of non-turbulent external fluid into the wake is dominated by large-scales. Wake growth in both the CC and DC turbulent wakes is dominated by the shear aligned jet motions that protrudes outwards into the free stream at the back of the stretched horseshoe-like vortices or double rollers. These mixing jet outward motions that dominate wake growth are coupled with a vertical inflow of fluid from the free stream into the wake at the front of each vortical structure, and a lateral fluid intake due to the rotation of the stretched double rollers, both causing and enhancing a direct transfer of momentum from the free flow. The intermittently entrained free stream fluid into wake makes fully actionable nibbling and smaller scale transfer mechanisms across the wake, completing the energy cascade from large, and in this case coherent large scales, to the smallest dissipative scales of the turbulent flow.

The current findings have several implications beyond the possible devel-

opment of engineering tools to increase (or suppress) turbulent mixing rates. First, with respect to self-preserving flows, it is well known that the virtual origin of self-preserving plane turbulent wakes is variable for different bluff bodies or for similar bluff bodies but in different laboratory settings. The implication from the current work is that enhancing shear-aligned vorticity in the initial conditions should decrease the position of the virtual origin, i.e., enhancing wake thickness and reducing velocity defect. Modifying the values of L/D and S/D for the DC would do this, as could other geometric (including variable cylinder diameters along the span) or flow discontinuities for circular cylinders. Second, for other turbulent shear flows, enhancing shear aligned vorticity should have similar effects. This would include plane turbulent jets and plane mixing layers, which, like plane turbulent wakes, tend to have primary instabilities which induce the formation of vortices that are orthogonal to the mean shear. This could also include the effects of trips for the transition of turbulent boundary layers. However, examination of such details remains for future work.

Bibliography

[1] Karman, V. & Rubach, H. 1912 Über den mechanismus des Flüssigkeits- und Luftwiderstandes. *Phys. Zeitschrift XIII.*

[2] Taylor, G. J. 1915 Pressure distribution around a cylinder. *Techn. Rep. Adv.Com. for Aeronamities.*

[3] Gerrard, J. H. 1967 Experimental investigation of separated boundary layer undergoing transition to turbulence. *Phys. fluids, 10, S98-100.*

[4] Roshko, A. & Fiszdon, W. 1969 On the persistence of transition in the near wake. *SIAM, Problems of Hydrodynamics and Continuum Mechanics, 606-616.*

[5] Zdravkovich, M. M. 1990 Conceptual overview of laminar and turbulent flows past smooth and rough cylinders. *Journal of Wind Engineering and Industrial Aerodynamics, 33, 53-62.*

[6] Williamson, C. H. K. 1996 Vortex dynamics in a cylinder wake. *Annual Review of Fluid Mechanics, 28, 477-539.*

[7] Norberg, C. 2003 Fluctuating lift on a circular cylinder: review and new measurements. *J. Fluids Struct., 17, 57-96.*

[8] Cantwell, B. & Coles, D. 1983 An experimental study of entrainment and transport in the turbulent near wake of a circular cylinder. *J. Fluid Mech., 136, 321-374.*

[9] Hayakawa, M. & Hussain, F. 1989 Three-dimensionality of organized structures in a plane turbulent wake. *J. Fluid Mech., 206, 375-404.*

[10] Ferré, J. A. & Giralt, F. 1989a Pattern-recognition analysis of the velocity field in plane turbulent wakes. *J. Fluid Mech., 198, 27-64.*

[11] Yamane, R., Oshima, S., Okubo, M. & Kotani, J. 1988 Coherent structures in the turbulent wake behind a circular cylinder 3. Flow visualization and hot wire measurements. *Fluid Dynamics Research, 4, 47-56.*

[12] McClure, J., Pavan, C. & Yarusevych, S. 2019 Secondary vortex dynamics in the cylinder wake during laminar-to-turbulent transition. *Phys. Rev. Fluids 4, 124702.*

[13] Theodorsen, T. 1952 Mechanism of turbulence. *In Proc. 2nd Midwestern Conf. Fluid Mech., Ohio State Univ., Columbus.*

[14] Townsend, A. A. 1956 The Structure of Turbulent Shear Flow. *1st edition, Cambridge University Press.*

[15] Grant, H. L. 1958 The large eddies of turbulent motion. *J. Fluid Mech., 4, 149-190.*

[16] Payne F. R. & Lumley, J. L. 1967 Large eddy structure of the turbulent wake behind a circular cylinder. *Phys. Fluids, 10, S194-S196.*

[17] Lumley, J. L. 1965 Theoretical aspects of research on turbulence in stratified flows. *Proc. Intl. Colloq. On Atmospheric Turb. and Radio Wave Propagation, ed. A. M. Yaglom and V. I. Tatarsky, Moscow, 121-128.*

[18] Keffer, J. F. 1965 The uniform distortion of a turbulent wake, J. Fluid Mech., 22, 135-159.

[19] Keffer, J. F. 1967 A note on the expansion of turbulent wakes. *J. Fluid Mech., 28, 183-193.*

[20] LaRue, J. C. & Libby, P. A. 1974 Temperature and intermittency in the turbulent wake of a heated cylinder. *Phys. Fluids, 17(5), 873-878.*

[21] Mumford, J. C. 1983 The structure of the large eddies in fully developed turbulent shear flows. Part 2. The plane wake. *J. Fluid Mech., 137, 447-456.*

[22] Ferré, J. A. & Giralt, F. 1989b Some topological features of the entrainment process in a heated turbulent wake. *J. Fluid Mech., 198, 65-78.*

[23] Ferré, J. A., Mumford, J. C., Savill, A. M. & Giralt, F. 1990 Three-dimensional large-eddy motions and fine-scale activity in a plane turbulent wake. *J. Fluid Mech., 210, 371-414.*

[24] Kopp, G. A., Kawall, J. G. & Keffer, J. F. 1995 The evolution of the coherent structures in a uniformly distorted plane turbulent wake. *J. Fluid Mech., 291, 299-322.*

[25] Giralt, F. & Ferré, J. A. 1993 Structure and flow patterns in turbulent wakes. *Phys. fluids, A5, 1783-1789.*

[26] Vernet, A., Kopp, G. A., Ferré, J. A. & Giralt, F 1997 Simultaneous velocity and temperature patterns in the far region of a turbulent cylinder wake. *Journal of Fluids Engineering, 119, 463-466.*

[27] Vernet, A., Kopp, G. A., Ferré, J. A. & Giralt, F. 1999a Three-dimensional structure and momentum transfer in a turbulent cylinder wake. *J. Fluid Mech., 394, 303-337.*

[28] Philip, J. & Marusic, I. 2012 Large-scale eddies and their role in entrainment in turbulent jets and wakes. *Phys. Fluids, 24, 055108.*

[29] Marusic, I. & Adrian, R. A. 2013 The eddies and scales of wall turbulence. *Ten Chapters in Turbulence, edited by Davidson, P. A., Kaneda, Y. and Sreenivasan K. R. (Cambridge University Press).*

[30] Chevray, R. 1982 Entrainment interface in free turbulent shear flows. *Prog. Energy Combust Sci, 8, 303-315.*

[31] Bisset, D. K., Hunt, J. C. R. & Rogers, M. M. 2002 The turbulent/non-turbulent interface bounding a far wake. *J. Fluid Mech., 451, 383-410.*

[32] Hunt, J. C. R., Eames, I. & Westerweel, J. 2006 Mechanics of inhomogeneous turbulence and interfacial layers. *J. Fluid Mech., 554, 499-519.*

[33] Corrsin, S. & Kistler, A. L. 1955 Free-stream boundaries of turbulent flows. *Technical report TN-1244, NACA, Washington, DC.*

[34] Townsend, A. A. 1976 The Structure of Turbulent Shear Flow. *2nd edition, Cambridge University Press.*

[35] Kopp, G. A., Giralt, F. & Keffer, J. F. 2002 Entrainment vortices and interfacial intermittent turbulent bulges in a plane turbulent wake. *J. Fluid Mech., 469, 49-70.*

[36] Mathew, J. & Basu, A. J. 2002 Some characteristics of entrainment at a cylindrical turbulence boundary. *Phys. Fluids, 14, 2065-2072.*

[37] Westerweel, J., Fukushima, C., Pedersen, J. M. & Hunt, J. C. R. 2005 Mechanics of the turbulent and non-turbulent interface of a jet. *Physical Review Letters, 17, 174501.*

[38] Da Silva, C. B., & Pereira, J. C. F. 2008 Invariants of the velocity-gradient, rate-of-strain, and rate-of-rotation tensors across the turbulent/nonturbulent interface in jets. *Phys. Fluids, 20, 055101.*

[39] Westerweel, J., Fukushima, C., Pedersen, J. M. & Hunt, J. C. R. 2009 Momentum and scalar transport at the turbulent/non-turbulent interface of a jet. *J. Fluid Mech, 631, 199-230.*

[40] Chauhan, K., Philip, J., de Silva, C., Hutchins, N. & Marusic, I. 2014 The turbulent/non-turbulent interface and entrainment in a boundary layer. *J. Fluid Mech., 742, 119-151.*

[41] Philip, J., Meneveau, C., De Silva, C. M. & Marusic, I. 2014 Multiscale analysis of fluxes at the turbulent/non-turbulent interface in high Reynolds number boundary layers. *Phys. Fluids, 26, 015105.*

[42] Brown, G. L. & Roshko, A. 1974 On density effects and large structure in turbulent mixing layers. *J. Fluid Mech., 64, 775-816.*

[43] Dahm, W. J. A. & Dimotakis, P. E. 1987 Measurements of entrainment and mixing in turbulent jets. *AIAA J., 25, 1216-1223.*

[44] Holzner, M., Liberzon, A., Nikitin, N., Kinzelbach, W. & Tsinober, A. 2007 Small-scale aspects of flows in proximity of the turbulent/nonturbulent interface. *Phys. Fluids, 19, 071702.*

[45] Hunt, J. C. R., Eames, I., Da Silva, C. B. & Westerweel, J. 2011 Interfaces and inhomogeneous turbulence. *Philos. Trans. R. Soc. London, Ser. A., 369, 811-832.*

[46] Zdravkovich, M. M., Brand, V. P., Mathew, G. & Weston, A. 1989 Flow past short circular cylinders with two free ends. *J. Fluid Mech. 203, 557-575.*

[47] Norberg, C. 1994 An experimental investigation of the flow around a circular-cylinder - influence of aspect ratio. *J. Fluids Mech. 258, 287-316.*

[48] Zdravkovich, M. M., Flaherty, A. J., Pahle, M. G. & Skelhorne, I. A. 1998 Some aerodynamic aspects of coin-like cylinders. *J. Fluid Mech. 360, 73-84.*

[49] Inoue, O. & Sakuragi, A. 2008 Vortex shedding from a circular cylinder of finite length at low reynolds numbers. *Phys. Fluids 20, 033601.*

[50] Mandava, V. S. R., Kopp, G. A., Herrero, J. & Giralt, F. 2009 Experimental investigation of the wake behind a discontinuous cylinder. *Sixth International Symposium on Turbulence and Shear Flow Phenomena, ed. N. Kasagi, F. Rainer, J. A. C. Humphrey and H. J. Sung, Seoul vol. 3 pp. 1089-1094.*

[51] Bailey, S. C. C., Martinuzzi, R. J. & Kopp, G. A. 2002 The effects of wall proximity on vortex shedding from a square cylinder: Three-dimensional effects. *Phys. Fluids, 14(12), 4160-4177.*

[52] Martinuzzi, R. J., Bailey, S. C. C. & Kopp, G. A. 2003 Influence of wall proximity on vortex shedding from a square cylinder. *Experiments in Fluids, 34, 585-596.*

[53] Dol, S. S., Kopp, G. A. & Martinuzzi, R. J. 2008 The suppression of periodic vortex shedding from a rotating circular cylinder. *Journal of Wind Engineering and Industrial Aerodynamics, 96, 1164-1184.*

[54] Taylor, Z. J., Palombi, E., Gurka, R. & Kopp, G. A. 2011 Features of the turbulent flow around symmetric elongated bluff bodies. *Journal of Fluids and Structures, 27, 250-265.*

[55] Dimotakis, P. E. 2000 The mixing transition in turbulent flows. *J. Fluid Mech., 409, 69-98.*

[56] King, L. V. 1914 On the convection of heat from small cylinders in a stream of fluid: Determination of the convection constants of small platinum wires, with applications to hot-wire anemometry. *Proc. Royal Soc. A 90, 563-570.*

[57] Smagorinsky, J. 1963 General cirulation experiments with the primitive equations: I. The basic equations. *Mon. Weather Rev., 91, 99-164.*

[58] Germano, M., Piomelli, U., Moin, P. & Cabot, W. H. 1991 A dynamic subgrid-scale eddy viscosity model. *Phys. fluids, A3(7), 1760-1765.*

[59] Lilly, D. k. 1992 A proposed modification of the Germano subgrid-scale closure method. *Phys. Fluids A, 4(3), 633-635.*

[60] Sagaut, P. 2001 Large-eddy Simulation for Incompressible Flows, An Introduction. *Springer-Verlag, Berlin.*

[61] Werner, H. & Wengle, H. 1993 Large-eddy simulation of turbulent flow over and around a cube in a plate channel. *Selected Papers from the Eighth International Symposium on Turbulent Shear Flows, Munich, Germany, September 9-11, 1991. In Turbulent Shear Flows , vol. 8, F. Durst et al. (eds.). Springer-Verlag, Germany.*

[62] Mahesh, K., Constantinescu, G. & Moin, P. 2004 A numerical method for large-eddy simulation in complex geometries. *J. Comput. Phys., 197, 215-240.*

[63] Rhie, C. M. & Chow, W. L. 1983 A numerical study of the turbulent flow past an isolated airfoil with trailing edge separation. *AIAA J., 21, 1525-1532.*

[64] Hairer, E. & Wanner, G. 1996 Solving Ordinary Differential Equations II. Stiff and Differential-Algebraic Problems. *2nd. ed., Springer Series in Computational Mathematics, Springer-Verlag, Berlin, Germany.*

[65] Dong, S., Karniadakis, G. E., Ekmekci, A. & Rockwell, D. 2006 A combined direct numerical simulation-particle image velocimetry study of the turbulent near wake. *J. Fluid Mech., 569, 185-207.*

[66] Louchez, P. R., Kawall, J. G. & Keffer, J. F. 1987 Investigation of the detailed spread characteristics of plane turbulent wakes. *Turbulent shear flows 5, edited by Bradbury, L. J. S., Durst, F., Launder, B. E., Schmidt, F. W and Whitelaw, J. H. (Springer-Verlag, Berlin), 98.*

[67] Norberg, C. 1998 LDV-measurements in the near wake of a circular cylinder. *Advances in understanding of bluff body wakes and vortex induced vibrations, Washington DC, June 1998.*

[68] Afgan, I., Kahil, Y., Benhamadouche, S. & Sagaut, P. 2011 Large eddy simulations of the flow around single and two sis-by-side cylinders at subcritical Reynolds numbers. *Phys. Fluids, 23, 075101.*

[69] Ong, L. & Wallace, J. 1996 The velocity field of the turbulent very near wake of a circular cylinder. *Experiments in Fluids 20, 441-453.*

[70] Ma, X., Karamanos, G. S. & Karniadakis, G. E. 2000 Dynamics and low-dimensionality of a turbulent near wake. *J. Fluid Mech. 410, 29-65.*

[71] Diaz, F., Gavalda, J., Kawall, J. G., Keffer, J. F. & Giralt, F. 1985 Asymmetrical wake generated by a spinning cylinder. *AIAA J., 23, 49-54.*

[72] Vernet, A. 1999b *Private communication.*

[73] Tang, S. L., Antonia, R. A., Djenidi, L. & Zhou, Y. 2016 Complete self-preservation along the axis of a circular cylinder far wake. *J. Fluid Mech., 786, 253-274.*

[74] Holzner, M., Liberzon, A., Guala, M., Tsinober, A. & Kinzelbach, W. 2006 Generalized detection of a turbulent front generated by an oscillating grid. *Exp. Fluids, 41, 711-719.*

[75] Anand, R. K., Boersma, B. J. & Agrawal, A. 2009 Detection of turbulent/non-turbulent interface for an axisymmetric turbulent jet: evaluation of known criteria and proposal of a new criterion. *Exp. Fluids, 48, 995-1007.*

[76] Hedley, T. B. & Keffer, J. F. 1974 Turbulent/non-turbulent decisions in an intermittent flow. *J. Fluid Mech., 64, 625-644.*

[77] LaRue, J. C. & Libby, P. A. 1976 Statistical properties of the interface in the turbulent wake of a heated cylinder. *Phys. Fluids, 19(12), 1864-1875.*

[78] Tabatabai, M., Kawall, J. & Keffer, J. F. 1989 Choice of the threshold in a velocity based conditional sampling procedure. *Phys. Fluids A, 1, 307-311.*

[79] Cao, H. L., Chen, J. G., Zhou, T., Antonia, R. A. & Zhou, Y. 2014 Three-dimensional momentum and heat transport in a turbulent cylinder wake. 19th Australasian Fluid Mechanics Conference, Melbourne, Australia, 8-11 December.

Appendix A

New algorithm to generate grid in the gap region between the cylinder segments

New algorithm was developed to generate the quadrilateral cells in '2B' region. This new algorithm develops the quadrilateral cells almost similar in size. The inputs to this algorithm are the total number of nodes (N) on the outer surface and their (x, y) co-ordinates. Based on the distance between the two successive points on the outer surface/layer, and to keep the quadrilateral cells more squarer than rectangular, it establishes equally spaced N/8 layers in the circular region, and it also generates nodes on each layer in such a way that the number of nodes on the first layer, which is closest to the centre of the circle, are eight, and then it increases the number of nodes from layer 2 to $N/8$ in a way that the number of nodes on each layer are eight more than its inner layer. By making the number of nodes on each layer and the radius change in arithmetic progression, the edges of the cells would be about the same size.

The co-ordinates of node points on each layer are calculated as

$$x = A_l \; cos(\alpha) \tag{A.1}$$

$$y = A_l \; sin(\alpha) \tag{A.2}$$

where α is varied from layer to layer and is taken as the equally spaced angle, e.g., in the first inner layer there are 8 grid points and the α would be 45^o, and in the second layer α would be 22.5^o as there are 16 points in the layer, and so on. A_l is such that

$$x^{E_l} + y^{E_l} = R_l^{E_l} \tag{A.3}$$

where R_l is different from layer to the layer and it is the distance on $x-$axis from centre to the layer, and it varies from 0 to the radius of the circle. E_l varies in arithmetic progression from 3 to 2 from inner layer to the out layer, respectively, and by making the exponent varies from 3 to 2, it generates layers, from inner layer to the outer layer, with gradual change from square-like to circular layers, because $x^3 + y^3 = R_l^3$ is more squared than the circle with $x^2 + y^2 = R_l^2$.

If N is not multiple of eight, it will adjust the number of nodes in the last two layers, which are close to the outer layer.

Appendix B

Vortex realignment in the DC near wake

The vorticity equation, which is the curl of the Navier-Stokes equations, can be written in index notation form as below

$$\frac{D\omega_i}{Dt} = \underbrace{\omega_j \frac{\partial u_i}{\partial x_j}}_{\text{Vortex tilting \& stretching}} + \underbrace{\nu \frac{\partial^2 \omega_i}{\partial x_j \, \partial x_j}}_{\text{Diffusion}} \tag{B.1}$$

The three components of vorticity equation, mainly focusing on vortex tilting and stretching terms, are

$$\frac{D\omega_x}{Dt} = \underbrace{\omega_x \frac{\partial u}{\partial x}}_{\text{Vortex stretching}} + \underbrace{\omega_y \frac{\partial u}{\partial y}}_{\text{Vortex tilting}} + \underbrace{\omega_z \frac{\partial u}{\partial z}}_{\text{Vortex tilting}} + Diffusion$$

$$\frac{D\omega_y}{Dt} = \underbrace{\omega_x \frac{\partial v}{\partial x}}_{\text{Vortex tilting}} + \underbrace{\omega_y \frac{\partial v}{\partial y}}_{\text{Vortex stretching}} + \underbrace{\omega_z \frac{\partial v}{\partial z}}_{\text{Vortex tilting}} + Diffusion \tag{B.2}$$

$$\frac{D\omega_z}{Dt} = \underbrace{\omega_x \frac{\partial w}{\partial x}}_{\text{Vortex tilting}} + \underbrace{\omega_y \frac{\partial w}{\partial y}}_{\text{Vortex tilting}} + \underbrace{\omega_z \frac{\partial w}{\partial z}}_{\text{Vortex stretching}} + Diffusion$$

The large scale structures in the DC wake are double roller (DR) or horse-shoe vortices (HSV) and figure 6.5 shows the three-dimensional view of three

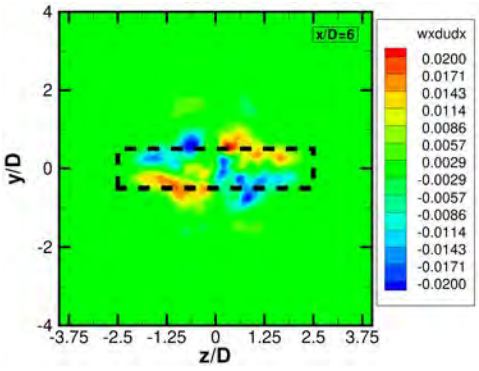

(a)

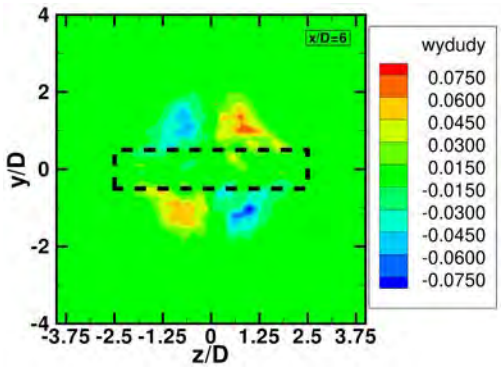

(b)

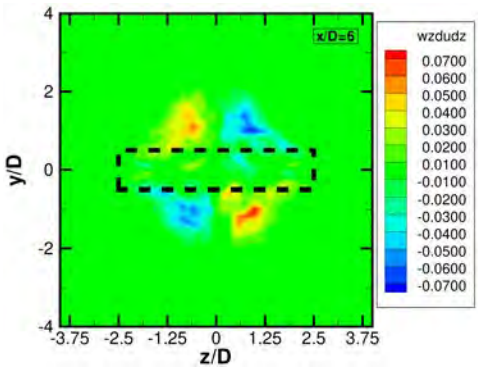

(c)

Figure B.1: Contours of mean stretching and tilting terms in $x-$vorticity equation (a) $\overline{\widetilde{\omega}}_x \frac{\partial \overline{\widetilde{u}}}{\partial x}$, (b) $\overline{\widetilde{\omega}}_y \frac{\partial \overline{\widetilde{u}}}{\partial y}$, and (c) $\overline{\widetilde{\omega}}_z \frac{\partial \overline{\widetilde{u}}}{\partial z}$, on $y-z$ plane at downstream station $x/D = 6$ in the DC wake. LES results.

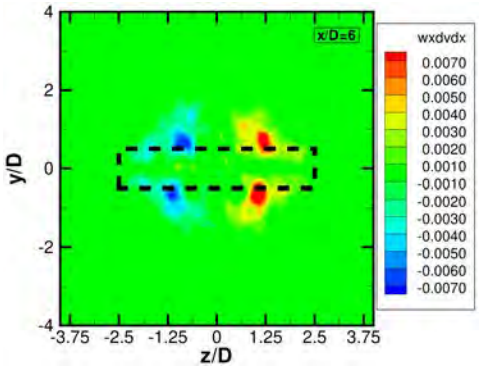

(a)

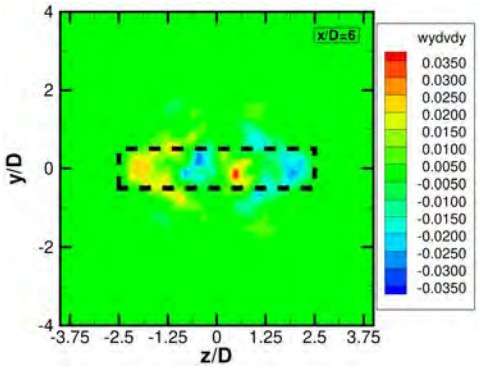

(b)

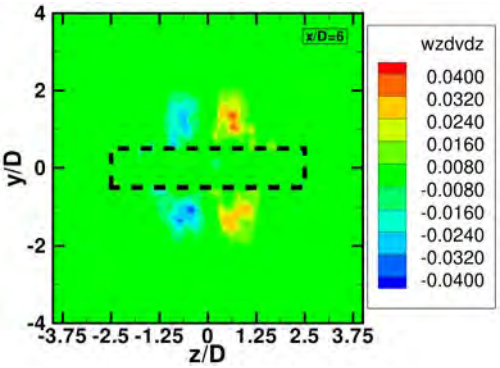

(c)

Figure B.2: Contours of mean stretching and tilting terms in $y-$vorticity equation (a) $\overline{\widetilde{\omega}}_x \frac{\partial \overline{\widetilde{v}}}{\partial x}$, (b) $\overline{\widetilde{\omega}}_y \frac{\partial \overline{\widetilde{v}}}{\partial y}$, and (c) $\overline{\widetilde{\omega}}_z \frac{\partial \overline{\widetilde{v}}}{\partial z}$, on $y-z$ plane at downstream station $x/D = 6$ in the DC wake. LES results.

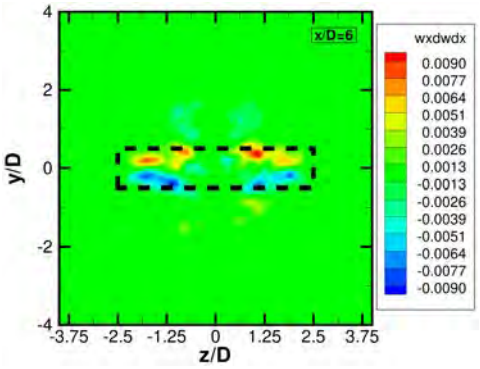

(a)

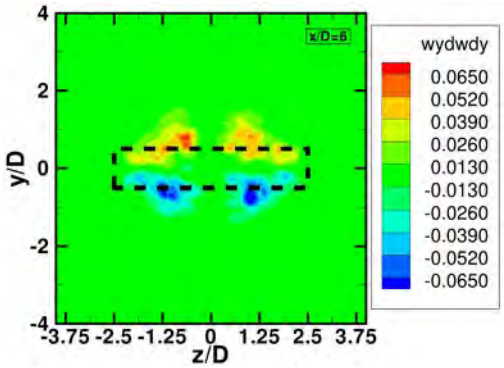

(b)

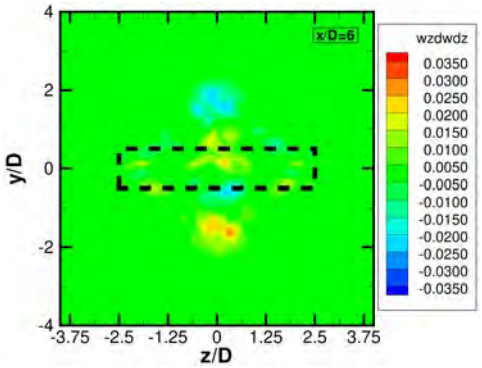

(c)

Figure B.3: Contours of mean stretching and tilting terms in $z-$vorticity equation (a) $\overline{\widetilde{\omega}}_x \frac{\partial \overline{\widetilde{w}}}{\partial x}$, (b) $\overline{\widetilde{\omega}}_y \frac{\partial \overline{\widetilde{w}}}{\partial y}$, and (c) $\overline{\widetilde{\omega}}_z \frac{\partial \overline{\widetilde{w}}}{\partial z}$, on $y-z$ plane at downstream station $x/D = 6$ in the DC wake. LES results.

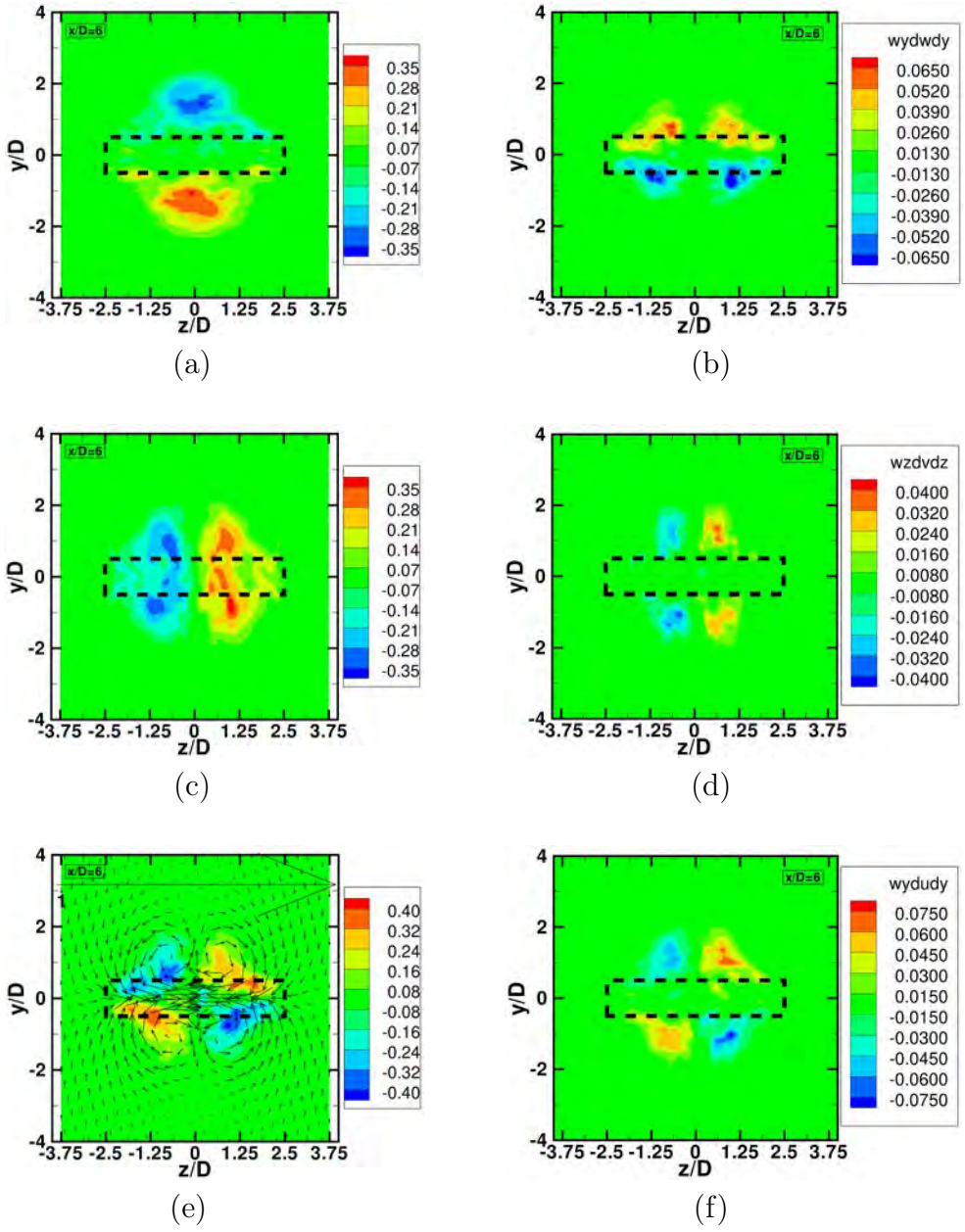

Figure B.4: The mean vorticity contours in the vertical planes with $x/D = 6$ (a, c, e), and the mean tilting terms of the vorticity equation, with the contribution from the interaction between mean vorticity and mean velocity gradients in the vertical planes with $x/D = 6$ (b, d, f), obtained from the DC LES simulation. (a) Spanwise (z) vorticity component, $\overline{\widetilde{\omega}}_z\ D/U_0$, (c) Vertical ($y$) vorticity component, $\overline{\widetilde{\omega}}_y\ D/U_0$, (e) Streamwise ($x$) vorticity component, $\overline{\widetilde{\omega}}_x\ D/U_0$, together with the mean velocity vector plots ($\overline{\widetilde{v}}, \overline{\widetilde{w}}$). In the plot the velocity vectors are scaled so that an arrow length equal to the horizontal span of the plot would denote the reference velocity level, U_0.

different instantaneous HSVs shed sequentially. The presence of HSVs early in the near wake ($x/D \leq 10$) may be related to the relatively high momentum flow in the gap region enter to the wake on wake centerline ($y = 0$) and kink the Kármán vortices (or $z-$aligned large scale vortices) formed directly behind the cylinder segments and forms the HSVs early in the near wake (figure 6.6). Figures B.1, B.2, and B.3 show the contours of mean stretching and tilting terms in $x-$, $y-$ and $z-$vorticity equations, respectively. Among the mean stretching and tilting terms in the $z-$vorticity equation terms (figure B.3), the tilting term ($\overline{\widetilde{\omega}}_y \ \frac{\partial \overline{\widetilde{w}}}{\partial y}$) dominates and shows that the $z-$vorticity is being turned into $y-$vorticity because of the bending of the vortices (figure B.4b), and consistently the strongest of the three $y-$vorticity equation terms (figure B.2) is the tilting by $z-$vorticity ($\overline{\widetilde{\omega}}_z \ \frac{\partial \overline{\widetilde{v}}}{\partial z}$), which is clearly signalling the (average) upwards/downwards bending of the vortices (figure B.4d). The upwards/downwards tilting/bending is not only vertical, as the vortices raise they also being slanted forwards, thus it also shows the presence of the corresponding dominating tilting term ($\overline{\widetilde{\omega}}_y \ \frac{\partial \overline{\widetilde{u}}}{\partial y}$) in the $x-$vorticity equation terms (figures B.1b & B.4f). Note that in all three cases the consistency between the signs of the tilting terms (figure B.4b, d, f) and the signs of the mean vorticity components (figure B.4a, c, e). In the $\overline{\widetilde{\omega}}_x$ and $\overline{\widetilde{\omega}}_y$ plots the spatial 'correlation of colours' (coloured patches) is very good and in the ω_z case it is also good, as the plotted term was a destruction term (negative correlation), that is, 'what is lacking' in terms of $\overline{\widetilde{\omega}}_z$ on both sides (away from $z = 0$) agrees reasonably well with 'what is being destroyed' on both sides.

The early $z-$aligned vortices, resembling von Kármán vortices (VKV), in the DC wake (figure 6.6a) are shaped into HSV by means of the bending and subsequent slanting forward processes that are induced by the lateral fluid entrainment (figure 6.6c). The VKV to HSV transformation can be interpreted, on the time-averaged fields, in terms of vortex realignment (tilting) by the mean velocity gradients (figure B.4 and equations B.1 & B.2).

Appendix C

Flow pattern around an instantaneous HSV, shear production and HSV leg stretching

Instantaneous horseshoe vortices (HSV) in the DC wake were shown in chapter 6 with iso-surface of pressure (figure 6.5). The corresponding flow pattern on plane $z/D = 0$ is shown in figure C.1a. This particular instantaneous horseshoe structure is not centered on $z/D = 0$ but it is centered on a plane, which is slightly away from the centerline ($z/D = -0.25$), so the flow pattern on plane $z/D = -0.25$ is also shown in figure C.1b. The contour of instantaneous vorticity modulus ($|\omega| = 0.35$) is used to show the approximate interface of the wake (figure C.1). The threshold for the vorticity modulus to show the approximate interface for the whole near wake region ($x/D \leq 10$) was chosen carefully for the flow in the near wake region of DC, based on the mean profiles of vorticity modulus (figure C.2). Instantaneous shear production (PD_{shr}) is the product of instantaneous Reynolds stresses and the instantaneous shear, i.e.

$$PD_{shr}(t, x, y, z) = (u_i^f u_j^f)\ \frac{\partial \tilde{u}_i}{\partial x_j} \tag{C.1}$$

In all the plots in this Appendix C, unless mentioned, red coloured lines are instantaneous contours of pressure fluctuations (p^f), which were calculated as $p^f(t, x, y, z) = (\hat{p}(t, x, y, z) - \overline{\hat{p}}(x, y, z))/(\rho U_0^2)$, to show the vortex regions in the wake and the green coloured line is an instantaneous contour of vorticity modulus ($|\omega|$) to show the approximate wake interface and the gray scale contours are to show the instantaneous shear production term (PD_{shr}).

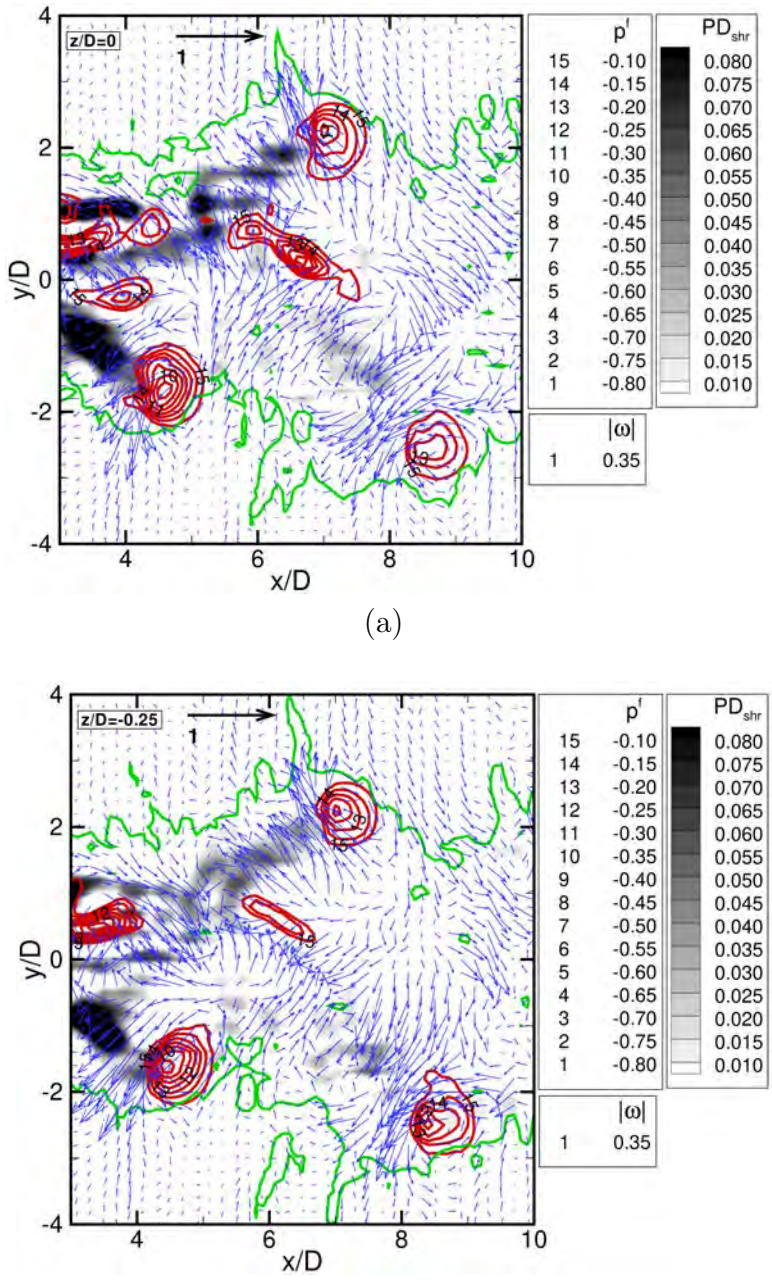

Figure C.1: Instantaneous contours of pressure fluctuations (red lines), vorticity modulus (green line) and production term (gray scale) and vectors of velocity (u^f, v^f) fluctuations on vertical $x-y$ plane at (a) $z/D = 0$ (b) $z/D = -0.25$. LES results.

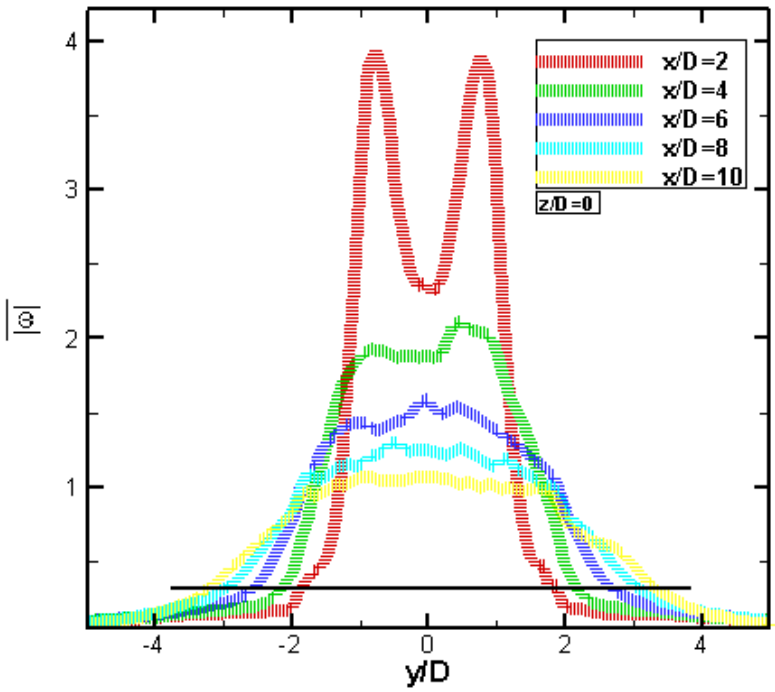

Figure C.2: Profiles of mean vorticity modulus in the vertical plane at middle of the cylinder piece ($z = 0$) at several downstream locations in the DC wake. This is to choose the better threshold for the vorticity modulus to show the approximate wake interface in near wake region ($x/D \leq 10$) of the DC. LES results.

The used contour levels of each variable in all the plots in this Appendix C are the same.

Figure C.1 shows the head ($z-$vorticity) of the HSV brings non-turbulent fluid through the interface towards the wake centerline ($y/D = 0$). The contours of production term shows that the shear production occurs in the region between the legs of the horseshoe (ejection or mixing jet region), which may be related to as shown before that the legs ($x-$vorticity) of HSV eject the momentum transferred from the free-stream gap region, together with the flow entered to the wake through the top/bottom interface by the rotation of the head of the HSV close to the top/bottom interface, to the non-turbulent external flow region, alternating side by side. That ejection of the turbulent flow by the rotation of the HSV legs from the center of the wake to towards the non-turbulent external flow region may also be the reason for the presence of thick wake behind the head ($z-$vorticity) of each HSV as found in $x-y$ plane at $z = 0$ (figure C.1).

Figure C.3 shows the instantaneous flow pattern on $y-z$ planes at x/D =7.5, 8.0 and 8.5 (with reference to the 3D instantaneous HSVs shown in figure 6.5). The flow entrained by the head of HSV2 moves towards wake centerline ($y/D = 0$) from the top interface (figure C.3a). The counterrotating motion of the two legs of HSV1 entrain fluid laterally from the freestream flow in the gap region between the cylinder segments and ejects, together with the flow entrained by the head ($z-$vorticity) of HSV2, to towards bottom interface (figure C.3b). Part of the ejected flow from the wake centerline to the outer interface, displaced laterally outwards from the vertical plane $z = 0$ and downwards to the horizontal plane $y = 0$ (C.3b) and the rest is incorporated to the rotating motion at the top of the HSV1 (C.3c). The contours of shear production show that the mixing occurs in the mixing jet region between the legs of the HSV (figures C.1 & C.3a,b).

The mean shear production term ($\overline{PD}_{shr}(x,y,z) = (\overline{u_i' u_j'})\ \frac{\partial \overline{u}_i}{\partial x_j}$) was calculated from the PIV measurements data on the vertical $x-y$ planes at $z = 0$. Figure C.4 shows that the highest production rates occur at $y_{1/2}$ and at the centre of the HSV for $x/D \geq 5$ in the DC wake.

A variable vortex stretching (ω_{str}) is defined as the summation of diagonal terms of vortex tilting and stretching tensor (equations B.1 & B.2), and is given below

$$Vortex\ stretching\ (\omega_{str}) = \omega_x\ \frac{\partial u}{\partial x} + \omega_y\ \frac{\partial v}{\partial y} + \omega_z\ \frac{\partial w}{\partial z} \qquad \text{(C.2)}$$

Figure C.5a shows the instantaneous contours of vortex stretching variable (gray scale) on vertical ($x-y$) plane at middle of the cylinder piece ($z/D = 0$). There is no hint of vortex stretching activity between the legs of

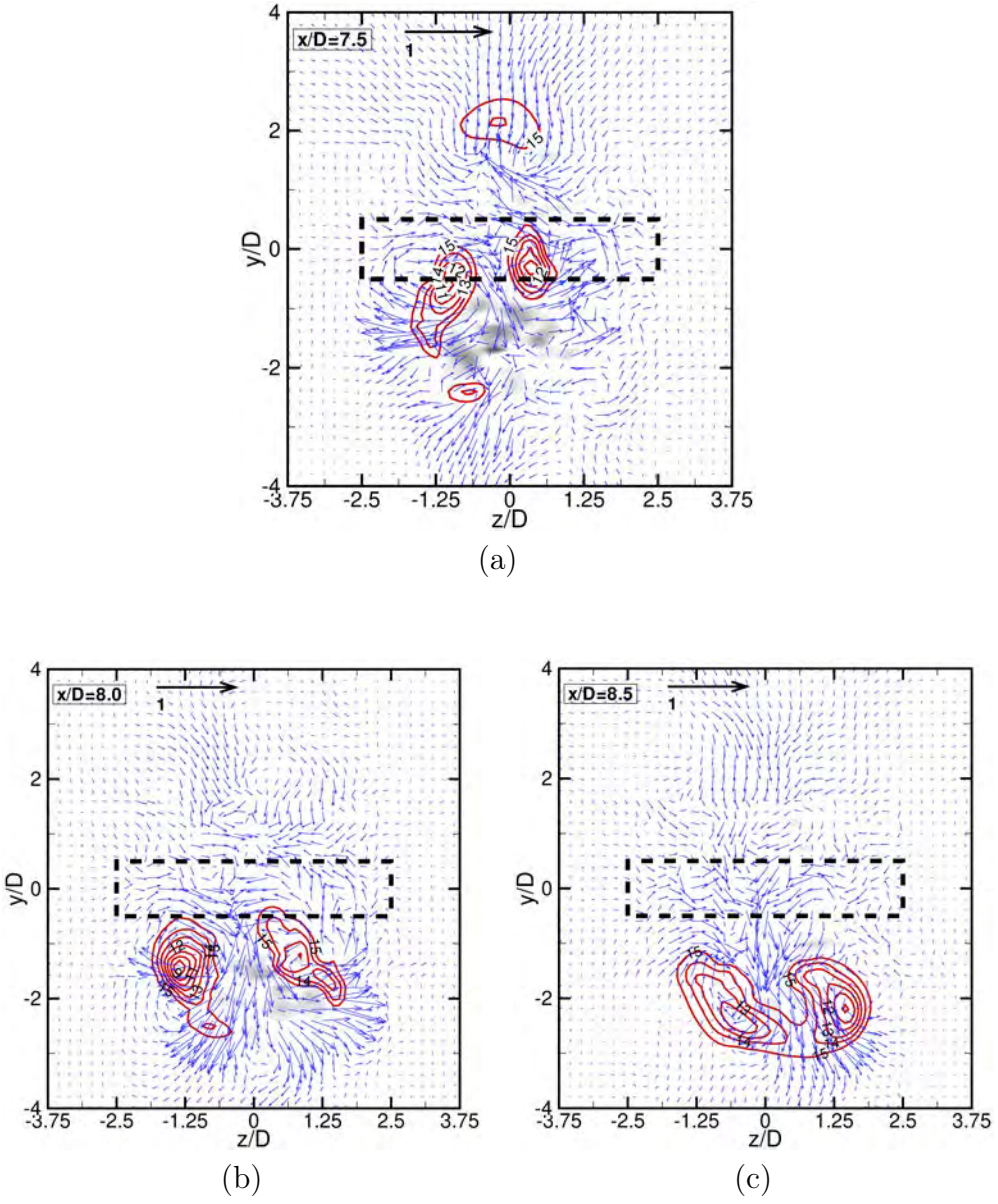

(a)

(b)

(c)

Figure C.3: Instantaneous contours of pressure fluctuations (red lines) and production term (gray scale) and vectors of velocity components (v, w) on vertical $y - z$ planes at (a) $x/D = 7.5$, (b) $x/D = 8.0$, and (c) $x/D = 8.5$. LES results.

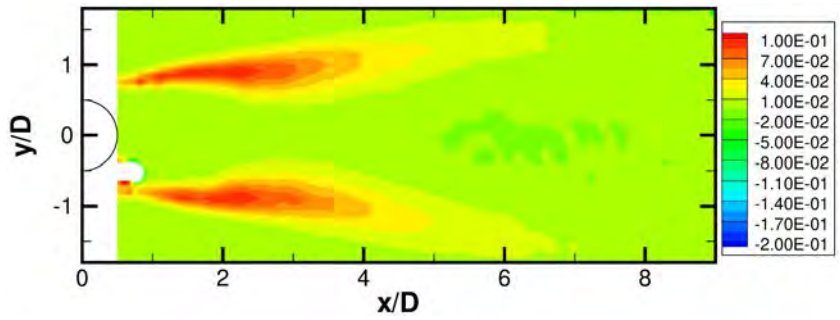

(a)

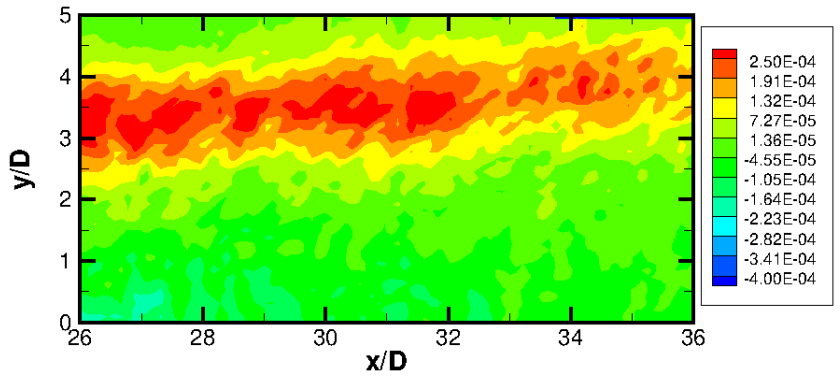

(b)

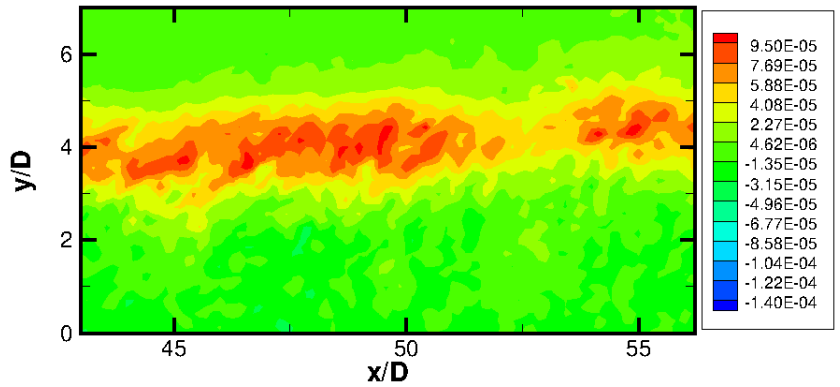

(c)

Figure C.4: The contours of mean shear production term ($\overline{PD}_{shr}$) in the vertical $x-y$ plane at $z=0$ in the DC (a) near wake, (b) mid wake, and (c) mid-far wake. PIV results.

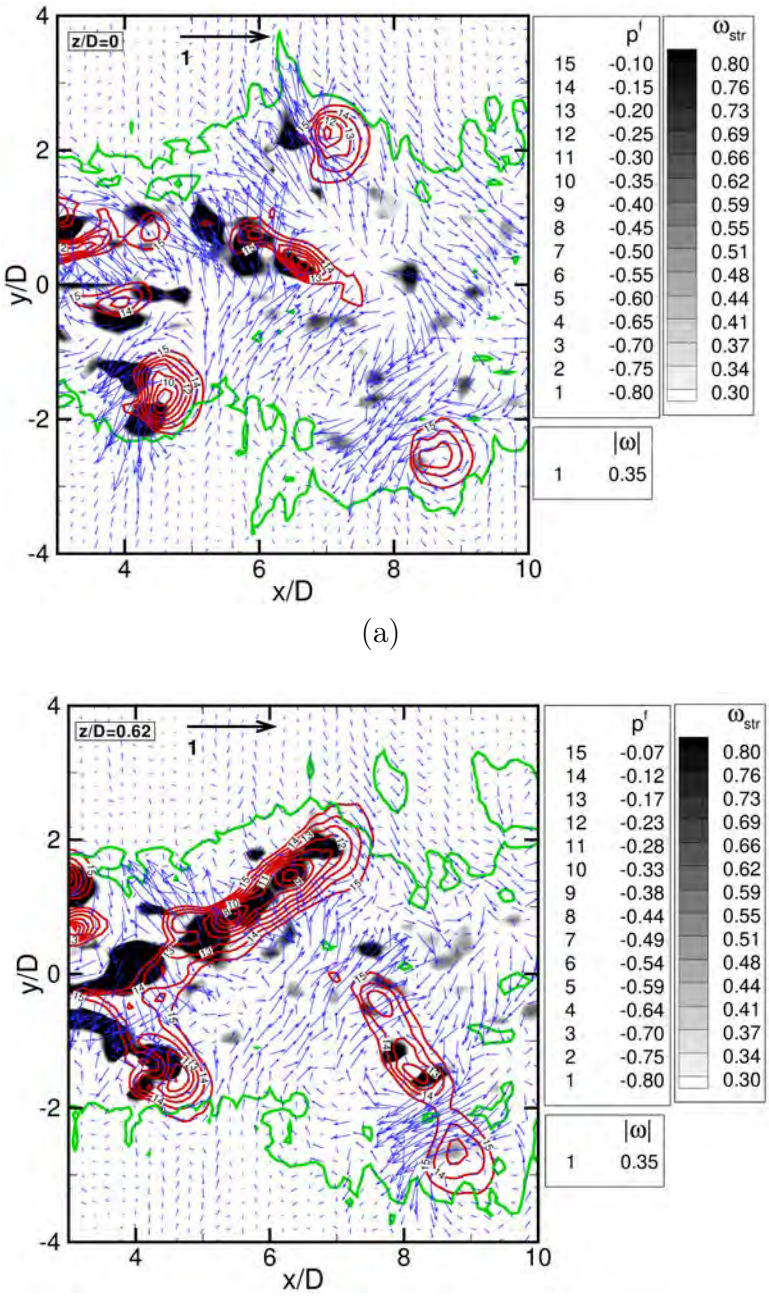

Figure C.5: Instantaneous contours of vortex stretching (ω_{str}), pressure fluctuations (p^f) and vorticity modulus ($|\tilde{\omega}|$), and vectors of velocity (u^f, v^f) fluctuations on vertical ($x-y$) plane at (a) middle of the cylinder piece, $z/D = 0$ and (b) across a horseshoe leg, $z/D = 0.62$. LES results.

the HSV in the plane at the middle of the cylinder piece ($z/D = 0$), as the vorticity at top of the horseshoe ($\overline{\widetilde{\omega}}_z$) is not aligned with the flow (orthogonal to the flow) and in the region below to the top of the horseshoe, in the same plane at $z/D = 0$, the strain field interacts with less/zero vorticity. Figure C.5b shows the contours of vortex stretching variable on vertical plane across the leg of the instantaneous HSV2 presented in figure 6.5, at $z/D = 0.62$. It shows that as vorticity (leg of HSV2) is aligned with the flow, the leg is getting stretched towards top interface.

Sixth International Symposium on Turbulence and Shear Flow Phenomena
Seoul, Korea, 22-24 June 2009

Appendix D

EXPERIMENTAL INVESTIGATION OF THE WAKE BEHIND A DISCONTINUOUS CYLINDER

V. S. R. Mandava[1], G. A. Kopp[2], J. Herrero[1], Francesc Giralt[1]

[1]Department d'Enginyeria Quimica
Universitat Rovira i Virgili
Av. Països Catalans 26, Tarragona, Catalunya, 43007, Spain
fgiralt@urv.cat

[2]Boundary Layer Wind Tunnel Laboratory
University of Western Ontario
London, Ontario, N6A 5B9, Canada
gakopp@uwo.ca

ABSTRACT

The effect of a discontinuous cylinder geometry on the near wake structures was investigated experimentally. This 'discontinuous' circular cylinder has gaps so that solid segments 5D long are followed by gaps 2.5D long, in a repeating pattern, where D is the diameter of the cylinder. A thin steel plate was used to hold all of the cylinder pieces together. Thus, a three-dimensional (3D) wake was created at the origin with the intent to force the near wake flow to have similar structural characteristics to the far wake behind an 'infinite' cylinder, i.e., a near wake flow with horseshoes or double rollers formed by rapid kinking of Kármán-like vortices. Since the kinetic energy associated with the fluctuations of these near-wake 3D vortical structures was high, the flow system was considered suitable to clarify the role of these velocity patterns in the entrainment process of wake flows, which is still the subject of controversy. Particle image velocimetry (PIV) measurements were made in the wake behind the discontinuous cylinder up to x/D=56, at a Reynolds number Re=10,000. The development of double rollers resulting from the interaction between the high momentum flow through the gaps and the Kármán-like vortices formed behind the solid cylindrical segments was confirmed. They have a dominant role in the initial wake growth which occurs under significant momentum transfer in the spanwise direction. This overall flow dynamics is similar to the momentum transfer that takes place at the scale of the intermittent turbulent bulges that protrude from the wake in the far region and that were reported to be associated with double rollers.

INTRODUCTION

Understanding the kinematics and dynamics of entrainment and mixing is important in many practical engineering situations. Entrainment has been considered by many researchers as a large-scale process (e.g., Townsend, 1976; Bevilaqua and Lykoudis, 1977) and several phenomenological descriptions have been proposed in the past. Examples are the vortex sheet roll-up due to a Kelvin-Helmholtz instability and entrapment of external fluid into the core of the vortex (Prandtl and Tietjens, 1934; Sreenivasan et al., 1989; Caulfield and Peltier, 2000); Townsend´s (1966, 1976) growth-decay model; 'sweeping' non-turbulent fluid into the turbulent region by rotational motions (Bevilaqua and Lykoudis, 1977). These theories or phenomenological models do not explain the role of large scale vortical structures in relation to the initial conditions that generate them. In contrast to the large-scale approaches to entrainment just mentioned, Mathew and Basu (2002) and Westerweel et al. (2005) concluded that the mechanism of entrainment process is dominated by small scales (nibbling). Thus, it is still not clear whether the entrainment process occurs as a result of outward spreading of small-scale vortices "nibbling" or by the action of large-scale eddies in the turbulent-non turbulent flow interfacial region.

Wakes are an ideal flow system to study the genesis of large scale vortices and their dynamical evolution with respect to initial flow conditions. The instability and transition in the near wake has been studied by many researchers (e.g., Gerrard, 1967; Roshko and Fiszdon, 1969; Mc Crosky, 1977; Zdravkovich, 1990; Williamson, 1996; Norberg, 2003; Dong, 2006). Several numerical and experimental studies have also been carried out in the past to characterize the three-dimensional (3D) nature of wake flows and vortex shedding by exciting 3D modes at the originating body (e.g., Bearman and Tombazis, 1993; Bernman and Owen, 1998; Darekar and Sherwin, 2001; Lam et al., 2004; Wu et al., 2005; Lee and Nguyen, 2007; Ling and Lin, 2008). Control of initially perturbed wake flows has also raised attention (e.g., Dobre et al., 2006). A more radical initial perturbation in a 2D wake flow behind an infinite body in the spanwise direction could be attained by alternating solid with discontinuous segments of the same body in a repeating pattern. This would have the benefit of not changing the basic body geometry that generates the wake flow.

In the current study we have considered a 3D cylinder configuration with gaps, i.e., pieces of equidistant cylinders

Sixth International Symposium on Turbulence and Shear Flow Phenomena
Seoul, Korea, 22-24 June 2009

along the cylinder center axis. With this arrangement part of the free stream flow passes through the gaps while the rest passes over the 3D cylinder pieces forming a 3D wake. The free stream flow through the gaps would move inwards towards each wake behind the cylindrical pieces due to pressure gradients. Simultaneously, Kármán-like vortices would be formed behind the solid segments together with other vortical structures at both ends. This new configuration of the initial flow conditions should cause the lifting or kinking of the segmented, 3D Kármán-like vortices and horseshoe/double-rollers/o-ring kind of vortices would be generated in the near wake. These are the vortices that usually occur in the far wake region behind an infinite cylinder (e.g., Ferré and Giralt, 1988; Giralt and Ferré, 1993; Vernet et al., 1999; Kopp et al., 2002). As a consequence, the current flow configuration may help explaining how double rollers could be generated earlier in the wake, how they evolve with respect to initial flow conditions, and shed light on the entrainment and mixing mechanisms in turbulent free flows.

EXPERIMENTAL DETAILS

A portion of the experiments were carried out at the Boundary Layer Wind Tunnel Laboratory (BLWTL), University of Western Ontario, Canada, while the remaining experiments were conducted in the open return wind tunnel of the Chemical Engineering Department at the Universitat Rovira i Virgili in Tarragona. At both places, measurements were conducted with the same discontinuous cylinder model and at the same free-stream velocity U = 9.2m/s, thus, at the same Reynolds number Re = 10^4. The diameter (D) of the cylinder pieces was 0.0163m, the length of each segment was 5D, and the gap between the cylinder pieces was 2.5D. A thin steel plate, whose thickness was 0.81mm and width equal to the cylinder diameter, held the cylinder pieces together without interfering significantly with the dominant 3D flow structure upstream and downstream of the model. The dimensions of the model and co-ordinate system used are shown in Fig. 1. At Re = 10^4 the boundary layer is laminar and the near wake is fully turbulent (Dimotakis, 2000). Particle image velocimetry (PIV) was used to measure the instantaneous velocity field in the wake region with a flash lamp laser of frequency 15Hz to illuminate particles in the flow.

First, several measurements were conducted in Canada, in the near wake region up to 8.5 diameters downstream on transverse(x-y) planes, along the cylinder axis. Planes at every half a diameter width, from center of the middle cylinder piece (z/D=0) to the end of the middle cylinder piece (z/D=2.5), were examined. Two measurements were carried out within the gap region between cylinder pieces, one at 0.5D away from the edge of the cylinder piece (i.e., at z/D=3.0) and the other at the center of the gap region (z/D=3.75). Several experiments were carried out on transverse(x-y) planes to check flow symmetry.

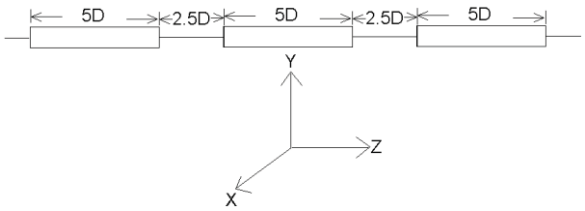

Figure 1. Cylinder model and co-ordinate system

The experiments were repeated with stereo particle image velocimetry in Tarragona, Spain, with the same discontinuous cylinder configuration (Fig. 1) but with five cylinder pieces, instead of the three in the earlier setup. The data obtained were in reasonable agreement with the earlier experimental data determined in Canada.

Measurements were extended in Tarragona to further downstream in the wake on several vertical (x-y) planes, x/D=9 to 16, 26 to 36 and 43 to 56, at the middle plane of the discontinuous cylinder (z/D=0). Experiments were also conducted on the horizontal (x-z) planes in the downstream wake from x/D=10 to 20 at y/D=2, and 27 to 36 at y/D=3. Data for the corresponding wake of an infinite cylinder were also collected at all the vertical and horizontal planes. The aspect ratio of the infinite cylinder was 37 and the blockage in the tunnel was 2.7%. The TSI Insight3G software was used, in all cases, for frame to frame correlation to generate instantaneous velocity fields, with an interrogation window of size 32 x 32 pixels with 50% overlap. These instantaneous velocity fields were then ensemble averaged to determine the mean streamwise and transverse velocities, root mean square (r. m. s) velocity fluctuations, mean Reynolds shear stresses and mean z-vorticity patterns on all the transverse (x-y) and horizontal (x-z) planes. The instantaneous data on horizontal planes were used to identify the footprints of double rollers in the near wake.

RESULTS

Current data for the infinite cylinder were compared and found in reasonable agreement with the literature measurement (Dong et al., 2006; Norberg, 1998). In the following sections discontinuous and infinite cylinder data are compared. The plots presented in the paper are, unless specified, on transverse planes at z/D=0. In all contour plots flow direction is from left to right and, positive and negative magnitude of contours are indicated by solid and dashed lines, respectively.

For the discontinuous cylinder case, note that the velocity defect and vorticity levels at the wake behind the steel plate are much smaller than those at the wake behind each cylinder piece (Fig. 2), and their effects on wake data were neglected.

Sixth International Symposium on Turbulence and Shear Flow Phenomena
Seoul, Korea, 22-24 June 2009

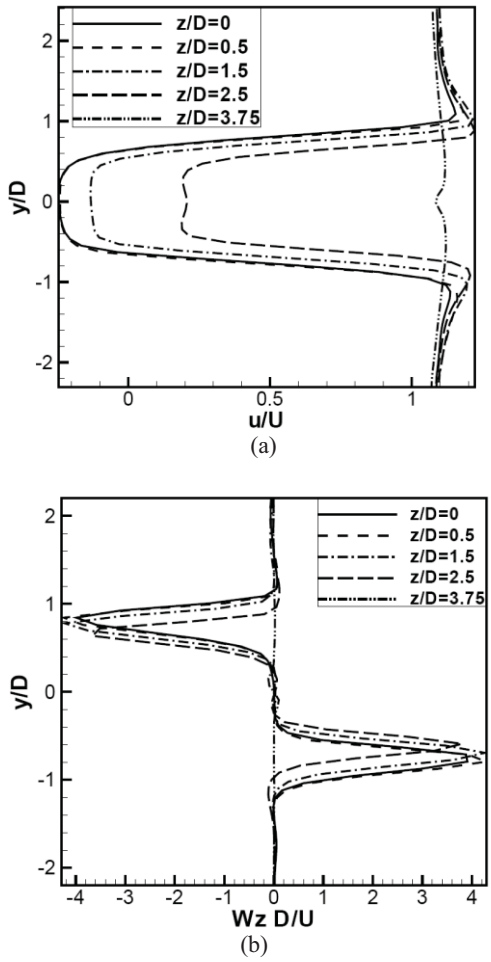

Figure 2. (a) Profiles of mean streamwise velocity (u/U) at x/D=1; (b) Profiles of mean z-vorticity (w_zD/U) at x/D=1

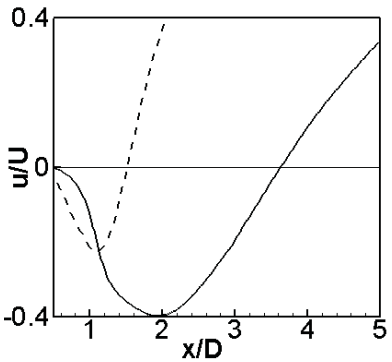

Figure 3. Mean stramwise velocity (u/U) at wake center line (y/D=0) of discontinuous (—) and infinite (----) cylinders

Wake characteristics

The variations in base suction are associated with variations in vortex formation length. It is the distance between separation point and the location at which the vortex is fully formed, before it is shed (Gerrard 1966). Definitions of the formation length are given elsewhere (Bloor, 1966; Woo et al., 1983; Norberg, 1986 and 1998; Govardhan, 2001). The formation length of the wake for the discontinuous cylinder is 3.62D, and the corresponding value for the infinite cylinder is 1.5D by the present experiments and 1.52D by Norberg (1998). As in the reference Norberg (1998), we have used time averaged closure point (point of zero u/U at wake centerline in Figure 3) to measure the formation length.

The mean streamwise velocities at wake center line (Fig. 3) show strong negative values (reverse flow) in the wake region. The magnitude of the minimum velocity and the location where this occurs are different from the infinite cylinder case. The maximum magnitude of the negative velocity is 0.4 and the corresponding value for the infinite cylinder is 0.225 in the current experiments, 0.228 in Dong et al. (2006) from their 2D PIV experiment, and 0.38 in Norberg (1998) from Laser Doppler Velocimetry (LDV) analysis. The width of the wake at x/D=1.5 is much wider than the wake behind an infinite cylinder (Fig. 4a). The wake has more velocity deficit in the region close to the cylinder when compare to the infinite cylinder case, but as the wake grows downstream it recovers quickly (Fig. 4).

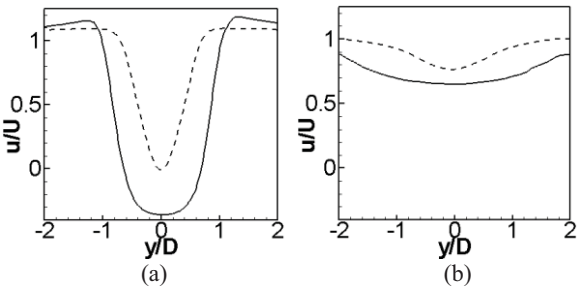

Figure 4. Comparison of mean streamwise velocity in discontinuous (—) and infinite (----) cylinder at (a) x/D=1.5; (b) x/D=8

The u′ and v′ are the streamwise and transverse root mean square velocities. The magnitude of the maximum fluctuations of the normalized root mean square streamwise velocity (u′/U) for the discontinuous cylinder is smaller. The corresponding location is displaced further downstream compared to the infinite cylinder case. The maximum value is 0.30 and occurs at x/D=2.5. The corresponding values for the infinite cylinder are 0.45 at x/D=1.4 in the current experiments, 0.5 at x/D=1.14 in Dong et al. (2006) and 0.43 at x/D=1.5 in Norberg (1998).

The double peak behavior in the streamwise normal stress in Fig 5 arises as a result of the alternating nature of the shed vortices and the formation of a 3D vortex street with kinked Kármán-like vortices. As the wake flow develops, the peaks become less and less prominent. The wake characteristics remain similar along the cylinder axis at x/D=1 (Fig. 2), but at further downstream positions, for example at x/D=5, it is clear from Fig. 5 that the peaks of stream-wise normal stress slowly disappear; the peaks at the plane z/D=1.5 are less prominent than at the middle plane z/D=0 because of the momentum input occurring through the gaps into the wake.

Sixth International Symposium on Turbulence and Shear Flow Phenomena
Seoul, Korea, 22-24 June 2009

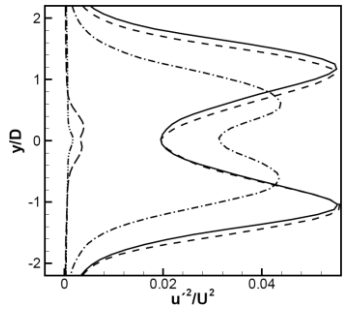

Figure 5. The profiles of mean streamwise Reynolds normal stress at x/D=5, z/D=0 (—), z/D=0.5 (----), z/D=1.5 (-.-.-.-), z/D=2.5 (– – –) and z/D=3.75 (-..-..-..-)

The dominant peak level of normalized Reynolds shear stress ($u'v'/U^2$) is smaller and the corresponding location displaced downstream in wake of the discontinuous cylinder wake compared to the infinite cylinder flow situation. The peak level is 0.05 and it occurs at location x/D=3, while the corresponding values for the infinite cylinder are 0.12 at x/D=1.64 in the present experiments and 0.14 at x/D=1.4 in Dong et al. (2006). The contour patterns of the normalized shear stress ($u'v'/U^2$) for the discontinuous cylinder, not shown here, show that regions of high shear have moved relatively away from the cylinder surface compared to the infinite cylinder case. This may be related to the converging streamlines in the wake from ends of the cylinder segments. Velocity fluctuations are largest at the vortex centers. When Vortices are shed into the near wake and are advected downstream they move away from the centerline.

Entrainment process

The flow around a short cylinder segment is essentially three-dimensional. The end effects play a dominant role and strongly modify the structure of vortices in the near wake region. Initially the evolving Kármán-like vortices are connected to the ends of the cylinder. When shed from the cylinder they are kinked and form a horseshoe like structure that may reconnect, due to converging streamlines in the wake, and form a vortex-ring-like structure. At times, these vortices can be strongly distorted, which may result in a much more complicated flow pattern.

The horseshoe eddy is a structure with two legs which are shear aligned and connected at the top with spanwise vorticity. The cross-section of the two legs forms a double roller pattern on the horizontal plane. These double roller structures, which are known to appear in the far wake region behind an infinite cylinder, are also observed in the near wake (xD≈15) of the discontinuous cylinder, as shown in Fig.6. The vectors of streamwise and spanwise velocity fluctuations on horizontal (x-z) plane clearly depict in this figure the footprints of double roller vortices early in the discontinuous wake development. Similar kind of double roller structures are found on the horizontal plane further downstream (xD≈30) behind the discontinuous cylinder, as shown in Fig. 7. This indicates that once formed they remain because are capable of extracting energy by stretching while diffusing in the spanwise direction and moving downstream by advection.

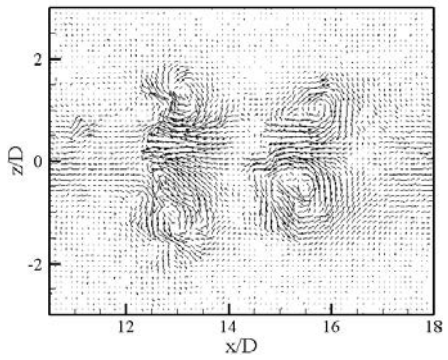

Figure 6. The normalized (u,w) velocity fluctuations in the near wake behind the discontinuous cylinder

The corresponding spanwise profiles of y-vorticity and u'w' shear stress are presented in Fig. 8. The flow of high momentum fluid entering the wake through the gaps, which moves towards the regions behind the cylinder segments, causes a lift upwards and downwards of the alternating Kármán-like vortices that these segments shed. As a result, the initially dominant z-vorticity projects into y-vorticity at the central z-x plane. Fig. 8a shows how this y-vorticity decreases with x/D as double rollers are advected downstream and diffuse. The u'w' shear stress also diminishes with x/D (Fig. 8b). which is indicative of the wake evolution towards fully development ($u'w'/U^2=0$).

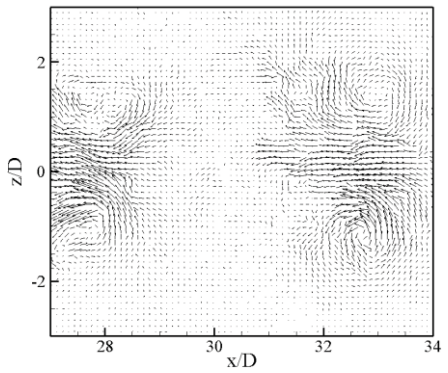

Figure 7. The normalized (u,w) velocity fluctuations in the medium far wake behind the discontinuous cylinder.

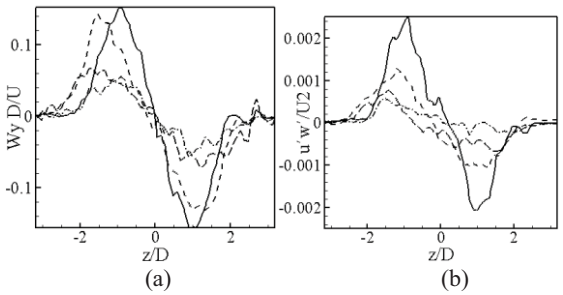

Figure 8. The profiles of (a) mean y-vorticity (Wy D/U), at x/D=11 (—), x/D=19 (----), x/D=28 (-.-.-.-) and x/d=36 (– – –); (b) mean shear stress ($u'w'/U^2$), at x/D)=11 (—), x/D=19 (----), x/D=28 (-.-.-.-), and x/D=36 (– – –)

Double rollers are responsible for maintaining the correlation between the streamwise and lateral velocity fluctuations, with correlation being largest at the center plane of the structure (Vernet et al., 1997). The profiles of normalized shear stress ($u'v'/U^2$) at several downstream locations on wake center line are shown in Fig. 9. The shear stress peaks close to the wake formation length at x/D=3, and then decreases as x/D increases. Again, the input of momentum by the high velocity flow in the gap seems evident.

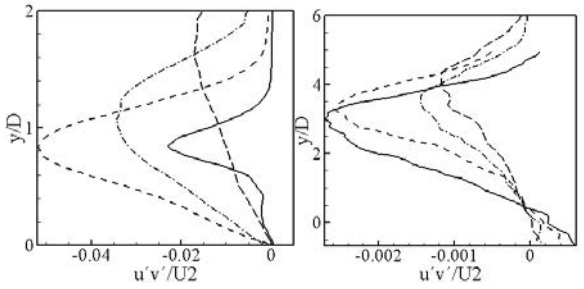

Figure 9. The profiles of mean shear stress ($u'v'/U^2$) at (a) x/D=1.5 (—), x/D=3 (----), x/D=5 (-.-.-.-) and x/d=8 (– – –); (b) x/D)=26 (—), x/D=32 (----), x/D=44 (-.-.-.-), and x/D=56 (– – –)

The profiles of mean spanwise vorticity (Wz D/U) at several downstream stations are shown in Fig. 10. The magnitude of negative vorticity is maximum close to the cylinder, and decreases in magnitude as the wake gradually develops. Profiles in the downstream wake reflect, with maximum negative vorticity values, the mean path of the top of the horseshoe vortices which have high spanwise negative vorticity.

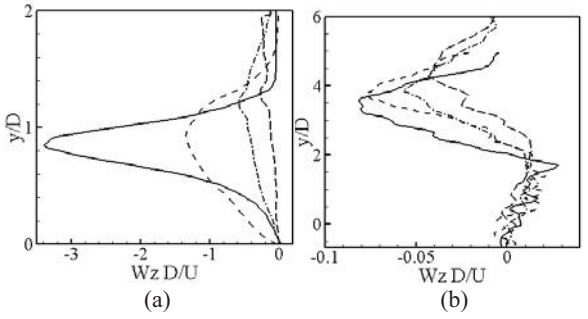

Figure 10. The profiles of mean z-vorticity (W_z D/U) at (a) x/D=1.5 (—), x/D=3 (----), x/D=5 (-.-.-.-) and x/d=8 (– – –); (b) x/D)=26 (—), x/D=32 (----), x/D=44 (-.-.-.-), and x/D=56 (….)

Finally, Fig. 11 shows that the wake thickness and growth rate in the current discontinuous cylinder case are both larger than for the 2D cylinder wake. These results illustrate the important role of large scale 3D motions, such as double rollers, in the entrainment process. LES calculations not reported here are in agreement with experimental data.

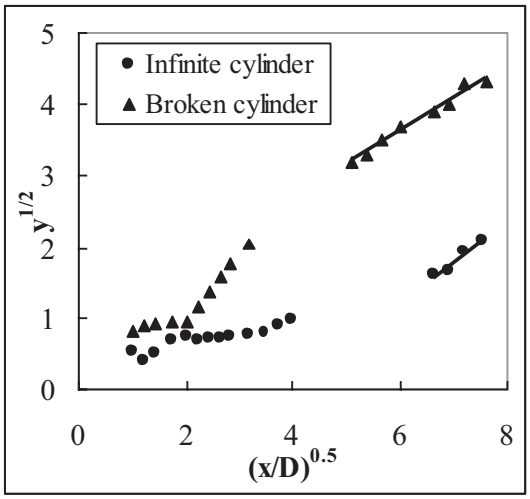

Figure 11. Variation of the wake half-width with streamwise location for both the discontinuous and 2D cylinder

CONCLUSIONS

The effect of inflow conditions on the near wake structure behind a discontinuous cylinder, at Reynolds number 10,000 was investigated experimentally. The flow statistics such as mean velocities, r. m. s. velocity fluctuations, mean Reynolds shear stress and mean z-vorticity of the discontinuous cylinder have been compared with the corresponding data for an infinite cylinder wake. The wake bubble behind the segments of the discontinuous cylinder, which is indicative of reverse flow, is significantly longer than that for the infinite cylinder, i.e; the formation length is enlarged. This delay shedding may be related to the converging streamlines in the wake from ends of the cylinder due to the inflow of high momentum fluid through the gaps. The wake width of the discontinuous cylinder is much wider and grows faster than that for the infinite cylinder. The velocity deficit is larger in the near wake region, but as the wake grows downstream it recovers quickly. The peaks of the streamwise normal stress are less prominent as wake grows downstream. Once Kármán-like vortices are shed they are kinked in the very-near wake due to effect of the flow input through the gaps and form double rollers. Footprints of double-roller vortices have been unambiguously identified on the horizontal planes in the wake of the discontinuous cylinder, both from experimental data and LES results not reported here.

ACKNOWLEDGMENT

The current study was supported by the grants FIS2005-07194 and CTQ2008-04857/PPQ (MEC, Spain) and 2005SGR-00735 (DURSI, Generalitat de Catalunya). Francesc Giralt acknowledges the Distinguished Researcher Award, Generalitat de Catalunya. Gregory Kopp gratefully acknowledges the support of the Canada Research Chairs Program.

Sixth International Symposium on Turbulence and Shear Flow Phenomena
Seoul, Korea, 22-24 June 2009

REFERENCES

Bearman P.W., Tombazis N., 1993, The effects of 3-dimensional imposed disturbances on bluff-body near wake flows, *Jounal Wind Engineering and Industrial Aerodynamics*, Vol. 49(1-3), pp. 339-349.

Bearman P.W., Owen J.C., 1998, Reduction of bluff-body drag abd suppression of vortex shedding by the introduction of wavy separation lines, Jounal of Fluids and Structures, Vol. 12, pp. 123-130.

Bevilaqua P.M., Lykoudis P.S., 1977, Some observation on the mechanisms of entrainment, AIAA Journal, Vol. 15, pp. 1194-1196.

Bloor S., 1966, The transition to turbulence in the wake of a circular cylinder, Journal of Fluid Mechanics, Vol. 19, pp. 290-304.

Caulfield C.P., Peltier W.R., 2000, The anatomy of mixing transition in homogeneous and stratified free shear layers, Journal of Fluid Mechanics, Vol. 413, pp. 1-47.

Darekar R.M., Sherwin S.J., 2001, Flow past a bluff body with a wavy stagnation face, Journal of Fluids and Structures, Vol. 15(3-4), pp. 587-596.

Dimotakis P.E., 2000, The mixing transition in turbulent flows, Journal of Fluid Mechanics, Vol. 409, pp. 69-98.

Dobre A., Hangan H., Vickery B.J. 2006 Wake control based on spanwise sinusoidal perturbations, AIAA Journal, Vol. 44(3), pp. 485-492.

Dong S., Karniadakis G.E., Ekmekci A., Rockwell D., 2006, A combined direct numerical simulation – particle image velocimetry study of the turbulent near wake, Journal of Fluid Mechanics, Vol. 569, pp. 185-207.

Ferré J.A., Giralt F., 1988, Pattern recognition analysis of the velocity field in plane turbulent wakes, Journal of Fluid Mechanics, Vol. 198, pp. 27-64.

Gerrard J.H., 1966, The mechanics of the vortex formation region of vortices behind bluff bodies, Journal of Fluid Mechanics, Vol. 25, pp. 401-413.

Gerrard J.H., 1967, Experimental investigation of separated boundary layer undergoing transition to turbulence, Physics of Fluids, Vol. 10, pp. S98-100.

Giralt F., Ferré J.A., 1993, Structure and flow pattern in turbulent flow, Physics of Fluids, Vol. A5, pp. 1783-1789.

Govardhan R., Williamson C.H.K., 2001, Mean and fluctuating velocity fields in the wake of a freely vibrating cylinder, Journal of Fluids and Structures, Vol. 15, pp. 489-501.

Kopp G.A., Giralt F., Keffer J.F, 2002, Entrainment vortices and interfacial intermittent turbulent bulges in a plane turbulent wake, Journal of Fluid Mechanics, vol. 469, pp. 49-70.

Lam K., Wang F.H., Li J.Y., So R.M.C., 2004, Experimental investigation of the mean and fluctuating forces of wavy (varicose) cylinders in a cross-flow, Journal of Fluid and Structures, Vol. 19(3), pp. 321-334.

Lee S.J., Nguyen A.T., 2007, Experimental investigation on wake behind a wavy cylinder having sinusoidal cross-sectional area variation, Fuid Dynamics Research, Vol. 39(4), pp. 292-304.

Ling G.C., Lin L.M., 2008, A note on the numerical simulations of flow past a wavy square-section cylinder, Acta Mechanica Sinica, Vol. 24(1), pp. 101-105.

Mathew J., Basu A.J., 2002, Some characteristics of entrainment at a cylindrical turbulence boundary, Physics of Fluids, Vol. 14, pp. 2065-2072.

McCroskey W.J., 1977, Some current research in unsteady fluid dynamics – the 1976 freeman scholar lecture, Journal of Fluids Engineering, Vol. 99, pp. 8-39.

Norberg C., 1986, Interaction between freestream turbulence and vortex shedding for a single tube in cross flow, Journal of Wind engineering And Industrial Aerodynamics, Vol. 23, pp. 501-514.

Norberb C., 1998, LDV-measurements in the near wake of a circular cylinder, Advances in understanding of bluff body wakes and vortex induced vibrations, Washington DC, June 1998.

Norberg C., 2003, Fluctuating lift on a circular cylinder: review and new measurements, Journal of Fluids and Structures, Vol. 17, pp. 57-96.

Prandtl L., Tietjens O.G., 1934, Fundamentals of hydro- and aeromechanics, United engineers Trustees.

Roshko A., Fiszdon W., 1969, On the persistence of transition in the near wake, Problems of Hydrodynamics and Continuum Mechanics, pp. 606-616. SIAM

Sreenivasan K.R., Ramshankar R., Meneveau C., 1989, Mixing, entrainment and fractal dimensions of surfaces in turbulent flows, Proc. R. Soc. Lond. A, Vol. 421, pp. 79-108.

Townsend A.A., 1976, The structure of turbulence shear flow, 2nd edn. Cambridge University Press.

Townsend A.A., 1966, The mechanism of entrainment in free turbulent flows, Journal of Fluid Mechanics, Vol. 26, pp. 689-715.

Vernet A., Kopp G.A., Ferré J.A., Giralt F., 1999, Three-dimensional structure and momentum transfer in a turbulent cylinder wake, Journal of Fluid Mechanics, Vol. 394, pp. 303-337.

Vernet A., Kopp G.A., Ferré J.A., Giralt F., 1997, Simultaneous velocity and temperature patterns in the far region of a turbulent cylinder wake, Journal of fluids Engineering, Vol .119, pp. 463-466.

Westerweel J., Fukushima C., Pedersen J.M., Hunt, J.C.R., 2005, Mechanics of the turbulent and non-turbulent interface of a jet, Physical Review Letters, Vol. 17, pp. 174501.

Williamson C.H.K., 1996, Vortex dynamics in a cylinder wake, Annual Review of Fluid Mechanics, vol.28, pp. 477-539.

Wu S.J., Miau J.J., Hu C.C., Chou J. H, 2005, On low-frequency modulations and three-dimensionality in vortex shedding behind a normal plate, Journal of Fluid Mechanics, Vol. 526, pp. 117-146.

Woo H.G., Cermak J.E., Peterka J.A., 1993, On vortex locking-on phenomenon for a cable in linear shear flow , Journal of Wind Engineering and Industrial Aerodynamics, Vol. 14, pp. 289-300.

Zdravkovich M.M., 1990, Conceptual over view of laminar and turbulent flows past smooth and rough cylinders, Journal of Wind Engineering and Industrial Aerodynamics, Vol. 33, pp. 53-62.

Appendix E

Proceedings of ASME 2010 3rd Joint US-European Fluids Engineering Summer Meeting and 8th international conference on Nanochannels, Microchannels and Minichannels
FEDSM2010-ICNMM2010
August 2-4, 2010, Montreal, Canada

FEDSM2010-ICNMM2010-30498

EXPERIMENTAL INVESTIGATION OF THE WAKE OF A DISCONTINUOUS CYLINDER

V. S. R. Mandava
Universitat Rovira i virgili
Department d'Enginyeria quimica
Tarragona, Cataluña, Spain

Gregory A. Kopp
University of Western Ontario
Faculty of Engineering
London, Ontario, Canada
e-mail: gakopp@uwo.ca

Joan Herrero
Universitat Rovira i Virgili
Department d'Enginyeria quimica
Tarragona, Cataluña, Spain

Francesc Giralt
Universitat Rovira i Virgili
Department d'Enginyeria quimica
Tarragona, Cataluña, Spain
e-mail: fgiralt@urv.cat

ABSTRACT

The effects of a discontinuous cylinder geometry on the near wake structures was investigated experimentally. This 'discontinuous' circular cylinder has gaps so that solid segments 5D long are followed by gaps 2.5D long, in a repeating pattern, where D is the diameter of the cylinder. A thin steel plate was used to hold all of the cylinder pieces together. Thus, a three-dimensional (3D) wake was created at the origin with the intent to force the near wake flow to have similar structural characteristics as the far wake behind an 'infinite/continuous' cylinder, i.e., a near wake flow with horseshoes or double rollers formed by rapid kinking of Kármán-like vortices. Since the kinetic energy associated with the fluctuations of these near-wake 3D vortical structures is high, the flow system is considered suitable to clarify the role of these velocity patterns in the entrainment process of wake flows, which is still the subject of controversy. Particle Image Velocimetry (PIV) and Hot-Wire Anemometry (HWA) techniques were used to analyze the flow at two Reynolds numbers, Re=10000 and 4000, in the wake of the discontinuous cylinder up to x/D=190 downstream. The development of double rollers resulting from the interaction between the high momentum flow through the gaps and the Kármán-like vortices formed behind the solid cylindrical segments was confirmed. The Strouhal number of the double rollers in the wake is 0.14. These vortices have a dominant role in the initial wake growth. Thus, the overall flow dynamics are similar to the momentum transfer that takes place at the scale of the intermittent turbulent bulges that protrude from the wake in the far region and that were reported to be associated with double rollers.

INTRODUCTION

Understanding the kinematics and dynamics of entrainment and mixing is important in many practical engineering situations. Entrainment has been considered by many researchers as a large-scale process, e.g., [1,2] and several phenomenological descriptions have been proposed in the past. Examples are the vortex sheet roll-up due to a Kelvin-Helmholtz instability and entrapment of external fluid into the core of the vortex [3-5]; Townsend´s growth-decay model [1,6]; 'sweeping' non-turbulent fluid into the turbulent region by rotational motions [2]. These theories or phenomenological models do not explain the role of large scale vortical structures in relation to the initial conditions that generate them. In contrast to the large-scale approaches to entrainment just mentioned, Mathew and Basu [7] and Westerweel et al. [8] concluded that the mechanism of entrainment process is dominated by small scales (nibbling). Thus, it is still not clear whether the entrainment process occurs as a result of outward spreading of small-scale vortices by "nibbling" or by the action of large-scale eddies in the region of the turbulent-nonturbulent interface.

Wakes are an ideal flow system to study the genesis of large scale vortices and their dynamical evolution with respect to initial flow conditions. The instability and transition in the near wake has been studied by many researchers [9-15]. Several numerical and experimental studies have also been carried out in the past to characterize the three-dimensional (3D) nature of wake flows and vortex shedding by exciting 3D modes at the originating body, e.g., [16-22]. A more radical initial perturbation in a 2D wake flow behind a continuous/infinite body in the spanwise direction could be attained by alternating solid with discontinuous segments of the same body in a repeating pattern. This would have the benefit of not changing the basic body geometry that generates the wake flow.

In the current study, we have considered a 3D cylinder configuration with gaps, i.e., segments of equidistant cylinders along the cylinder center axis. With this arrangement, part of the free stream flow passes through the gaps while the rest passes over the 3D cylinder segments, forming a 3D wake. The free stream flow through the gaps would move inwards towards each wake behind the cylindrical segments due to the pressure gradients. Simultaneously, Kármán-like vortices would be formed behind the solid segments together with other vortical structures at both ends. This new configuration of the initial flow conditions should cause kinking of the segmented, 3D Kármán-like vortices with horseshoe/double-rollers vortices generated in the near wake. These are the vortices that usually occur in the far wake region behind a continuous/infinite cylinder, e.g., [23-26]. As a consequence, the current flow configuration may induce the generation of double rollers early in the wake and show how they evolve with respect to initial flow conditions.

NOMENCLATURE

All lowercase letters represents the mean flow variables and they are also normalized with free-stream velocity (U) and cylinder diameter (D)

D	Diameter of a cylinder piece (m)
U	Free stream velocity (m/sec)
u	Stream-wise velocity
v	Transverse velocity
w	Span-wise velocity
u′	Stream-wise root mean square velocity
u′u′	Stream-wise normal stress
u′v′	Shear stress on x-y plane
u′w′	Shear stress on x-z plane
v′	Transverse root mean square velocity
v′v′	Transverse normal stress
ω_y	Transverse vorticity
ω_z	Span-wise vorticity
$y^{1/2}$	wake half-width

EXPERIMENTAL DETAILS

Preliminary experiments were carried out in a small open-return wind tunnel at the Boundary Layer Wind Tunnel Laboratory (BLWTL), University of Western Ontario, Canada, while the majority of the experiments were conducted in the open return wind tunnel of the Chemical Engineering Department at the Universitat Rovira i Virgili in Tarragona. In both wind tunnels, measurements were conducted with the same discontinuous cylinder model and at the same free-stream velocity, U = 9.2m/s, thus, at the same Reynolds number Re = 10^4. The diameter (D) of the cylinder pieces was 0.0163m, the length of each segment was 5D, and the gap between the cylinder pieces was 2.5D. A thin steel plate, whose thickness was 0.81mm and width equal to the cylinder diameter, held the cylindrical pieces together without interfering significantly with the flow between the gaps. The dimensions of the model and co-ordinate system used are shown in Fig. 1. At Re = 10^4, the boundary layer on the cylinder surfaces is laminar, while the wake is fully turbulent [27]. Particle image velocimetry (PIV) was used to measure the instantaneous velocity field in the wake region.

First, several measurements were conducted in Canada, in the near wake region up to 8.5 diameters downstream on transverse (x-y) planes, along the cylinder axis. Planes at every half a diameter width, from center of the middle cylinder piece (z/D=0) to the end of the middle cylindrical section (z/D=2.5), were examined. Two measurements were carried out within the gap region between cylindrical section, one at 0.5D away from the edge of the cylinder piece (i.e., at z/D=3.0) and the other at the center of the gap region (z/D=3.75). Several experiments were carried out on transverse(x-y) planes to check flow symmetry.

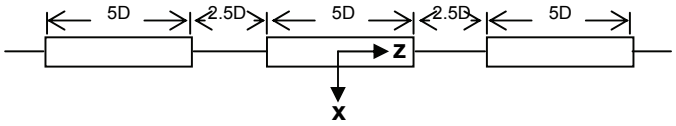

Figure 1. Cylinder model and co-ordinate system; y is vertical upwards for a normal right-handed Cartesian coordinate system

The experiments were repeated with stereo particle image velocimetry in Tarragona, Spain, with the same discontinuous cylinder configuration (Fig. 1) but with five cylinder segments, instead of the three in the earlier setup. The data obtained were in agreement, within the measurement uncertainty, with the earlier experimental data obtained in Canada.

Measurements in Tarragona extended further downstream in the wake at several vertical (x-y) planes, x/D=9 to 16, 26 to 36, 43 to 56, 70 to 90, 110 to 130, and 170 to 190, in the central plane of the discontinuous cylinder (z/D=0). Experiments were also conducted in the horizontal (x-z) planes in the wake, from x/D=10 to 20 at y/D=2, and 27 to 36 at y/D=3. All PIV experiments up to x/D=56 downstream wake were conducted at flow Reynolds

number Re=10000 and the experiments in the wake further downstream were carried out at the Reynolds number Re=4000. Data for the corresponding wake of an infinite cylinder were also collected in the same vertical and horizontal planes. The aspect ratio of the infinite cylinder was 37 and the blockage in the tunnel was 2.7%. TSI Insight 3G software was used, in all cases, for frame to frame correlation to generate instantaneous velocity fields, with an interrogation window of size 32 x 32 pixels with 50% overlap. These instantaneous velocity fields were then ensemble averaged to determine the mean streamwise and transverse velocities, root mean square (r. m. s) velocity fluctuations, mean Reynolds shear stresses and mean z-vorticity patterns on all the transverse (x-y) and horizontal (x-z) planes. The instantaneous data on horizontal planes were used to identify the footprints of double rollers in the near wake.

Hot-wire anemometry (HWA) experiments were also carried out at several downstream stations (x/D=12, 16, 26, 52, 76, 120, 170 and 190), in the near and far wake regions of the wake at Reynolds number Re=4000. A horizontal rake, which is movable on transverse axis, was placed parallel to spanwise axis in the wake. The rake consists of three normal wire probes, positioned at the center of the middle cylinder piece (z/D=0), at the end of the middle cylinder piece (z/D=2.5) and at the center of the gap region (z/D=3.75), respectively, and was used to collect the streamwise velocity (u) data at three spanwise locations simultaneously. At every downstream station, the rake was moved on transverse axis and collected data from middle of the wake (y/D=0) to the outer edge of the wake. The used spatial resolutions on transverse axis were different from near wake to the far wake and are shown in table 1. At all points, the data were acquired for 120sec at a sampling rate of 5 kHz and low pass filtered at 2 kHz and stored on a computer for subsequent processing. These data are used to show the spectra and the evolution of mean and rms (root-mean–square) values of the fluctuations of the stream-wise velocity. The data were also used to verify the consistency of the PIV data.

Down stream station (x/D)	Spatial resolution (Spacing/D)
12	0.11
16	0.11
26	0.15
52	0.23
76	0.31
120	0.38
170	0.46
190	0.46

Table 1. Spatial resolution on transverse axis at different downstream stations.

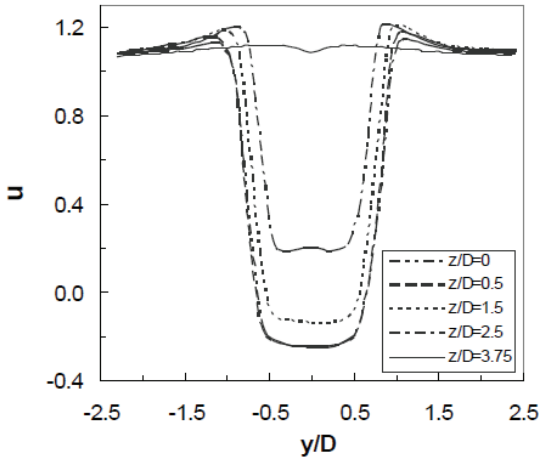

(a)

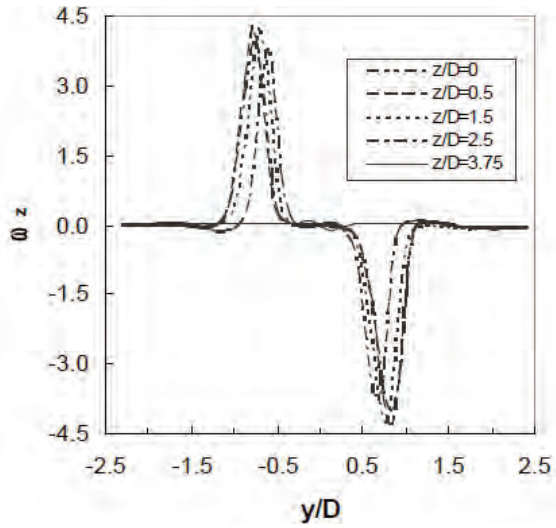

(b)

Figure 2. (a) Profiles of mean streamwise velocity (u) at x/D=1; (b) profiles of mean z-vorticity (ω_z) at x/D=1

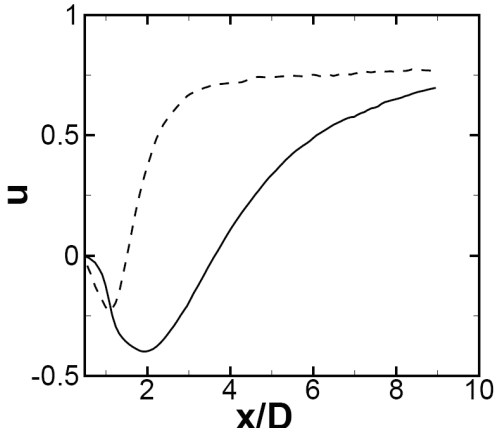

Figure 3. Mean streamwise velocity (u) on wake centerline (y/D=0) of discontinuous (—) and continuous (----) cylinders

WAKE CHARACTERISTICS

Current data for the continuous/infinite cylinder were compared and found in reasonable agreement with measurements reported in the literature [15,28]. In the following sections, discontinuous and infinite cylinder data are compared. The plots presented in the paper are, unless specified, on transverse planes at z/D=0. In all contour plots flow direction is from left to right and, positive and negative magnitude of contours are indicated by solid and dashed lines, respectively.

For the discontinuous cylinder case, note that the velocity defect and vorticity levels in the wake downstream of the gaps are much smaller than those in the wake directly behind each cylindrical section (Fig. 2).

The vortex formation length is defined as the distance between the separation point and the location at which the vortex is fully formed [28-32]. The formation length for the wake for the discontinuous cylinder is 3.62D, and the corresponding value for the infinite cylinder is 1.5D in the present experiments, consistent with the result found by Norberg [28]. As used in Norberg [28], we have used time-averaged closure point (i.e., the saddle point on the wake centerline in Figure 3) to measure the formation length.

The mean streamwise velocities on the wake centerline (Fig. 3) show strong negative values (reversed flow) in the base region. The magnitude of the minimum velocity and the location where this occurs are different from the infinite cylinder case. The maximum magnitude of the negative velocity is 0.40 and the corresponding value for the infinite cylinder is 0.23 in the current experiments. The width of the wake at x/D=1.5 is much wider than the wake behind the infinite cylinder (Fig. 4a). The wake has a greater velocity deficit in the region close to the cylinder when compared to the infinite cylinder case, but as the wake grows downstream it recovers quickly (Fig. 4).

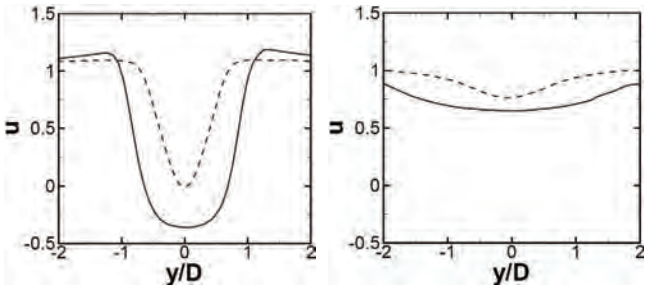

Figure 4. Comparison of mean streamwise velocity (u) in discontinuous (—) and continuous (----) cylinder wakes at (a) x/D=1.5; (b) x/D=8

The u′ and v′ are the streamwise and transverse rms velocities. The magnitude of the maximum fluctuations of the normalized rms streamwise velocity (u′) for the discontinuous cylinder is smaller. The corresponding location is displaced further downstream compared to the infinite cylinder case. The maximum value is 0.30 and occurs at x/D=2.5. The corresponding values for the infinite cylinder are 0.45 at x/D=1.4 from the current experiments.

ENTRAINMENT PROCESS

The horseshoe eddy is a structure with two legs which are shear aligned and connected at the top with spanwise vorticity. The cross-section of the two legs forms a double roller pattern on the horizontal plane [25,26]. These double roller structures, which are known to appear in the far wake region behind an infinite cylinder, are also observed in the near wake (x/D≈15) of the discontinuous cylinder, as shown in Fig. 5. The vectors of streamwise and spanwise velocity fluctuations on horizontal (x-z) plane clearly depict in this figure the footprints of double roller vortices early in the discontinuous wake development. Similar kind of double roller structures are found on the horizontal plane further downstream (x/D≈30) behind the discontinuous cylinder, as shown in Fig. 6.

The corresponding mean streamwise velocity (u) profiles at different downstream stations in the plane z/D=0 are shown below (Fig. 7). The profiles in the wake up to x/D=12 downstream are Gaussian (Fig. 4 & Fig. 7), while further downstream wake the profile has two minima, probably because of the rotation of the double rollers, which will input momentum close to the interface (lower defects with steeper u-velocity gradients) and a negative input closer to the center line (opposed rotation or the wake movement).

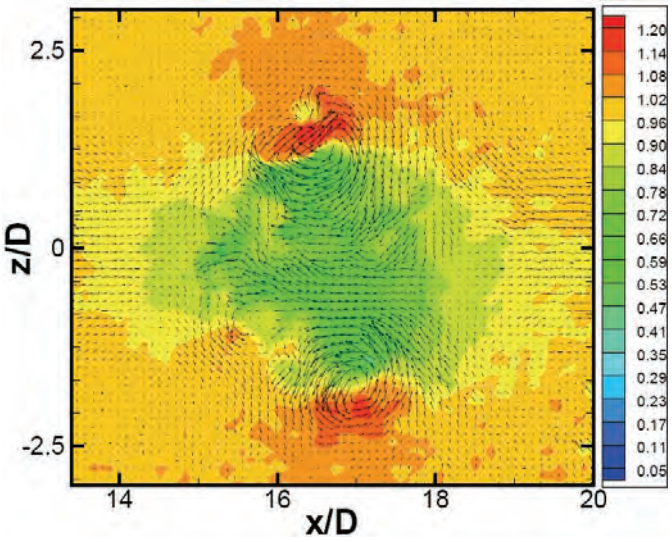

Figure 5. An example of normalized (u,w) velocity fluctuations and u velocity contours in the near wake behind the discontinuous cylinder, at y/D=2, showing double roller patterns.

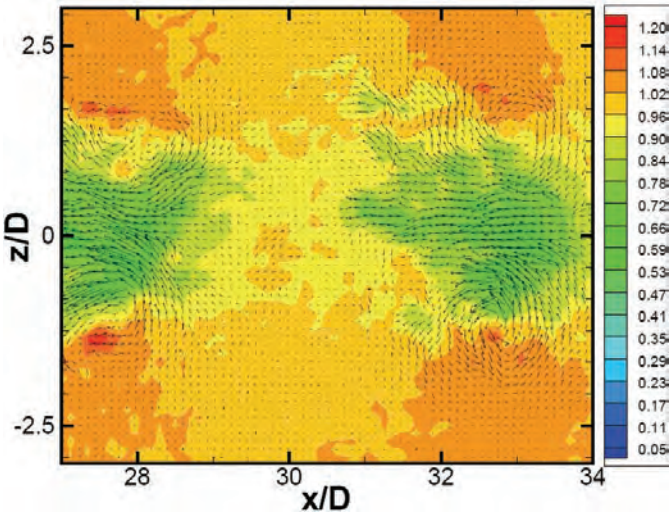

Figure 6. An example of normalized (u,w) velocity fluctuations and u velocity contours in the medium far wake behind the discontinuous cylinder, at y/D=3, showing double roller patterns.

The corresponding profiles of streamwise rms velocity fluctuations (u´) at several downstream stations are show in Fig. 8. At the downstream station, x/D=190, the peak in the profile almost disappears and the profile looks flat with very low fluctuation levels.

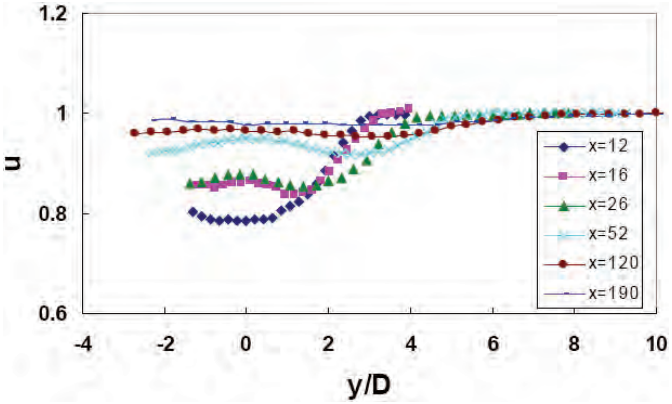

Figure 7. The profiles of mean streamwise velocity (u) at several downstream stations in the plane z/D=0

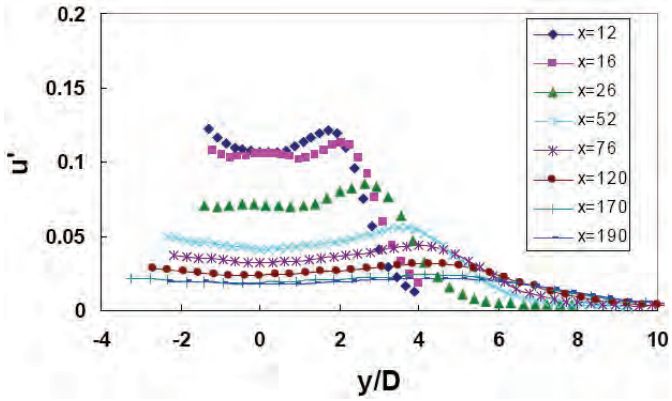

Figure 8. The profiles of rms streamwise velocity fluctuations in the plane z/D=0

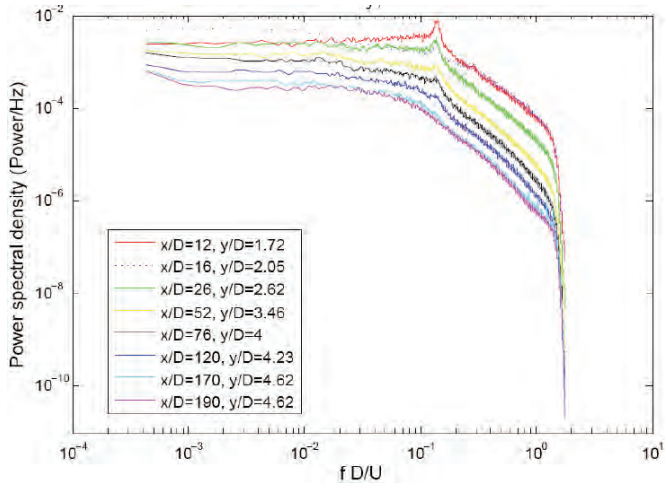

Figure 9. Spectra at different down stream stations in the plane z/D=0

The spectra at several down stream stations in the plane z/D=0 is shown in Fig. 9. It shows that the non dimensional shedding frequency (Strouhal number) of the dominant structures in the wake is 0.14. The corresponding value for the continuous cylinder wake is 0.2. The spectra also shows that the dominant structures in the wake have higher energy levels up to x/D=120, and further downstream in the wake they are comparable with the energy levels of the surrounding turbulent flow.

The corresponding spanwise profiles of mean y-vorticity and mean u'w' shear stresses are presented in Fig. 10. The Fig. 10a shows how the y-vorticity decreases with x/D as double rollers are advected downstream and diffused. The u'w' shear stress also diminishes with x/D (Fig. 10b), which is indicative of the wake evolution towards fully development (u´w´=0).

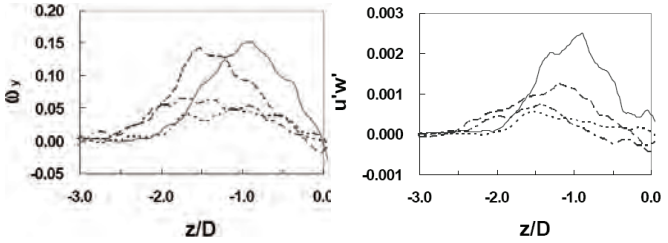

(a) (b)

Figure 10. The profiles of (a) mean y-vorticity (ω_y), at x/D=11 and y/D=2 (—), x/D=19 and y/D=2 (– – –), x/D=28 and y/D=3 (……) and x/D=36 and y/D=3 (-.-.-.-); (b) mean shear stress (u´w´), at x/D)=11 and y/D=2 (—), x/D=19 and y/D=2 (– – –), x/D=28 and y/D=3 (……), and x/D=36 and y/D=3 (-.-.-.-)

Double rollers are responsible for maintaining the correlation between the streamwise and lateral velocity fluctuations, with correlation being largest at the center plane of the structure [33]. The profiles of normalized shear stress (u´v´) at several downstream locations on wake center line are shown in Fig. 11. The shear stress peaks close to the wake formation length at x/D=3, and then decreases as x/D increases. Again, the input of momentum by the high velocity flow in the gap seems evident.

The Fig. 12 shows that the wake thickness and growth rate in the current discontinuous cylinder case are both larger than for the continuous cylinder wake. The Dumax and Ducl are the maximum velocity deficit and the wake centerline velocity deficit respectively, at that downstream station.

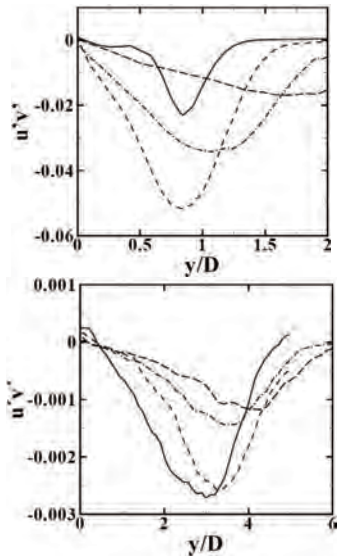

(a) (b)

Figure 11. The profiles of mean shear stress (u´v´) at (a) x/D=1.5 (—), x/D=3 (----), x/D=5 (-.-.-.-) and x/D=8 (– – –); (b) x/D)=26 (—), x/D=32 (----), x/D=44 (-.-.-.-),x/D=56 (– – –)

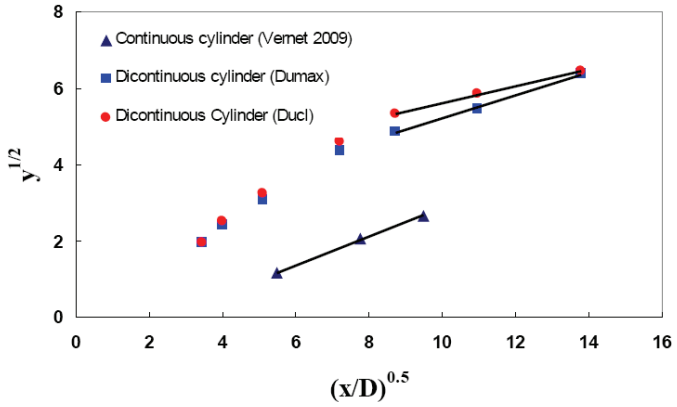

Figure 12. Variation of the wake half-width with streamwise location for both the discontinuous and continuous cylinder

Spanwise variation of the wake

The comparison of the wake behind a cylinder piece and in the gap region is shown below with the profiles of streamwise rms velocity fluctuations (Fig. 13) and spectra (Fig. 14). Close to the cylinder the mean flow is far from uniform in the span-wise direction but at x/D=190 the flow is uniform on spanwise direction, probably this is because of the 3D structures formed in the near wake are diffused to span-wise direction as they advect to downstream.

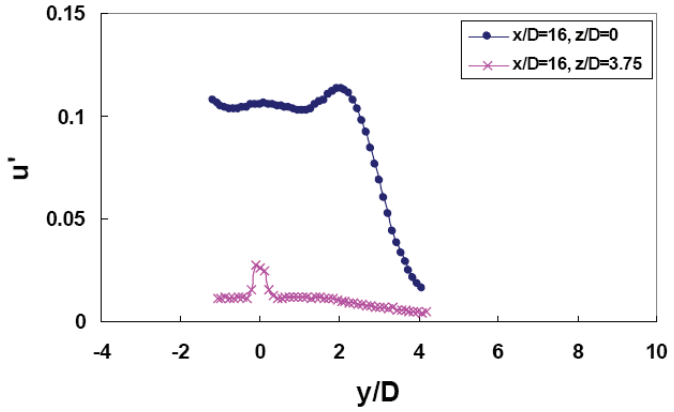

(a)

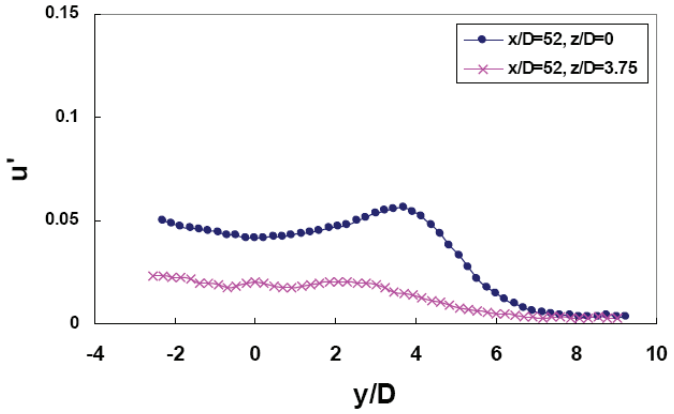

(b)

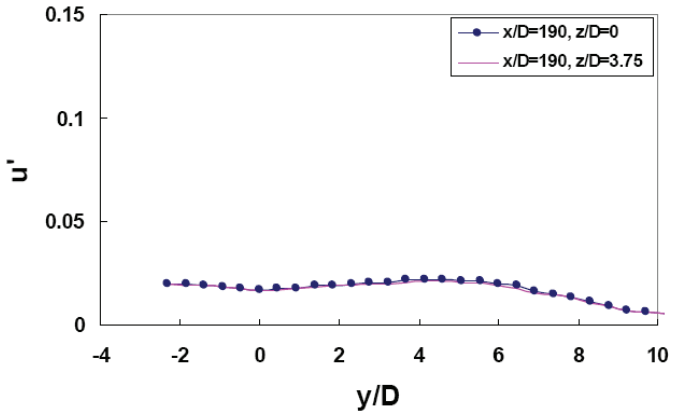

(c)

Figure 13. Comparison of the profiles of streamwise rms velocity fluctuations in the planes z/D=0 and z/D=3.75, at (a) x/D=16 (b) x/D=52, (c) x/D=190

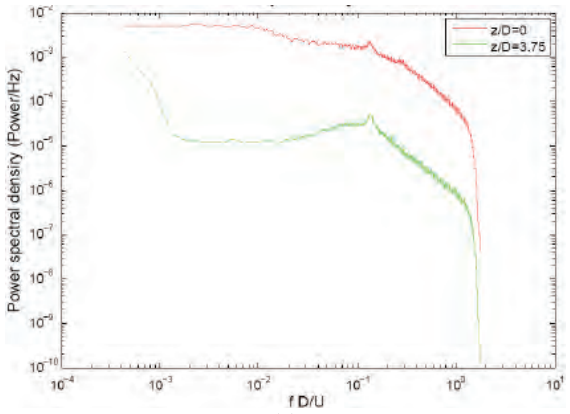

(a)

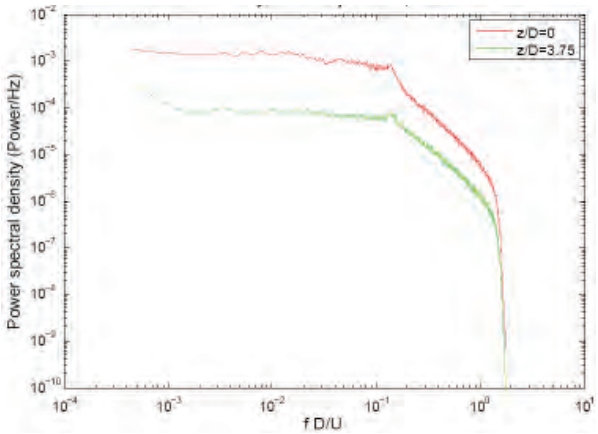

(b)

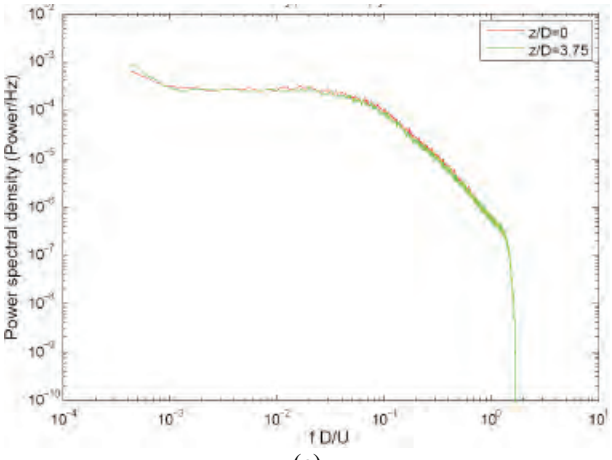

(c)

Figure 14. Comparison of the spectra in the planes z/D=0 and z/D=3.75, at (a) x/D=16 (b) x/D=52 (c) x/D=190

CONCLUSIONS

The effect of inflow conditions on the near wake and far wake structures behind a discontinuous cylinder, at Reynolds numbers Re=10000 and 4000 was investigated experimentally. The flow statistics such as mean velocities, rms velocity fluctuations, mean Reynolds shear stress and mean z-vorticity of the discontinuous cylinder have been compared with the corresponding data for an infinite cylinder wake. The wake bubble behind the segments of the discontinuous cylinder is significantly longer than that for the infinite cylinder, i.e., the formation length is longer. This delay shedding may be related to the converging streamlines in the wake from ends of the cylinder due to the inflow of high momentum fluid through the gaps. The wake width of the discontinuous cylinder is much wider and grows faster than that for the infinite cylinder. The velocity deficit is larger in the near wake region, but as the wake grows downstream it recovers quickly. Footprints of double-roller vortices have been unambiguously identified on the horizontal planes in the wake of the discontinuous cylinder. The non-dimensional shedding frequency (Strouhal number) of the double rollers in the wake is 0.14. The wake is far from uniform on spanwise axis at close to the cylinder, but at downstream station x/D=190 it is uniform on spanwise direction. The spread rate for the discontinuous cylinder is substantially larger than the continuous cylinder.

ACKNOWLEDGMENTS

The current study was supported by the grants FIS2005-07194 and CTQ2008-04857/PPQ (MEC & MICINN, Spain), and 2005SGR-00735 and 2009SGR-01529 (DURSI, Generalitat de Catalunya). Francesc Giralt acknowledges the Distinguished Researcher Award, Generalitat de Catalunya. G.A. Kopp gratefully acknowledges the support of the Canada Research Chairs Program.

REFERENCES

[1] Townsend, A. A., 1976, "The structure of turbulence shear flow," 2nd edn. Cambridge University Press.
[2] Bevilaqua, P. M., and Lykoudis, P. S., 1977, "Some observation on the mechanisms of entrainment," AIAA Journal, 15, pp. 1194-1196.
[3] Prandtl, L., and Tietjens, O. G., 1934, "Fundamentals of hydro- and aeromechanics," United engineers Trustees.
[4] Sreenivasan, K. R., Ramshankar, R., and Meneveau C., 1989, "Mixing, entrainment and fractal dimensions of surfaces in turbulent flows," Proc. R. Soc. Lond. A, 421, pp. 79-108.
[5] Caulfield, C. P., and Peltier, W. R., 2000, "The anatomy of mixing transition in homogeneous and stratified free shear layers," Journal of Fluid Mechanics, 413, pp. 1-47.
[6] Townsend, A. A., 1966, "The mechanism of entrainment in free turbulent flows, Journal of Fluid Mechanics," 26, pp. 689-715.
[7] Mathew, J., and Basu, A. J., 2002, "Some characteristics of entrainment at a cylindrical turbulence boundary," Physics of Fluids, 14, pp. 2065-2072.
[8] Westerweel, J., Fukushima, C., Pedersen, J. M., and Hunt, J. C. R., 2005, "Mechanics of the turbulent and non-turbulent interface of a jet," Physical Review Letters, 17, pp. 174501.
[9] Gerrard, J. H., 1967, "Experimental investigation of separated boundary layer undergoing transition to turbulence," Physics of Fluids, 10, pp. S98-100.
[10] Roshko, A., and Fiszdon, W., 1969, "On the persistence of transition in the near wake," Problems of Hydrodynamics and Continuum Mechanics," pp. 606-616. SIAM
[11] McCroskey, W. J., 1977, "Some current research in unsteady fluid dynamics – the 1976 freeman scholar lecture," Journal of Fluids Engineering, 99, pp. 8-39.
[12] Zdravkovich, M. M., 1990, "Conceptual over view of laminar and turbulent flows past smooth and rough cylinders," Journal of Wind Engineering and Industrial Aerodynamics, 33, pp. 53-62.
[13] Williamson, C. H. K., 1996, "Vortex dynamics in a cylinder wake," Annual Review of Fluid Mechanics, 28, pp. 477-539.
[14] Norberg, C., 2003, "Fluctuating lift on a circular cylinder: review and new measurements," Journal of Fluids and Structures, 17, pp. 57-96.
[15] Dong, S., Karniadakis, G. E., Ekmekci, A., and Rockwell, D., 2006, "A combined direct numerical simulation – particle image velocimetry study of the turbulent near wake," Journal of Fluid Mechanics, 569, pp. 185-207.
[16] Bearman, P. W., and Tombazis, N., 1993, "The effects of 3-dimensional imposed disturbances on bluff-body near wake flows," Jounal Wind Engineering and Industrial Aerodynamics, 49(1-3), pp. 339-349.
[17] Bearman, P. W., and Owen, J. C., 1998, "Reduction of bluff-body drag abd suppression of vortex shedding by the introduction of wavy separation lines," Jounal of Fluids and Structures, 12, pp. 123-130.
[18] Darekar, R. M., and Sherwin, S. J., 2001, "Flow past a bluff body with a wavy stagnation face," Journal of Fluids and Structures, 15(3-4), pp. 587-596.
[19] Lam, K., Wang, F. H., Li, J.Y., and So, R. M. C., 2004, "Experimental investigation of the mean and fluctuating forces of wavy (varicose) cylinders in a cross-flow," Journal of Fluid and Structures, 19(3), pp. 321-334.
[20] Wu, S. J., Miau, J. J., Hu, C. C., and Chou, J. H, 2005, "On low-frequency modulations and three-dimensionality in vortex shedding behind a normal plate," Journal of Fluid Mechanics, 526, pp. 117-146.
[21] Lee, S. J., and Nguyen, A. T., 2007, "Experimental investigation on wake behind a wavy cylinder having sinusoidal cross-sectional area variation," Fuid Dynamics Research, 39(4), pp. 292-304.
[22] Ling, G.. C., and Lin, L. M., 2008, "A note on the numerical simulations of flow past a wavy square-section cylinder," Acta Mechanica Sinica, 24(1), pp. 101-105.

[23] Ferré, J. A., and Giralt, F., 1988, "Pattern recognition analysis of the velocity field in plane turbulent wakes," Journal of Fluid Mechanics, 198, pp. 27-64.
[24] Giralt, F., and Ferré, J. A., 1993, "Structure and flow pattern in turbulent flow," Physics of Fluids, A5, pp. 1783-1789.
[25] Vernet, A., Kopp, G.. A., Ferré, J. A., and Giralt, F., 1999, "Three-dimensional structure and momentum transfer in a turbulent cylinder wake," Journal of Fluid Mechanics, 394, pp. 303-337.
[26] Kopp, G.. A., Giralt, F., and Keffer, J. F, 2002, "Entrainment vortices and interfacial intermittent turbulent bulges in a plane turbulent wake," Journal of Fluid Mechanics, 469, pp. 49-70.
[27] Dimotakis, P. E., 2000, "The mixing transition in turbulent flows," Journal of Fluid Mechanics, 409, pp. 69-98.
[28] Norberb, C., 1998, "LDV-measurements in the near wake of a circular cylinder, Advances in understanding of bluff body wakes and vortex induced vibrations," Washington DC, June 1998.
[29] Bloor, S., 1966, "The transition to turbulence in the wake of a circular cylinder, Journal of Fluid Mechanics," 19, pp. 290-304.
[30] Woo, H. G., Cermak, J. E., and Peterka, J. A., 1983, "On vortex locking-on phenomenon for a cable in linear shear flow," Journal of Wind Engineering and Industrial Aerodynamics, 14, pp. 289-300.
[31] Norberg, C., 1986, "Interaction between freestream turbulence and vortex shedding for a single tube in cross flow," Journal of Wind engineering And Industrial Aerodynamics, 23, pp. 501-514.
[32] Govardhan, R., and Williamson, C. H. K., 2001, "Mean and fluctuating velocity fields in the wake of a freely vibrating cylinder," Journal of Fluids and Structures, 15, pp. 489-501.
[33] Vernet, A., Kopp, G. A., Ferré, J. A., and Giralt F., 1997, "Simultaneous velocity and temperature patterns in the far region of a turbulent cylinder wake," Journal of fluids Engineering, 119, pp. 463-466.
[34] Vernet, A., 2009, Private communication

J. Fluid Mech. (2022), *vol*. 936, A4, doi:10.1017/jfm.2022.32

Appendix F

Wake behind a discontinuous cylinder: unveiling the role of the large scales in wake growth and entrainment

V.S.R. Mandava[1], Joan Herrero[1], Gregory A. Kopp[2] and Francesc Giralt[1],†

[1]Departament d'Enginyeria Química, Universitat Rovira i Virgili, Tarragona, Catalunya 43007, Spain

[2]Boundary Layer Wind Tunnel Laboratory, Faculty of Engineering, University of Western Ontario, London, ON N6A 5B9, Canada

(Received 25 February 2021; revised 25 October 2021; accepted 28 December 2021)

The turbulent flow in the wake of a discontinuous cylinder (DC) was investigated. The DC geometry consisted of cylinder segments $5D$ long (with D being the diameter of the cylinder) separated by gaps of width $2.5D$. Particle image velocimetry and hot-wire anemometry were used to analyse the flow at two Reynolds numbers, $Re = 4000$ and 10 000, for $x/D \leq 180$. Large eddy simulations for both the DC and the infinite continuous cylinder (CC) wakes were also carried out at $Re = 10\,000$. The DC configuration was devised to trigger the shedding of horseshoe vortices (HSV) in the very-near-wake region with the intent of illustrating the role that these three-dimensional HSVs, previously identified in the far-wake region of CC, play in the entrainment process in turbulent wakes. The DC geometry produced HSVs by the interaction between the high momentum flow through the gaps and the main spanwise vortex shed behind each cylinder segment, while in the CC wake they evolve from near-wake instabilities straddled with hairpin vortices that detach spanwise vorticity from the shed Kármán vortices. The DC wake was found to grow and spread in the transverse direction with a much faster rate than for the CC wake, up until approximately $x/D \approx 50$. Prior to this location, the enhanced growth rate caused by the shear-aligned HSV led to a wake width of approximately 3 times that of the CC wake, with a maximum mean velocity deficit that was approximately half.

Key words: vortex shedding, wakes, turbulent convection

1. Introduction

1.1. *Background and objectives*

Entrainment is the process that enables the growth and spread of turbulent shear flows. Because of its importance for many engineering and geophysical applications, the physics

† Email address for correspondence: fgiralt@urv.cat

of turbulent entrainment have been thoroughly investigated. A concept that has commonly been used in studies of entrainment and growth of turbulent shear flows is the existence of a turbulent/non-turbulent interface (TNTI), which separates the regions of turbulent flow from those of non-turbulent flow. Corrsin & Kistler (1955) postulated two important hypotheses: (i) that there is a step-like change in velocity across the TNTI, and (ii) that the spreading process of turbulence into the non-turbulent flow region is similar to turbulent diffusion, a process that has been commonly referred to as 'nibbling'. The first point indicates that the TNTI is typically sharp, with a thickness of approximately one to two orders of magnitude smaller than the integral flow scale (Chevray 1982; Bisset, Hunt & Rogers 2002; Hunt, Eames & Westerweel 2006). The latter point suggests that engulfment, which is the name given to the process where large eddies draw fluid from the non-turbulent region into the turbulent flow (Brown & Roshko 1974; Townsend 1976), does not play a major role in the entrainment process. Townsend (1976) disagreed with Corrsin & Kistler's (1955) second hypothesis and claimed that the bulk motion is sufficient to determine the wake spreading and entrainment rates in free shear flows.

Within the core of turbulent shear flows, there is typically a region where the flow is fully turbulent. For example, for the far field of plane turbulent wakes, the intermittency factor, which is the proportion of time that the flow is turbulent at a point, is unity for $y/y_{1/2} <\approx 1$ (Kopp, Giralt & Keffer 2002), where y is the distance from the centreline and $y_{1/2}$ is the mean velocity half-width. For distances further from the centreline, the turbulent flow is intermittent and is made up of turbulent bulges of varying sizes. LaRue & Libby (1974) found that the bulges are consistent with the three-dimensional double roller vortices first proposed by Grant (1958). Thus, Corrsin & Kistler's (1955) velocity step change across the TNTI is connected to the coherent structures (CS) in the flow field. Further, Kopp *et al.* (2002) found that (i) the bulges are, in fact, made up of the both the three-dimensional horseshoe/double roller vortices and a region of high strain in the region immediately upstream of these vortices, and that (ii) the shape of the interface depends on this structure with the upstream edge being shear-aligned while the downstream edge is not. This implies that the growth or spread of the plane turbulent wake, as indicated by the evolution of the TNTI is controlled by the nature of the CS within the turbulent bulges.

However, the historical disagreement regarding the mechanism of entrainment remains. For example, more recent studies (e.g. Mathew & Basu 2002; Westerweel *et al.* 2005; Holzner *et al.* 2007; DaSilva & Pereira 2008; Hunt *et al.* 2011) suggest that nibbling is the main mechanism of entrainment in turbulent jet flow, in agreement with the second hypothesis of Corrsin & Kistler (1955). Westerweel *et al.* (2009) showed that large-scale engulfment would account for less than 10 per cent of the total fluid mass entrained and suggested that the entrainment process is mainly dominated by small-scale nibbling. More recently, Philip & Marusic (2012) showed that the mean velocities and second-order statistics in jet and wake flows could be obtained by a large-scale eddy model that they proposed and concluded that the primary cause of entrainment could be the large-scale engulfment, combined with small-scale nibbling.

Thus, while the rate of entrainment of non-turbulent flow into a turbulent shear flow is clearly related to the characteristics of the TNTI, the role of the motions present in the turbulent region near the TNTI remains unclear. Given these discrepancies, it appears that entrainment must be flow dependent. The purpose of the paper is to examine this issue, i.e. to determine the role of flow-dependent CS in controlling the entrainment rate and the mechanisms of nibbling and engulfment. To achieve this, we develop a three-dimensional flow based on careful modifications to the flow field of the circular cylinder, as discussed next.

1.2. *Role of CS in entrainment for plane turbulent wakes*

The wake behind a circular cylinder is an ideal flow system to study the genesis of large-scale structures and their dynamical evolution with respect to initial flow conditions. Numerous numerical and experimental studies have been carried out in the past to characterize the large-scale structures in the near-, mid- and far-wake regions. Early classical works investigated the vortex street (Kármán & Rubach 1912) and the variation of drag of cylinders with aspect ratio (Taylor 1915). Flow instability and transitions in the near wake have been studied by many researchers (e.g. Gerrard 1967; Roshko & Fiszdon 1969; Zdravkovich 1990; Williamson 1996; Norberg 2003). Cantwell & Coles (1983) used flying hot-wire devices together with phase averaging techniques to obtain conditional averages of normal and shear stresses, intermittency, vorticity and velocities in the near turbulent wake of a circular cylinder at a Reynolds number of $Re = 1.4 \times 10^5$. The Reynolds number is defined as $Re = U_0 D/\nu$, where U_0 is the free-stream velocity, D is the cylinder diameter and ν is the fluid (air) kinematic viscosity.

These authors concluded that the mechanism of turbulence production was likely to be vortex stretching at intermediate scales. Entrainment was also found to be closely associated with saddles located between the Kármán vortices, where the maximum value of random shear stress, which is not related to the von Kármán vortices, occurs, suggesting the presence of other three-dimensional structures in the near wake. These three-dimensional structures were later observed by Hayakawa & Hussain (1989).

Hayakawa & Hussain (1989) observed the presence of three-dimensional organized structures in the von Kármán vortex street in the near and mid–far wake, ($10 \leq x/D \leq 40$; x is the streamwise coordinate) at a Reynolds number of $Re = 13\,000$. These authors employed a methodology based on the detection of vorticity peaks in the hot-wire time histories. They reported that the von Kármán vortices (VKV) could be interconnected with secondary vortices having streamwise vorticity. Ferré & Giralt (1989*a*), using a pattern recognition approach, analysed the evolution of large-scale organized motions in the range $10 \leq x/D \leq 40$ at $Re = 9000$. They found and that the periodic activity of the Kármán vortices persists up to 60 diameters downstream. Yamane *et al.* (1988) analysed the wake behind a circular cylinder at $Re = 2100$ and 4200, using a flow visualization technique and simultaneous hot-wire measurements. They reported the predominance of Kármán vortices at $x/D = 10$, the presence of a complex flow field near $x/D = 60$, where transition from Kármán vortices to some new CS takes place, with far-wake large-scale structures that are formed by $x/D = 90$. More recently, the direct numerical simulations carried out by McClure, Pavan & Yarusevych (2019) showed that Kelvin–Helmholtz instabilities led to the formation of hairpin structures in the near wake for $Re \geq 800$ when streamwise vortex pairs pinch off vorticity from Kármán vortices and reorient to form the legs of hairpins. They reported that this regime is characterized by a significant increase in vortex deformation and a wake flow with a large number of hairpin formations.

The existence of large-scale CS in the turbulent far wake of the cylinder has been known for quite long. More generally, the importance of three-dimensional structures in turbulent wakes was well established by the pioneering works of Theodorsen (1952), Townsend (1956) and Grant (1958). Theodorsen (1952) proposed that the predominant structure in a developed wake should be a horseshoe-like vortex. Grant (1958) postulated, on the basis of a comprehensive set of correlation measurements in the far wake of a cylinder at $x/D = 533$, the existence of shear-aligned double roller eddies and 'mixing jets' as ejections of turbulent flow from the centre of the wake towards the non-turbulent external flow region. Ferré & Giralt (1989*a*) refined the pattern recognition technique, previously developed by Mumford (1983), to analyse large-scale motion at $x/D = 140$.

They found that the large-scale flow organization consisted of double roller eddies. Similar double roller-like structures in the far wake were identified later by several researchers (e.g. Ferré & Giralt 1989*b*; Hayakawa & Hussain 1989; Ferré *et al.* 1990; Kopp, Kawall & Keffer 1995). In particular, Giralt & Ferré (1993) determined that the double roller structure, i.e. a pair of counter-rotating vortices, is simply a horizontal slice through a horseshoe vortex near the wake half-width. Vernet *et al.* (1997) gave further evidence, based on their simultaneous temperature and velocity measurements, that Townsend's and Grant's double roller and mixing jet structures are simply different views of a single flow structure, likely a horseshoe-shaped vortex. Vernet *et al.* (1999) identified the complete three-dimensional topology of the large-scale structures by using conditional sampling. They confirmed that the structure shape was similar to a horseshoe vortex. Philip & Marusic (2012) proposed a simplified axisymmetric wake model, based on randomly inclined vortical structures, which was able to reproduce the experimental mean velocity and normal and shear stress profiles. The genesis of these large-scale structures present in the far wake should be the secondary hairpin vortices characterized by McClure *et al.* (2019) in the near wake.

Successful models for plane mixing layer entrainment, with overall rates being determined by the engulfing action of large eddies, were constructed for plane mixing layers (Brown & Roshko 1974). Dahm & Dimotakis (1987) used visualizations and measurements of a scalar concentration in the near field of a jet to show that the entrainment process was dominated by the engulfment of large-scale structures. They also showed that local large scales of the flow can be used to characterize the rate of the entrainment process. Ferré & Giralt (1989*b*) analysed the organized motions of the temperature field in the wake of a heated cylinder at $x/D = 140$ and from the distribution of colder and warmer spots in vertical and horizontal planes they concluded that the double roller vortices are in fact associated with the large-scale entraining motions in the wake. Ferré *et al.* (1990) and Giralt & Ferré (1993) argued that horseshoe vortices should play an important role in the momentum transfer as they maintain the correlation between the streamwise and vertical velocity fluctuations (i.e. Reynolds shear stress). According to this scenario, the external fluid is first ingested by the highly stretched and twisted interior turbulent flow pattern (large-scale structures) and is then mixed to molecular level by the action of the small-scale velocity fluctuations (Kopp *et al.* 2002).

To summarize, there have been several important observations in the literature. First, CS within turbulent shear flows play an important role in setting the details of the TNTI and the rate of entrainment. Second, CS develop and evolve depending on the initial and boundary conditions of the flow. These two observations imply that the relative importance of the nibbling and engulfment mechanisms depend on the flow conditions and the particular details of the CS. Thus, by controlling the development of the CS, like near wake instabilities leading to the formation of hairpins do in a continuous cylinder (CC) turbulent wake, one should control the extent to which each of the mechanisms contribute to the overall entrainment rate. The key question, then, is how to do that, i.e. how to generate hairpin-like structures with high vorticity under turbulent conditions in the near wake. Our hypothesis is that enhancing vortices in the very near wake that are in alignment with the mean shear will increase the rate of entrainment. The shear alignment is critical since it allows the engulfing mechanism to be maintained for a significant duration because vortex stretching will maintain the vorticity in the CS, while in contrast, a lack of shear alignment allows them to decay. This implies that far-wake-type structures such as the shear-aligned horseshoe vortices should have relatively higher entrainment and growth rates than typical near-wake structures such as VKV, which are not shear aligned. The objective of the paper

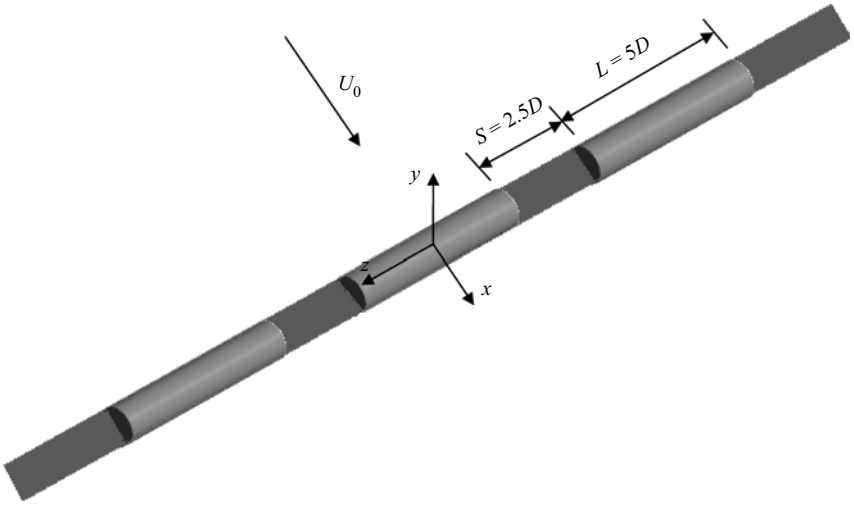

Figure 1. Sketch of the DC model, M_1, used in BLWTL along with the coordinate system.

is to test this hypothesis; namely that shear alignment of CS enhances the entrainment rate by increasing engulfment. To test this hypothesis, we develop what we call a discontinuous cylinder wake, described below, such that relatively intense horseshoe or hairpin vortices are formed much earlier in the wake as a result of a primary instability, increasing the growth rate significantly.

2. Methods

2.1. *Approach*

To investigate our hypothesis, we developed and examined the wake of a segmented circular cylinder, which we refer to as a discontinuous cylinder (DC). As depicted in figure 1, the DC is defined with two non-dimensional parameters: the ratio of the solid segment length to cylinder diameter, L/D, and the gap between the solid segments, S/D. The idea here is to choose values of L/D and S/D such that there is early formation of horseshoe vortices (HSV), as depicted in figure 2, but with a far wake that is two-dimensional in the mean. By forcing the early occurrence of HSV, rather than allowing the normal development of three-dimensional structures in the CC wake, we can examine differences in the overall rates of entrainment. By maintaining a two-dimensional far wake, the self-preserving states between the DC and CC wakes can be compared. Analysis of the self-preserving state provides a framework for the comparison. In particular, if the growth rate of the self-preserving states of the two far wakes are the same, then the difference in wake thickness quantifies the difference in entrainment due to the near DC wake structure.

Several studies have examined the effects of finite cylinder length on the vortex structure in the near wake (e.g. Zdravkovich *et al.* 1989; Norberg 1994; Williamson 1996; Zdravkovich *et al.* 1998; Inoue & Sakuragi 2008). These studies have found a complex dependence of the near-wake vortices on the aspect ratio, L/D. Of importance for the current study, Inoue & Sakuragi (2008) found periodic shedding of HSV for $L/D = 5$ at $Re = 300$ using direct numerical simulations. This size compares favourably with the spanwise extent of HSV in the far wake, which Vernet *et al.* (1999) found to be about $5D$. This suggests that L/D should be similar and, hence, a value of $L/D = 5$ was chosen.

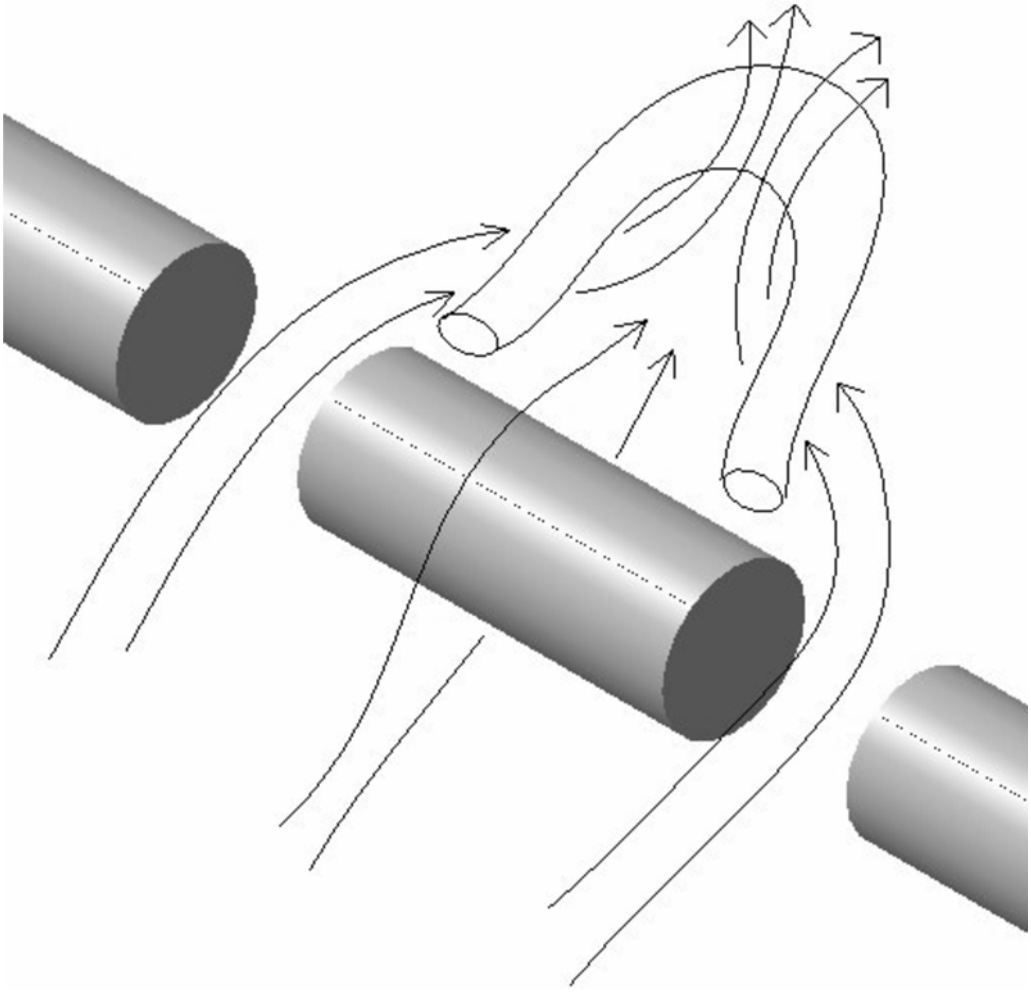

Figure 2. Sketch of the flow in the proximity of the DCs.

To obtain a far wake behind the DC that is two-dimensional in the mean, the gap between the solid cylinder segments, S, should not be too large. However, if S is too small, the gap may be ineffective in allowing the HSV to form in the near wake. Several direct numerical simulations carried out by Mandava *et al.* (2009) at $Re = 300$, when designing their experimental set-up, led to the conclusion that $S/D = 2.5$ and $L/D = 5$ were optimal to shed HSVs behind each segment of the DC configuration in a synchronized manner. This shedding was confirmed experimentally and reported by these authors to also form in the near wake of the DC for $Re = 10\,000$, further investigated here. When these rows of HSVs alternating with jet-like flows in the spanwise direction get randomized, as they are advected downstream, these spanwise variations are smeared away by turbulence and the far wake becomes two-dimensional on average, as is also the case in the CC far wake. It should also be noted that, given the intricately variable wake structures that occur for finite cylinders, the additional parameter, S/D, for the DC could also lead to a rich set of vortical structures. This remains to be explored in future work. We carried out particle image velocimetry (PIV) and hot-wire anemometry (HWA) measurements as well as large

Model name	M_1	M_2	M_3
Wind tunnel label	BLWTL	URV	URV
Cylinder diameter, D (m)	0.0163	0.0163	0.0065
Length of cylinder segment	$5D$	$5D$	$5D$
Gap between cylinder segments	$2.5D$	$2.5D$	$2.5D$
Number of cylinder segments	3	5	7
Plate thickness, λ (mm)	0.815	0.815	0.30
D/λ	20	20	21.67
Tunnel cross-section (m × m)	0.45 × 0.45	0.60 × 0.60	0.60 × 0.60
Tunnel length (m)	1.5	3.0	3.0
Free-stream velocity, U_0 (m s^{-1})	9.2	9.2	9.2
Reynolds number, Re	1.0×10^4	1.0×10^4	4.0×10^3
Free-stream flow turbulence intensity (%)	1.0	0.2	0.2
Measurements in wake region	$0 \le x/D \le 9$ At several z stations	$0 \le x/D \le 56$ At $z = 0$	$70 \le x/D \le 180$ At $z = 0$
Type of measurement plane and PIV system used	x–y planes Two-dimensional PIV	x–y planes Stereo PIV x–z planes Two-dimensional PIV	x–y planes Stereo PIV x–z planes Two-dimensional PIV

Table 1. Geometrical details of the three DC configurations, wind tunnel specifications and experimental conditions.

eddy simulations (LES) to analyse/characterize the wake growth and entrainment rates in the near and far wake of the DC and the analogous CC at the same Re.

2.2. *Experimental details*

Three DC models were used in the current study, as defined in table 1. Two of the DC models, M_1 and M_2, were used to carry out the measurements in the near- and intermediate-wake regions (up to $x/D = 56$) in the Boundary Layer Wind Tunnel Laboratory (BLWTL) at the University of Western Ontario (UWO) and the wind tunnel at Universitat Rovira i Virgili (URV). The discontinuous cylinder configuration, depicted in figure 1, utilized 3 and 5 cylindrical segments in the BLWTL at UWO and URV wind tunnels, respectively. The cylinder diameter was $D = 0.0163$ m in these two models. A thin steel plate having a thickness of $\lambda = 0.815 \times 10^{-3}$ m and a width equal to D held the cylinder segments together without interfering significantly with the flow between the gaps.

To carry out the measurements in the far-wake region, $70 \le x/D \le 180$, a third DC model (M_3) with seven cylinder segments having a smaller diameter ($D = 0.0065$ m) was used in order to bring the far wake into the optimal measurement region of the wind tunnel. The thickness of the steel plate in the M_3 model was reduced to $\lambda = 0.30 \times 10^{-3}$ m in order to maintain the D/λ ratio (see table 1). Since the same free-stream speed was maintained for the M_3 experiments, the Reynolds number in the far wake measurements was lower, as indicated in table 1. The experiments were carried out in an open-return wind tunnel at BLWTL in Canada and in the open-return wind tunnel at URV in Tarragona, Spain. The wind tunnel at BLWTL is of the suction type with a cross-section of

$(x/D_{start}, y/D_{start})$–$(x/D_{end}, y/D_{end})$ plane window	$(0, -2D)$–$(9D, 2D)$							
z/D	0	0.5	1	1.5	2	2.5	3	3.75

Table 2. Two-component PIV window sizes and x–y measurement planes in the near-wake region ($0 \leq x/D \leq 9$), carried out with model M_1.

$(x/D_{start}, y/D_{start})$–$(x/D_{end}, y/D_{end})$ plane window at $z = 0$		DC Model
$(0, -2)$	$(9, 2)$	M_2
$(9, -2)$	$(16, 2)$	M_2
$(26, -2)$	$(36, 6)$	M_2
$(43, -2)$	$(56, 8)$	M_2
$(70, -2)$	$(90, 8)$	M_3
$(110, -2)$	$(130, 8)$	M_3
$(170, -2)$	$(180, 10)$	M_3

Table 3. Stereo PIV window sizes and x–y measurement planes in the near- and far-wake regions. Model M_2 was used for $0 \leq x/D \leq 56$ and model M_3 was used for $70 \leq x/D \leq 180$.

0.45 m × 0.45 m and a length of 1.5 m. The intake flow was straightened through a honeycomb and fine screen prior to entering a 7.4 : 1 contraction. This tunnel was used earlier for wide range of inflow velocities from 1.25 to 17.8 m s^{-1} (see e.g. Bailey, Martinuzzi & Kopp 2002; Martinuzzi, Bailey & Kopp 2003; Dol, Kopp & Martinuzzi 2008; Taylor *et al.* 2011). The free-stream turbulence intensity was 1 %. The wind tunnel at URV was also of the suction type with a cross-section of 0.6 m × 0.6 m and a length of 3 m. A set of flow straighteners and filters and a contraction zone of ratio 9 : 1 produced a low turbulence (less than 0.2 %) for the $U_0 = 9.2$ m s^{-1} free-stream velocity of the current experiments. Previous measurements carried out in this tunnel were published by Vernet *et al.* (1999) and Kopp *et al.* (2002). The value of the Reynolds number, $Re = 1.0 \times 10^4$, was chosen for the present experiments because at this Reynolds number the boundary layer on the cylinder surface is laminar while the flow in the wake is fully turbulent (Dimotakis 2000).

We carried out PIV measurements in the two wind tunnels. In both tunnels atomized olive oil was used for seeding particles of an average size of 1 μm, which were illuminated by Nd:YAG lasers yielding 120 mJ pulse^{-1} at a wavelength of 532 nm. Charge-coupled device cameras were used to capture the images with a resolution of 1200 pixels × 1600 pixels, at a rate of 15 double frames per second in both cases. Two-component PIV was used in the BLWTL measurements whereas both two-component and stereo PIV were used in the measurements conducted at URV. The locations of the measurement windows in the different sets of PIV measurements carried out in both tunnels are shown in tables 2, 3 and 4.

A set of measurements carried out with the M_1 model were conducted in the near-wake region with $x/D \leq 9$ at several transverse x–y planes along the cylinder axis (see table 2). A few measurements were also carried out on the same x–y window at selected axial locations with $z < 0$ to check flow symmetry. An additional set of consistency-check measurements on the same x–y window at $z = 0$ were performed in the URV tunnel with model M_2, i.e. with five cylinder segments instead of three. The data obtained in the URV tunnel were in good agreement with the earlier data obtained in the BLWTL.

$(x/D_{start}, z/D_{start})$–$(x/D_{end}, z/D_{end})$ plane window		y/D	DC Model
(10, −4)	(20, 4)	2.0	M_2
(26, −4)	(36, 4)	3.3	M_2
(43, −4)	(56, 4)	3.7	M_2
(72, −4)	(86, 4)	5.0	M_3
(119, −4)	(132, 4)	6.0	M_3

Table 4. Two-component PIV window sizes and x–z measurement planes in the intermediate- and far-wake regions. Model M_2 was used for $10 \leq x/D \leq 56$ and model M_3 was used for $70 \leq x/D \leq 132$, in the wind tunnel at URV.

Measurements in the URV tunnel extended further downstream in the wake with DC models, M_2 and M_3. The corresponding experiments with the continuous cylinder models were also carried out in the URV tunnel using stereo PIV. In these CC experiments the measurement windows were chosen to be the same as those used in the DC measurements listed in table 3. The diameters and experimental conditions of the two CC models were identical to those of the DC models M_2 and M_3 except, of course, for the absence of gaps and splitter plates. Measurements at several horizontal (x–z) planes using two-component PIV were also conducted in the URV tunnel in the mid ($10 \leq x/D \leq 56$) and far ($72 \leq x/D \leq 132$) wake regions with models M_2 and M_3, respectively, as summarized in table 4. A total of 4500 instantaneous image pairs were collected and saved to disk in each experimental run in BLWTL and URV. The TSI Insight 3G software was used, in all cases, for a frame-to-frame correlation to generate instantaneous velocity fields with an interrogation window of size 32×32 pixels with 50 % overlap.

HWA experiments were also carried out in the wake region in the wind tunnel at URV with the DC model M_3, at $Re = 4.0 \times 10^3$. Three normal-wire constant temperature anemometers (DISA 55M01/55M10 bridges and 55P11 probes) were used to sample the turbulent streamwise velocities in the wake. The normal wires were operated at an overheat ratio of 1.8, and calibrated assuming King's law (King 1914). Measurements were carried out at several downstream stations ($x/D = 12$, 16, 26, 52, 76, 120 and 170), in the near- and far-wake regions of the DC wake. A horizontal rake, which is movable on the transverse axis, was placed parallel to the spanwise axis. The rake consists of three normal-wire probes, positioned at the centre of the middle cylinder piece ($z = 0$), at the end of the middle cylinder piece ($z/D = 2.5$) and at the centre of the gap region ($z/D = 3.75$). It was used to measure the streamwise velocity (u) data at three spanwise locations simultaneously. At every downstream station, the rake was moved on the transverse axis and collected data from middle of the wake ($y = 0$) to the outer edge of the wake. The spatial resolutions on the transverse axis were different from the near wake to the far wake, as shown in table 5. At all points, the data were acquired for 120 s at a sampling rate of 5 kHz, lowpass filtered at 2 kHz and stored on a computer for subsequent processing. These data were used to characterize the evolution of the mean and root-mean-square streamwise velocity and to further verify the consistency of the PIV results.

2.3. *Mathematical model*

Calculations were performed for both the CC and DC flow configurations for a geometry and flow conditions similar to that of models M_1 and M_2 in table 1 except that only two

Downstream station (x/D)	Measurement spacing ($\Delta y/D$)
12	0.11
16	0.11
26	0.15
52	0.23
76	0.31
120	0.38
170	0.46

Table 5. Measurement spacing for the HWA measurements on the y-axis at different downstream stations in the DC wake, using model M_3 in the wind tunnel at URV.

cylinder segments were considered. The free-stream velocity was set to $U_0 = 9.2\,\mathrm{m\,s^{-1}}$ to yield a Reynolds number of $Re = 1.0 \times 10^4$. The length, height and width of the computational domain were $L/D = 65$, $H/D = 30$ and $W/D = 15$, respectively, and the cylinder axis was placed 15 diameters downstream from the inlet plane.

We assumed an incompressible flow of a Newtonian fluid governed by the Navier–Stokes equations, which for the Cartesian coordinate system may be written as,

$$\frac{\partial u_i}{\partial t} + \frac{\partial u_i u_j}{\partial x_j} = -\frac{1}{\rho}\frac{\partial p}{\partial x_i} + \frac{\partial}{\partial x_j}\left(\nu \frac{\partial u_i}{\partial x_j}\right), \tag{2.1}$$

where u_i (with the $i = 1$, 2 and 3 indices standing for the x, y and z axes, respectively) are the components of the instantaneous velocity field, p is the modified pressure, which incorporates the hydrostatic head induced by gravity, ρ is the fluid density and ν is its kinematic viscosity. The mass conservation (continuity) equation may be written as

$$\frac{\partial u_i}{\partial x_i} = 0. \tag{2.2}$$

Because of the huge computational cost that would be involved in a direct numerical solution of (2.1) and (2.2), we adopted the LES approach instead. In LES, the large three-dimensional unsteady motions are directly represented, whereas the effects of the small-scale motions are modelled. The instantaneous velocity and pressure fields are decomposed as the sum of a filtered (resolved) component and a residual (or subgrid-scale, SGS) component

$$u_i(x, t) = \tilde{u}_i(x, t) + u_i'(x, t) \tag{2.3a}$$

$$p(x, t) = \tilde{p}(x, t) + p'(x, t) \tag{2.3b}$$

When the decomposition (2.3) is introduced into the Navier–Stokes (2.1) and continuity (2.2) equations the equations that govern the dynamics of large-scale motion are obtained

$$\frac{\partial \tilde{u}_i}{\partial t} + \frac{\partial \tilde{u}_i \tilde{u}_j}{\partial x_j} = -\frac{1}{\rho}\frac{\partial \hat{p}}{\partial x_i} + \frac{\partial}{\partial x_j}\left(\nu \frac{\partial \tilde{u}_i}{\partial x_j} - \tau_{ij}^r\right) \tag{2.4}$$

$$\frac{\partial \tilde{u}_i}{\partial x_i} = 0. \tag{2.5}$$

In (2.4), the term τ_{ij}^r is the anisotropic residual stress tensor

$$\tau_{ij}^r = \widetilde{u_i u_j} - \tilde{u}_i \tilde{u}_j - \tfrac{2}{3} k_r \delta_{ij}, \tag{2.6}$$

with the residual kinetic energy, k_r, defined as $2k_r = \widetilde{u_i u_i} - \tilde{u}_i \tilde{u}_i$. Note that the isotropic part of τ_{ij}^r is added to the filtered pressure, $\tilde{p}$, so that the modified filtered pressure appearing in (2.4) is obtained, i.e. $\hat{p} = \tilde{p} + 2/3\rho k_r$. The τ_{ij}^r tensor, which incorporates the effects of small-scale flow eddies into the large-scale motion, needs to be modelled. We assumed the classical (Smagorinsky 1963) model

$$\tau_{ij}^r = -2\nu_t \tilde{S}_{ij}, \tag{2.7}$$

where ν_t is the eddy viscosity and $\tilde{S}_{ij}$ is the filtered/resolved strain tensor

$$\tilde{S}_{ij} = \frac{1}{2}\left(\frac{\partial \tilde{u}_i}{\partial x_j} + \frac{\partial \tilde{u}_j}{\partial x_i}\right). \tag{2.8}$$

Under the assumption of universality of the small eddies, Smagorinsky proposed the SGS model

$$\nu_t = (C_s \Delta)^2 \tilde{S} = (C_s \Delta)^2 (2\tilde{S}_{ij}\tilde{S}_{ij})^{1/2}, \tag{2.9}$$

where Δ denotes the filter width and $C_s = 0.15$. It was later found, however, that the value of the Smagorinsky coefficient, C_s, is not constant but it depends on the flow regime at the local level. We therefore adopted the dynamic SGS model (Germano *et al.* 1991; Lilly 1992) where the filter width, Δ, is locally defined as a function of the computational mesh spacing and C_s is not a constant but is instead calculated as a function of the local values of the filtered strain tensor, $\tilde{S}_{ij}$.

A well-known limitation of LES is that SGS models may become inoperative in the vicinity of a solid surface because of its inability to properly represent the flow mechanisms within the turbulent boundary layer region (Sagaut 2001). Such a limitation can be overcome by prescribing a sufficiently fine computational mesh within the turbulent boundary layer. Because of the large computational resources that would be involved in such an approach, we opted instead for the use of wall laws. In particular, we implemented the Werner & Wengle (1993) model, which assumes the following velocity profile near a wall:

$$u^+ = \begin{Bmatrix} y^+ & \text{if } y^+ \le 11.81 \\ 8.3(y^+)^{1/7} & \textit{otherwise} \end{Bmatrix}, \tag{2.10}$$

where the tangential velocity, u_t, and the normal distance from the wall, y, are scaled with the norm of the wall shear stress at the surface (τ_w), i.e. $u^+ = u_t/u^*$ and $y^+ = yu^*/\nu$ with $u^* = (\tau_w/\rho)^{1/2}$. Integration of the profile (2.10) provides an estimate for the components of the instantaneous wall shear stress as a function of the tangential components of instantaneous velocity at the adjacent calculation node. Note that the Werner & Wengle (1993) wall model is, therefore, suitable for turbulent boundary layer flows having separation points.

2.4. *Numerical methods*

Equations (2.4) and (2.5) were discretized in space according to a second-order accurate finite-volume methodology similar to the one reported by Mahesh, Constantinescu & Moin (2004). These authors used a predictor–corrector scheme that emphasizes the local energy

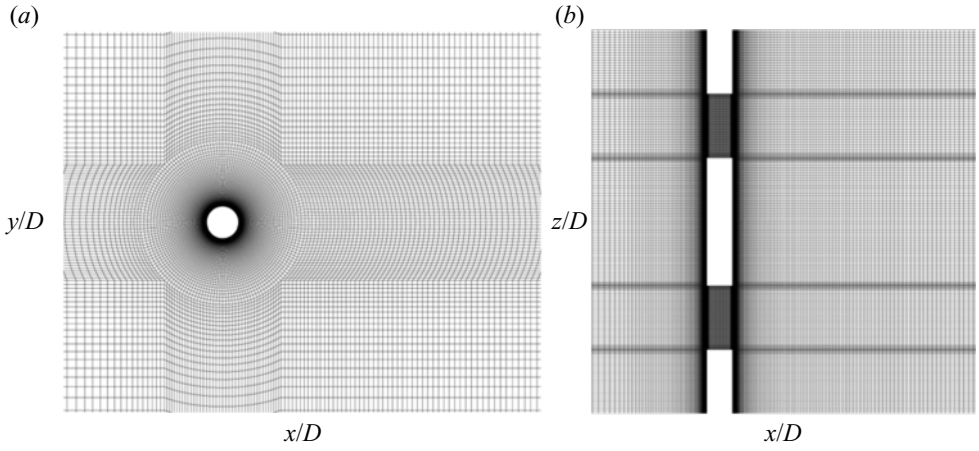

Figure 3. Cross-section of the computational mesh used in the LES calculations of the DC flow: (*a*) x–y plane with $z = 0$, and (*b*) x–z plane with $y = 0$. In both cases the extent of the x-domain is limited to $-5 \leq x/D \leq 10$.

conservation for the convection and pressure gradient terms in mesh elements of arbitrary shapes. A collocated variable arrangement was used, similar to the one in Rhie & Chow (1983) method although the details of the discretization were different.

The three-dimensional (3-D) computational mesh consisted of hexahedral volume cells. First, a two-dimensional (2-D) mesh with 29 940 quadrilateral cells was generated. As can be seen in figure 3(*a*), the grid nodes were clustered in the boundary layer region around the cylinder and in the wake region. The nodes adjacent to the cylinder surface were placed at a radial distance equal to $0.001D$ from the wall (this represents, on average, a dimensionless normal distance of approximately $y^+ = 1$). The size of the cells then increases gradually as we move from the near wake to the far wake region, to the point that the $x-$spacing at the outflow boundary ($x/D = 50$) was set equal to one diameter. In those z-locations where there is no cylinder, i.e. in the $2.5 < |z/D| < 5$ gap (see figure 3*b*), 4480 additional quadrilateral cells were added to fill the region of the x–y plane that would be occupied by the cylinder had not it been discontinued.

The 2-D meshes in the x–y plane were subsequently extruded along the spanwise (z) direction to generate the 3-D mesh. In the CC model simulation, a uniform z-mesh with one 101 x–y identical planes was deployed so that the total number of hexahedral cells was $29\,940 \times 100 = 2\,994\,000$. In the DC model simulation, a total of 175 x–y planes, non-uniformly distributed along the z-axis, were generated. These planes were clustered at the edges of the cylinder segments with the z-spacing varying from $0.05D$ at the edge of a segment to $0.1D$ at its centre (see figure 3*b*). The total number of hexahedral cells in the 3-Dcomputational mesh for the DC model was 5 487 320.

The left and right z-boundaries of the calculation domain were truncated at the middle of a cylinder segment (see figure 3*b*) and periodic boundary conditions were applied. A turbulence-free uniform flow was prescribed at the inflow boundary ($x/D = -15$) whereas at the right x-boundary ($x/D = 50$) an outlet condition consisting of a zero velocity gradient together with a constant level (p_{atm}) of the surfaced-averaged pressure was applied. A symmetry boundary condition was applied to the top and bottom y-boundaries ($y/D = \pm 15$). The choice of such boundary conditions along the y- and z-directions, motivated by the rationale of avoiding unnecessary degrees of freedom in the calculations, precludes an accurate simulation of the real flow near the walls of the wind tunnel.

Notwithstanding, we checked that the main goal of the simulations, that is, the accurate characterization of the flow dynamics in the near wake was in no way hindered by the use of such approximate boundary conditions.

The system of ordinary differential equation resulting from the spatial discretization of (2.4) and (2.5) was advanced in time using the implicit second-order backward-differencing scheme, which has the property of being A-stable (Hairer & Wanner 1996). As we implemented an implicit time-marching scheme, we had to adapt Mahesh *et al.* (2004) method for the velocity–pressure coupling. At each time step, several internal pseudo-time steps were performed. Within each internal time step, the new velocity values on each computational cell were first calculated and afterwards corrected using the newly calculated pressure values. Internal pseudo-time steps were carried out until the prescribed accuracy for global convergence of both momentum and mass conservation equations was achieved. The number of internal pseudo-time steps per real time step was always modest, only three were required, at most.

All time integrations were performed using a constant time step of $\Delta t = 3 \times 10^{-5}$ s $= 0.017(D/U_0)$. Assuming a Strouhal number of $S_t = D/(TU_0) = 0.14$ (where T denotes the mean period of a shedding cycle) for the main flow oscillation in the DC model, it follows that the average number of time steps per shedding cycle was $T/\Delta t \approx 422$. After an initial transient equivalent to about 21 shedding cycles, time marching in the DC simulation was carried for a further period of about 53 shedding cycles (equivalent to $376D/U_0$). Instantaneous velocity and pressure values were recorded every one out of ten time steps, that is, approximately 42 times per shedding cycle. In the CC model simulation, a Strouhal number of $S_t = 0.202$ (Norberg 2003) was assumed and the integration period after the initial transient was equivalent to about 51 shedding cycles ($248D/U_0$). Note that the integration period used to calculate the mean field in the present study was larger than the value of ($150D/U_0$) adopted previously by Mahesh *et al.* (2004) and also larger than the 40–50 shedding cycles of Dong *et al.* (2006) in their respective numerical simulations.

3. Wake characteristics and growth rate in the vertical plane

3.1. *Large-scale structures in DC wake*

The DC geometry was devised to replicate the self-preserving structures of the far wake of the continuous circular cylinder, but in the near-wake region, which are commonly referred to as HSV or double roller (DR) vortices (Ferré & Giralt 1989*b*; Vernet *et al.* 1997). A well-established method to portray the shape of flow structures is to plot iso-surfaces with a certain level of pressure. Figure 4 shows pressure iso-surfaces obtained from an instantaneous field in the LES calculation of the DC wake. These plots clearly indicate the shape of the three-dimensional HSV and that the genesis of HSV is early in the wake, with their presence clearly observed by $x/D \approx 3$ to 4. This is distinct from the CC wake for which the three-dimensional rib structures take some time to develop (Hayakawa & Hussain 1989). Figure 5 shows vector plots of velocity fluctuations in the x–y plane with $z = 0$ for an instantaneous field obtained from PIV measurements in the DC wake. We will use the u, v and w symbols to denote the x-, y- and z-velocity components, while an overbar on a quantity will denote its mean (time-averaged) value. In the near wake ($x/D < 10$), the rolls portrayed in figure 5(*a*) remind one of the typical patterns that are generated by the VKV in the CC wake, indicating that wake periodicity is maintained. Spectra of the streamwise velocity fluctuations (not shown for brevity) indicate that the Strouhal number is $S_t = 0.137$ in the DC wake, which is considerably lower than the corresponding values for the CC wake ($St = 0.202$ from current LES at $Re = 10^4$, in good agreement with the

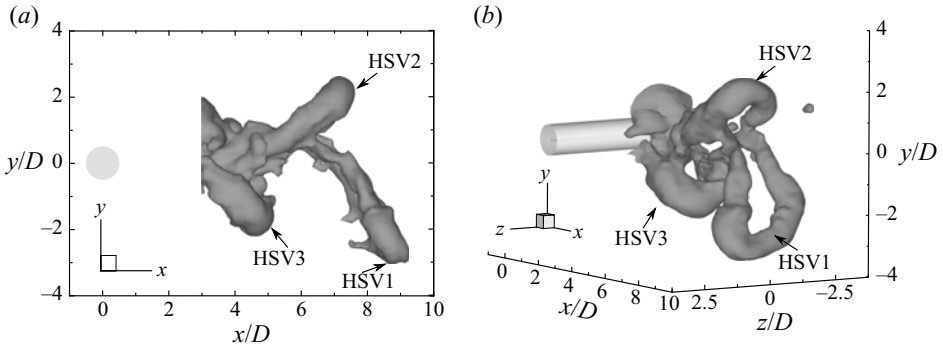

Figure 4. Iso-surfaces of $(\hat{p} - p_{atm})/(\rho U_0^2) = -0.1346$ in the DC near wake at one instant of time from the LES simulation at $Re = 1.0 \times 10^4$. (*a*) Side view of *x*–*y* plane and (*b*) three-dimensional view of three different instantaneous vortices, labelled as HSV1, HSV2 and HSV3.

$St = 0.202$ and 0.203 values respectively reported by Norberg (2003) and Dong *et al.* (2006) at similar *Re*). Figures 5(*b*) and 5(*c*) show that further downstream ($x/D > 30$), the intensity of these vortices in the *x*–*y* plane is still high and that the centres have been displaced considerably further from the centreline.

Figure 6 depicts instantaneous velocity fluctuation vectors, again obtained from PIV measurements, in *x*–*z* planes at two different vertical levels. In this plane, the projection of the 'legs' of the HSV becomes apparent and illustrate why the HSV are also called double rollers. Relatively high strength rotation is observed around the HSV legs at a streamwise location as far downstream as $x/D = 80$, as shown in figures 6(*b*) and 6(*c*). Consistent with the pressure contours in figure 4 and the velocity vectors in figure 6, figure 7 depicts the mean velocity vectors in the *y*–*z* plane at $x/D = 10$ along with the iso-contours of the three mean vorticity components. In this figure, the alignment of the streamwise vorticity component with the DR pattern is clear. However, the *y*-vorticity is also aligned with the legs, while the *z*-vorticity can be seen further from the centreline. This mean flow pattern, with the periodic repetition of HSV, indicates the clear momentum exchange from the free stream in the gap region (i.e. between the solid cylinder segments) into the wake region. There are strong horizontal *z*-velocity components between the HSV near $y \approx 0$, which connects to the vertical momentum exchange associated with the head (or top) of the HSV (i.e. the *z*-vorticity, as seen in figures 5(*a*) and 7(*a*)). Figure 8 shows the mean streamwise vorticity along with the mean velocity vectors in *y*–*z* planes at $x/D = 20$ and 30. The relatively strong mean cross-stream circulation in these plots indicates that this flow pattern remains for a remarkably long downstream distance. Thus, the footprint of the HSVs on the mean velocity field is a quite regular one, which impacts both the mean and fluctuating statistics of the flow. Further upstream, figures 9(*a*) and 9(*b*) show the centreline ($y = 0$) profiles of the mean *z*- and *x*-velocity components, respectively, at several streamwise locations in the near wake ($x/D \leq 10$). Figure 9(*a*) indicates that there are high values of the *z*-velocity moving fluid into the legs of the HSV that originates by $x/D = 2$. Again, this points to the early formation of the HSV and the importance of the lateral entrainment as the HSV form. This lateral momentum transfer contributes to the relatively fast momentum recovery in the DC near wake, illustrated by the streamwise *x*-velocity component in figure 9(*b*) and which will be explored further in the next two subsections.

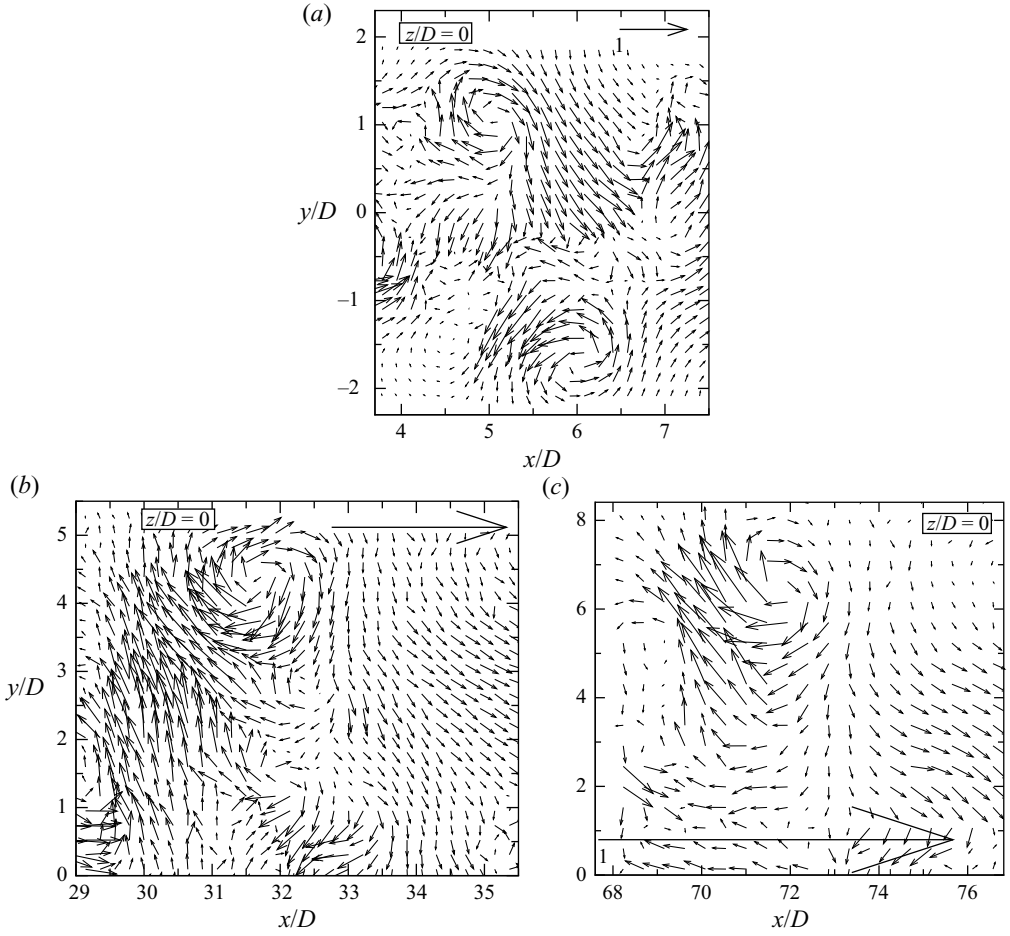

Figure 5. Vector plots of the instantaneous velocity fluctuations (u', v') in the x–y plane at $z = 0$ (*a*) in the near ($3.5 \leq z/D \leq 7.5$), (*b*) middle–far ($29 \leq z/D \leq 35$) and (*c*) far ($68 \leq z/D \leq 76$) wakes of the DC. The vector scale used in (*b*) is 2.4 times larger than in (*a*). In each case, the arrow near the top of the figure frame denotes the length for the reference velocity, U_0. The data are from PIV measurements with model M_2 at a Reynolds number of $Re = 1.0 \times 10^4$ for panels (*a*,*b*), and with model M_3 at a Reynolds number of $Re = 4.0 \times 10^3$ for panel (*c*).

3.2. *Comparison of the continuous and DC near wakes*

In this subsection we compare the CC near wake ($x/D \leq 10$) with the DC near wake using PIV measurements and LES results for $Re = 1.0 \times 10^4$. The instantaneous data were ensemble averaged to determine the mean streamwise and transverse velocities, Reynolds shear stress and mean vorticity patterns on the measurement planes. Figure 10 shows the streamwise profiles of the mean streamwise velocity component ($\bar{u}$) on the flow centreline ($y = 0$, $z = 0$). Both simulations and measurements show that the recirculation length, i.e. the wake closure length (L_R), which is defined as the mean (time-averaged) closure point (i.e. the saddle point on the wake centreline, $y = 0$), is much larger in the DC wake ($L_R/D = 3.63$ from PIV measurements) than it is for the CC wake ($L_R/D = 1.51$). Accordingly, the minimum value in the DC profile of figure 10 is much lower (more negative) than it is for the CC profile. It is observed that the CC profile recovers quite

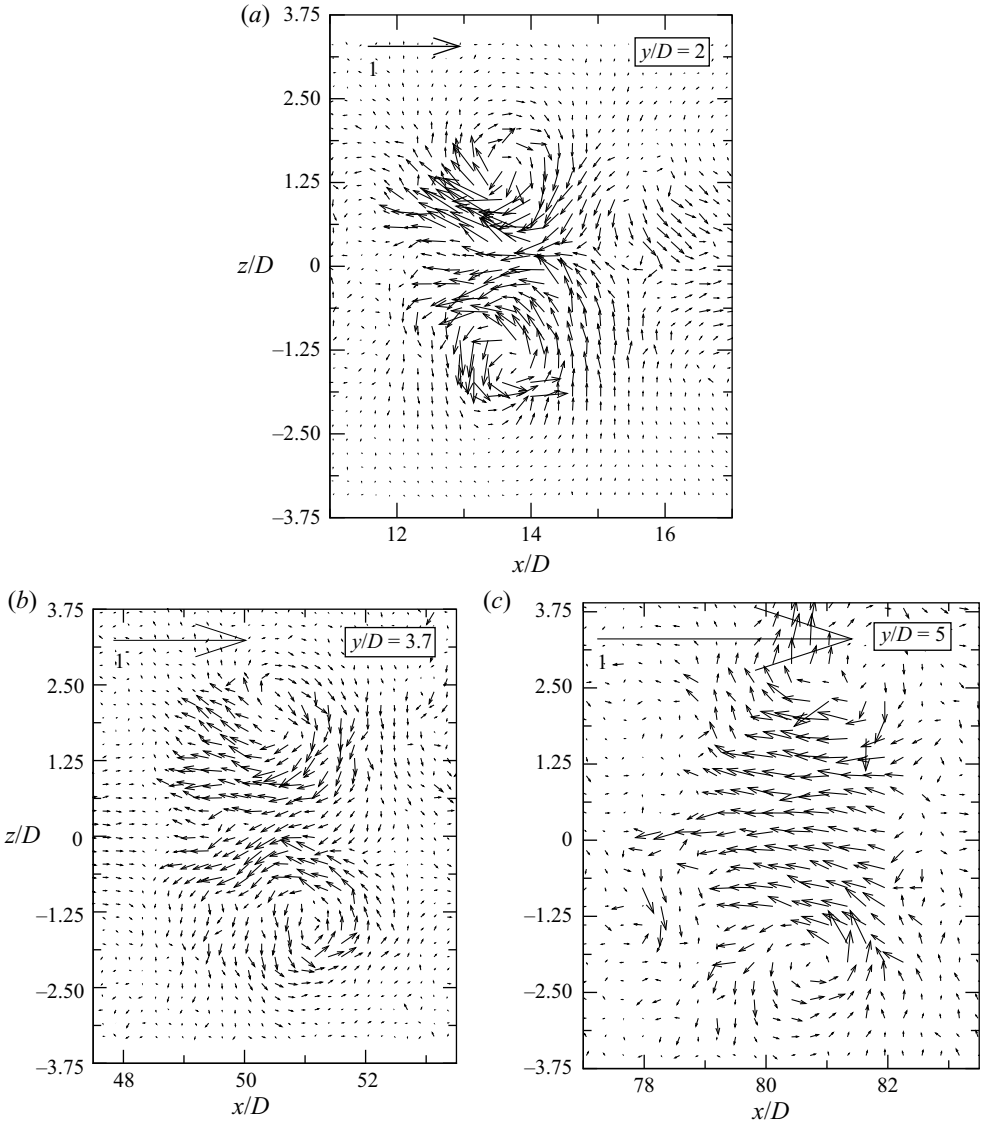

Figure 6. Vector plots of the instantaneous velocity fluctuations (u', w') in x–z planes (a) at $y/D = 2$ in the middle $(11 \leq z/D \leq 17)$, (b) at $y/D = 3.7$ in the medium–far $(48 \leq z/D \leq 53)$ and (c) at $y/D = 5$ in the far $(77 \leq z/D \leq 83)$ wakes of the DC. The arrow near the top of the figure frame denotes the length for the reference velocity, U_0. The data are from PIV measurements with model M_2 at a Reynolds number of $Re = 1.0 \times 10^4$ for panels (a,b), and with model M_3 at a Reynolds number of $Re = 4.0 \times 10^3$ for panel (c).

soon $(x/D \approx 3)$ to a value as high as $\bar{u}/U_0 \approx 0.70$, but there is a rapid slope change at $x/D \approx 3$ with much slower changes as the flow evolves downstream. In contrast, the momentum recovery is initially slower in the DC profile, but the rate of change (i.e. the slope of the curve) is much higher for the DC wake for $x/D > 3$. At $x/D = 10$ both profiles have attained an almost identical level of $\bar{u}/U_0 \approx 0.75$ at the $y = 0$ centreline, although the slope remains higher for the DC wake at this point.

As discussed in the previous subsection, the HSV are formed by $x/D \approx 3$, with significant spanwise inflow by $x/D = 2$ such that the rate of change of the centreline

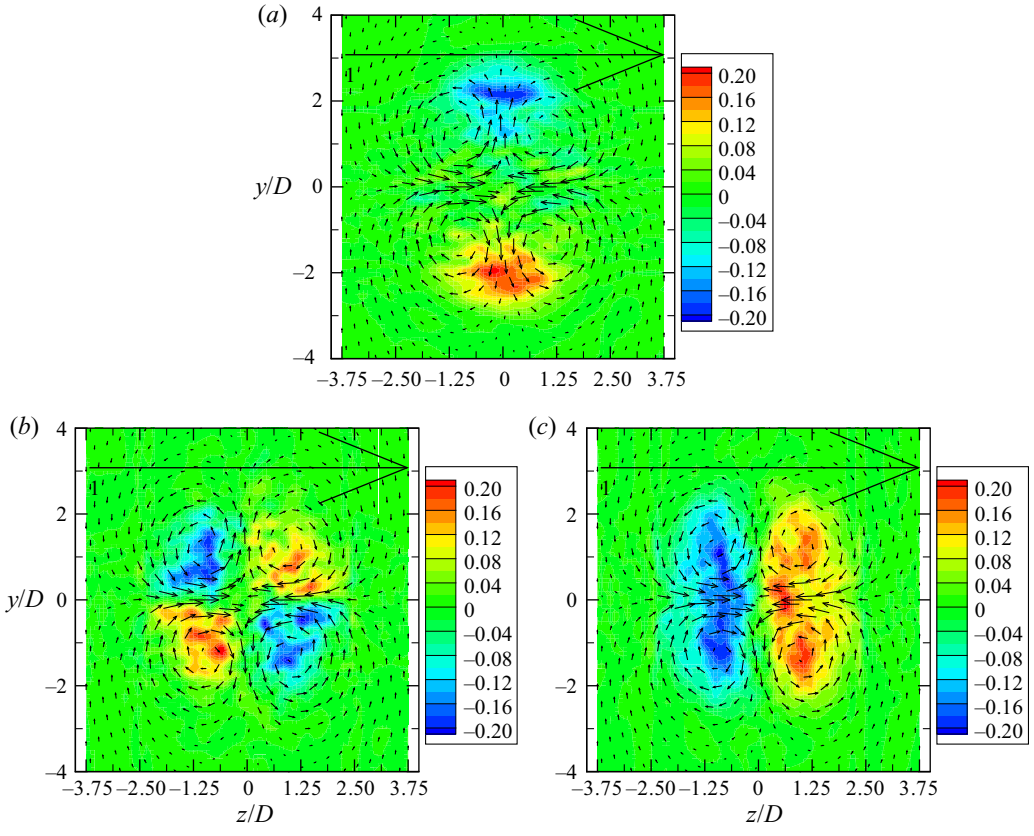

Figure 7. Mean velocity vectors and mean vorticity contours in the y–z plane at $x/D = 10$, obtained from the LES simulation: (*a*) spanwise vorticity component ($\overline{\tilde{\omega}}_z D/U_0$), (*b*) streamwise vorticity component ($\overline{\tilde{\omega}}_x D/U_0$) and (*c*) vertical vorticity component ($\overline{\tilde{\omega}}_y D/U_0$). In each case, the arrow near the top of the figure frame denotes the length for the reference velocity, U_0.

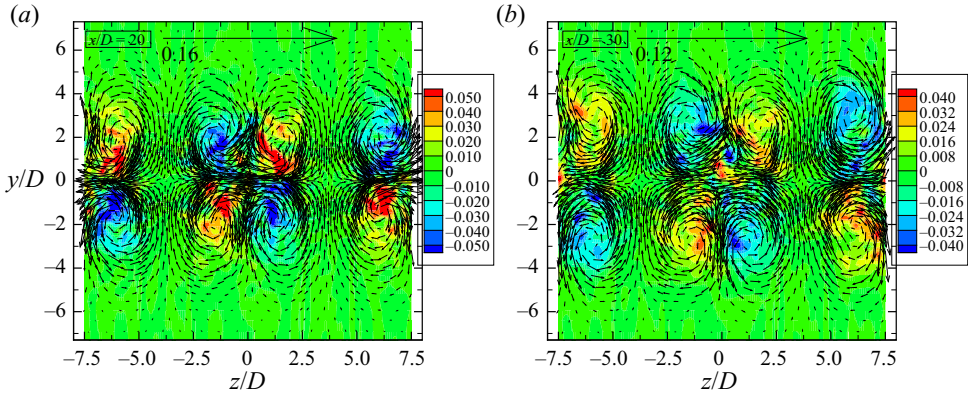

Figure 8. Mean velocity vector plots ($\overline{\tilde{v}}, \overline{\tilde{w}}$) and mean vorticity contours ($\overline{\tilde{\omega}}_x D/U_0$) in the y–z plane at (*a*) $x/D = 20$ and (*b*) $x/D = 30$ from the LES simulation. In each case, the arrow near the top of the figure frame denotes the length for the reference velocity, U_0.

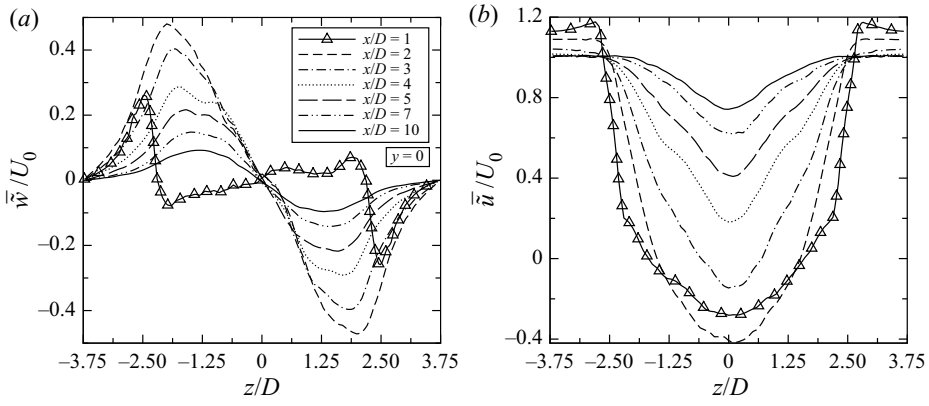

Figure 9. Profiles of (*a*) mean velocity $\bar{\tilde{w}}/U_0$ and (*b*) mean velocity $\bar{\tilde{u}}/U_0$ components in the spanwise direction on the DC wake centreline ($y = 0$) at several streamwise locations from the LES simulation.

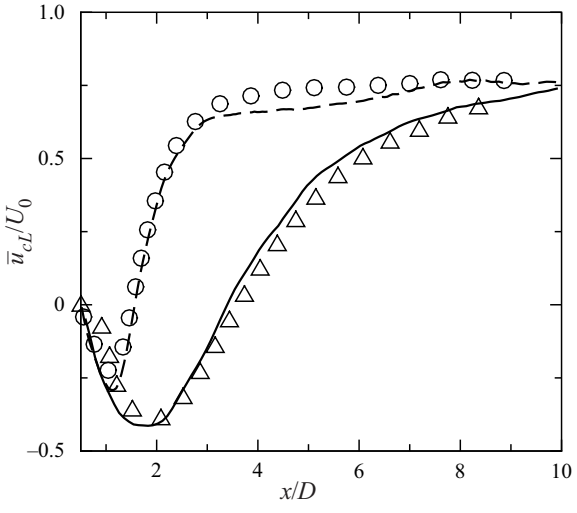

Figure 10. Comparison of mean streamwise velocity ($\bar{u}/U_0$) on wake centreline ($y = 0$) and mid-plane ($z = 0$) for the DC and CC wakes. Lines show the LES results: DC wake (—), CC wake (– –). Symbols show the PIV results: DC wake (△), CC wake (○).

velocity is likely related to the significant role of the HSV downstream of this point. In contrast, the VKV have emerged prior to $x/D = 1$. For example, Cantwell & Coles (1983) found a wake closure point of approximately $x/D = 1.2$, with the VKV formed by approximately $x/D \approx 0.7$. This relationship between the formation of a quasi-2-D vortex street and the wake closure point seems fairly consistent. The minimum in the streamwise velocity is closely related to the formation point of the vortices (see, e.g. the results of Taylor, Gurka & Kopp (2014) for a range of 2-D bluff body shapes), with the vortices accelerating downstream, away from the formation point. For the CC, the inflow (entrainment) is dramatic in the range $1 < x/D < 3$, as indicated by the rapid increase in $\bar{u}/U_0$ in this range. In contrast, the HSV form further into the wake and do not have the same initial slope of $\bar{u}/U_0$. As pointed out above, the slope remains higher for the DC wake for an extended distance downstream with the $\bar{u}/U_0$ values becoming equal near

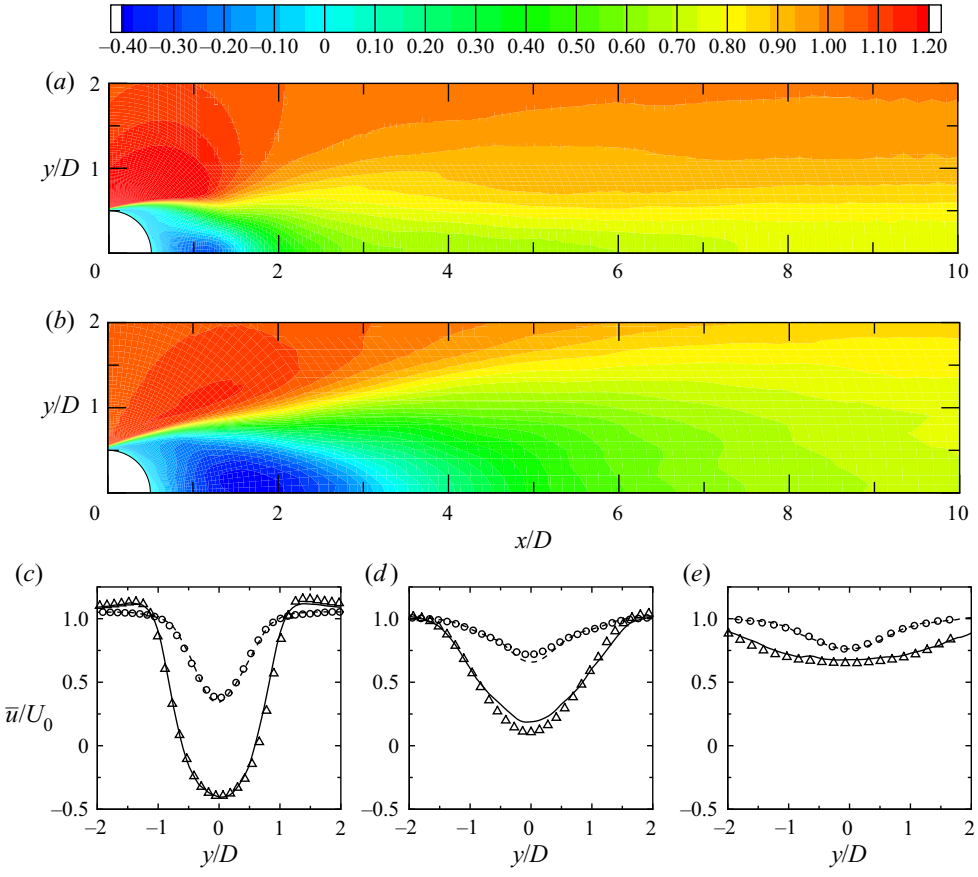

Figure 11. Vertical distribution of mean streamwise velocity ($\bar{u}/U_0$) in the CC and DC wakes at $z = 0$. Contours show LES results for (*a*) the CC wake and (*b*) the DC wake. Vertical profiles from the LES calculations for the DC (—) and CC (– –) wakes, along with the measured ones for the DC (△) and CC (○) wakes at three downstream locations: (*c*) $x/D = 2$, (*d*) $x/D = 4$ and (*e*) $x/D = 8$.

$x/D = 10$. Figure 11 shows the contours and selected vertical profiles of ($\bar{u}/U_0$) in the CC and DC wakes. Comparison of the contours in figures 11(*a*) and 11(*b*) confirms the differences in the length and intensity of the respective recirculation bubbles that were already inferred by figure 10. In addition, the contour plot for the DC wake in figure 11(*b*) reveals the comparatively high momentum deficit for the DC wake in the region behind the recirculation bubble. Inspection of the vertical $\bar{u}/U_0$ profiles in figure 11(*c*) together with the contour plots in figure 11(*a*,*b*) provides an indication of the different rates of flow development for these wakes. At the streamwise station, $x/D = 2$, it is probably too early for the concept of wake width to make sense since the formation of the wake vortices is incomplete. However, at $x/D = 4$, the corresponding DC and CC profiles (figure 11*d*) suggest that the widths of both wakes are similar since the limiting $\bar{u} = U_0$ values are reached at $y/D \approx \pm 1.5$. Further downstream, by $x/D = 8$ (figure 11*e*), the DC wake has become significantly wider. Note that the same effect can be observed in the contour plots of figure 11(*a*,*b*) when examining the isoline for $\bar{u}/U_0 = 1$. Figures 12(*a*) and 12(*b*) show the contours of the mean vertical component of velocity ($\bar{v}/U_0$) in the CC and DC wakes, respectively. The vertical $\bar{v}/U_0$ profiles at selected streamwise locations in figure 12(*c*–*e*) shows again the good agreement between the current PIV measurements

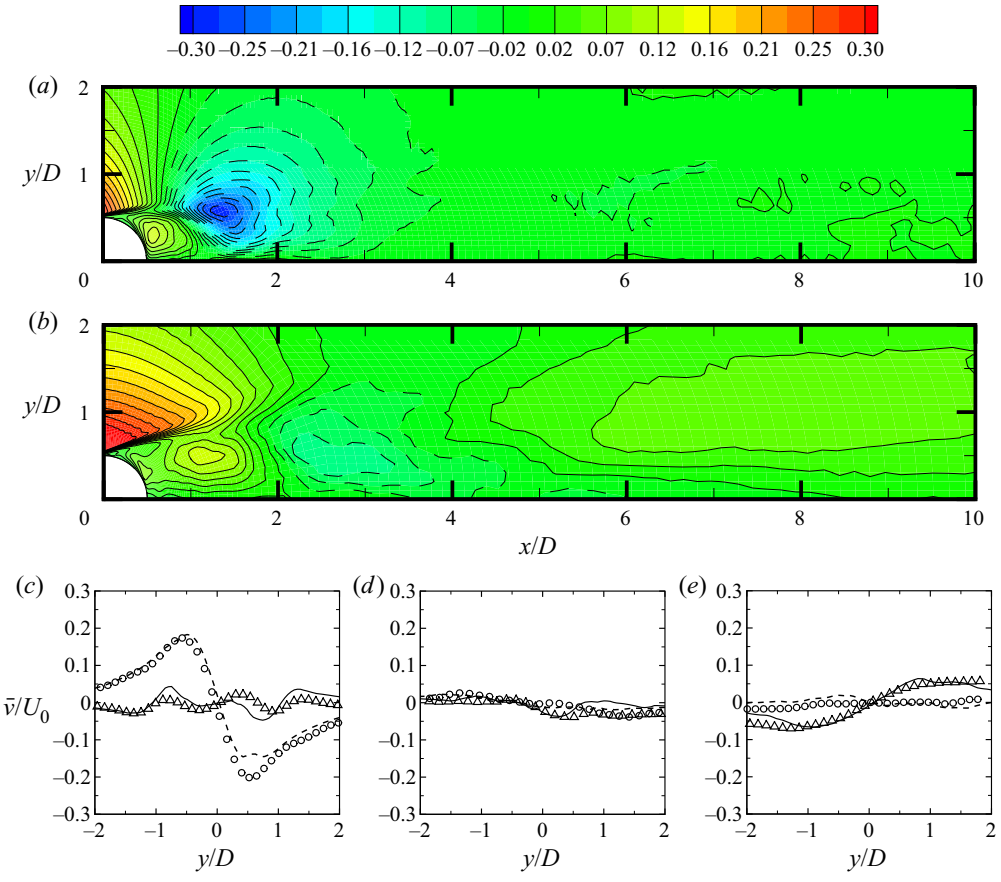

Figure 12. Vertical distribution of mean vertical velocity ($\bar{v}/U_0$) in the CC and DC wakes at $z = 0$. Contours show LES results for (*a*) the CC wake and (*b*) the DC wake. Vertical profiles from the LES calculations for the DC (—) and CC (– –) wakes, along with the measured ones for the DC (△) and CC (○) wakes at three downstream locations: (*c*) $x/D = 2$, (*d*) $x/D = 4$ and (*e*) $x/D = 8$.

and LES calculations. Figure 12(*a*) shows the presence of strongly negative $\bar{v}$ values in the near wake ($x/D \leq 2$) of the CC wake, with a local minimum of $\bar{v}/U_0 = -0.29$ at $(x/D, y/D) \approx (1.34, 0.58)$. The presence of such foci of highly negative (or positive, in the $y < 0$ half-plane) $\bar{v}$ means that, on the average, fluid with higher momentum is driven inwards toward the midplane ($y = 0$) region, a mechanism that explains the fast momentum recovery of the CC near wake in figures 10 and 11(*a*), following the formation of the VKV, as discussed by Cantwell & Coles (1983), Ong & Wallace (1996) and Ma, Karamanos & Karniadakis (2000). In the corresponding $\bar{v}$ contours of the DC wake, figure 12(*b*), we see that the downwards (upwards for $y < 0$) flow pattern associated with the entrainment mechanism is considerably weaker and it occurs further downstream, $2 \leq x/D \leq 4$. Figure 12(*b*) also shows that this flow pattern in the DC wake is stronger closer to the cylinder, $x/D \leq 2$, prior to the formation of the HVS. Another significant difference between the CC and DC contours of figures 12(*a*) and 12(*b*) is that, in the latter, there is a small but consistent flow pattern with fluid moving upwards in the upper half-wake in the $4 \leq x/D \leq 10$ streamwise region, a fact that is also reflected in the DC vertical profile of figure 12(*e*) (to be discussed later in § 4). This is associated with outward motions in the mid-plane of the HSV, as indicated in figures 5 and 6.

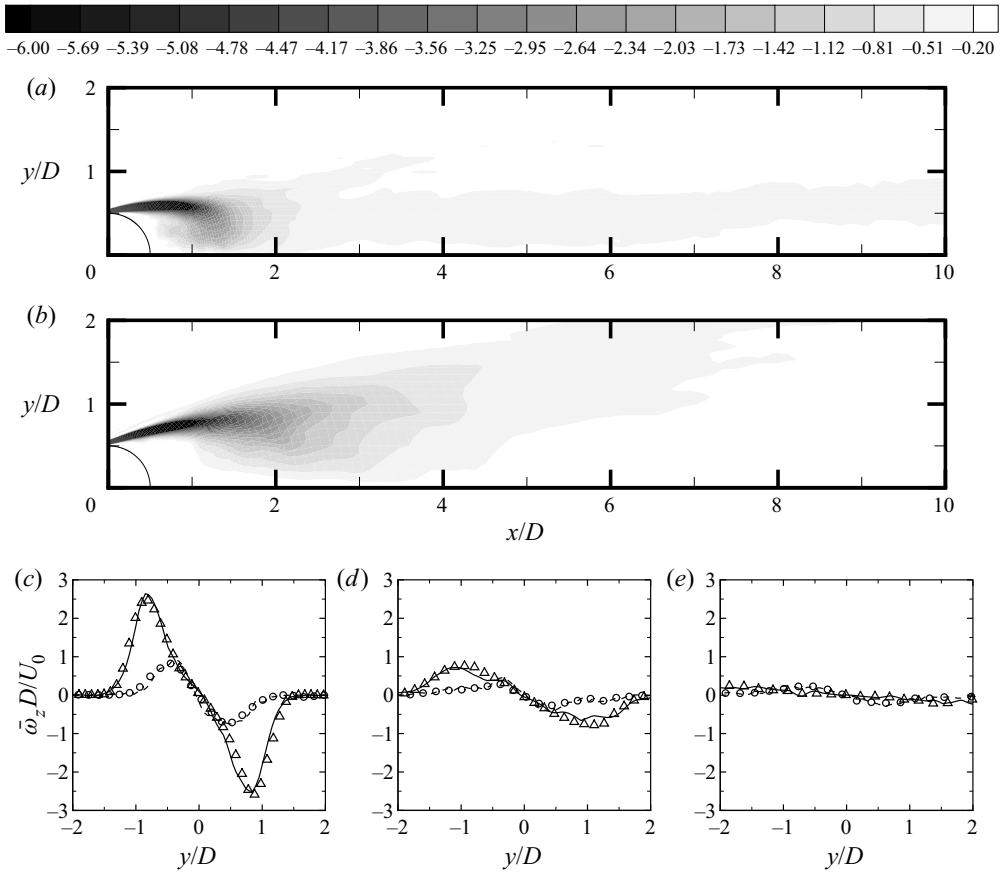

Figure 13. Vertical distribution of mean spanwise vorticity ($\bar{\omega}_z D/U_0$) in the CC and DC wakes at $z = 0$. Contours show LES results for (*a*) the CC wake and (*b*) the DC wake. Vertical profiles from the LES calculations for the DC (—) and CC (– –) wakes, along with the measured ones for the DC (△) and CC (○) wakes at three downstream locations: (*c*) $x/D = 2$, (*d*) $x/D = 4$ and (*e*) $x/D = 8$.

Thus, the outward flow related to the vertical motions in the centre of HSV is more significant than the inward vertical motions, but the 3-D motions induced by the legs of the HSV are more important. Again, this contrasts with the near wake of the CC where the VKV vortices induce inward motions, which are strong initially, but decay rapidly as indicated by figure 12(*c–e*).

The contours of the mean spanwise vorticity component, $\overline{\omega}_z$, for the CC wake flow, shown in figure 13(*a*), confirm a strong average vortical activity in the CC near-wake region closest to the cylinder ($x/D \leq 2$). Moreover, this plot also shows a horizontal strip with relatively low spanwise vorticity ($\overline{\omega}_z \leq -0.2$), which is basically circumscribed within the midplane region, $|y/D| \leq 1$. By comparison, the DC wake contours depicted in figure 13(*b*) show that large-scale vortices are similarly being generated behind the cylinder but instead of traveling close to the wake centreline they also move away from the horizontal midplane (see also figure 12*b*). Not surprisingly, figure 13(*b*) also shows highly negative $\overline{\omega}_z$ values in the $2 \leq x/D \leq 4$ streamwise region of the DC wake, that is, the region where strong downwards motion (figure 12*b*) was also observed. Note also in figure 13(*b*) that the region with significant spanwise vorticity levels ($\overline{\omega}_z \leq -0.2$) reaches the $y/D = 2$ edge of the plot at a streamwise location slightly below $x/D = 8$. This means

that in the DC wake the large-scale vortices move away from the $y = 0$ midplane as they travel downstream, as shown in figure 6. This is distinct to what is observed for the CC wake in figure 13(*a*). This evidence of fluid with significant vorticity and comparatively low momentum moving away from the midplane, hints again at the possibility of an enhanced growth rate of the DC wake (compared with the CC wake), a notion that will be analysed in detail below.

3.3. *Wake growth characteristics*

In this subsection the comparative analysis of the CC and DC wake flows is extended to the mid- and far-wake regions. Figure 14 shows the streamwise evolution of the maximum velocity defect, $(\bar{u}_d)_{max} = (U_0 - \bar{u})_{max}$, as measured in mid- and far-wake regions of the CC and DC wakes. The DC wake, as shown in figure 10, features high values in the base region, but further downstream, mean momentum in the DC wake recovers quickly. Figure 14 indicates that the enhanced mean momentum recovery in the DC wake persists in the mid-wake region with $10 \leq x/D \leq 20$. For example, at $x/D = 16$ (i.e. $(x/D)^{-0.5} = 0.25$), $(\bar{u}_d)_{max} = 0.19U_0$ for the DC wake is clearly smaller than the corresponding value of $(\bar{u}_d)_{max} = 0.23U_0$ for the CC wake. Further downstream, we can see that the momentum recovery rates are similar in the two wakes, as indicated by the same slopes. However, the DC wake has a much smaller maximum momentum deficit at the same physical locations. As a result, the maximum velocity defect in the DC wake at $x/D = 50$ is $(\bar{u}_d)_{max} \approx 0.089U_0$, which can be found at about $x/D = 127$ in the CC wake; at just ten diameters further downstream in the DC wake ($x/D = 60$) the equivalent streamwise location in the CC wake would be $x/D \approx 172$. Thus, even though the DC wake has a higher momentum deficit initially, it recovers much faster than the CC wake such that the maximum defect is significantly lower in the self-preserving far-wake region. A second quantity often used to characterize the growth rate of the CC wake is $y_{1/2}$, defined as the vertical location where the mean velocity is half of the maximum of $\overline{u}_d$. Figure 15 shows that in the near to mid wake of the DC, up to $x/D \approx 40$, $y_{1/2}$ rises much faster with downstream location than for the CC wake. In the streamwise region with $40 \leq x/D \leq 170$, $y_{1/2}$ increases at approximately the same rate in both wakes, i.e. both trendlines are parallel. For example, at $x/D = 50$ we have $y_{1/2} \approx 4.33D$ in the DC wake whereas the equivalent streamwise location in the CC wake would be $x/D \approx 235$. Furthermore, a value of $y_{1/2} \approx 4.54D$ for the DC wake at $x/D = 60$ would be found at $x/D \approx 258$ in the CC wake.

Figure 15 depicts two distinct growth rates for the DC wake. For $x/D \leq 56$ the spanwise periodicity of the HSVs, which are shed periodically from the DC, control the dynamics of the initial DC wake development. As the HSVs are advected downstream, the DC wake evolves towards a 2-D flow on the average since the HSVs are progressively randomized and their energy becomes indistinguishable from that of turbulence (as indicated by power spectra, not included here). These vortex structures lead to a significantly higher growth rate for the DC wake than for the CC wake, as discussed earlier. Beyond $x/D = 56$, the dynamics of the DC wake corresponds, on the average, to that of a CC, but with a virtual origin that is located far upstream of the physical origin. In fact, the position of this virtual origin so far upstream of the physical origin is an indicator of the enhanced entrainment and growth in the DC near wake since the growth rates of the DC and CC wakes are similar in the far wake (beyond $x/D = 56$).

It might be argued that quantities such as centreline $\overline{u}_d$ and $y_{1/2}$, which were originally devised to characterize the growth rate of the CC wake, may not work well when applied to the analysis of the DC wake. In fact, the $\overline{u}_d$ vertical profiles for the DC wake in figure 16(*a*)

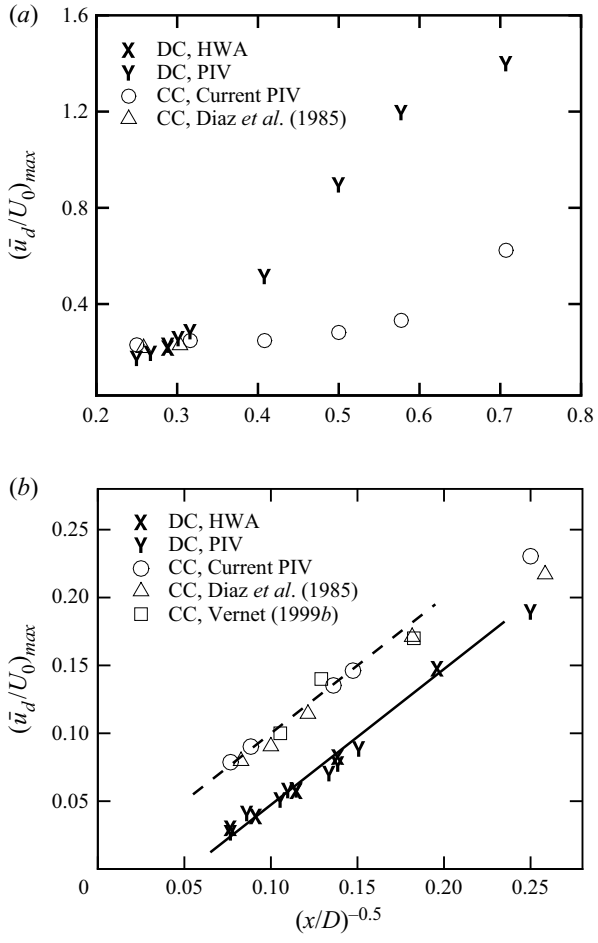

Figure 14. Streamwise variation of the maximum mean velocity defect $(\bar{u}_d/U_0)_{max}$ in the x–y vertical plane at $z = 0$ in the CC and DC mid–far wake: (*a*) $2 \leq x/D \leq 25$; (*b*) $16 \leq x/D \leq 180$. All of the HWA and PIV measurements in the $70 \leq x/D \leq 180$ range were obtained with model M_3 at a Reynolds number of $Re = 4.0 \times 10^3$ (see tables 3 and 5). PIV measurements in the $10 \leq x/D \leq 56$ range were obtained at $Re = 1.0 \times 10^4$. Diaz *et al.*'s (1985) and Vernet's (1999) results were obtained at $Re = 9.0 \times 10^3$ and 7.0×10^3, respectively. The dashed and solid lines for the CC and DC data, respectively, indicate the $1/(x/D)^{0.5}$ variation associated with the self-preserving solution.

show an unexpected feature with a local maximum at an intermediate vertical location, which is not present in the corresponding CC wake profiles (not shown here). Note that the local maximum in the $\bar{u}_d$ profile of figure 16(*a*) first appears at $x/D = 16$. Similarly, an unexpected feature is also apparent in the u_{RMS} vertical profiles shown in figure 16(*b*). In particular, the u_{RMS} profiles early in the DC wake ($x/D \leq 26$) feature a local minimum in the vertical region with $0 \leq y/D \leq 2$, with two peaks, one on the centreline and the other off the centreline. As the wake grows, the u_{RMS} peak values gradually decrease and at downstream station $x/D = 170$, the profile is flatter, with low fluctuation levels, with maxima close to $y_{1/2}$.

In order to elucidate whether the fast rise of $y_{1/2}$ for the DC wake in figure 15 is related to the vortical activity in the wake, we have plotted the vertical locations of maximum/peak values of u_{RMS}, $\overline{u'v'}$ and $\overline{\omega}_z$ at several streamwise locations in figure 17(*a*). Figure 17(*a*)

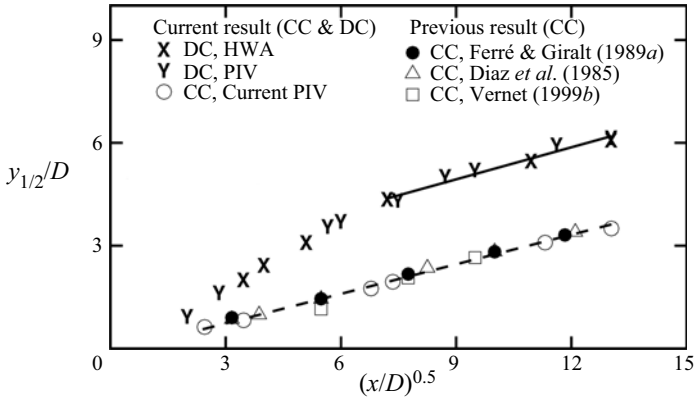

Figure 15. Variation of $y_{1/2}/D$ with streamwise location in the CC and DC wake. All of the HWA and PIV measurements in the $70 \leq x/D \leq 180$ range were obtained with model M_3 at a Reynolds number of $Re = 4.0 \times 10^3$. PIV results in the $0 \leq x/D \leq 56$ range (both CC and DC) were obtained at $Re = 1.0 \times 10^4$. Diaz *et al.*'s (1985) and Ferré & Giralt's (1989*a*) data were obtained at $Re = 9.0 \times 10^3$ whereas Vernet's (1999) data were obtained at $Re = 7.0 \times 10^3$. The fitted equations of the self-preserving solutions for the CC wake (dashed line) and the DC wake (solid line) are $y_{1/2}/D = 0.28((x/D) - 3.05)^{0.5}$ and $y_{1/2}/D = 0.40((x/D) + 67.63)^{0.5}$, respectively.

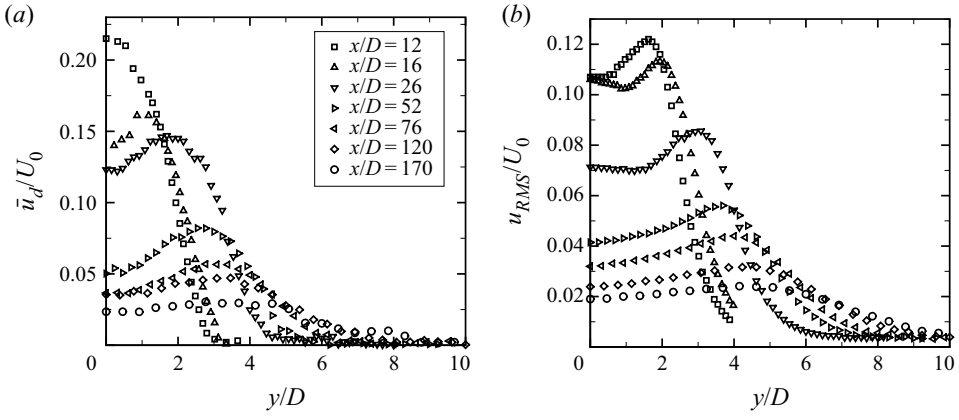

Figure 16. Vertical profiles of (*a*) the mean streamwise velocity defect $\overline{u}_d/U_0$ and (*b*) the root mean square streamwise velocity, u_{RMS}/U_0, at several streamwise stations in the x–y plane at $z = 0$ in the DC wake for HWA measurements with the DC model, M_3, at a Reynolds number of $Re = 4.0 \times 10^3$.

shows that there is a good agreement between the vertical locations of the $\overline{\omega}_z$, $\overline{u'v'}$ and u_{RMS} peaks suggesting that the peak locations in the mean field are indeed indicative of the periodic passage of coherent vortical structures. The similar plot for the CC wake is shown in figure 17(*b*). As expected, this plot confirms the well-known fact that in the CC wake the von Kármán vortices are moving away from the vertical midplane ($y = 0$) as they travel downstream. However, comparison of figure 17(*b*) with 17(*a*) indicates that such a progressive vertical displacement of the vortical structures is much faster in the DC wake, which may be at least partially self-induced by the streamwise vorticity in the legs of the HSV, which are also stretched by the mean shear. For example, the VKV are located, on average, at approximately $y/D = \pm 1.6$ to 1.7 at $x/D = 55$, which is smaller than the $y/D = \pm 4$ observed for the DC wake in figure 17(*a*) (noting that the latter vertical location

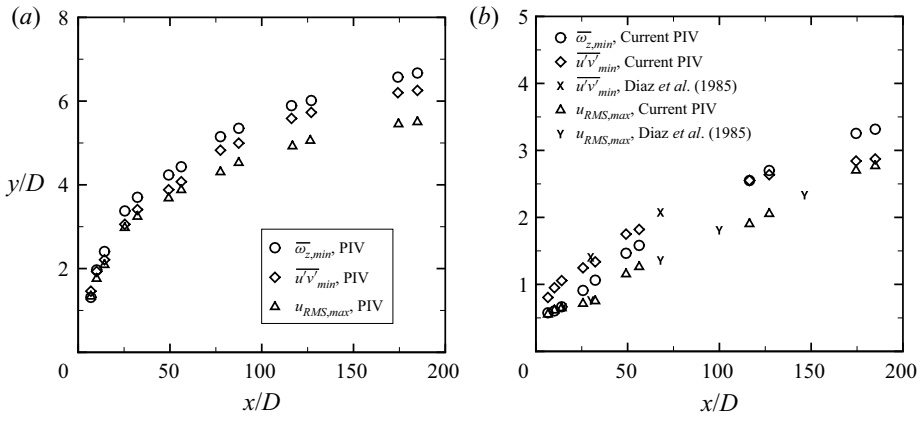

Figure 17. Variation of the peak location in the $y-$profiles of several flow variables for the (a) DC and (b) CC wakes. All of the data in this figure were obtained from PIV measurements. Measurements for $x/D \leq 56$ were obtained with the model M_2 at $Re = 1.0 \times 10^4$ whereas measurements for $x/D \geq 70$ were obtained with the model M_3 at $Re = 4.0 \times 10^3$. In (b) the experimental data previously reported by Diaz *et al.* (1985), obtained at $Re = 9.0 \times 10^3$, have been included.

is never reached in the CC wake for $x/D \leq 180$). We have, therefore, seen that momentum recovery (figure 14), vertical spreading (figure 15) and upraising of vortical structures (figure 17) takes place much sooner in the DC wake than it does in the CC wake. Thus, it can be said that the downstream position where wake is considerably reduced (i.e. $\overline{u}_d$ approaches 0) occurs much earlier because of the segmentation of the cylinder, at which point the wake is much thicker.

Self-preservation analysis applied to the far wake of the continuous cylinder (Townsend 1956; Tang *et al.* 2016) provides the following scaling laws for the centreline $\overline{u}_d/U_0$ and $y_{1/2}/D$ quantities:

$$\frac{\overline{u}_d}{U_0} = C_1 \left[\frac{x - x_0}{D}\right]^{-0.5} \tag{3.1}$$

$$\frac{y_{1/2}}{D} = C_2 \left[\frac{x - x_0}{D}\right]^{0.5}. \tag{3.2}$$

Considering that, as will be discussed further below, the vertical growth of the wake is closely related to the vertical displacement of vortical structures, it makes sense to use (3.2) to compare both wakes. For the CC far wake, values of $C_2 \approx 0.20$ and $-x_0/D$ in the $25 - 125$ range have been reported in the literature (see Tang *et al.* (2016), and references therein). For the DC data in figure 15, we have $C_2 = 0.63$ and $x_0 = 1.9D$ in the region with $4 \leq x/D \leq 36$ and $C_2 = 0.40$ and $x_0 = -67D$ for $52 \leq x/D \leq 170$.

4. Scaling of wake growth and entrainment

We have seen that the difference between the DC and the CC wake is not at the conceptual level: in both cases, the notion of the wake being a region with low mean velocity and high vorticity fluctuation levels holds. The difference between the two wakes is not in their turbulence intensity: the velocity and vorticity fluctuation levels (in the $z = 0$ plane) in the DC and the CC wakes are of the same order of magnitude. The reason for the different wake growth rates between both wakes is due to the significant changes in the large-scale

vortices induced in the near wake by the discontinuity in the cylinder geometry. In the DC near wake, the flow is three-dimensional ($\overline{\tilde{w}}/U_0 \neq 0$) and dominated by the shed HSV and the strong shear-aligned vorticity in their legs. In the CC, the mean flow is initially almost two-dimensional ($\overline{\tilde{w}}/U_0 = 0$) and controlled by the spanwise vorticity of the shed Kármán vortices with also the weaker vorticity associated with the ribs or legs of incipient hairpin vortices. A complete analogy between both wakes, on an average flow basis, would only hold when z-velocities are close to zero in the DC wake ($\overline{\tilde{w}}(x, y, z)/U_0 \approx 0$), a situation only possible at large downstream distances. Notwithstanding, it should be noted that the dynamics of HSV in the DC wake will help to understand their role in wake growth and entrainment in both wake flows.

Let us consider a simple scaling analysis to illustrate the effects on the three-dimensional mean flow associated with the shedding of HSV in the DC wake. The (mean) mass conservation requirement on a small control volume around the mid-span centreline, $(x, 0, 0)$ is

$$\frac{\partial \overline{\tilde{u}}}{\partial x}(x, 0, 0) = -\frac{\partial \overline{\tilde{w}}}{\partial z}(x, 0, 0) - \frac{\partial \overline{\tilde{v}}}{\partial y}(x, 0, 0). \tag{4.1}$$

If we consider that $\partial \overline{\tilde{w}}/\partial z \approx \Delta w/L$, Δw can be estimated as the total drop (from peak to peak) measured in a centreline z-profile (see figure 9*a*), and assume that the scaling $(\overline{u}_d/U_0) \approx (x/D)^{-0.5}$ (see § 3.3 and figure 14*a*) is approximately valid in the near DC wake, then (4.1) becomes

$$\frac{\partial \overline{\tilde{u}}}{\partial x}(x, 0, 0) = -\frac{\partial \overline{\tilde{u}}_d}{\partial x}(x, 0, 0) \approx \frac{1}{2}\left(\frac{U_0}{D}\right)\left(\frac{x}{D}\right)^{-1.5} \approx \frac{\Delta w(x)}{L} - \frac{\partial \overline{\tilde{v}}}{\partial y}(x, 0, 0). \tag{4.2}$$

If we assume that the inflow in the y-direction and toward the midplane $(x, 0, 0)$ that is induced at the front of each HSV by its top rotation, is approximately balanced by the outflow in the opposite y-direction and toward the external flow that occurs at the back of each HSV, then $\partial \overline{\tilde{v}}/\partial y \approx 0$ or smaller than $\partial \overline{\tilde{w}}/\partial z$ in absolute terms. If this is the case, $\partial \overline{\tilde{u}}/\partial x \approx -\partial \overline{\tilde{w}}/\partial z$, and all $\overline{\tilde{w}}$ profiles should scale as $(\overline{\tilde{w}}/U_0)(x/D)^{1.5}$.

Figure 18 depicts the centreline ($y = 0$) z-profiles of the dimensionless spanwise velocity $(\overline{\tilde{w}}/U_0)(x/D)^{1.5}$ at several streamwise locations. The profiles in this figure show that the proposed scaling for $\overline{\tilde{w}}$ holds in the DC wake for $x/D \leq 30$ in the spanwise direction. These results also show that the lateral fluid exchange mechanism and momentum transfer in the spanwise direction associated with the HSV, contribute significantly to the asymptotic increase with x/D of the average centreline velocity $\overline{\tilde{u}}(x, 0, z)$ toward U_0. It should be noted that, as HSV are advected downstream and their spanwise and vertical locations progressively randomized by turbulence, and as the mean spanwise velocity tends to zero, $\overline{\tilde{w}} \approx 0$, the role of $\partial \overline{\tilde{v}}/\partial y$ in DC wake growth and entrainment progressively becomes predominant. Simultaneously, the dominant contribution of the HSV to the total kinetic energy of the DC wake flow should also progressively diminish. The power spectral density of the streamwise velocity fluctuations, not shown here, indicates that this occurs for $x/D \geq 120$.

The implications of the above scaling analysis (figure 18) in the early DC wake development and growth by the large-scale motions that are linked to the progressive stretching of HSV, can only be fully understood when analysing the streamwise evolution of $\overline{\tilde{v}}$ profiles in the transverse direction at $z/D = 3.75$ and 0. Figure 19(*a*) shows that the transverse $\overline{\tilde{v}}$ profiles at the middle of the gap between cylinder segments ($z/D = 3.75$)

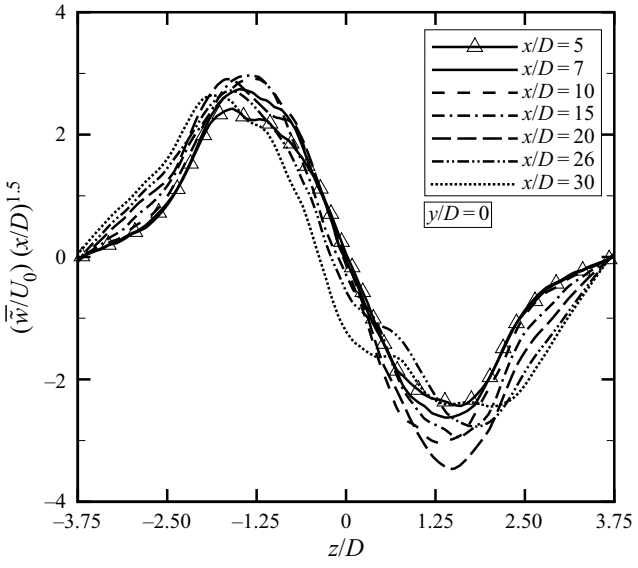

Figure 18. Selected spanwise profiles of normalized mean z-velocity, $(\overline{\tilde{w}}/U_0)(x/D)^{1.5}$, at the centreline ($y = 0$) and several streamwise locations in the DC wake, as indicated in the legend, from LES simulations.

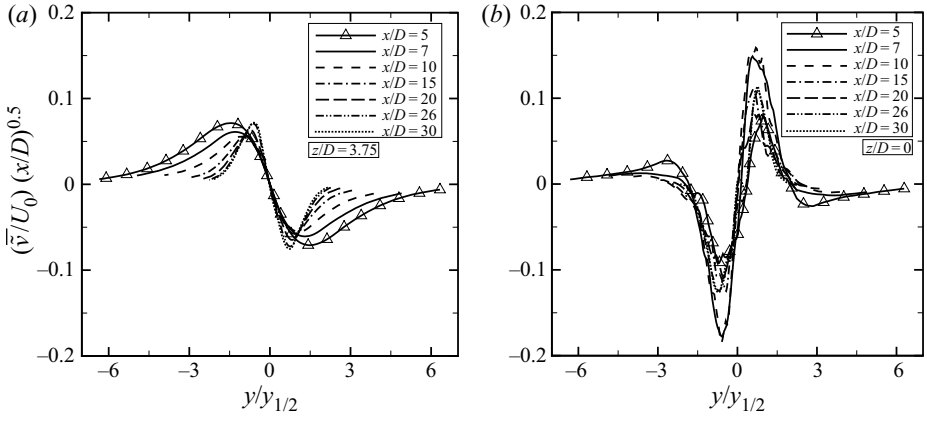

Figure 19. Selected vertical profiles of the normalized mean y-velocity, $(\overline{\tilde{v}}/U_0)(x/D)^{0.5}$, at several streamwise locations in the DC wake at (*a*) the mid-gap spanwise location ($z/D = 3.75$) and (*b*) the mid-segment spanwise location ($z = 0$), from the LES simulations.

tend towards self-similarity as x/D increases, when scaled as $(\overline{\tilde{v}}/U_0)(x/D)^{0.5}$. According to (4.2), this can only be the case if $\overline{\tilde{w}} = 0$ and $\partial\overline{\tilde{w}}/\partial z = 0$, as is the case in figure 18, and the streamwise variations of $\overline{\tilde{u}}$ and $\overline{\tilde{v}}$ are solely caused by a net vertical inflow of fluid from the external, at both sides of the wake, towards the centre plane. Since this is also the case for a fully developed CC wake, it justifies the current adoption of the scaling arising from the self-preservation analysis of the CC far wake (Tang *et al.* 2016), where $(\overline{\tilde{v}}/U_0) \propto (x/D)^{-0.5}$, with distances normalized with $y_{1/2}$. Results in figure 19(*a*) are consistent with the mean vertical motions portrayed in figure 8.

The vertical $\overline{\tilde{v}}$ profiles at the mid-segment ($z = 0$) spanwise locations shown in figure 19(*b*) also scale well with $(\overline{\tilde{v}}/U_0)(x/D)^{0.5}$ for $x/D \leq 30$. At this spanwise location at the centre of the HSV ($z/D = 0$) the vertical fluid motion has to be outward, with

$\partial\overline{\tilde{v}}(x,0,0)/\partial y > 0$, and opposite to that in figure 19(*a*) for $z/D = 3.75$, because HSV protrude vertically into the external flow to drive wake growth while stretched by the strain field, as reported by Kopp *et al.* (2002) for a fully developed CC turbulent wake. In this CC case, HSV were located inside turbulent bulges that protruded into the external flow and defined the intermittent turbulent/non-turbulent wake interface.

Let us assume that such a scale for the mean vertical motion in the DC wake, say V_ω, is also proportional to the rate of vertical growth of the wake. Then if $\delta(x_0)$ is the thickness of the DC wake at a reference streamwise location x_0, we can infer the following scaling for the wake rate of growth,

$$\delta(x) - \delta(x_0) \approx V_\omega \triangle t \propto U_0 \left(\frac{x}{D}\right)^{-0.5} \left(\frac{x - x_0}{U_0}\right) \propto \left(x^{0.5} D^{-0.5}\right), \tag{4.3}$$

or, equivalently, a wake vertical growth according to $\triangle\delta(x)/D \propto (x/D)^{0.5}$. Note the consistency of this result with the $y_{1/2}/D \propto (x/D)^{0.5}$ behaviour observed in subsection 3.3 for the DC near-to-mid wake (see figure 15). The outward vertical motion of the HSV shown in figure 19(*b*), together with the increase in the centreline streamwise velocity as x/D increases, has to fulfil continuity and be matched by the vertical inward fluid motion of figure 19(*b*), coupled with the spanwise motion towards the centre of the HSV ($\partial\overline{\tilde{w}}/\partial z \ll 0$), as illustrated in figure 18 and discussed in detail below.

Figures 19(*a*) and 19(*b*) show, on a comparable ordinate scale, the evolution of the initial growth of the DC wake in terms of the transverse velocity at the spanwise side and at the centre of the HSV, respectively. These streamwise evolutions of dimensionless vertical velocities, which are clearly related to momentum transfer into the wake from the external flow and to wake growth by HSV stretching, respectively, are dominated by the shedding of HSVs. These two figures show that both inward and outward transverse profiles progressively evolve towards self-similar profiles at both spanwise locations as x/D increases. Figure 19(*a*) shows that at $z/D = 3.75$ the recirculation associated with the shed HSV causes a reverse flow inward at the sides of each HSV, which is linked to the upward flow observed at their centre ($z/D = 0$) in figure 19(*b*). This recirculation pattern, which also involves the spanwise velocity component of figure 18, is initially dominated by the kinking of the shed HSVs caused by the flow from the gap between cylinder segments toward the back of each cylinder centre. As a result, the highest vertical velocities occur at the centre of the HSV for $x/D < 10$, as observed in figure 19(*b*). Further downstream, as x/D increases, vertical velocities and the wake growth shown in figures 14 and 15, become more and more controlled by the stretching of the HSV. This alignment and stretching by the strain field, makes the HSV to protrude toward the external flow, with vertical velocities progressively showing a self-similar behaviour for $x/D \geq 26$ in figure 19(*b*). Thus, all vertical motions clearly associated with the HSV in the DC wake show self-similarity in figures 19(*a*) and 19(*b*) when scaled according to CC wake velocity and length reference parameters. This is also the case for the gradients of the vertical profiles at the centre of the HSV in figure 19(*b*), where $\partial\overline{\tilde{v}}/\partial y(x,0,0) \propto (U_0/D)(x)^{-1.6}$ for $x/D \leq 30$, which is very close to the -1.5 power variation that holds for fully developed turbulent CC wakes. Thus, the average fluid motions that are related wake growth and entrainment by the HSV in the DC near wake scale as in the CC wake, where large-scale structures like the current HSV have been identified and claimed to play a dominant role in wake growth and entrainment.

The smooth and self-equilibrating evolution towards self-similarity and self-preservation in the DC wake flow shown in figure 19, which is controlled by shed HSV, from genesis to self-preservation, is consistent with the streamwise variations of the maximum mean velocity-defect and of $y_{1/2}/D$ shown in figures 14 and 15, respectively, for the DC wake.

The same behaviour towards self-similarly and wake growth mechanism associated with donut-like vortices or DRs was also reported by Vernet *et al.* (1999) and Kopp *et al.* (2002), respectively, in CC turbulent wakes, but for much larger streamwise distances. In the CC case, the large-scale coherent motions that develop from the hairpin vortices arising from instabilities in the VKV street (Cao *et al.* 2014; McClure *et al.* 2019), require much larger advection times or streamwise distances to develop and become shear aligned, i.e. $\partial\overline{\tilde{v}}/\partial y(x, 0, 0) \propto (U_0/D)(x)^{-1.5}$. The vertical profiles at the mid-gap ($z/D = 3.75$) and mid-segment ($z = 0$) spanwise locations, shown in figure 19, together with the scaling of (4.3), confirm that the DC geometry brings into the near wake, not only the HSV, but also another characteristic feature of the far CC wake, i.e. the self-preservation of the mean velocity profiles.

The incorporation of high momentum free-stream fluid by the linked lateral–vertical entrainment process, depicted in figures 8 and 5(*b*,*c*), which is governed by HSV, implies the extraction of energy from the mean flow and the persistence of turbulence in the wake. Mean shear production contours calculated from PIV data measured in the DC, not shown here, indicate that the highest production rates occur at $y_{1/2}$ and at the centre of the HSV for $x/D \geq 5$. This is consistent with the momentum transfer associated with the donut-like structures reported by Vernet *et al.* (1999) in a CC wake at $x/D = 150$, and with the role in the entrainment process that has been claimed for the DR identified in the far wake of a CC by Kopp *et al.* (2002). When this entrainment process is completely established in the wake of the DC at approximately $x/D = 50$, i.e. when the wake grows with $(x/D)^{0.5}$, as shown in figure 15, and $\partial\overline{\tilde{v}}/\partial y(x, 0, 0) \propto (U_0/D)(x)^{-1.5}$, HSV should be shear aligned, optimally stretched, and scalable according to (4.2) and figure 19. The CC wake also grows with $(x/D)^{0.5}$, as shown in figure 15. Note that turbulent bulges and the corresponding large-scale motions or DR in both the DC and CC wakes (Kopp *et al.* 2002) are in a region where high momentum free stream fluid can be entrained, as shown for the DC in figures 5, 6, 7 and 8. Current findings also confirm that the entrainment process is the result of linked lateral rotating motions and vertical outward jet-like motions and the rear of the DR. The overall process is strongly dominated by the stretching of the shear aligned vortex legs, i.e. by lateral entraining motions and inward motions at the front of the HSV, that in turn generate the outward jet-like motions responsible for wake growth. Turbulent diffusion seems to play a secondary role in the entrainment process but necessary one in the energy cascade and dissipative nature of the turbulent wake flow.

5. Conclusions

A study of the existing literature indicates that there is a lack of agreement regarding the mechanism of entrainment, with various studies finding differences in the relative importance of the nibbling and engulfment mechanisms. This suggests a significant flow dependence and that by controlling the development of the large-scale structures, one can control the extent to which each of these mechanisms contribute to the overall entrainment rate. The hypothesis motivating this study is that enhancing vortices that are in alignment with the mean shear will increase the rate of entrainment based on observations of flow structure and entrainment in the self-preserving regions of far wakes. We test this hypothesis by modifying the formation of the vortices in the near wake of a circular cylinder such that shear-aligned HSV are formed early in the wake. We contrast this with growth and spread of the circular cylinder wake, which is controlled by the von Kármán vortex street in the near wake. To achieve this, we develop and examine what we call a DC wake.

The turbulent flow in the wake of the DC was investigated both experimentally and numerically to ascertain the nature of the large-scale flow patterns and how these alter the overall growth and spread of the wake. The dominant flow structures in the DC wake are shown to be quasi-periodic, 3-D HSV, which are fully formed by about $x/D \approx 3$. This structure contrasts with the periodic quasi-2-D VKV in the near wake of the CC. Following the vortex formation region of both wakes, the DC wake grows at a much more rapid rate than the CC wake, although the rate of initial development of the quasi-2-D Kármán vortices is significantly higher within $x/D <\approx 3$. However, the Kármán vortices decay quickly because of the lack of shear alignment and the HSV then develop a high rate over a significantly longer spanwise distance. So, while the wakes are about the same thickness at $x/D = 4$, the DC wake is substantially thicker by $x/D \approx 8$ and maintains a higher growth rate until approximately $x/D \approx 50$. Further downstream, beyond $x/D \approx 50$, the wakes grow at the same rates, consistent with the 2-D self-preserving solution. However, the DC wake is significantly thicker, such that, at $x/D = 50$, the mean velocity half-width almost 3 times larger than that for the CC at the same physical location. At this same point, the maximum velocity defect for the DC is approximately half that for the CC even though the maximum velocity defect is significantly greater in the cylinder base region. All of this indicates a much greater entrainment rate for the DC with fully formed HSV in the near-wake region. The results indicate that the DC wake has a self-preserving form in the near wake region, but with a rate that is higher than in the fully developed far wake region. A simple scaling analysis indicates that the lateral entraining motions and the vertical stretching of the HSV can explain the growth rate of the wake.

The current findings have several implications beyond the possible development of engineering tools to increase (or suppress) turbulent mixing rates. First, with respect to self-preserving flows, it is well known that the virtual origin of self-preserving plane turbulent wakes is variable for different bluff bodies or for similar bluff bodies but in different laboratory settings. The implication from the current work is that enhancing shear-aligned vorticity in the initial conditions should decrease the position of the virtual origin, i.e. enhancing wake thickness and reducing the velocity defect. Modifying the values of L/D and S/D for the DC would do this, as could other geometric (including variable cylinder diameters along the span) or flow discontinuities for circular cylinders. Second, for other turbulent shear flows, enhancing shear-aligned vorticity should have similar effects. This would include plane turbulent jets and plane mixing layers, which, like plane turbulent wakes, tend to have primary instabilities which induce the formation of vortices that are orthogonal to the mean shear. This could also include the effects of trips for the transition of turbulent boundary layers. However, examination of such details remains for future work.

Declaration of interests. The authors report no conflict of interest.

Author ORCIDs.
V.S.R. Mandava https://orcid.org/0000-0001-5385-004X;
Francesc Giralt https://orcid.org/0000-0001-5375-3194.

References

Bailey, S.C.C., Martinuzzi, R.J. & Kopp, G.A. 2002 The effects of wall proximity on vortex shedding from a square cylinder: three-dimensional effects. *Phys. Fluids* **14** (12), 4160–4177.

Bisset, D.K., Hunt, J.C.R. & Rogers, M.M. 2002 The turbulent/non-turbulent interface bounding a far wake. *J. Fluid Mech.* **451**, 383–410.

BROWN, G.L. & ROSHKO, A. 1974 On density effects and large structure in turbulent mixing layers. *J. Fluid Mech.* **64**, 775–816.

CANTWELL, B. & COLES, D. 1983 An experimental study of entrainment and transport in the turbulent near wake of a circular cylinder. *J. Fluid Mech.* **136**, 321–374.

CAO, H.L., CHEN, J.G., ZHOU, T., ANTONIA, R.A. & ZHOU, Y. 2014 Three-dimensional momentum and heat transport in a turbulent cylinder wake. In *19th Australasian Fluid Mechanics Conference*. AFMS.

CHEVRAY, R. 1982 Entrainment interface in free turbulent shear flows. *Prog. Energy Combust. Sci.* **8**, 303–315.

CORRSIN, S. & KISTLER, A.L. 1955 Free-stream boundaries of turbulent flows. *Technical Rep.* TN-1244. NACA.

DAHM, W.J.A. & DIMOTAKIS, P.E. 1987 Measurements of entrainment and mixing in turbulent jets. *AIAA J.* **25**, 1216–1223.

DASILVA, C.B. & PEREIRA, J.C.F. 2008 Invariants of the velocity-gradient, rate-of-strain, and rate-of-rotation tensors across the turbulent/nonturbulent interface in jets. *Phys. Fluids* **20**, 055101.

DIAZ, F., GAVALDA, J., KAWALL, J.G., KEFFER, J.F. & GIRALT, F. 1985 Asymmetrical wake generated by a spinning cylinder. *AIAA J.* **23**, 49–54.

DIMOTAKIS, P.E. 2000 The mixing transition in turbulent flows. *J. Fluid Mech.* **409**, 69–98.

DOL, S.S., KOPP, G.A. & MARTINUZZI, R.J. 2008 The suppression of periodic vortex shedding from a rotating circular cylinder. *J. Wind Engng Ind. Aerodyn.* **96**, 1164–1184.

DONG, S., KARNIADAKIS, G.E., EKMEKCI, A. & ROCKWELL, D. 2006 A combined direct numerical simulation-particle image velocimetry study of the turbulent near wake. *J. Fluid Mech.* **569**, 185–207.

FERRÉ, J.A. & GIRALT, F. 1989*a* Pattern-recognition analysis of the velocity field in plane turbulent wakes. *J. Fluid Mech.* **198**, 27–64.

FERRÉ, J.A. & GIRALT, F. 1989*b* Some topological features of the entrainment process in a heated turbulent wake. *J. Fluid Mech.* **198**, 65–78.

FERRÉ, J.A., MUMFORD, J.C., SAVILL, A.M. & GIRALT, F. 1990 Three-dimensional large-eddy motions and fine-scale activity in a plane turbulent wake. *J. Fluid Mech.* **210**, 371–414.

GERMANO, M., PIOMELLI, U., MOIN, P. & CABOT, W.H. 1991 A dynamic subgrid-scale eddy viscosity model. *Phys. Fluids* **A3** (7), 1760–1765.

GERRARD, J.H. 1967 Experimental investigation of separated boundary layer undergoing transition to turbulence. *Phys. Fluids* **10**, S98–100.

GIRALT, F. & FERRÉ, J.A. 1993 Structure and flow patterns in turbulent wakes. *Phys. Fluids* **A5**, 1783–1789.

GRANT, H.L. 1958 The large eddies of turbulent motion. *J. Fluid Mech.* **4**, 149–190.

HAIRER, E. & WANNER, G. 1996 *Solving Ordinary Differential Equations II. Stiff and Differential-Algebraic Problems*, 2nd edn, Springer Series in Computational Mathematics. Springer.

HAYAKAWA, M. & HUSSAIN, F. 1989 Three-dimensionality of organized structures in a plane turbulent wake. *J. Fluid Mech.* **206**, 375–404.

HOLZNER, M., LIBERZON, A., NIKITIN, N., KINZELBACH, W. & TSINOBER, A. 2007 Small-scale aspects of flows in proximity of the turbulent/nonturbulent interface. *Phys. Fluids* **19**, 071702.

HUNT, J.C.R., EAMES, I., DA SILVA, C.B. & WESTERWEEL, J. 2011 Interfaces and inhomogeneous turbulence. *Phil. Trans. R. Soc. Lond.* A **369**, 811–832.

HUNT, J.C.R., EAMES, I. & WESTERWEEL, J. 2006 Mechanics of inhomogeneous turbulence and interfacial layers. *J. Fluid Mech.* **554**, 499–519.

INOUE, O. & SAKURAGI, A. 2008 Vortex shedding from a circular cylinder of finite length at low Reynolds numbers. *Phys. Fluids* **20**, 033601.

KÁRMÁN, V. & RUBACH, H. 1912 Über den mechanismus des flüssigkeits- und luftwiderstandes. *Phys. Z.* **XIII**, Fourty nine-fifty nine.

KING, L.V. 1914 On the convection of heat from small cylinders in a stream of fluid: determination of the convection constants of small platinum wires, with applications to hot–wire anemometry. *Proc. R. Soc.* A **90**, 563–570.

KOPP, G.A., GIRALT, F. & KEFFER, J.F. 2002 Entrainment vortices and interfacial intermittent turbulent bulges in a plane turbulent wake. *J. Fluid Mech.* **469**, 49–70.

KOPP, G.A., KAWALL, J.G. & KEFFER, J.F. 1995 The evolution of the coherent structures in a uniformly distorted plane turbulent wake. *J. Fluid Mech.* **291**, 299–322.

LARUE, J.C. & LIBBY, P.A. 1974 Temperature and intermittency in the turbulent wake of a heated cylinder. *Phys. Fluids* **17** (5), 873–878.

LILLY, D.K. 1992 A proposed modification of the Germano subgrid-scale closure method. *Phys. Fluids* A **4** (3), 633–635.

MA, X., KARAMANOS, G.S. & KARNIADAKIS, G.E. 2000 Dynamics and low-dimensionality of a turbulent near wake. *J. Fluid Mech.* **410**, 29–65.

MAHESH, K., CONSTANTINESCU, G. & MOIN, P. 2004 A numerical method for large-eddy simulation in complex geometries. *J. Comput. Phys.* **197**, 215–240.

MANDAVA, V.S.R., KOPP, G.A., HERRERO, J. & GIRALT, F. 2009 Experimental investigation of the wake behind a discontinuous cylinder. In *Sixth International Symposium on Turbulence and Shear Flow Phenomena* (ed. N. Kasagi, F. Rainer, J.A.C. Humphrey & H.J. Sung), vol. 3, pp. 1089–1094.

MARTINUZZI, R.J., BAILEY, S.C.C. & KOPP, G.A. 2003 Influence of wall proximity on vortex shedding from a square cylinder. *Exp. Fluids* **34**, 585–596.

MATHEW, J. & BASU, A.J. 2002 Some characteristics of entrainment at a cylindrical turbulence boundary. *Phys. Fluids* **14**, 2065–2072.

MCCLURE, J., PAVAN, C. & YARUSEVYCH, S. 2019 Secondary vortex dynamics in the cylinder wake during laminar-to-turbulent transition. *Phys. Rev. Fluids* **4**, 124702.

MUMFORD, J.C. 1983 The structure of the large eddies in fully developed turbulent shear flows. Part 2. The plane wake. *J. Fluid Mech.* **137**, 447–456.

NORBERG, C. 1994 An experimental investigation of the flow around a circular-cylinder - influence of aspect ratio. *J. Fluids Mech.* **258**, 287–316.

NORBERG, C. 2003 Fluctuating lift on a circular cylinder: review and new measurements. *J. Fluids Struct.* **17**, 57–96.

ONG, L. & WALLACE, J. 1996 The velocity field of the turbulent very near wake of a circular cylinder. *Exp. Fluids* **20**, 441–453.

PHILIP, J. & MARUSIC, I. 2012 Large-scale eddies and their role in entrainment in turbulent jets and wakes. *Phys. Fluids* **24**, 055108.

RHIE, C.M. & CHOW, W.L. 1983 A numerical study of the turbulent flow past an isolated airfoil with trailing edge separation. *AIAA J.* **21**, 1525–1532.

ROSHKO, A. & FISZDON, W. 1969 On the persistence of transition in the near wake. In *SIAM Problems of Hydrodynamics and Continuum Mechanics*, pp. 606–616. SIAM.

SAGAUT, P. 2001 *Large-Eddy Simulation for Incompressible Flows. An Introduction*. Springer.

SMAGORINSKY, J. 1963 General circulation experiments with the primitive equations: I. The basic equations. *Mon. Weath. Rev.* **91**, 99–164.

TANG, S.L., ANTONIA, R.A., DJENIDI, L. & ZHOU, Y. 2016 Complete self-preservation along the axis of a circular cylinder far wake. *J. Fluid Mech.* **786**, 253–274.

TAYLOR, G.J. 1915 Pressure distribution around a cylinder. *Tech. Rep.* Advisor Committee for Aeronamities.

TAYLOR, Z.J., GURKA, R. & KOPP, G.A. 2014 Effects of leading-edge geometry on the vortex shedding frequency of an elongated bluff body at high Reynolds number. *J. Wind Engng Ind. Aerodyn.* **128**, 66–75.

TAYLOR, Z.J., PALOMBI, E., GURKA, R. & KOPP, G.A. 2011 Features of the turbulent flow around symmetric elongated bluff bodies. *J. Fluids Struct.* **27**, 250–265.

THEODORSEN, T. 1952 Mechanism of turbulence. In *Proceedings of the 2nd Midwestern Conference on Fluid Mechanics*. pp. 1-19. Ohio State University.

TOWNSEND, A.A. 1956 *The Structure of Turbulent Shear Flow*, 1st edn. Cambridge University Press.

TOWNSEND, A.A. 1976 *The Structure of Turbulent Shear Flow*, 2nd edn. Cambridge University Press.

VERNET, A. 1999 Private communication.

VERNET, A., KOPP, G.A., FERRÉ, J.A. & GIRALT, F. 1997 Simultaneous velocity and temperature patterns in the far region of a turbulent cylinder wake. *J. Fluids Engng* **119**, 463–466.

VERNET, A., KOPP, G.A., FERRÉ, J.A. & GIRALT, F. 1999 Three-dimensional structure and momentum transfer in a turbulent cylinder wake. *J. Fluid Mech.* **394**, 303–337.

WERNER, H. & WENGLE, H. 1993 Large-eddy simulation of turbulent flow over and around a cube in a plate channel. Selected Papers from the Eighth International Symposium on Turbulent Shear Flows, 1991. In *Turbulent Shear Flows* (ed. F. Durst *et al.*), vol. 8. Springer.

WESTERWEEL, J., FUKUSHIMA, C., PEDERSEN, J.M. & HUNT, J.C.R. 2005 Mechanics of the turbulent and non-turbulent interface of a jet. *Phys. Rev. Lett.* **17**, 174501.

WESTERWEEL, J., FUKUSHIMA, C., PEDERSEN, J.M. & HUNT, J.C.R. 2009 Momentum and scalar transport at the turbulent/non-turbulent interface of a jet. *J. Fluid Mech.* **631**, 199–230.

WILLIAMSON, C.H.K. 1996 Vortex dynamics in a cylinder wake. *Annu. Rev. Fluid Mech.* **28**, 477–539.

YAMANE, R., OSHIMA, S., OKUBO, M. & KOTANI, J. 1988 Coherent structures in the turbulent wake behind a circular cylinder. 3. Flow visualization and hot wire measurements. *Fluid Dyn. Res.* **4**, 47–56.

ZDRAVKOVICH, M.M. 1990 Conceptual over view of laminar and turbulent flows past smooth and rough cylinders. *J. Wind Engng Ind. Aerodyn.* **33**, 53–62.

ZDRAVKOVICH, M.M., BRAND, V.P., MATHEW, G. & WESTON, A. 1989 Flow past short circular cylinders with two free ends. *J. Fluid Mech.* **203**, 557–575.

ZDRAVKOVICH, M.M., FLAHERTY, A.J., PAHLE, M.G. & SKELHORNE, I.A. 1998 Some aerodynamic aspects of coin-like cylinders. *J. Fluid Mech.* **360**, 73–84.